STUDY OF WAVE INTERACTION WITH VERTICAL PILES INTEGRATED WITH OSCILLATING WATER COLUMNS

A DISSERTATION SUBMITTED TO THE GRADUATE DIVISION OF THE UNIVERSITY OF HAWAIʻI AT MĀNOA IN PARTIAL FULFILLMENT OF THE REQUIREMENTS FOR THE DEGREE OF

DOCTOR OF PHILOSOPHY

IN

OCEAN AND RESOURCES ENGINEERING

DECEMBER 2018

By

Conghao Xu

Dissertation Committee:

Zhenhua Huang, Chairperson
Albert S. Kim
Gérard C. Nihous
Kwok Fai Cheung
Oceana Francis

Keywords: wave-structure interaction, hydrodynamics, pile structure, renewable energy, coastal structure, shore protection, oscillating water column, scour

ACKNOWLEDGMENTS

I would like to express my sincere gratitude to my advisor and committee chair, Prof. Zhenhua Huang, for providing me with valuable academic guidance, constructive criticism, and encouragement. I also would like to sincerely thank all committee members, Prof. Kwok Fai Cheung, Prof. Gérard C. Nihous, Prof. Oceana Francis and Prof. Albert S. Kim for making time to serve on my PhD dissertation committee. Very special thanks are due to Prof. Cheng-Hsien Lee for his important support and valuable help in multiphase flow numerical modeling and sediment scouring part of my research.

I am also grateful to Dr. Yu Yao, Dr. Zhengzhi Deng, Dr. Fang He, Dr. Linlin Li, and fellow researchers in Department of Ocean and Resources Engineering, particularly Linyan Li for their valuable support during the course of my PhD study. My thanks also go to Mrs. Natalie Nagai for her help with many administrative matters.

Moreover, I would like to acknowledge the support of my parents, whose support and encouragement extends far beyond my PhD research. Many thanks also to my fiancée, Dr. Jinxian Li, who have endured a long separation across the Pacific Ocean and has always been loving, supportive, and understanding.

The material is based on work supported partially by the National Science Foundation under grant No. 1706938. Any opinions, findings, and conclusions or recommendations expressed in this material are those of the author(s) and do not necessarily reflect the views of the National Science Foundation.

ABSTRACT

Ocean wave energy is a source of abundant renewable and clean energy. However, a host of challenges including construction and maintenance costs and structural reliability have prevented the large-scale commercial application of ocean wave energy converters (WECs). Integrating WECs with shore-protection structures may significantly reduce the costs associated with wave energy utilization. One such integration is vertical piles integrated with oscillating water columns (OWCs), which can help achieve costs sharing and overcome the cost hurdles facing the wave energy industry.

This study examines performance of circular piles integrated with OWC devices (OWC-piles) in terms of wave energy extraction and wave scattering. Two configurations of OWC-piles, a loosely spaced configuration and a closely spaced configuration, are investigated. For the loosely spaced configuration, the spacing is large enough so that the interference between adjacent OWC-piles can be ignored. So that the performance of the loosely spaced configuration can be studied by examining the performance of a standalone OWC-pile. In chapter 2, the performance of a standalone OWC-pile configuration is investigated theoretically, experimentally, and numerically. A quadratic power takeoff model is implemented in the study. The viscous loss associated with vortex shedding is discussed based on a comparison between the theoretical and experimental results. The possible effects of spatial non-uniformity including resonant sloshing are discussed. The performance of the loosely spaced configuration is discussed. In chapter 3, the study is extended to investigate experimentally the performance of a row of closely spaced OWC-piles in terms of wave energy extraction and wave scattering. A comparative evaluation of the performance of the proposed OWC-pile in both configurations are performed. In chapter 4, a computational fluid dynamics study is presented to understand the detailed hydrodynamics involved in the wave interaction with OWC-piles for both configurations. Chapter 5 reports an experimental study investigating the scour around a row of closely spaced piles without OWC device, which affects the safety of the pile structures, especially in extreme events such as tsunamis. The purpose of this study is to provide understanding of the scour induced by the unsteady jet flow created by the narrow gaps between piles. Future work includes a three-phase simulation of the sediment dynamics around OWC-pile

structures, and numerical and experimental studies of the shore protection performance of the closely spaced OWC-piles. The three-phase flow model for these future research can be partially validated using data from chapter 5.

TABLE OF CONTENTS

LIST OF TABLES

LIST OF FIGURES

NOMENCLATURE

α	Opening ratio of the orifice (the ratio of the area of the orifice to the inner cross-sectional area of the OWC chamber)
α_R	Relaxation factor
$\bar{\eta}$	Spatial averaged water-surface displacement inside the OWC chamber
$\bar{C}_f$	Mean value of C_f of different test conditions
$\bar{w}$	Spatial average velocity of the water-surface oscillation inside the OWC chamber
Δp	Pressure difference across the orifice as a PTO mechanism
η	Free surface time series
η'	The sloshing component of the water-surface displacement inside the OWC chamber
η_I	The water-surface displacement inside the OWC chamber due to incident wave
η_{air}	Efficiency correction factor due to air compressibility
η_{gen}	Generator efficiency
η_{pneu}	OWC pneumatic efficiency
η_{rtr}	Rotor efficiency
γ	Specific weight of sand
λ	Capture width
λ/D	Capture width ratio
$\mathbf{I}$	Identity tensor
μ_t	Dynamic eddy viscosity
ω	Angular frequency
ω_t	Mean frequency of the turbulence (Specific turbulence dissipation rate)
Ω_z	The z-component of vorticity
ρ_a	Density of air

ρ_w Density of water

τ_b Bed shear stress

θ Shields parameter

$\tilde{\lambda}$ Capture width computed using wave gauge measurement

$\tilde{C_f}$ Quadratic coefficient computed using wave gauge measurement

$\tilde{w}$ Wave gauge measured vertical velocity of water surface

A_0 Cross-sectional area of the OWC chamber

A_i Incident wave amplitude

A_r Reflected wave amplitude

A_t Transmitted wave amplitude

B Width of the wave flume

c_a Speed of sound

C_c Contraction coefficient

C_D Drag coefficient

C_d Wave-power removal coefficient

$C_d^{(OWC)}$ wave-power extraction coefficient of the dual functional wave-power plant

$C_d^{(vis)}$ Viscous dissipation coefficient

C_f Quadratic loss coefficient of an orifice as a PTO mechanism

C_g Wave group velocity

C_M Inertia coefficient

C_r Reflection coefficient

C_t Transmission coefficient

D Diameter of piles

D_o Diameter of the orifice

D_r Draft of the lower skirt of the OWC chamber

D_s The distance between the lower tip of the skirt of the OWC chamber and the bottom

D_v Characteristic size of vortex

d_{50} Sediment median diameter

F Wave force

f Frequency

G Gap size between adjacent piles

g Gravitational acceleration

H Wave height

h Water depth

H/D Dimensionless wave height

h/D Dimensionless water depth

h_d The maximum deposition height

k Wave number

KC Keulegan-Carpenter number

L Wave length

L_g inertia length scale

L_h The length of the scour hole on the up-wave side

L_R Length of relaxation zone

L_s The length of the scour hole on the down-wave side

n Gap-diameter ratio

P_i Incident wave power per unit wave crest width

$P_{OWC}^{(N)}$ Period averaged OWC power output for N periods

Re Reynolds number

s Maximum scour depth

s_c Geometric scale factor

s_e The equilibrium scour depth

S_v Vortex strength

s_w Saturation of water in Volume of Fluid method

$T\sqrt{g/D}$ Dimensionless wave period

T Wave period

t Time

t_* Dimensionless characteristic time scale for scour process

T_0 A time scale in scouring

t_0 A reference instant of time

t_n Dimensionless equivalent scour time

T_r Resonant period

T_s Equivalent wave period for solitary wave

u Horizontal velocity

u_* Bed shear velocity

U_m Maximum velocity in wave

U_v Characteristic velocity of vortex

v Vertical velocity/ Water surface oscillation velocity

V_0 The complex amplitude of water surface oscillation velocity

V_c OWC chamber volume

V_d Volume of deposited sand

V_s Volume of scoured sand

$W^{(N)}$ Net work done by N waves on structure

CHAPTER 1
INTRODUCTION

In this study, a combination of the Oscillating Water Column (OWC) device with closely spaced pile breakwaters is proposed to reduce the costs for wave energy utilization and improve the performance of the breakwaters for shore protection. The purpose of this study is to provide understanding about the performance of the proposed structure as a wave farm and as a shore protection facility, and also provide some analysis of some of the research problems associated with wave energy utilization. A few research problems related to the fundamental hydrodynamics and sediment transport arise in understanding the performance, characteristics, and issues with such a structure that, which has not been studied previously in the literature, giving rise to the necessity of conducting a systematic and in-depth study around it. In this chapter, existing research and understanding of key relevant issues, including the hydrodynamics and sediment transport around a standalone pile and pile group structures as well as OWC wave energy conversion devices are reviewed, critical research gaps are identified based on a literature review, and research objectives and motivation are discussed.

1.1 Background

In the last few decades, the progressive depletion of fossil fuel resources and the significant environmental footprints associated with fossil fuel-based energy have triggered widespread interest in the development, testing, and commercial utilization of renewable energies. Taking Hawaii as an example, the state is surrounded by the Pacific Ocean, and a core strategic goal of its energy policy is to maximize affordable clean energy. The state has determined to achieve 100 percent renewable energy generation by 2045 (Hawaii State Energy Office, 2007). The ocean is a tremendous source of renewable energy, and ocean wave energy is one of the four main sources of energy in the ocean. Ocean wave energy is clean and abundant; it is estimated that the available ocean wave energy globally is on the terawatt level (Falnes, 2007; Bureau of Ocean Energy Management, 2017).

However, despite the rich abundance and widespread interest, large-scale commercial utilization of ocean wave energy has yet to manifest. This is mainly due to the fact that currently, electricity produced from ocean wave energy is not economically viable. A host of challenges, including high costs incurred in using current technologies to generate electricity(López et al., 2013), have made the electricity generated by wave energy devices economically less competitive. These challenges include reducing construction and operation costs, increasing reliability, being suitable for a wide range of wave conditions, and minimizing potential environmental impacts. For example, while a wave energy conversion (WEC) device must be optimized to the local prevailing wave conditions, its structure must withstand local extreme events, which will significantly increase the construction and maintenance costs of wave-power plants. To make wave energy economically competitive,

innovative concepts to reduce costs are crucial in order to overcome the cost hurdle associated with wave energy utilization.

Among all WEC devices studied so far, Oscillating-Water-Column (OWC) type devices are one of the most studied and tested. A typical OWC device consists of a semi-closed and semi-submerged pneumatic chamber and a power take-off (PTO) system (e.g., a turbine and an electric generator). Incident waves create a fluctuation of the air pressure inside the pneumatic chamber, which forces the air trapped in the chamber to drive a turbine connected to a generator for electricity generation (Evans, 1978). Figure. 1.1 shows a sketch of an OWC device.

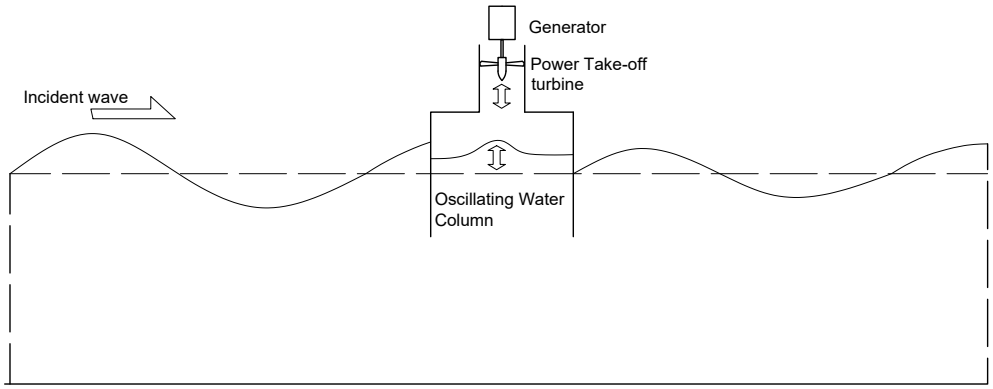

Figure 1.1: An illustrative sketch of the mechanism of an oscillating water column device.

Like all other wave energy conversion devices, the economic viability of OWC type devices is also a hurdle towards the large-scale commercial application. OWC type devices are the most studied and tested WEC devices because the design is simple and robust, which is beneficial for cost-control. Notably, the PTO mechanism of the OWC device is not submerged; thus the reliability of the PTO is better compared to many other types of WEC device. However, structural reliability issues still make investments in such wave energy conversion risky. In order to further reduce the construction and maintenance cost, while improving the reliability of OWC wave energy devices, incorporation between coastal structures and OWC devices is proposed and tested (Martins-Rivas and Mei, 2009; Henriques et al., 2013; Torre-Enciso et al., 2009; Boccotti, 2007a; Arena et al., 2013, etc). All of the existing studies proposing and testing such ideas have mainly looked at combining OWC devices with either a seawall/vertical wall, or caisson structures sitting on rubble mound foundations as breakwaters. The combination of OWC devices with these coastal structures has two advantages. First, the construction costs are shared between the two purposes of the combined structure, which effectively reduces the cost of ocean wave energy. Second, coastal structures are traditionally designed to withstand local extreme wave conditions, which in effect improves the structural reliability of the OWC devices incorporated into them. Laboratory experiments have also found that incorporation of OWC devices with seawalls and caisson breakwaters significantly increased the wave energy extraction efficiency of the OWC device, due to the strong reflection in

front of such coastal structures. However, as noted by Mustapa et al. (2017), these structures are usually constructed in very shallow water or along the coastline. Various wave energy dissipation mechanism including bottom friction loss and more importantly, wave breaking, could effectively reduce the amount the wave energy reaching the OWC devices, thus reducing the effective power output of the devices. It is thus of interest to build such devices deeper and just outside the surf zone. Rubble mound structures and caissons become prohibitively expensive in deeper water, which means innovative structures are needed. Several theoretical and laboratory studies have proposed the incorporation of OWC devices with floating moored or pile-supported structures (e.g., He et al., 2013; He and Huang, 2014). However, the reliability of floating structures strongly depend on the mooring systems and could suffer from bio-fouling. In terms of safety and maintenance costs, it may be more effective to combine OWC devices with a bottom-sitting vertical pile breakwater, which can be easily constructed outside the surf zone to make more wave energy available for extraction, while potentially providing shore protection functionalities.

Traditionally, segments of rubble mound breakwaters, caisson breakwaters, and wave barriers such as slotted barriers and pile-curtain breakwaters have been used along coastlines to control the cross-shore and longshore sediment transport induced by the incident wave for shore protection purposes (Dally and Pope, 1986; Thomalla and Vincent, 2003). Figure 1.2 shows an example of a beach nourishment project utilizing segments of rubble mound breakwaters to protect and nourish sandy beach. Breakwater segments reduce the amount of wave energy reaching shoreline by reflecting and dissipating part of the incident wave energy. When OWC devices are incorporated into these wave barriers, the additional effect of wave energy extraction may further reduce the amount of wave energy reaching inside the structure, thus enhance the shore protection function of the structure. It has been found that offshore wave farms could reduce beach erosion along a certain section of coastline behind the OWC-wave barrier wave farms, a feature greatly desired by the shore protection community. When the wave farm is located far away from the shoreline, the wave climate near the shoreline is minimally affected (Millar et al., 2007). However, Abanade et al. (2014) and Mendoza et al. (2014) found through numerical simulation that when a wave farm in the form of loosely spaced WEC devices is placed near the shoreline, the wave climate between the wave farm and the shoreline can be reduced and the sediment transport weakened to reduce beach erosion at certain locations. This finding indicates that the incorporation of OWC devices with permeable breakwaters could be a good method for enhanced shore protection.

Pile breakwaters are shore-parallel structures, which have been traditionally used at small boat harbors or marinas. A typical pile breakwater consists of a row of closely spaced piles (Kakuno and Liu, 1993; Sundar, 2002; Suh et al., 2007). Compared to traditional bottom-sitting breakwaters, the construction cost of pile breakwaters is relatively insensitive to water depth, allowing such structures to be built deeper outside the surf zone. Compared to floating moored and pile-supported breakwaters, pile breakwaters are structurally more reliable because they have no moving parts or

Figure 1.2: A example of a beach nourishment project using segments of rubble mound breakwater for beach nourishment and shore protection in Miami, US (Cederberg et al., 2018).

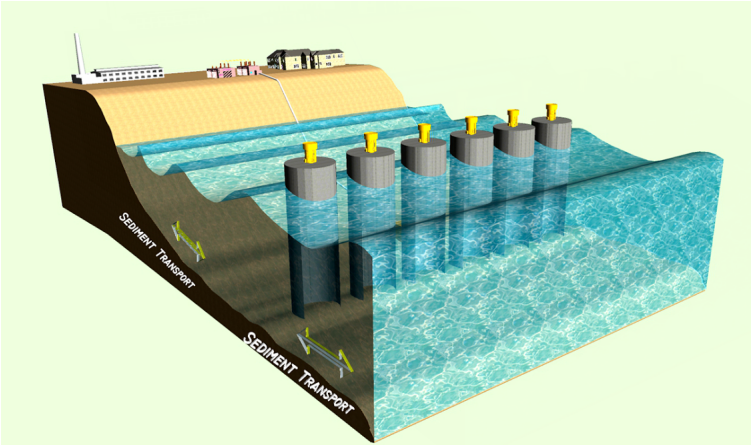

Figure 1.3: A concept of the proposed dual functional OWC-pile breakwater and wave farm. From Xu and Huang (2018).

mooring requirements. Pile breakwaters are also easy to pre-fabricate and have a small ecological footprint (by allowing water, marine life and sediment exchange across the breakwater). Thus, pile breakwaters are ideal for integrating with OWC devices for wave energy extraction and shore protection for sustainable coastal development.

1.2 Motivation and objective of this work

In this study, a combination of OWC devices integrated with vertical pile structures and permeable breakwaters is proposed for wave power generation and shore protection. The proposed structure is a row of closely spaced vertical piles with OWC devices incorporated into them. Figure 1.3 shows an artist's concept of the proposed combined structure. Compared to existing wave power generation devices, the proposed structure is reliable and relatively cheap to construct, even when sited deeper outside the surf zone. Compared to existing shore protection devices, the added wave energy extraction of the proposed structure could effectively reduce the wave energy reaching the shoreline, which could potentially improve the shore protection performance. Compared to other wave farms with shore protection potential studied in the literature, the proposed structure is closely spaced and covers a more extended section of shoreline, and thus could perform more effectively in terms of both wave energy conversion and shore protection.

To understand the performance of the proposed dual functional OWC-pile breakwater wave farm and the physical processes of wave interacting with such a structure, a few performance and physical aspects are identified that requires systematic study. In Section 1.3, these aspects are discussed, and a general review of the current understanding of these aspects is given.

Based on the literature review and nature of the proposed combined dual functional OWC-pile wave farm and breakwater, the following questions can be raised regarding the performance and characteristics of hydrodynamics and sediment transport of the proposed concept:

1. How would the OWC pile in a standalone configuration or loosely spaced configuration perform in terms of wave power extraction?

2. How would the spatial non-uniformity inside a axisymmetrical OWC chamber influence the measurement of wave power extraction?

3. How would the OWC piles in a closely spaced configuration perform in terms of wave power extraction and wave transmission/reflection?

4. In a closely spaced configuration, how would the wave power extraction due to the OWC device affect the wave energy dissipation?

5. What are the characteristics of vortex shedding from a OWC pile?

6. What is the spatial and temporal scour pattern and maximum scour depth at the OWC-pile breakwater on a sandy seabed?

7. How would the critical flow structures such as horseshoe vortex be affected by the narrow gaps formed by the closely spaced OWC piles?

The research presented in this study is focused on answering the first five questions and partially answering questions 6 and 7 within the frame of available resources. As part of a larger research project, the work presented in this study establishes a solid foundation for further studies, which will be conducted by the author and the author's successor. The principal objectives of the study described in this dissertation are as follows:

1. Perform theoretical, laboratory and numerical investigations of the hydrodynamic performance and wave energy extraction performance of the proposed OWC-pile device in a standalone and loosely spaced arrangement. The non-linear PTO should be modeled properly to provide an accurate representation of the original concept as tested physically. The spatial non-uniformity effect of this particular OWC chamber geometry need to be investigated systematically to provide an accurate estimation of the magnitude of influence of the spatial non-uniformity under different wave conditions. Based on the results obtained, the performance of a wave farm with loosely spaced OWC-piles is evaluated.

2. Perform laboratory and numerical investigations of the hydrodynamic performance and wave energy extraction performance of the proposed dual functional OWC-pile breakwater wave farm. The focus should be given to the evaluation of the performance of the proposed concept in wave field, as well as the wave energy dissipation due to viscous effects.

3. Based on the laboratory and numerical results mentioned in objectives 1 and 2, a systematic investigation on the vortex dynamics and energy dissipation around OWC-pile breakwater in waves is necessary to provide insight into the detailed hydrodynamics.

4. Implementation, testing and critical evaluation of a sophisticated numerical model that is capable of simulating the hydrodynamic, wave energy and sediment transport phenomenon in three-dimension with adequate detail and accuracy.

5. Perform laboratory experiments to investigate the sediment scouring around a row of closely spaced piles without OWC devices under wave condition. A detailed three-dimensional scour profile should be obtained so that validation with the three-dimensional numerical model can be performed. This experiment also represent a cornerstone towards understanding the sediment transport and scouring around the dual-functional OWC-pile breakwater wave farm under the effect of waves.

1.3 Relevant previous studies

The performance of the combined structure of OWC-pile breakwater is evaluated from two aspects. Firstly, its performance as a breakwater for shore protection, i.e., the wave transmission, reflection and wave energy removal from the wave field, sediment transport and scouring at the foundation as well as shoreward of the structure. Secondly, its performance as a wave farm, i.e., maximum wave energy extraction efficiency and the width of the frequency band with high efficiency. The former aspect can be generalized as a generic problem of wave interaction with pile structures; the latter aspect can be generalized as the performance and optimization of OWC wave energy conversion devices. These two aspects are closely related and affect each other in the combined structure. For example, the structure's performance in reflecting wave energy may potentially affect the structure's overall wave energy output, while the structure's wave energy output could, in turn, affect the total amount of wave energy removed from the wave field. In this section, previous studies relevant to these two aspects are reviewed and discussed.

1.3.1 Oscillating water column and its integration into breakwaters

For decades, theoretical studies (Evans, 1978, 1982; Sarmento and ao, 1985; Evans and Porter, 1995; Martins-Rivas and Mei, 2009; Deng et al., 2013, 2014), as well as laboratory and prototype experiments (ao, 2000; Goda et al., 1991; Morris-Thomas et al., 2007; He et al., 2013; Falcão and Henriques, 2014) have been carried out to investigate the hydrodynamic performance and energy conversion efficiency of OWC devices with the primary goal of increasing efficiency and reducing cost. It has been found that for each particular OWC chamber design and characteristics of the PTO mechanism, a peak energy conversion efficiency can be achieved at a characteristic frequency. On the other hand, little or no energy conversion may be present if the incident wave excites the sloshing mode inside the OWC chamber. The PTO mechanism is a critical part of an OWC device as it controls how the pneumatic energy captured by the OWC chamber converts into mechanical energy for electricity generation and how the water column oscillation damping in the OWC chamber is characterized (Falcão, 2010; Falcão et al., 2012; López et al., 2015a). The PTO mechanism can be categorized into two types based on the pressure-velocity relationship of the device: linear PTO such as a Wells turbine (Brito-Melo et al., 2002; Gato et al., 1996), and nonlinear PTO such as the self-rectifying impulse turbine (Setoguchi and Takao, 2006; ao et al., 2013). In laboratory conditions, orifices are usually used to mimic the pressure-velocity behavior of nonlinear PTO mechanisms. Existing theoretical models based on potential flow and linear wave theory models the PTO mechanism as a linear PTO. Using these theoretical models to predict the performance of OWC devices with nonlinear PTOs may be inappropriate and can result in large errors.

For different types of OWC devices, a few issues remain inadequately answered. One is the effect

of the spatial non-uniformity of water surface inside the chamber on the accuracy of laboratory OWC measurements, particularly for axisymmetric or irregular shaped chambers. Another one is the amount and influence of additional energy loss due to vortex shedding induced by the OWC structure . The early theoretical study assumed a flat water surface inside the OWC chamber, i.e., the water surface inside the OWC chamber was treated as a rigid weightless piston (Evans, 1978). Later theoretical studies considered the effect of spatial non-uniformity inside the OWC chamber under the linear model framework (Evans, 1982; Evans and Porter, 1995; Martins-Rivas and Mei, 2009; Lovas et al., 2010; Deng et al., 2013, 2014), which is capable of resolving the spatial non-uniformity due to fundamental wave. However, these models are not able to consider the spatial non-uniformity associated with vortex shedding and higher harmonic effects. The spatial non-uniformity of water surface oscillation inside the OWC chamber may create a problem in laboratory experiments as the water surface inside the chamber can only be represented by a finite number of wave gauges inside the chamber. For laboratory experiments involving rectangular OWC chambers, the error induced by spatial non-uniformity can be reduced by placing two or three wave gauges inside the chamber (He and Huang, 2014; Bingham et al., 2015; Vyzikas et al., 2017). He and Huang (2017) proposed to perform two-point wave separation using two wave gauges inside a rectangular OWC chamber and thus eliminating the error associated with longitudinal non-uniformity and yielded satisfactory results. However, for OWC chambers with irregular shape, it is difficult to estimate and eliminate the effect of spatial non-uniformity on the accuracy of OWC wave energy conversion measurement. So far, there is no systematic investigation into the modes, mechanisms, and impact of the spatial non-uniformity effect in laboratory experiments with OWC models.

Wave energy dissipation due to viscous effects is an important performance aspect of the OWC device. The portion of energy dissipated due to viscous effects cannot be utilized by the wave energy converter, even if the OWC chamber and PTO system are ideally optimized. Sharp edges or lips on the OWC device, such as the lower skirt of the OWC chamber, could be significant sources of vortex shedding and, therefore, energy dissipation in a wave field. By carefully designing the shape of the OWC structure, it is possible to reduce vortex shedding, thus reducing energy dissipated due to the viscous effect of vortex shedding (Graw et al., 2000). Traditionally, quantification of the amount of energy lost in the viscous dissipation of vortex shedding is indirect, usually performed by measuring the transmission, reflection and wave energy extraction while invoking the energy balance equation (Tseng et al., 2000; He et al., 2016). With the progress of measurement technology, experimental studies utilizing particle image velocimetry (PIV) are able to provide detailed flow field locally and partially reveal the vortex shedding and energy dissipation rate around an OWC device (Fleming et al., 2012). However, even with a sophisticated PIV technique, only a portion of the flow field could be obtained experimentally. For OWC structures with a complex geometric layout such as a circular OWC-pile, PIV along cannot provide enough information for a detailed account and

characterization of energy loss due to viscous effect.

Three-dimensional numerical modeling is a good way to provide more insight into both the spatial non-uniformity of the water surface inside the chamber, and the energy loss due to viscous effect. However, numerical studis of OWC devices using computational fluid dynamics tools have long been limited by the computational capability. In recent years, with the development of computational power, it has become possible to fulfill the heavy computational demand raised by the explicit modeling of the PTO simulating orifice. Simonetti et al. (2015) numerically investigated the geometric optimization of a type of fixed OWC device with rectangular chamber cross-sections using OpenFOAM. A large eddy simulation was implemented for turbulence modeling, and the PTO orifice was modeled explicitly by mesh refinement. Iturrioz et al. (2015) reported a numerical study of an OWC device using OpenFOAM, RANS turbulence closure was used in the study and the PTO orifice was modeled explicity. The authors reported notably good agreement with the experiment in terms of air and water pressure, as well as free surface elevation both inside and outside the OWC chamber. Elhanafi et al. (2016a) used StarCCM to numerically investigate the 2D hydrodynamic performance of a fixed OWC device with rectangular chamber cross-section. A detailed validation was performed to reproduce the flow field including turbulence characteristics in the OWC chamber accurately and the numerical model was then used to investigate the effect of various design parameters on the performance of the OWC device.

It has been reported that integration of OWC wave energy converters with marine structures such as breakwaters may be able to effectively reduce the construction, installation and maintenance cost by cost sharing (Mustapa et al. 2017). The first attempt to incorporate an OWC device with a breakwater was located at Sakata Port in Japan (Takahashi et al., 1992). This device was constructed as a 7m-wide single block structure connected to a caisson breakwater. Two of Wells turbines were used as the power take-off and conversion mechanism. Boccotti (2007a), Boccotti et al. (2007) and Boccotti (2007b) proposed a caisson breakwater with a U-OWC device. They showed theoretically and experimentally that by properly optimizing the design of the caisson breakwater-OWC system, the efficiency of the U-OWC device could be greatly improved. A prototype caisson breakwater with a U-OWC was later constructed in the Mediterranean Sea in REWEC3 project (Arena et al., 2013) in the harbor of Civitavecchia, Italy. Another application of the incorporation of an OWC and breakwater was put to service in Mutriku wave energy plant in Spain (Tease et al., 2007). The Mutriku wave energy plant is a multi-chamber OWC array built into a 600m long rubble mound breakwater with a concrete core. The OWC array consists of 16 OWC chambers and is 100 m long in the center section of the breakwater. The Mutriku wave energy plant has an installed power of 296kW, and is estimated to be able to accommodate around 250 households. Currently, all proposed combination of OWC devices with marine structures tested as prototypes are impermeable and built in shallow water. For novel permeable OWC-breakwater designs, He et al. (2012) and He et al. (2013) investigated experimentally the hydrodynamic per-

formance of a floating moored breakwater with symmetric and asymmetric OWC chambers. It was demonstrated that the performance of the structure as a floating breakwater with the OWC chambers added has increased, and asymmetric design of the OWC chamber was able to improve its performance in wave energy extraction. He and Huang (2014) extended this study to a floating pile-supported breakwater with OWC built-in. As mentioned in Section 1.1, the reliability of the mooring system and bio-fouling issues with the pile-supported design remain challenging issues.

1.3.2 Hydrodynamics and sediment transport around a single pile

Vertical piles are one type of marine structure. They can be used as pile breakwaters (sometimes referred to as "wave barriers") and supporting structures for other marine structures such as offshore wind farm monopiles, coastal bridge piles and piers. Figure 1.4 shows a photo of a wave barrier in the form of a row of closely spaced circular piles. Compared to conventional rubble mound or caisson structures that mainly rely on gravity to provide stability, pile structures are light, permeable, and cheaper for use at large water depths. As the first step to more complex pile group structures, understanding the sediment transport, scouring, and hydrodynamics around single piles in flow is important.

Figure 1.4: A wave barrier in the form of a row of closely spaced circular piles (Huang et al., 2011).

The hydrodynamics of flow interaction with a single pile has been studied extensively in the literature. For the scenario of a single pile structure in a current, the pile blocks the current flow and creates two critical types of flow structures: horseshoe vortex and lee wake vortex (Richardson and Panchang, 1998; Salaheldin et al., 2004). The lee wake vortices are generated by the boundary layer separation on the surface of the pile structure (Barbi et al., 1986). Under a higher Reynolds number, the lee wake vortices become unsteady and may be shed from the back of the pile, creating a vortex street. The horseshoe vortex is generated by the three-dimensional bottom boundary layer separation caused by the adverse pressure gradient in front of the pile structure near the

bed (Salaheldin et al., 2004; Melville and Raudkivi, 1977; Dargahi, 1989). The adverse pressure gradient originates from the bow wave, which is a raised water surface due to blockage by the pile. The bow wave also creates a downflow right in front of the pile (Ahmed and Rajaratnam, 1998). The mixture of the downflow and the separated boundary layer flow excites a rotational flow and thus forms the horseshoe vortex. It is also found that the horseshoe vortices may occasionally roll up towards cylinder surface and become a primary lee wake vortex system (Sahin et al., 2007), this indicates that lee wake vortices may be dependent on the horseshoe vortex.

While there is relatively abundant documentation on the flow structure of single pile structure exposed to steady currents, existing literature investigating the flow structure of single pile structure under wave conditions is scarce. In a laboratory experiment by Sumer et al. (1997), they found that in the case of regular waves, the size and lifespan of the horseshoe vortex and lee wake vortices are strongly affected by the Keulegan-Carpenter number $KC = U_m T/D$, where U_m is the maximum wave induced orbital velocity at the bottom, T is the incident wave period and D is the characteristic cross-section dimension of the pile. An increased KC number leads to increased size and lifespan of the horseshoe vortex. Recently, the numerical work of Baykal et al. (2017) provided a detailed visualization of vorticity and amplification of bed shear stress near the pile structure. These visualization and quantitative analysis clearly show the difference in the horseshoe vortex and wake vortices near a vertical pile under waves, compared to that under steady current. Under wave condition, the horseshoe vortex only exists for a portion of the half period of the wave before flow reversal, and there may not be enough time for the lee wake vortex to develop. One of the reasons for such difference can also be attributed to the small wave boundary layer thickness.

When a pile is placed on a sandy bottom, the altered hydrodynamics caused by the pile also changes the sediment transport and scouring pattern around the pile. The horseshoe vortex has been demonstrated to amplify the bed shear stress by a factor of 7 to 11 times compared to its undisturbed value in steady currents (Baker, 1979). In case of regular waves, the amplification of bed shear stress due to the horseshoe vortex can be as large as 7 times, depending on the KC number (Sumer et al., 1997). Increased bed shear stress causes increased sediment transport and scouring around the single pile structure, which gives rise to the need to further understand sediment transport and scouring around single pile structures.

Sediment transport around vertical pile structures has been extensively studied in the last century. The first of such studies were motivated by attempts to understand the scour pattern of bridge piles under steady current (Richardson et al., 1993; Breusers et al., 1977; Melville and Sutherland, 1988; Johnson, 1995; Melville and Chiew, 1999). Empirical formulas for the equilibrium scour depth around pile structures were proposed. A distinction has been made to distinguish clear water scour (when the undisturbed flow creates a shear stress smaller than the critical shear stress of an erodible bed, and no sediment transport is occurring in undisturbed flow) and live bed scour (when the undisturbed flow creates shear stress large enough to mobilize a static erodible bed).

In general, a relatively good understanding of the scouring around pile structures under steady current has been generated.

During the past 40 years, studies have been extended to study the sediment transport and scouring induced by the interaction of pile structures with more transient flow conditions such as tidal currents (Sumer et al., 1992b; Escarameia and May, 1999; McGovern et al., 2014) and waves (e.g., Zhao et al., 2010; Baykal et al., 2017; Sumer et al., 1992a). For more transient flow, timescale becomes an important factor to scouring because it determines whether the critical hydrodynamic flow structure can be fully developed, or its size and lifespan before being destroyed by the variation of the flow. It was found that the scour depth around the pile structure is related to the KC number (Sumer et al., 1992b, 1993). Horseshoe vortex and the lee wake vortex are found to be responsible for the sediment suspension and removal from around the pile under most conditions. For a very small KC number ($KC < 2$), the main mechanism of enhanced scouring is the steady streaming effect induced by the averaged transport of the incident wave (Sumer and Fredsöe, 2001a).

1.3.3 Hydrodynamics and sediment transport around pile groups

When more than one pile structure is placed in a flow, the hydrodynamic and sediment transport characteristics may be significantly different compared to that of a single pile. Particularly, the distance between piles is a critical factor; if the distance between piles is small, local flow contraction effect may induce high-speed jet flow in the gap between piles, resulting in more complex flow structure, significantly higher bed shear stress and thus more significant scouring. The jet flow also poses difficulty in numerical modeling as it limits the time step size determined by numerical stability conditions. Considering this change of flow pattern, we categorize pile groups into loosely spaced pile groups (gap size between piles are more than 50% of the pile diameter) and closely spaced pile groups (gap size between piles are less than 50% of the pile diameter).

Zdravkovich (1987) characterized the interference of neighboring pile members in an emerged pile group or array into several parts: 1) proximity interference, which occurs when the piles are close to each other, 2) wake interference, which occurs when a pile is in the lee wake vortex of another pile; 3) combined proximity and wake interference, which occurs when the conditions of the former two items are satisfied at the same time; or 4) no interference, which occurs when the piles are far enough from each other so that no significant contraction of flow or lee wake vortex interference is present. The mechanism of interference between piles may be slightly different for loosely spaced and closely spaced pile groups, and relevant studies of these two types of pile groups are thus reviewed in the following.

Existing research on the hydrodynamics of loosely spaced pile groups in steady currents mainly focused on three pile arrangement layouts: side-by-side (Brun et al., 2004; Zhao and Sheppard, 1999), tandem (Jendrzejczyk and Chen, 1985; Wu et al., 1994) and staggered (Hu and Zhou, 2008a,b; Zhao and Sheppard, 1999). The total number of piles in the pile group studied ranges

from 2 to more than 50. It was found that the most important factor that affects the hydrodynamics of pile groups is the pile spacing. The closer together the piles are, the more interference is observed. Physical details such as the pressure gradient in front of the toe of the pile members, momentum transfer (Hu and Zhou, 2008b) and wake flow structure (Hu and Zhou, 2008a) have been investigated experimentally. Important flow structures observed in flow interaction with a single pile, such as horseshoe vortex, is still observed in a loosely spaced group of piles.

In terms of the hydrodynamics of a loosely spaced pile group in a wave field, existing research mostly focused on the wave scattering by a pile group consists of multiple rows of piles (Li and Mei, 2007; Hu and Chan, 2005; Linton and Evans, 1990). Scattering theories describing wave propagation past rows of piles are derived (Ohkusu, 1972; Spring and Monkmeyer, 1975; McIver and Evans, 1984; Simon, 1982). These proposed models approached to solve the wave field around pile groups by considering the wave scattering effect; the drag effect is not considered, this suggests that these models are most suitable for large cylinder members that are widely apart from each other, so that the contracted jet flow is not formed. The performance of such theoretical models when applied to closely spaced pile groups is hence unwarranted.

When the distance between neighboring piles are very close, i.e., the gap size between the piles are less than 50% of the size of the piles, flow through the narrow gap gets contracted, and a significant jet flow may form at the gap. If the overall dimension of the pile group is not very large, the pile group starts to behave like a single larger pile (Zdravkovich, 1987). If the overall dimension of the pile group is very large, for example, if it is a very long array of piles (see, for example, Figure 1.4), the pile array acts as a screen barrier that blocks flow, and thus can be used as a breakwater. Different from the hydrodynamics of loosely spaced pile groups, in which case wave scattering and inertia effect are the main hydrodynamic feature, for closely spaced pile groups, the contraction jet flow is a very important phenomenon. The contraction jet flow effectively dissipates flow energy and largely determines the flow field and energy structure in the flow.

Wide spreading interest in breakwaters and sea walls have motivated numerous studies to derive theories that predict the hydrodynamic performance of pile breakwaters. The hydrodynamic performance of a pile breakwater is usually characterized by three core functional dimensionless values, the reflection coefficient C_r (ratio between the incident wave height and the reflected wave height), the transmission coefficient C_t (ratio between the incident wave height and the transmitted wave height), and the wave energy dissipation coefficient C_d^{vis}, characterizing the portion of energy dissipated by the structure through viscous effects.

Extensive research aimed at understanding the hydrodynamics of wave interaction with pile breakwater and providing prediction models is carried out theoretically and experimentally (Kriebel, 1993; Kakuno and Liu, 1993; Huang, 2007; Suh et al., 2011) as well as numerically (Jiang et al., 2015; Wang and Wu, 2010). The main goal of these studies was to investigate the wave reflection and transmission during the process of wave interaction with pile breakwaters. It is apparent that

for permeable breakwaters, the wave reflection and transmission coefficients are directly related to the amount of energy that is dissipated by the breakwater. The more energy dissipated, the less wave energy could be reflected or transmitted. For closely spaced piles, the contraction jet flow has been identified as the critical flow phenomenon affecting the energy dissipation. The theoretical model of drag effect of wave interacting with closely spaced piles usually involves the characterization of the contraction jet flow and the pressure drop across the narrow gap (Mei, 1989). In case of long waves with large KC number, the effect of drag is the dominating factor in wave scattering and energy dissipation of wave interaction with closely spaced pile groups, hence the effect of inertia becomes less important. Thus, some models for long wave interaction with pile breakwaters consider the effect of drag but not inertia (Kriebel, 1993; Huang, 2007). For shorter waves or larger pile sizes in which cases the KC value is small, both drag effect and inertia effect may be important and both needs to be considered in theoretical models (Kakuno and Liu, 1993; Suh et al., 2011). The prediction capability of models proposed in the literature are generally good for slender pile members and linear waves, but the prediction accuracy of these models in case of larger pile members and non-linear wave conditions are mixed (see, for example, Suh et al., 2011).

The interaction between flow and pile structures alters local flow field and hydrodynamic conditions, generating turbulent flow structures, which can enhance the sediment transport and scouring locally (Sumer et al., 1992a). The stability of the pile structure could thus be jeopardized due to the enhanced scouring at the foundation, and may lead to the failure of the structure (Sumer et al., 1993). Therefore, understanding the enhanced sediment transport and scouring around pile structures is important from a structural safety point of view.

Research focusing on the scouring around loosely spaced pile groups in flow is abundant in the literature, most of them are motivated to understand the scouring under a bridge pile group exposed to steady currents. Studies have been carried out to investigate the scouring induced by steady current to multiple rows of loosely spaced piles (Sumer et al., 2005; Amini et al., 2012; Ataie-Ashtiani and Beheshti, 2006; Lanca et al., 2013), and a single row of loosely spaced piles (Ataie-Ashtiani and Beheshti, 2006). The effect of pile arrangement layout, spacing (Amini et al., 2012; Amini and Solaimani, 2017; Lanca et al., 2013), sediment grain size (Ataie-Ashtiani and Beheshti, 2006) and incident wave skew angle (Ataie-Ashtiani and Beheshti, 2006; Lanca et al., 2013) over the scour depth and pattern have been studied experimentally. Empirical formulas for prediction of equilibrium scour depth based on upstream flow conditions and sand bed properties have been established and widely applied in engineering applications. Since sediment transport is controlled by the flow structures, the sediment scour around pile groups are strongly affected by the pile spacing. When the pile spacing is large enough, the scour approaches that of a standalone pile for each pile in the pile group. When the piles are closely spaced, the scour depth effectively enhances due to the enhanced jet flow through the narrow gaps formed between adjacent piles. In more transient flow condition such as regular waves, a clear correlation between the maximum

scour depth and the KC number is also clearly observed (Bayram and Larson, 2000; Myrhaug and Rue, 2005; Liang et al., 2012).

Compared to the relatively abundant documentation of studies of scouring around loosely spaced pile groups, the scouring around closely spaced pile groups received less attention in the literature. For the case of steady current, Ataie-Ashtiani and Beheshti (2006) reported a case with the pile group model within the closely spaced pile group region (gap size is 25% of the pile diameter), but only with two piles arranged side-by-side. It was found that for this particular case, the maximum scour depth was about 50% larger than the single pile value, also significantly larger than any of the other pile group cases tested. The authors intuitively attributed the reason of this enhanced scouring to the size of the horseshoe vortex and the high flow speed in the gap. The same phenomenon is also observed in a few closely spaced pile group scour tests in Amini et al. (2012). A correction factor was proposed by Ataie-Ashtiani and Beheshti (2006) to be used to correct the scour depth calculated using formulas intended for single piles to account for the effect of spacing between pile groups.

Only one report is seen in the open literature that systematically studied the scouring around closely spaced pile groups in waves. Sumer and Fredsøe (1998) conducted laboratory experiment investigating regular wave induced scouring around circular pile groups with a range of pile spacings. A wide range of pile spacing with the gap size 1% to 200% of the pile diameter was tested. It was found that for smaller pile spacing, the pile group acted as a single pile with much deeper scour depth, while for larger pile spacing, the influence of piles to each other diminishes and piles in the pile group acted as standalone piles. For the side-by-side cases, the scour depth reached maximum with the gap size being 30% of the pile diameter, further reducing the gap size have led the scour depth to decrease. The authors explained the reason for the enhanced scouring at closely spaced end to be the contraction jet and the lee wake vortex. It was also found that a short array of 2 piles has shallower equilibrium scour depth compared to a slightly longer array of 3 piles in side-by side arrangement, and both cases had significantly larger scour depth compared to standalone pile cases. This clearly shows how the scouring may be different between a shorter pile group and a longer pile group. Sumer and Fredsøe (1998) suggested this is due to the enlarged area of bed exposed to pile array influence in the longer array case. Sumer and Fredsøe (1998) highlighted the difference between standalone pile and pile arrays in wave conditions. However, they did not provide any information for highly non-linear wave such as solitary waves, or for straight and longer side-by-side pile arrays so that for the central pile members, the effect of the piles at the tip becomes negligible. Generally speaking, there is still very little literature on understanding the scour around a row of closely spaced piles in waves.

1.4 Dissertation outline

The organization of the rest of this dissertation is outlined as follows. Chapter 2 presents a combined experimental, theoretical and numerical study of a single axis-symmetric oscillating water column device with a quadratic power take-off model. Laboratory experiment data is reported, a theoretical model based on the work of Deng et al. (2013) and the quadratic PTO model is developed. A RANS-VOF based numerical model is tested and validated against experimental data and the effect of spatial non-uniformity is discussed based on experimental and numerical results. The numerical results are used to evaluate in prototype scale the performance of a row of loosely spaced OWC-piles for shore protection and electric power output. Moreover, the detailed flow field obtained by the numerical simulation is visualized to provide a qualitative analysis of the vortex dynamics and potential sediment scouring around a standalone OWC-pile exposed to regular waves.

Chapter 3 presents an experimental study of a row of closely spaced OWC piles as a dual functional OWC-pile breakwater wave farm. Experimental results are presented and a comparison of the hydrodynamic performance of the current device with a device with identical dimensions but without the OWC devices is conducted. A semi-theoretical model for the estimation of vortex shedding induced energy loss is presented. A scale-up of the tested model into prototype scale is proposed, and the performance of the prototype-scale device in terms of wave transmission and reflection, as well as electric power output, is presented. A comparative evaluation of the proposed loosely spaced and closely spaced configurations is conducted.

Chapter 4 presents a computational fluid dynamics study of a row of closely spaced OWC piles. In this chapter, numerical simulations of the experiment are carried out to provide insight into details of the flow field. Vortex structures found near the bed are visualized and their implications on the sediment scouring around the OWC pile structures are discussed. The results are also compared to the numerical results presented in chapter 2 and conclusions regarding the change in the flow field due to the addition of adjacent OWC pile members in a wave field are drawn.

Chapter 5 presents a laboratory experiment of sediment scour around a row of closely spaced piles without OWC devices under the effect of repeating solitary waves. Detailed three-dimensional bed profile data showing the temporal and spatial development of the scour profile is presented, and the effect of wave height and water depth is discussed.

Finally, in chapter 6, main findings and conclusions of this study are summarized. Moreover, because the present study is only a part of a bigger project aimed at investigating multiple aspects of the proposed structure, outstanding issues and future works are also identified.

CHAPTER 2
ON THE HYDRODYNAMIC AND WAVE ENERGY EXTRACTION OF AN AXISYMMETRIC OSCILLATING WATER COLUMN DEVICE WITH A QUADRATIC POWER TAKE-OFF MODEL

2.1 Introduction

As a first step in understanding the performance of the proposed OWC-pile breakwater wave farm concept, a combined study of the performance of the OWC-pile device is presented. The performance of the OWC-pile device in a wave field is a complicated water-structure-air interaction process, and multiple investigation methods including theoretical models, laboratory experiments and CFD numerical simulation are employed to provide an understanding of the performance of this device and other issues associated with OWC wave energy conversion.

Scaled laboratory experiments can provide observations of some physical processes during energy extraction of OWC devices and improve the PTO system optimization. A number of experimental studies on the hydrodynamics and energy extraction of OWC devices can be found in the literature. Existing experimental studies focused on understanding wave energy capture efficiency (Wang et al., 2002; He et al., 2013; Ning et al., 2016b; Xu et al., 2016; Fleming and Macfarlane, 2017; Vyzikas et al., 2017); and hydrodynamic characteristics such as vortex shedding, wave scattering, and the motion responses of floating OWC devices (Rapaka et al., 2004; He et al., 2013; He and Huang, 2014; Xu et al., 2016; Ning et al., 2016b; Fleming and Macfarlane, 2017). Falcão and Henriques (2014) discussed the model-prototype similarity issues encountered in OWC laboratory experiments. Challenges facing scaled experiments in the laboratory include consideration of air compressibility, correct representation of the air turbine used for electricity generation, and measurement of the complex water surface inside the OWC chamber.

It is widely acknowledged that spatial non-uniformity inside the OWC chamber plays a role in the measurement of OWC wave energy capture efficiency. Many small-scale laboratory tests studied two-dimensional (e.g., rectangular) OWC chambers (He and Huang, 2014; Bingham et al., 2015; Ning et al., 2016a,b) and used one wave gauge (Wang et al., 2002; Simonetti et al., 2015; Xu et al., 2016) to measure the waves inside the OWC chambers. The use of one wave gauge makes it difficult to accurately determine the mean motion of the air-water surface inside the OWC chamber. He and Huang (2017) proposed a method to reconstruct the water surface inside a rectangular-shaped OWC by using two wave gauges, which allows an accurate determination of the water surface inside the OWC chamber. Bingham et al. (2015) used two wave gauges inside the OWC chamber and examined the spatial non-uniformity including sloshing inside the chamber by comparing the measurements of the two wave gauges and also visually inspecting the water surface

during the experiment. Some experimental studies revealed the spatial non-uniformity inside the OWC chamber via CCD camera recordings (Ning et al., 2016b) or PIV techniques (Fleming and Macfarlane, 2017). Vyzikas et al. (2017) placed three wave probes in the width direction of the chamber to examine the lateral sloshing effect. However, systematic discussion on spatial non-uniformity and its effect on the measured capture efficiency in both two-dimensional (2D) and three-dimensional (3D) chamber geometries remains rare.

For cylindrical OWC devices where wave scattering is complicated, it is difficult to obtain a good description of the water surface non-uniformity using traditional devices such as wave gauges. Therefore, only one wave gauge is usually deployed inside the OWC chamber (e.g., Wang et al., 2002), which in the case of relatively short waves, can cause a misrepresentation of the water surface motion inside the OWC chamber, thus affecting the accuracy in the measured energy extraction efficiency. Theoretical models based on potential flow and linear wave theory can consider the spatial non-uniformity induced by the fundamental components of incident wave (Evans, 1982). However, in actual laboratory conditions, except for the spatial non-uniformity induced by the fundamental component of the incident wave, short-wave components also exist in nonlinear incident waves and can be generated by higher harmonic components in the fluctuating air pressure due to a nonlinear PTO, nonlinear wave-wave interaction, and the vortices shed from the edges of the OWC chamber. These higher harmonic waves may resonate in the OWC chamber, resulting in resonant sloshing mode inside the OWC chamber. These effects of higher harmonics and viscosity that cannot be addressed by potential flow and linear wave theory based frequency-domain solvers can be addressed by computational fluid dynamics (CFD) simulations. CFD simulations of wave interaction with OWC devices can provide valuable information about the flow field and spatial distribution of the water surface inside the OWC chamber, which is otherwise very difficult to obtain in wave-flume tests. Moreover, CFD simulation results can provide a very detailed description of the flow field around the OWC-pile device exposed to waves, which can serve as an important method in understanding the sediment transport and energy dissipation around the device. Therefore, it is beneficial to use numerical tools, particularly computational fluid dynamics tools to study wave interaction with the proposed OWC-pile device.

With the development of CFD and computing technology, an increasing number of numerical simulations of wave interaction with OWC devices can be found in the literature. Liu et al. (2008) used a 2D CFD model to study the oscillation amplitude of the water surface inside the OWC chamber and the effect of PTO mechanism on the water column oscillation. Zhang et al. (2012) proposed a numerical method based on two-phase level set and immersed boundary method to study the hydrodynamic performance of a 2D OWC device. Teixeira et al. (2013) used a numerical solver based on Navier-Stokes equations and an aerodynamic model in their investigation of optimization of OWC devices. The open source CFD library OpenFOAM® has been used to study bottom-fixed 2D OWC devices (Iturrioz et al., 2015; Simonetti et al., 2015). In these CFD

simulations, the turbulence was handled through either $k-\omega$ SST model or large-eddy-simulation (LES), and the air-water surface was tracked using the volume-of-fluid (VOF) method. Comparisons with experimental data showed that the OpenFOAM®-based simulations and experiments agreed well with each other in terms of chamber pressure and free surface elevation measured at single points, suggesting the potential of using OpenFOAM® based simulations to study 3D OWC devices further. More recently, Elhanafi et al. (2016a) and Elhanafi et al. (2017a) used StarCCM, which is a CFD software package based on Reynolds Averaged Navier-Stokes Equations (RANS) and VOF method, to study various hydrodynamic and energy conversion aspects of two types of rectangular OWC devices. López et al. (2016) reported the use of the RANS-VOF method in a numerical study aimed at finding optimum PTO damping under given local wave climate. Elhanafi et al. (2017b) studied the impact of air compressibility at different model scaling numerically using compressible and incompressible RANS-VOF method. They found that for the three-dimensional OWC device studied, ignoring air compressibility at full scale could introduce an error of 12% in the estimation of power extraction efficiency. All these aforementioned numerical studies have focused on OWC devices with 2D (rectangular) geometries with the exception of Elhanafi et al. (2017b), and the spatial non-uniformity of the water surface inside the OWC chamber is not the focus of these studies.

In previous theoretical studies of OWC devices, major assumptions were made on the power take-off (PTO) system and the viscous loss of wave energy. In order to obtain analytical solutions using linear wave theory, a linear PTO system was normally assumed. The effects of vortex shedding at the lower tip of the front skirt of the OWC chamber were not considered in published theoretical studies of OWC devices. Brendmo et al. (1996) proposed a way to account for the effects of viscous loss associated with the interaction of an OWC device with water waves; however, the numerical results and their validation are not articulated in the paper. A commonly used linear PTO system in theoretical studies is a Wells turbine. There are other types of turbines available for engineering applications of OWC devices, such as self-rectifying impulse turbines, which are nonlinear (ao et al., 2013). For scaled laboratory studies of OWC devices, nonlinear damping such as orifices,are commonly used to model the PTO mechanism, which calls for a new theoretical model that considers non-linear PTO damping.

Deng et al. (2013) proposed an OWC device design that has an axisymmetric (circular) OWC chamber and a C-shape supporting structure. A theory was developed to predict the pneumatic power extraction efficiency of the proposed device using matched eigenfunction expansion method. A linear power takeoff system is assumed in the theoretical modeling. To use the proposed OWC device in an OWC-pile breakwater, it is necessary to first explore theoretically and experimentally the performance of this OWC device. In laboratory experiments, it is cumbersome to implement a linear PTO system such as the Wells turbine. As a workaround, simple orifices are usually used to mimic the effect of the PTO (He et al., 2013; Morris-Thomas et al., 2007) which is a

nonlinear PTO. Direct application of Deng et al. (2013)'s theory thus become inappropriate due to the nonlinear PTO involved. Hence the need to add consideration for non-linear PTO system arises. This chapter first reports a systematic theory and laboratory experiment of a model of the Deng et al. (2013)'s OWC device with a quasi-linear PTO representation for the theoretical consideration of the efficiency of this OWC device. Additional discussions upon the effect of spatial non-uniformity and the additional viscous induced energy dissipation (viscous loss) of the single OWC device is carried out based on available experimental data and theoretical results. Then, a Reynolds Averaged Navier-Stokes (RANS) equation and Volume of Fluid (VOF) method based CFD model is used to perform a systematic numerical study of the device. The experimental results are first used to validate the numerical model, and then the numerical results are used in a detailed discussion of modes of enhanced spatial non-uniformity encountered in the experiment. The experimental and numerical results reported in this chapter are used to evaluate at prototype scale the performance of a row of loosely spaced OWC-piles for shore protection and electric power generation. Finally, based on the numerical simulation, the flow field near the bed around the OWC-pile device is visualized and interested flow features are identified. The implications of these flow features over sediment transport and scouring is also highlighted.

The rest of the chapter is divided into five parts. The first part is the experimental and theoretical work, which has been published in *Applied Ocean Research* (Xu et al., 2016). The second part is the numerical investigation, the complete manuscript prepared for the numerical investigation is included as Section 2.3 with small modifications to smooth the presentation. The third part is the evaluation of the performance of a row of loosely spaced OWC-piles for wave energy utilization and shore protection. A detailed flow visualization near the bed and associated discussions are presented in the fourth part, as Section 2.5. The main conclusions of this chapter are summarized in Section 2.6.

To facilitate further discussion, the coordinate system used in this study (including all chapters hereinafter) are defined in Figure 2.1 and Figure 2.9: The x-axis is horizontal with the positive direction pointing from the wave maker to the wave absorbing zone, the y-axis is vertical with the positive direction pointing vertically upwards, the z-axis is horizontal with the positive direction pointing towards the width direction of the wave flume, or laterally out of the paper.

2.2 Experimental and theoretical study of the standalone OWC-pile with quadratic PTO system

This section is based on "C. H. Xu, Z. H. Huang, and Z. Z. Deng. Experimental and theoretical study of a cylindrical oscillating water column device with a quadratic power take-off model" published in Applied Ocean Research 57:19-29, 2016.

2.2.1 Experimental setup, test conditions and data analysis

Tested model and experimental setup

Figure 2.1 shows a definition sketch of the OWC device model tested in the experiment. The model is made of stainless steel, with the outer diameter of the cylinder D = 12.5cm and the thickness of the plate being 3mm. The overall height of the OWC model is 40cm. The height of the C-shape supporting structure for the OWC chamber is 24.4cm. On top of the OWC chamber an orifice with diameter D_o=1.4cm is used to simulate a PTO mechanism, the lower tip of the OWC chamber is rounded using rubber bands to reduce the power loss due to vortex shedding at the lower tip edge.

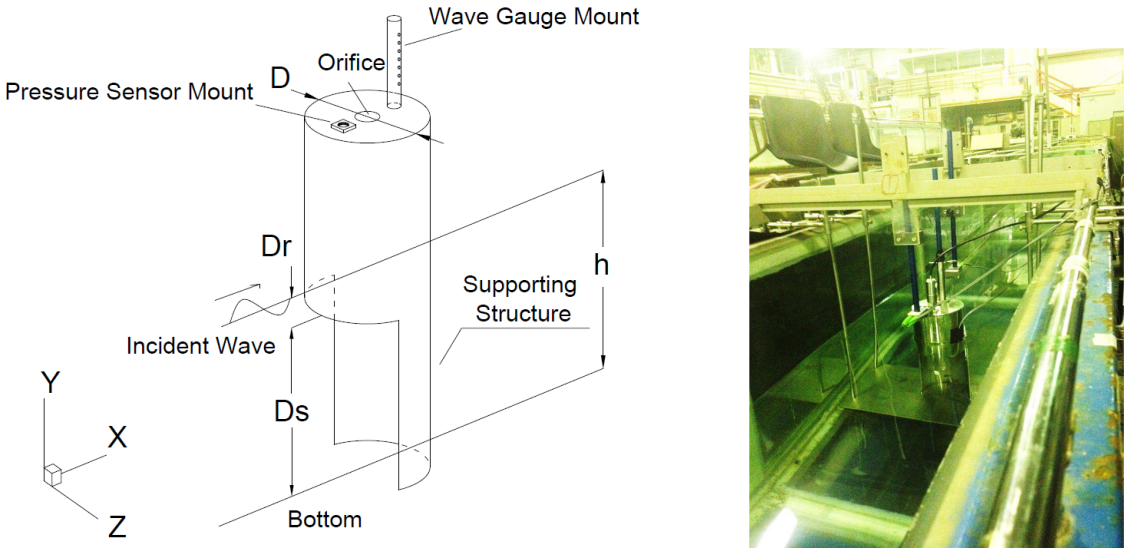

Figure 2.1: Definition sketch (left) and a photo (right) of the proposed OWC device.

Figure 2.2 shows the experimental setup, which is carried out in a wave flume of dimension 32.5m long, 0.54m wide and 0.6m deep in the Hydraulic Modeling Laboratory of Nanyang Technological University, Singapore. The OWC model is fixed in the wave flume firmly at 18.5m away from the wave maker at the centerline of the flume. Two ultrasonic wave gauges (S1 and S2) are placed 11m and 6m, respectively, from the OWC model to measure the incident wave. Another two resistance type wave gauges (G1 and G3) are placed 5cm in front of the OWC model and 5cm behind the OWC model, respectively. The data measured by these two gauges may be used to validate future numerical modeling. One resistance type wave gauge (G2) is placed inside the OWC chamber 3.7cm away from the center axis of the OWC chamber. This wave gauge is used to measure the water column oscillation inside the OWC chamber. To measure the air pressure fluctuation inside the OWC chamber, a piezoelectric pressure sensor is mounted on top of the OWC chamber 3.7cm away from the center axis of the model, on the opposite side of wave gauge G2 across the PTO orifice. Sensors mounted on top of the OWC chamber are sealed carefully to ensure they are air-tight and

no significant change to the total air volume inside the air chamber is introduced. All sensors are arranged along the centerline of the flume. A camera is used to record the wave motions around the OWC model. All sensors and the camera are synchronized using a digital synchronization data acquisition device.

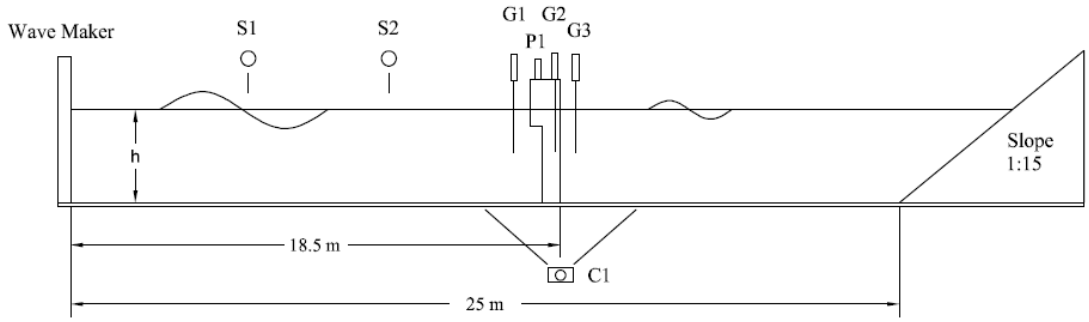

Figure 2.2: Experimental setup of the single OWC device test.

Test conditions

Test conditions are specifically designed to examine the effect of incident wave period, wave height and water depth (or OWC chamber draft) on the pneumatic power output and extraction efficiency of the OWC model. For the tests examining the effect of water depth or OWC chamber draft, two water depths (h=29cm and 31cm, corresponding to dimensionless OWC chamber draft $D_r/D = 0.32$ and 0.48) are used in the experiment. To test the effect of incident wave period, ten wave periods ranging from $T = 0.7$ s to 1.6 s with 0.1 s interval (corresponding to dimensionless wave length range $L/D = 6$ to 21, where L is the wave length) are examined for both water depths and a fixed wave height of $H = 3.7$ cm; to test the effect of incident wave height, experiments of four wave heights ranging from $H = 1.52$ cm to 4.75 cm are conducted for the water depth of $h = 31$ cm and three wave periods $T = 0.9$ s, 1.2 s and 1.4 s. A complete table of test conditions is shown in Table 2.1.

Experimental data analysis

The averaged pneumatic power extraction by the OWC device over one wave period is calculated by:

$$P_{OWC} = \frac{1}{NT}\int_{t_0}^{t_0+NT} p(t)v(t)A_0 dt \equiv \frac{C_f\rho}{2NT}\int_{t_0}^{t_0+NT} |v(t)|v(t)^2 A_0 dt, \tag{2.1}$$

where $p(t)$ is the air pressure drop across the orifice, $v(t)$ is the vertical speed of the water surface oscillation inside the chamber, A_0 is the cross-section area of the OWC chamber, N is an inte-

Table 2.1: A summary of all test conditions

Experiment A: h=0.29 m			Experiment B: h=0.31 m			Experiment C: h=0.31 m		
Case	H (m)	T (s)	Case	H (m)	T (s)	Case	T (s)	H (m)
1a	0.0370	0.7	2a	0.0379	0.7	3a	0.9	0.0157
1b	0.0378	0.8	2b	0.0379	0.8	3b	0.9	0.0261
1c	0.0385	0.9	2c	0.0379	0.9	3c	0.9	0.0460
1d	0.0380	1.0	2d	0.0362	1.0	3d	1.2	0.0170
1e	0.0387	1.1	2e	0.0369	1.1	3e	1.2	0.0271
1f	0.0364	1.2	2f	0.0364	1.2	3f	1.2	0.0472
1g	0.0370	1.3	2g	0.0363	1.3	3g	1.4	0.0170
1h	0.0382	1.4	2h	0.0371	1.4	3h	1.4	0.0272
1i	0.0384	1.5	2i	0.0369	1.5	3i	1.4	0.0474
1j	0.0381	1.6	2j	0.0365	1.6			

ger indicating the number of waves analyzed and t_0 is an arbitrary reference time instant. For incompressible air flowing through an orifice (see the end of this section for an analysis of the unimportance of air compressibility in this experiment), $p(t)$ can be modeled by:

$$p(t) = \frac{1}{2} C_f \rho_a |v(t)| v(t) + \rho_a L_g \frac{dv(t)}{dt}, \tag{2.2}$$

where ρ_a is the density of air, C_f is a quadratic loss coefficient related to drag effect, and L_g is an empirical length scale related to inertia forcing. Data fitting of Eq. (2.2) to measured pressure has shown that the effect of inertia is very small (less than 1%) and thus can be ignored.

The power extraction efficiency can be measured by the so-called capture width, which is defined as:

$$\lambda = \frac{P_{OWC}}{E_I C_g}, \tag{2.3}$$

where $E_I C_g$ is the wave power per unit wave crest, the incident wave energy E_I and the wave group velocity C_g are given by

$$E_I = \frac{1}{8} \rho_w g H_I^2, \quad C_g = \frac{L}{T} \left[\frac{1}{2} \left(1 + \frac{2kh}{\sinh(2kh)} \right) \right] \tag{2.4}$$

where h is the local water depth, ρ_w is the density of water, H_I is the incident wave height, L is the wave length, and $k = 2\pi/L$ is the wave number.

Unimportance of air compressibility for small-scale models

In the following we provide an analysis based on order of magnitude analysis that the air compressibility effect at the scale of the current experiment is not important. The mass flux through an

orifice is $d\left(\rho_a(t)V_c(t)\right)/dt$, where $\rho(t)$ is the instantaneous air density and $V_c(t)$ is the instantaneous air chamber volume. After linearization we have

$$\frac{d}{dt}\left(\rho_a(t)V_c(t)\right) = \rho_{a0}\frac{dV_c(t)}{dt} + V_{c0}\frac{d\rho_a(t)}{dt}, \tag{2.5}$$

where ρ_{a0} and V_{c0} are the undisturbed air density and the chamber volume, respectively. Assuming that the air is ideal and the process of air compression is isentropic, we can relate the air pressure $p(t)$ to the air density $\rho_a(t)$ by

$$c_a^2\frac{d\rho_a(t)}{dt} = \frac{dp(t)}{dt}, \tag{2.6}$$

where c_a is the sound speed in air at a constant temperature. Since the cross sectional area of the OWC chamber A_0 is a constant, we can write

$$\frac{dV_c(t)}{dt} = A_0 v(t), \tag{2.7}$$

where $v(t)$ is the spatially averaged velocity of the water surface inside the chamber, i.e., the instantaneous velocity of an imaginary weightless piston. We now can rewrite Eq. (2.5) as

$$\frac{d}{dt}\left(\rho_a(t)V_c(t)\right) = \rho_{a0}A_0 v(t) + \frac{V_{c0}}{c_a^2}\frac{dp(t)}{dt}, \tag{2.8}$$

The relative importance of the air compressibility can be evaluated by

$$\left(\frac{V_{c0}}{c_a^2}\frac{dp(t)}{dt}\right) / \left(\rho_{a0}A_0 v(t)\right) = \frac{\ell_0}{\rho_{a0}c_a^2 v(t)}\frac{dp(t)}{dt}, \tag{2.9}$$

where ℓ_0 is the initial height of the air chamber. For an orifice, the pressure $p(t)$ is controlled by $v(t)$. As an order of magnitude estimation, we can take $v(t) = O(\omega A)$ with ω being the angular frequency and A the wave amplitude, and $dp(t)/dt = O(C_f\omega\rho_{a0}|v(t)|^2)$ with ρ_{a0} being the undisturbed air density. Therefore we can have the following order of magnitude estimation:

$$\frac{\ell_0}{\rho_{a0}c_a^2 v(t)}\frac{dp(t)}{dt} = O(\frac{C_f\omega^2\ell_0 A}{c_a^2}), \tag{2.10}$$

In our experiment, $C_f = O(1\times 10^5)$, $\ell_0 = O(0.1)$ m , $\omega = O(6)$ rad/s, $A = O(0.02)$ m, and $c_a = 346$ m/s at room temperature. As a result, we have

$$\frac{C_f\omega^2\ell_0 A}{c_a^2} = O(6\times 10^{-2}) \ll 1, \tag{2.11}$$

Therefore, the effect of air compressibility on the mass flux through the orifice in our experiment is not important.

2.2.2 Theoretical modeling of quadratic PTO

Deng et al. (2013) provided a detailed solution of the radiation and diffraction wave field. The radiation wave generated by the OWC device is originated from the pressure fluctuation inside the OWC chamber, which is directly related to the PTO mechanism. A linear PTO mechanism is assumed in Deng et al. (2013) for calculation of OWC power extraction, making it inappropriate to apply this theory directly in this experiment. It is possible to make modifications to the treatment of the PTO mechanism in Deng et al. (2013)'s theory to account for the quadratic PTO mechanism. In this section we focus on the treatment of the quasi-linear PTO mechanism and leave out the other portions of the theory, the interested readers are referred to Xu et al. (2016) and Deng et al. (2013) for more details.

For the OWC device tested in the current experiment, it can be shown that the effect of air compressibility is not important, due to the large difference between the maximum airflow speed in this experiment and the speed of sound (refer to Appendix A of the attached paper for a discussion). For incompressible air flow through the PTO-simulating orifice used in the experiment, Eq. (2.2) describes the quadratic relationship between the water surface oscillation speed and the pressure. Since inertia effect can be neglected we can approximate the pressure drop across the orifice as:

$$p(t) = \frac{1}{2} C_f \rho_a |v(t)| v(t), \tag{2.12}$$

We also write the linearized pressure as:

$$p(t) = \rho_a C_e v(t), \tag{2.13}$$

where C_e is a linearized coefficient that can be determined by invoking Eq. (2.12) and (2.13) and using the Lorentz principle of equivalent work (Mei, 1983) by:

$$\frac{C_f}{2} \rho_a \overline{|v(t)| v^2(t)} = C_e \overline{\rho_a v^2(t)}, \tag{2.14}$$

where the overbar denotes taking the time average over one wave period. Physically, Eq. (2.14) ensures that the work done by the linearized pressure is the same as the work done by the quadratic pressure over one wave period.

If we write the vertical speed of the water surface oscillation inside the OWC chamber as:

$$v(t) = \mathcal{R}\left(V_0 e^{-i\omega t}\right), \tag{2.15}$$

where i is the imaginary number, V_0 is the complex amplitude and $Re()$ means taking the real part. Combining the above equation with Eq. (2.14), we then can obtain, after some manipulation, the following expression for C_e

$$C_e = \frac{C_f}{2}\frac{8}{3\pi}|V_0|, \tag{2.16}$$

We can write the linearized pressure as

$$p(t) = \mathcal{R}\left(p_a e^{-i\omega t}\right), \tag{2.17}$$

with

$$p_a = \rho_a C_e V_0, \tag{2.18}$$

The complex amplitude of the total volume flux of the air forced through the PTO system can be written as

$$q = V_0 A_0, \tag{2.19}$$

According to Deng et al. (2013), q is calculated by

$$q = \Gamma A_i - (B - iC)p_a \tag{2.20}$$

where Γ is a diffraction flux factor, A_i is the incident wave amplitude. B , C are the radiation conductance coefficient and the radiation susceptance coefficient, respectively. These three coefficients are solved in the diffraction and radiation problems formulated in Deng et al. (2013) independent of the PTO mechanism, thus the solved value could be utilized directly. Inserting Eq. (2.18) and Eq. (2.19) into Eq. (2.20) yields

$$V_0 = \frac{\Gamma A_i}{A_0 + (B - iC)C_e\rho}, \tag{2.21}$$

With the value of A and A_0 known and Γ,B and C given by the solution of Deng et al. (2013), Eq. (2.21) can be solved iteratively to get the value of U_0 and C_e. The theoretical capture width ratio for incompressible air can be calculated by

$$\lambda = \frac{\overline{p(t)v(t)}A_0}{E_I C_g} = \frac{1}{2}\frac{\rho_a C_e A_0 |V_0|^2}{E_I C_g}, \tag{2.22}$$

The capture width is usually normalized by either the wavelength (Lovas et al., 2010; Martins-Rivas and Mei, 2009) or a characteristic dimension of the energy converter. We choose the diameter

of the OWC model to normalize the capture width and refer to λ/D as the capture width ratio (CWR) in this study.

2.2.3 Results and discussion

Quadratic loss coefficient

The spatial non-uniformity inside the chamber introduces an error when using a single point water surface measurement to represent the averaged water surface inside the chamber. This error caused a relatively large variation in the fitted value of quadratic loss coefficient C_f from experimental data. A simple correction of the spatial non-uniformity induced error is made by reconstructing the spatial velocity amplitude distribution inside the OWC chamber using the velocity potential solutions, and obtaining the vertical velocity amplitude ratio between the location of single point measurement and the averaged value. This ratio is then used to correct the measured vertical speed. Please refer to Sections 3.3 and 4.3 of Xu et al. (2016) for more details of this correction. The resulting fitted value of C_f has a less variation after correction. Figures 2.3 and 2.4 show the fitted value of C_f after the spatial non-uniformity correction. The values of C_f ranged from 14×10^3 to 16×10^3 for $D_r/D = 0.48$ (or $h/D = 2.48$), which corresponds to $h = 0.31$ cm, and 13×10^3 to 15×10^3 for $D_r/D = 0.32$ (or $h/D = 2.32$), corresponding to $h = 0.29$ cm. It is also noted that the value of C_f is not sensitive to wave height.

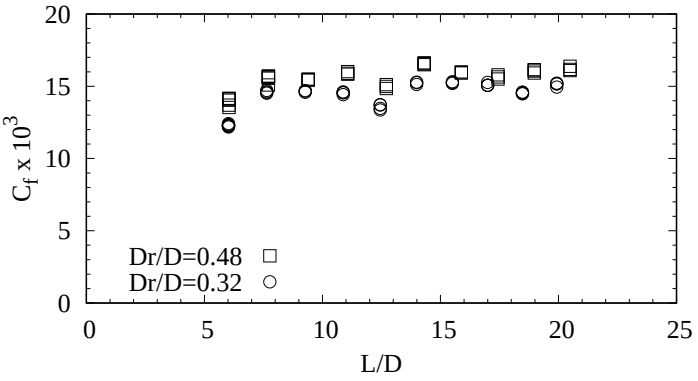

Figure 2.3: The fitted quadratic loss coefficient for different dimensionless wave length L/D.

Capture width ratio

Figures. 2.5 and 2.6 show the variation of experimental and theoretical dimensionless capture width ratio λ/D with dimensionless wavelength L/D and dimensionless wave height H/D. Averages of measured C_f values, $C_f = 14201$ for $D_r/D = 0.32$ and $C_f = 15527$ for $D_r/D = 0.48$ are used in the theoretical calculations. For long waves, the agreement between the experimental results and theoretical predictions is very good. It must be noted that the theoretical prediction

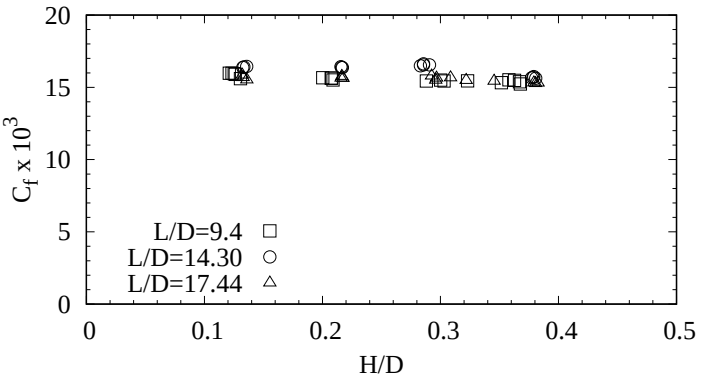

Figure 2.4: The fitted quadratic loss coefficient for different dimensionless wave height H/D.

of the variation of λ/D with L/D has two peaks, the first peak around $L/D = 5$ is due to the resonance of the oscillating water column system, the second peak and sudden drop to zero at around $L/D = 1.8$ is due to the resonance of sloshing waves. For shorter waves, the theoretical predictions overestimated the capture width ratio. A trend can be observed that the peak capture width ratio for the experimental condition occurs at a longer wavelength compared to the peak of theoretical predictions. For the variation of capture width ratio with dimensionless incident wave height, agreement between experimental results and theoretical predictions is again very good for longer wavelengths. For shortwave, the theoretical prediction overestimates when compared to experimental results. Increase of capture width ratio with increasing incident wave height is observed in the long wave case. For the short-wave case, the variation of capture width ratio with incident wave height is not obvious, but from the theoretical curve, the capture width ratio first increases with wave height then turn into a slightly decreasing trend.

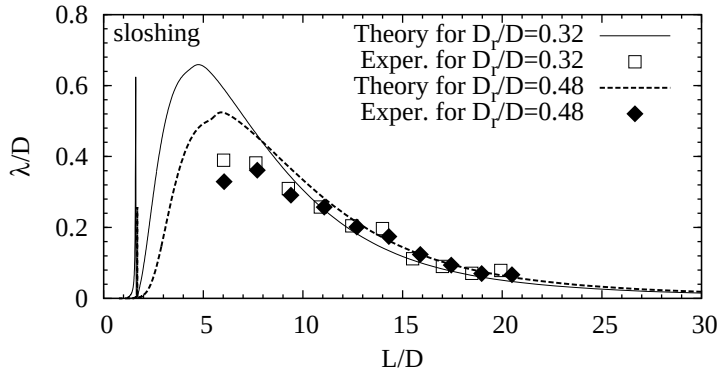

Figure 2.5: Comparison of the theoretical and experimental capture length for different dimensionless wave lengths.

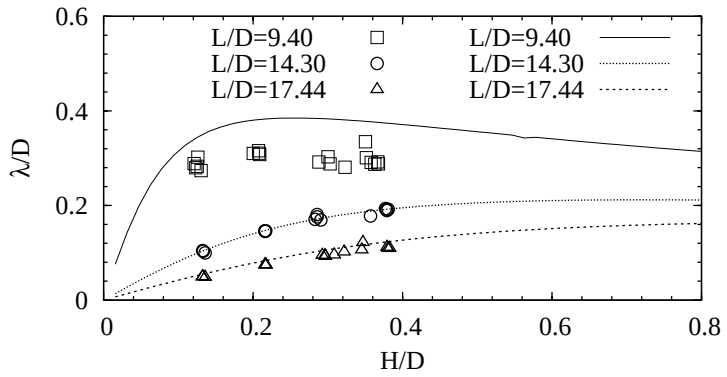

Figure 2.6: Comparison of the theoretical and experimental capture length for different dimensionless wave heights.

Viscous loss

Referring to Figures 2.5 and 2.6, the difference between the experimental result and the theoretical predictions are partly because the theoretical model is a potential solver which cannot account for the viscous effect. Thus, apart from measurement error (including error associated with the effect of spatial non-uniformity excited by the higher harmonic oscillations, which will be discussed in Section 2.3.4), a major portion of the difference between the experimental measurement and theoretical prediction can be attributed to the effect of viscous loss. This provides a way to make a rough estimation of the magnitude of viscous loss of the OWC device. This viscous loss is a combined effect of the energy dissipation from the turbulent wakes related to vortex shedding from the supporting structure and the vortices shed from the lower tip of the front skirt of the OWC chamber. The estimated viscous loss due to vortex shedding is expressed by:

$$\frac{\Delta\lambda}{D} = \frac{\lambda_p}{D} - \frac{\lambda_m}{D} \tag{2.23}$$

where λ_p is the theoretically predicted capture length and λ_m is the measured capture length.

Figures. 2.7 and 2.8 shows the variation in $\Delta\lambda/D$ with dimensionless wavelength and dimensionless wave height. The value of $\Delta\lambda/D$ reached 7% to 40% of the capture length for short waves with L/D ranging from 5 to 10, indicating a noticeable and sometimes significant effect of viscous loss. For long waves, the value of $\Delta\lambda/D$ is very small and the fluctuation around 0 is attributed to measurement error. Variation of $\Delta\lambda/D$ with incident wave height is not significant.

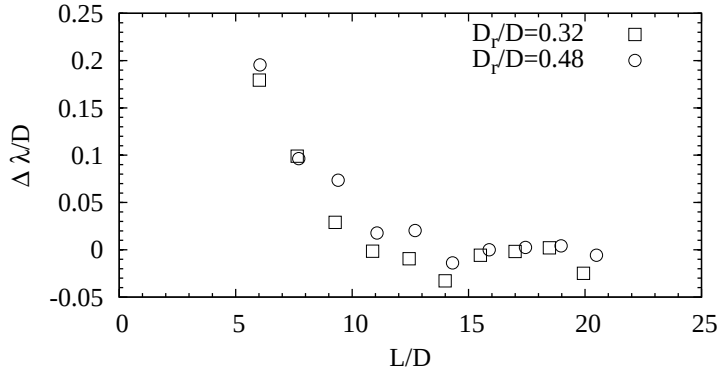

Figure 2.7: Comparison of the theoretical and experimental capture length for different dimensionless wave lengths.

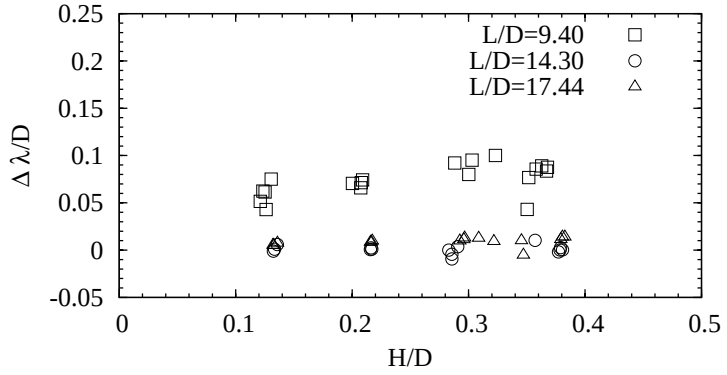

Figure 2.8: Comparison of the theoretical and experimental capture length for different dimensionless wave heights.

2.3 CFD simulation of a cylindrical OWC with a nonlinear power-takeoff: model validation and a discussion on resonant sloshing inside the chamber

This Section is based on the manuscript submitted to Ocean Engineering: "C. H. Xu, Z. H. Huang. CFD simulation of a cylindrical OWC with a nonlinear power-takeoff: model validation and a discussion on resonant sloshing inside the chamber". Ocean Engineering. In revision.

In this section, a CFD simulation of the laboratory experiment discussed in Section 2.2 is articulated. The purpose of this CFD numerical study is to (1) build and validate a numerical wave flume using existing CFD technique suitable for the simulation of wave energy extraction of OWC device in wave field; (2) provide insight into and study systematically the spatial non-uniformity inside the OWC-pile device and its effects; (3) suggest data analysis and experimental

design techniques that could potentially reduce the impact of spatial non-uniformity.

2.3.1 Description of the numerical model

Governing Equations

The numerical model is based on the open-source computational fluid dynamics library OpenFOAM®. The model employs the 3D incompressible Reynolds Averaged Navier-Stokes Equations (RANS) as the governing equations for a water-air mixture. Let s_w be the saturation of water in a particular volume, $s_w = 0$ for the air above the air-water surface and $s_w = 1$ for the water below the air-water surface. The air-water interface is treated as a thin layer of the water-air mixture with $0 < s_w < 1$. The density ρ and the dynamic viscosity μ of the water-air mixture are calculated by

$$\rho = s_w \rho_w + (1 - s_w)\rho_a, \tag{2.24}$$

$$\mu = s_w \mu_w + (1 - s_w)\mu_a, \tag{2.25}$$

where the subscripts w and a refer to water and air, respectively. The continuity equation for the water-air mixture is

$$\nabla \cdot \mathbf{u} = 0, \tag{2.26}$$

where $\mathbf{u}$ is the velocity field of the water-air mixture. The momentum equations are

$$\frac{\partial \rho \mathbf{u}}{\partial t} + \nabla \cdot [\rho \mathbf{u}\mathbf{u}^T] = \rho \mathbf{g} - \nabla p + \nabla \cdot [\mu \nabla \mathbf{u} + \rho \mathbf{T}], \tag{2.27}$$

where p is the pressure, $\mathbf{g}$ the gravitational acceleration, and $\mathbf{T}$ is the specific Reynolds stress tensor, which will be closed by a selected turbulence model (Rusche, 2003; Versteeg and Malalasekera, 2007).

In order to track the water-air interface, a modified VOF method is adopted, with the phase governing equation written as

$$\frac{\partial s_w}{\partial t} + \nabla \cdot [s_w \mathbf{u}] + \nabla \cdot [\mathbf{u}_r s_w (1 - s_w)] = 0, \tag{2.28}$$

where $\mathbf{u}_r$ is an interface compression velocity only present in the water-air interface to suppress the diffusive behavior of the interface. For more details of this modified interface compressive VOF scheme, please refer to Rusche (2003).

A $k - \omega$ turbulence model is used to provide closure to the specific Reynolds stress tensor $\mathbf{T}$

(Wilcox, 1993).

$$\frac{\partial \rho\omega_t}{\partial t} + \nabla \cdot [\rho \mathbf{u}\omega_t] = \alpha p_\omega - \beta\rho\omega_t^2 + \frac{\sigma_d}{\omega_t}\rho\nabla k \cdot (\nabla\omega_t)^T + \nabla \cdot \left[\left(\mu + \sigma_\omega \rho \frac{k}{\omega_t}\right)\nabla\omega_t\right], \tag{2.29}$$

and

$$\frac{\partial \rho k}{\partial t} + \nabla \cdot [\rho \mathbf{u} k] = p_k - \beta^* \rho\omega_t k + \nabla \cdot [(\mu + \sigma^* \mu_t)\nabla k], \tag{2.30}$$

where k is the turbulent kinetic energy and ω_t is a characteristic eddy frequency (or specific turbulence dissipation rate), p_k and p_ω are the production terms of k and ω_t, respectively. Following Mayer and Madsen (2000) and Jacobsen et al. (2012), the following forms are adopted for p_k and p_ω in order to suppress the abnormal growth of turbulent viscosity and turbulent kinetic energy in regular wave propagation that satisfies potential flow criteria,

$$p_k = \mu_t (\nabla \times \mathbf{u}) \cdot (\nabla \times \mathbf{u})^T, p_\omega = \frac{\omega_t}{k} p_k, \tag{2.31}$$

which are different from the original forms of turbulence production terms suggested by (Wilcox, 1993, 2008). Eq. (2.31) ensures that the production of turbulent kinetic energy is related to the vorticity of the fluid motion, not the strain rate of the fluid velocity.

The dynamic eddy viscosity μ_t is defined as

$$\mu_t = \rho \frac{k}{\tilde{\omega}_t}, \tag{2.32}$$

where

$$\tilde{\omega}_t = \max\left\{\omega_t, C_{lim}\sqrt{\frac{2\mathbf{S}:\mathbf{S}}{\beta^*}}\right\}, \tag{2.33}$$

with $\mathbf{S}$ being the strain rate tensor. The specific Reynolds stress tensor can be calculated by:

$$\mathbf{T} = \frac{2}{\rho}\mu_t \mathbf{S} - \frac{2}{3}k\mathbf{I} \tag{2.34}$$

where $\mathbf{S}$ is the strain rate tensor expressed by

$$\mathbf{S} = \frac{1}{2}[\nabla\mathbf{u} + (\nabla\mathbf{u}^T)] \tag{2.35}$$

and $\mathbf{I}$ is the identity tensor.

The coefficients of the $k-\omega$ model take the suggested values, i.e., $\alpha = 13/25$, $\beta = 0.072$, $\beta^* = 0.09$, $\sigma_\omega = 0.5$, $\sigma^* = 3/5$ and $C_{lim} = 7/8$ (Wilcox, 2008).

Setup of the numerical wave flume

Referring to Figure 2.9, a three-dimensional numerical wave flume of 14.00 m × 0.54 m× 0.60 m (length × width × height) is used to perform all numerical simulations. The numerical wave flume consists of three sections: the first section (from x=0.00 m to 4.00 m) is the wave generating zone; the second section (from x=4.00 m to 10.00 m) is the test section; the third section (from x=10.00 m to 14.00 m) is the wave absorbing zone.

The boundary conditions of the numerical wave flume are set up to resemble the actual test conditions in the wave flume tests (Xu et al., 2016). Wave inlet boundary conditions are used at x=0 m. Wall boundary conditions are used at the bottom, the two lateral boundaries, and at x=14 m. Atmospheric boundary condition is used at the top boundary of the computational domain. The walls of the OWC model are set to wall boundaries. All wall boundaries are assumed to be hydraulically smooth because the walls of the wave flume in the experiment were made of glass and the walls of the OWC model were made of stainless steel.

As in the wave-flume tests(Xu et al., 2016), the numerical OWC model is placed at x=7 m and z=0.25 m, and three numerical wave gauges (G_1, G_2 and G_3) are used to measure the surface displacements inside and outside the OWC model. The locations of G_1, G_2 and G_3 are shown in Figure 2.9: G_1 is on the up-wave side of and 5 cm away from the OWC model; G_2 is inside the OWC chamber, on the down-wave side of and 3.7 cm away from the geometrical axis of the OWC chamber; G_3 is on the down-wave side of and 5 cm away from the OWC model. One numerical pressure gauge is used to measure the air pressure inside the pneumatic chamber. The measured air pressure and the surface displacements at these three locations can be used to verify and validate the numerical model.

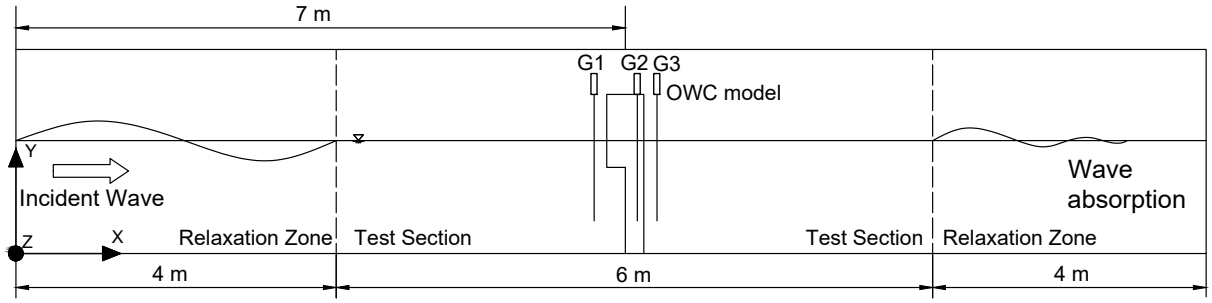

Figure 2.9: Sketch of the computational domain.

Wave generation and absorption

In the present study, the wave generation toolbox Waves2Foam (Jacobsen et al., 2012) is implemented to generate monochromatic waves and provide wave-absorbing boundaries. The method is based on the relaxation-zone concept. On a mesh cell located in the prescribed relaxation zone,

physical quantities have prescribed values that are computed using the following expression

$$\phi = \alpha_R \phi_c + (1 - \alpha_R)\phi_t, \tag{2.36}$$

where ϕ_c is the actual computed value, ϕ_t is the target value, and α_R is the relaxation factor defined by

$$\alpha_R(\chi_R) = 1 - \frac{\exp(\chi_R^{3.5}) - 1}{\exp(1) - 1}, \tag{2.37}$$

where $\chi_R = x/L_R$ is the location relative to the horizontal length of the relaxation zone and L_R is the length of the relaxation zone. Thus, it is ensured that at $\chi_R = 0$, which is the most upstream point, $\alpha_R = 0$ and $\phi = \phi_t$; while at $\chi_R = 1$ which is the boundary between relaxation zone and non-relaxed zone, $\alpha_R = 1$ and $\phi = \phi_c$. Between these two limits, the value of physical quantities such as $\mathbf{u}$ and s_w is a blend of the computed and target values. In this study, the target values are obtained from potential wave theories. Active wave absorption is intrinsically included in the wave generating relaxation zone.

The relaxation zone method is also used in the wave absorbing zone to reduce wave reflection. This is achieved by setting the target value for $\mathbf{u}$ to 0 everywhere in the absorbing zone, and setting the target value for s_w to the calculated value based on the still water line inside the flume. The reflection coefficient (defined by wave amplitude) of the wave-absorbing relaxation zone is generally smaller than 0.08 for the range of wave conditions tested.

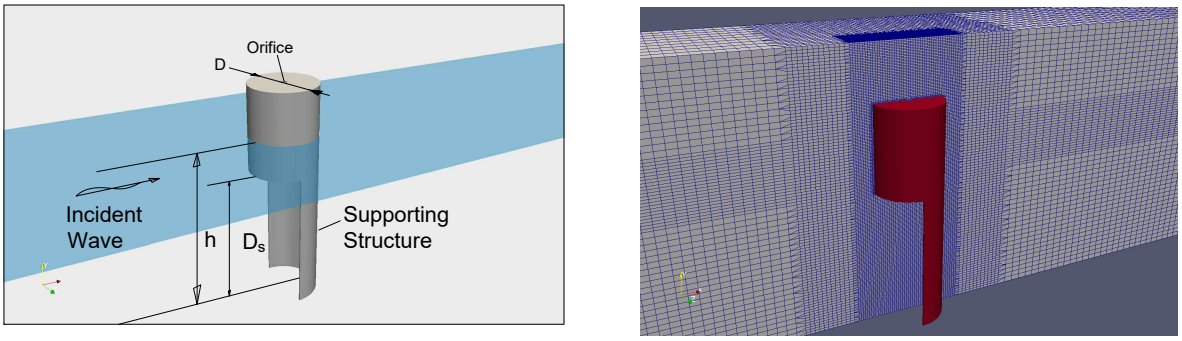

Figure 2.10: Left: a three-dimensional view of the OWC model as tested in Xu et al. (2016). Right: a view of the mesh configuration in the vicinity of the OWC model.

Mesh setup

An unstructured nested mesh is set up to cover the entire computational domain. The right panel of Figure 2.10 shows a slice of the mesh in detail. OpenFOAM built-in pre-processing mesh tools "blockMesh", "refineMesh" and "snappyHexMesh" are used to create, refine, deform, re-size, and remove mesh cells according to the geometry of the OWC model. In order to reduce the computational load, a coarse mesh of resolution 1.64 cm $\times$ 1.00 cm $\times$ 5.00 cm ($\Delta x \times \Delta y \times \Delta z$) is used in the relaxation zones. However, in the test section, the mesh is refined to a resolution of at least 0.82 cm $\times$ 1.00 cm $\times$ 2.50 cm. In order to accurately track the free surface, the mesh within $\pm$5 cm around the still water surface is further refined to a resolution of 0.82 cm $\times$ 0.25 cm $\times$ 1.25 cm, representing about 100 horizontal nodes in one wavelength and 8 to 20 vertical nodes (covering a single wavelength profile of 0.8 s wave period and 2 cm to 5 cm wave height). In the vicinity of the OWC model, an even more refined mesh is used to accurately snap the thin plates of the model, with a characteristic mesh resolution of 0.205 cm $\times$ 0.125 cm $\times$ 0.159 cm. The mesh snapping on the model surface results in two layers of even finer mesh with characteristic mesh resolution of 0.1 cm $\times$ 0.1 cm $\times$ 0.1 cm that closely snaps the surface of the OWC model. The total cell count of the final mesh is about 1.4 million.

2.3.2 Model verification and validation

This section presents the model verification and validation using the experimental results reported in Xu et al. (2016). These experimental results include the surface displacements measured at three locations inside and around the OWC model, the pressure of the air inside the OWC chamber, and the calculated capture width ratio and the characteristics of the PTO. These results are obtained for 29 test conditions. A typical simulation of about 20 wave periods takes about one week on a high-performance workstation with a total of 20 physical processors (dual Intel Xeon E5-2650 v3) and 128GB of DDR4 memory.

Simulated surface displacement and the air pressure inside the OWC chamber

Sample comparisons of the simulated and measured surface displacements are shown in the left panel of Figure 2.11 for location G_1, in the right panel of Figure 2.11 for location G_3, and in the left panel of Fig 2.12 for location G_2 . The agreement between the simulation and the measurement is very good at all three locations and for all test conditions.

The right panel of Fig 2.12 shows a comparison of the simulated and measured variations of the air pressure in the pneumatic chamber. The CFD simulation can capture the air-pressure variation very well, especially the nonlinear features associated with the quadratic nature of the PTO (a small orifice on the top cover of the pneumatic chamber).

The good agreement between the simulated and measured surface displacements at three lo-

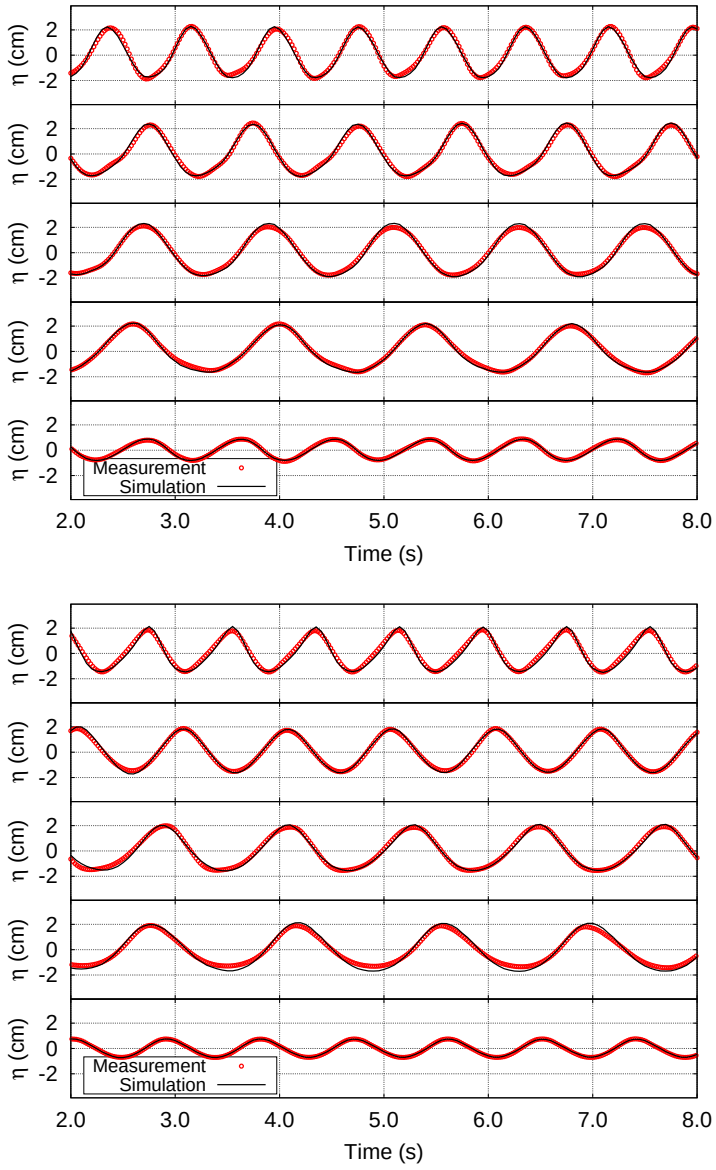

Figure 2.11: A comparison of the simulated and measured surface displacements at the location G_1 (upper panel) and G_3 (lower panel) for five test conditions (from the top to the bottom): 1b, 1d, 1f, 1h, and 3a.

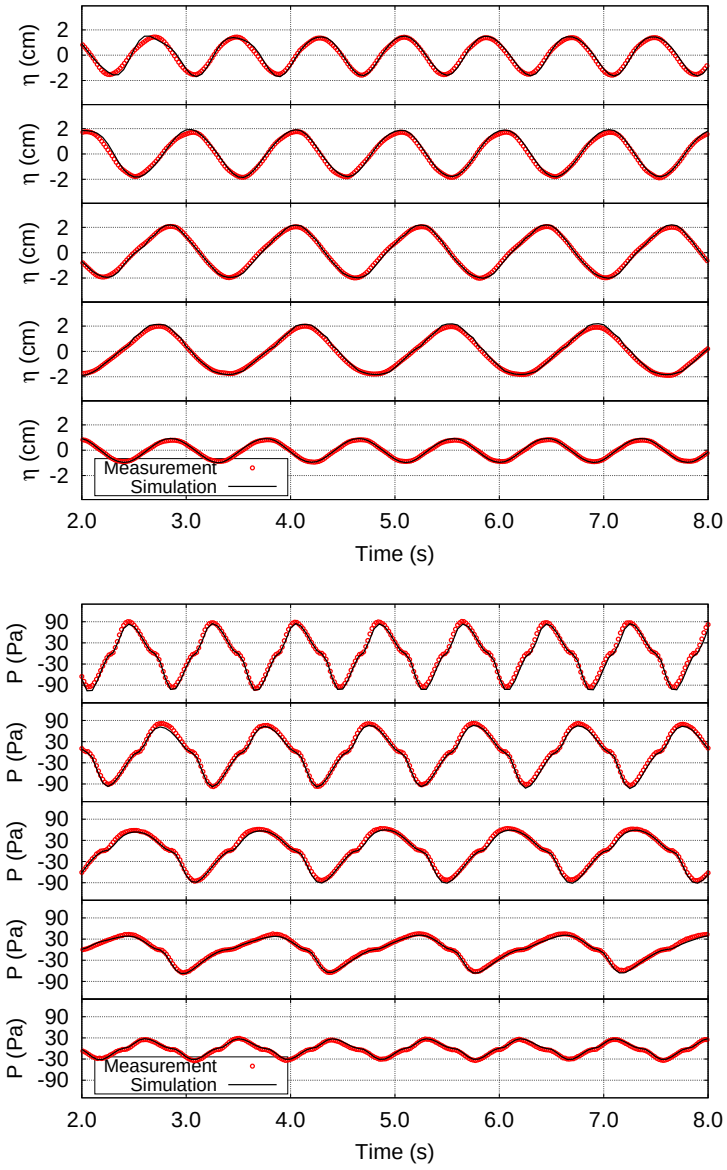

Figure 2.12: A comparison between the simulated and measured surface displacements at the location G_2 (upper panel) and a comparison between the simulated and measured air pressures inside the pneumatic chamber (lower panel): 1b, 1d, 1f, 1h, 3a.

cations and the air pressure inside the pneumatic chamber indicates that the present CFD model and numerical setup can adequately represent the important physical processes involved in the nonlinear wave interaction with the circular OWC device. Because the numerical simulation can provide a detailed flow field inside the OWC chamber, it is possible to address issues that cannot be addressed by wave-flume experiments, such as surface sloshing and its effects on the extraction efficiency determined using the velocity measured at one point inside the OWC chamber.

Extraction efficiency

The extraction efficiency of a wave energy converter is usually measured by the so-called capture width, which is defined as the ratio between the absorbed power and the available wave power per meter of wave crest of the incident waves. For an OWC-type wave energy converter, the wave power extracted by the device, denoted by P_{OWC}, is calculated by

$$P_{OWC} \equiv \frac{1}{NT} \int_{t_0}^{t_0+NT} \left(\iint_S p(t) v(x,z,t) dx dz \right) dt, \tag{2.38}$$

where S is the cross section of the OWC chamber, $p(t)$ is the air-pressure fluctuation inside the OWC chamber, $v(x,z,t)$ is the local velocity of the oscillation of the water surface inside the OWC chamber, t_0 is an arbitrary time instance, T is the wave period, and N is an integer. In terms of the spatial (i.e., cross-sectional) average velocity, $\bar{v}(t)$,

$$\bar{v}(t) = \frac{1}{A_0} \iint_S v(x,z,t) dx dz, \tag{2.39}$$

with A_0 being the cross-sectional area of the OWC pneumatic chamber, P_{OWC} can be written as

$$P_{OWC} = \frac{A_0}{NT} \int_{t_0}^{t_0+NT} p(t) \bar{v}(t) dt, \tag{2.40}$$

Therefore the capture width λ is obtained by

$$\lambda = \frac{P_{OWC}}{E_I C_g}, \tag{2.41}$$

with the incident wave energy per unit wave crest width E_I and the group velocity C_g being given by

$$E_I = \frac{1}{8} \rho_w g H_I^2, \quad C_g = \frac{L}{T} \left[\frac{1}{2} \left(1 + \frac{2kh}{\sinh(2kh)} \right) \right], \tag{2.42}$$

where h is the local water depth, ρ_w is the density of water, H_I is the incident wave height, L is the wave length, and $k = 2\pi/L$ is the wave number.

The spatial-average velocity $\bar{v}(t)$ is not obtainable in wave-flume experiments (usually a limited number of wave gauges are used to measure the surface motion at selected locations). In most wave-flume tests, the spatial-average velocity $\bar{v}(t)$ is usually approximated by the velocity measured at a single point inside the OWC chamber, i.e., G_2 in our experiment (Xu et al., 2016). We denote the velocity measured at a single point by $\tilde{v}$, and the pneumatic power extraction calculated using $\tilde{v}$, denoted by $\tilde{P}_{OWC}$, is

$$\tilde{P}_{OWC} = \frac{A_0}{NT} \int_{t_0}^{t_0+NT} p(t)\tilde{v}(t)dt. \tag{2.43}$$

In other words, the capture width measured in the experiment is actually $\tilde{\lambda}$

$$\tilde{\lambda} = \frac{\tilde{P}_{OWC}}{E_I C_g}. \tag{2.44}$$

The difference between λ and $\tilde{\lambda}$ is affected by the difference between $\bar{v}$ and $\tilde{v}$, which reflects the non-uniformity of the water surface inside the OWC chamber: for a uniform water surface (i.e., a weightless piston), $\bar{v} = \tilde{v}$ and $\lambda = \tilde{\lambda}$. If there is a surface sloshing, we should expect $\bar{v} < \tilde{v}$ and $\tilde{\lambda} > \lambda$.

The capture width is usually normalized by either the wave length (Lovas et al., 2010; Martins-Rivas and Mei, 2009) or a characteristic dimension of the energy converter (Xu et al., 2016). We choose the diameter of OWC model to normalize the capture width and refer to λ/D as the capture width ratio (CWR) in this study. Figure 2.13 shows a comparison of the capture width ratios obtained from the CFD simulation and the experiment for the three sets of the experiments listed in Table 2.1. It can be seen that the CFD simulation can reproduce the measured values of the capture width ratio $\tilde{\lambda}/D$ very well, implying that the present CFD simulation can reproduce satisfactorily both the magnitudes and phases of the air-pressure fluctuation and the water-surface oscillation inside the OWC chamber.

2.3.3 Quadratic loss coefficient

When using potential flow theory to study wave interaction with an OWC device with a nonlinear quadratic PTO in the frequency domain or time domain, a parametrization of the PTO is needed. In wave-flume tests, the PTO is usually modeled by an orifice, which causes a pressure drop between the pneumatic chamber and the surrounding air. For incompressible air, this pressure drop can be modeled by Eq. (2.2), which is re-written here considering spatial non-uniformity and a single water surface measurement:

$$p(t) = \frac{1}{2} C_f \rho_a \left|\bar{v}(t)\right| \bar{v}(t) + \rho_a L_g \frac{d\bar{v}(t)}{dt}, \tag{2.45}$$

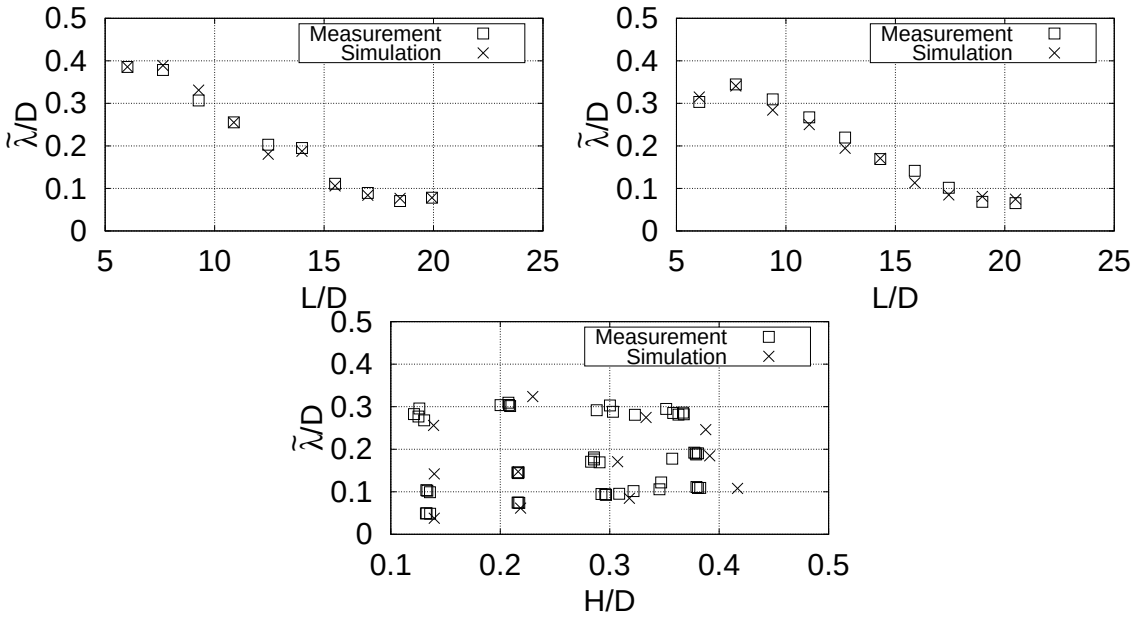

Figure 2.13: Comparisons between the simulated and measured values of capture width ratio for Experiment A (upper left) with $h/D = 2.32$, Experiment B (upper right) with $h/D = 2.48$, and Experiment C (lower panel) with $h/D = 2.48$.

where $p(t)$ is the relative pressure of the air inside the pneumatic chamber, ρ_a the density of the air, $\bar{v}(t)$ the spatial average velocity of the water-surface oscillation inside the OWC chamber, C_f the quadratic loss coefficient related to drag effect, and L_g the inertial length scale. The inertial effect represented by the last term in Eq. (2.45) is not important in small-scale wave-flume tests (Xu et al., 2016). Therefore, the nonlinear PTO can be parameterized by the quadratic loss coefficient C_f alone. We remark that the non-uniformity of the water surface inside the OWC chamber can introduce significant error in the value of C_f determined using Eq. (2.45) and the local velocity measured at a single point inside the OWC chamber.

In the wave flume experiment of Xu et al. (2016), which is reported here in Section 2.2, $p(t)$ is measured by a pressure sensor mounted on the top of the OWC pneumatic chamber and the surface displacement is measured at one location G_2 inside the OWC chamber. Therefore the spatial average velocity $\bar{v}$ is not obtainable from the wave flume experiment, and it is approximated by $\tilde{v}(t)$, the local velocity measured at the location G_2, which itself is calculated using the surface displacement measured at the location G_2. We denote the quadratic loss coefficient determined by using velocity $\tilde{v}$ as $\tilde{C}_f$:

$$p(t) = \frac{1}{2}\tilde{C}_f \rho_a \left|\tilde{v}(t)\right| \tilde{v}(t), \tag{2.46}$$

where, again the inertial term has been ignored (see Section 2.2.2).

The measured and simulated values of $\tilde{C}_f$ are shown in Figure 2.14. A satisfactory agreement

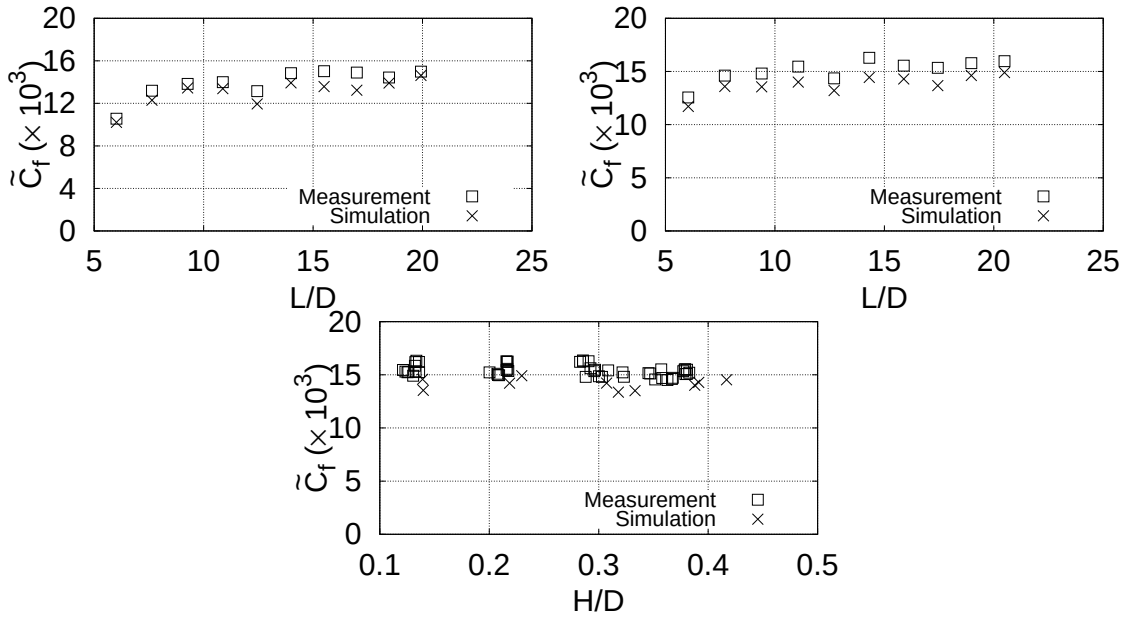

Figure 2.14: Comparisons between the simulated and measured values of $\tilde{C}_f$ for Experiment A (upper left) with $h/D = 2.32$, Experiment B (upper right) with $h/D = 2.48$, and Experiment C (lower panel) with $h/D = 2.48$.

between the simulation and the experiment can be observed for all test cases: the minor difference is mainly due to the difference in the local velocity $\tilde{v}$ obtained from the experiment and the simulation.

2.3.4 Spatial non-uniformity and resonant sloshing inside the OWC chamber

In Xu et al. (2016), a correction factor for spatial non-uniformity was proposed and used to correct the measurements of the water surface inside the OWC chamber. This correction factor was based on the spatial distribution of water surface oscillation amplitude solved by the theoretical model, which can only resolve the fundamental component of the incident wave. The higher harmonic effects and the vortex shedding induced oscillation cannot be considered. In this section, we provide a more accurate analysis of spatial non-uniformity by considering higher harmonic effects and vortex shedding in numerical simulations.

Using the CFD simulation results, we are able to obtain detailed flow information, which can help understand factors that affect the spatial non-uniformity and reduce the measurement error in the determination of capture width and the characteristics of the PTO.

Spatial non-uniformity of oscillation wave height inside the the OWC chamber

One way to partially consider the spatial non-uniformity of the water surface inside the OWC chamber is the spatial distribution of the oscillation wave height inside the OWC chamber as shown in Figure 2.15, where the wave height is the vertical distance between the local maximum

and the local minimum of the surface displacement measured within one wave period. Because there exists a partial standing wave pattern in front of the C-shaped support structure, the wave height is larger close to this reflective boundary. Both the wave period and the draft of the OWC chamber affect the non-uniformity of the water surface inside the OWC chamber: shorter waves generally give a stronger spatial non-uniformity, which is in general agreement with our intuition and the theoretical predictions of Xu et al. (2016), and increasing the draft of the OWC chamber reduces the non-uniformity of the water surface inside the OWC chamber. Because the velocity obtained at a single location was used to represent the spatial-averaged velocity, there is an error introduced to the calculated capture width λ and the quadratic loss coefficient C_f.

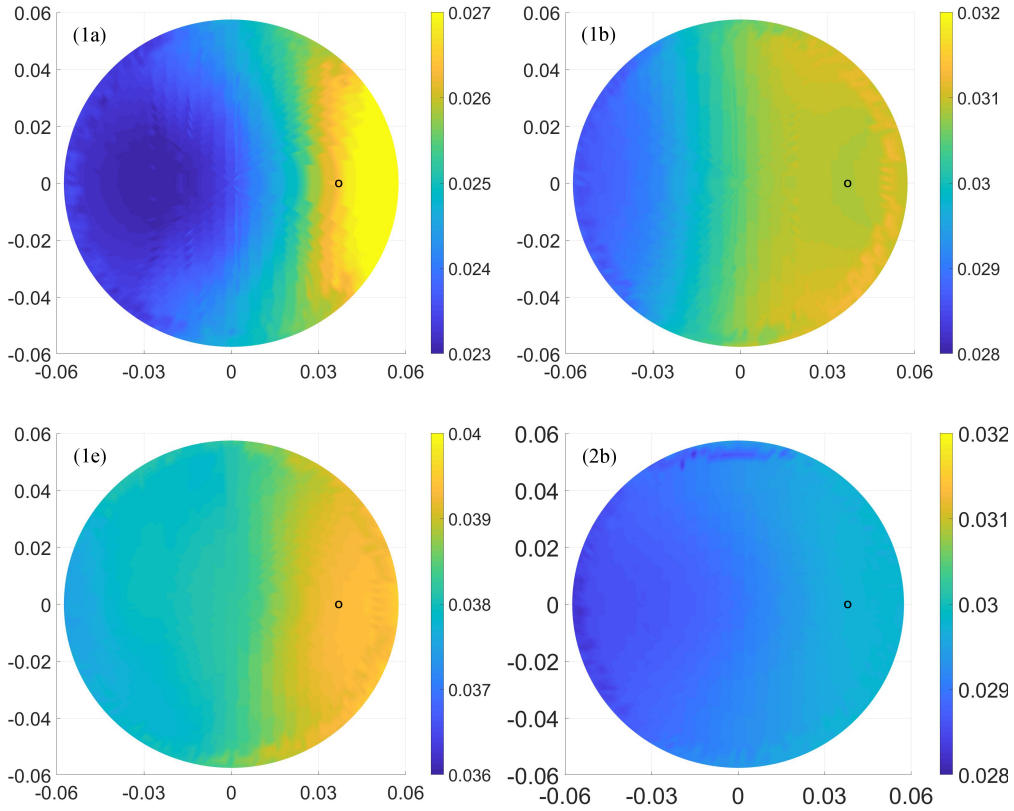

Figure 2.15: Distributions of the oscillation wave height inside the OWC chamber. Case 1a: t=0.7 s, h=0.29 m; Case 1b: t=0.8 s, h=0.29 m; Case 1e: t=1.1 s, h=0.29 m; Case 2b: t=0.8 s, h=0.31 m. The circle on each plot indicates the location of the wave gauge G_2 in the experiment of Xu et al. (2016)

Spectral analysis of the sloshing motion inside the OWC chamber

To further understand the non-uniformity of the water surface inside the OWC chamber, the simulated surface displacement $\eta(x, z, t)$ is decomposed into two components: the cross-sectional

average and deviation from the spatial average.

$$\eta(x,z,t) = \bar{\eta}(t) + \eta'(x,z,t), \tag{2.47}$$

where $\eta'(x,z,t)$ (the sloshing component) is the deviation from the cross-sectional average component $\bar{\eta}(t)$ (the spatial mean component) defined by

$$\bar{\eta}(t) = \frac{1}{A_0}\iint_S \eta(x,z,t)dxdz \tag{2.48}$$

with S being the cross section of the OWC chamber. By definition,

$$\iint_S \eta'(x,z,t)dxdz = 0 \tag{2.49}$$

In Eq. (2.47), $\bar{\eta}(t)$ represents a piston-like oscillation inside the OWC chamber, and $\eta'(x,z,t)$ represents the spatial non-uniformity superimposed on $\bar{\eta}(t)$. We refer to the motion associated with $\bar{\eta}$ as "spatial-average motion" and the motion associated with $\eta'(x,z,t)$ as "sloshing motion" hereinafter.

In a wave-flume experiment, the surface displacement is measured at a very limited number of points. As a result, the spatial-average motion $\bar{\eta}(t)$ and the sloshing motion $\eta'(x,z,t)$ are not measurable. In the wave-flume experiment of Xu et al. (2016), only one wave gauge (G_2, see Figure 2.9) was used to measure surface displacement inside the OWC chamber. The surface displacement measured at the location G_2 was used to approximate the spatial-average motion $\bar{\eta}(t)$.

When the surface displacement is measured at a given point, e.g., G_2 in the experiment of Xu et al. (2016), harmonic components in the spatial-average motion $\bar{\eta}(t)$ and the sloshing motion $\eta'(t)$ can be studied through an harmonic analysis using the numerical results. To understand the relationship between the incident waves and the motion of the air-water surface inside the OWC chamber, we will use the simulated data to show the spectrum characteristics of the incident waves, the spatial average motion and the sloshing motion inside the OWC chamber. For simplicity, we will use $\eta'(t)$ to represent $\eta'(x_{G_2}, z_{G_2}, t)$ hereinafter.

The incident waves can be expressed as

$$\eta_I = \frac{1}{2}\int_{-\infty}^{\infty} A(f)e^{-2\pi ift}df, \tag{2.50}$$

and the amplitude spectrum of $\eta_I(t)$ is $|A(f)|$. The displacements for the spatial-average motion and the sloshing motion can be expressed as

$$\bar{\eta} = \frac{1}{2}\int_{-\infty}^{\infty} \bar{B}(f)e^{-2\pi ift}df, \quad \eta'(t) = \frac{1}{2}\int_{-\infty}^{\infty} B'(f)e^{-2\pi ift}df \tag{2.51}$$

and the amplitude spectra of $\bar{\eta}(t)$ and $\eta'(x,z,t)$ are $|\bar{B}(f)|$ and $|B'(f)|$, respectively.

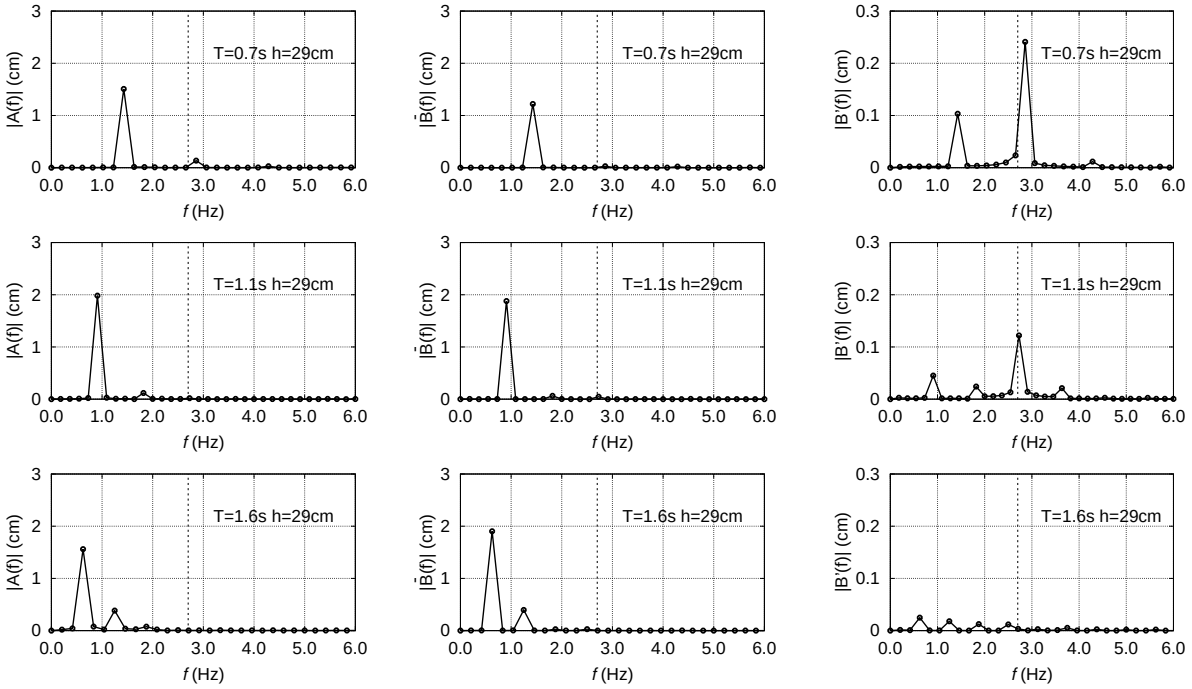

Figure 2.16: The amplitude spectra of $\eta_I(t)$, $\bar{\eta}(t)$ and $\eta'(t)$ for three test cases (T=0.7, 1.1 and 1.6 s) in Experiment A.

Figure 2.16 shows the amplitude spectra $|A(f)|$, $|\bar{B}(f)|$ and $|B'(f)|$ for three cases (T=0.7, 1.1, and 1.6 s) selected from Experiment A (h=0.29 m). The harmonic analysis is performed using the simulated results. The displacements for the spatial-average motion are obtained by interpolating and averaging the vertical water surface elevations across the OWC chamber over a mesh of 1mm resolution, and the sloshing motion is obtained using the surface displacement at the location of G_2. The vertical dashed line at f_n=2.717 Hz in Figure 2.16 indicates the resonant sloshing frequency of the OWC chamber (see Deng et al., 2013; Xu et al., 2016), which corresponds to a wavelength of about 1.8 times the diameter of the OWC chamber. Because the higher harmonic locked waves all have the same phase speed as that of the incident fundamental waves (i.e., the second harmonic locked waves have a length that is one half of the length of the first harmonic incident waves, and the third harmonic locked waves have a length that is one third of the length of the first harmonic incident waves), the resonant sloshing motion discovered by Deng et al. (2013) and Xu et al. (2016) is a free-standing wave whose phase speed is not locked to that of the incident waves. For all three wave periods, even though the incident waves have weak second harmonic components, the third harmonic components in the incident waves are negligibly small. Among the three wave periods, the incident waves with T=1.6 s have a relatively larger second harmonic component, which is about 25% of the amplitude of the first harmonic.

In the first row in Figure 2.16 for T=0.7 s, the amplitude of the first harmonic oscillation in the spatial-average motion is slightly smaller than that in the incident waves. The first harmonic in the sloshing motion also contributes to the non-uniformity of the water surface inside the OWC chamber. The amplitude of the second harmonic in the spatial-average component is negligibly small; The sloshing component, however, is significantly large: as large as 20% of the amplitude of the first harmonic in the spatial-average component. We remark that the second harmonic sloshing has a frequency close to the OWC's resonant sloshing frequency.

In the second row in Figure 2.16 where T =1.1 s, the spatial-average motion is dominated by the first harmonic motion that has an amplitude similar to that of the incident waves. The sloshing motion is dominated by the third harmonic motion, whose frequency is almost identical to that of the OWC's resonant sloshing frequency. The sloshing motion has a first harmonic component similar to that for T=0.7 s, but both the second and fourth harmonic components are small. Again, the third harmonic sloshing motion in this case has a frequency close to the OWC's resonant sloshing frequency.

For the third row in Figure 2.16 where T=1.6 s, in addition to the first harmonic motion, the spatial-average motion also has a noticeable second harmonic oscillation whose amplitude is about the same as that in the incident waves. The higher harmonics in the sloshing motion are all weak, which is in agreement with the generally accepted conclusion that the water surface acts like a weightless position for longer waves (Evans, 1982). No resonant sloshing occurred for this wave period.

Figure 2.17 shows the amplitude spectra $|A(f)|$, $|\bar{B}(f)|$ and $|B'(f)|$ for three cases (T=0.7, 1.1, and 1.6 s) selected from Experiment B (h=0.31 m). Again, results from the simulation are presented here. For all three wave periods, even though the incident waves have weak second harmonic components, the third harmonic components in the incident waves are negligibly small. The vertical dashed line at f_n=2.717 Hz indicates the resonant frequency of the OWC chamber (see Deng et al., 2013; Xu et al., 2016), which corresponds to a wavelength about 1.8 times the diameter of the OWC chamber. For a given design of the OWC pile, a deeper water depth means a deeper draft (or submergence) of the OWC chamber. Similar to h=0.29 m, the resonant sloshing occurs at the second harmonic for T=0.7 s, and the resonant sloshing occurs at the third harmonic for T=1.1 s. Comparing Figure 2.16 and Figure 2.17 shows that slightly increasing the draft can only slightly reduce the first harmonic amplitudes in both the spatial-average motion and sloshing motion, but can noticeably reduce the higher harmonic amplitudes in the sloshing motion.

From Figure 2.16 and 2.17, some important conclusions about the sloshing motion inside the OWC chamber can be drawn. For T=0.7 s, resonant sloshing is excited by the second harmonic forcing; for T=1.1 s, the resonant sloshing is excited by the third harmonic forcing. For T=1.6 s, there is no resonant sloshing. The excitation forcing that feeds energy into resonant sloshing cannot be the higher harmonic locked waves for two reasons: (i) the third harmonic locked waves

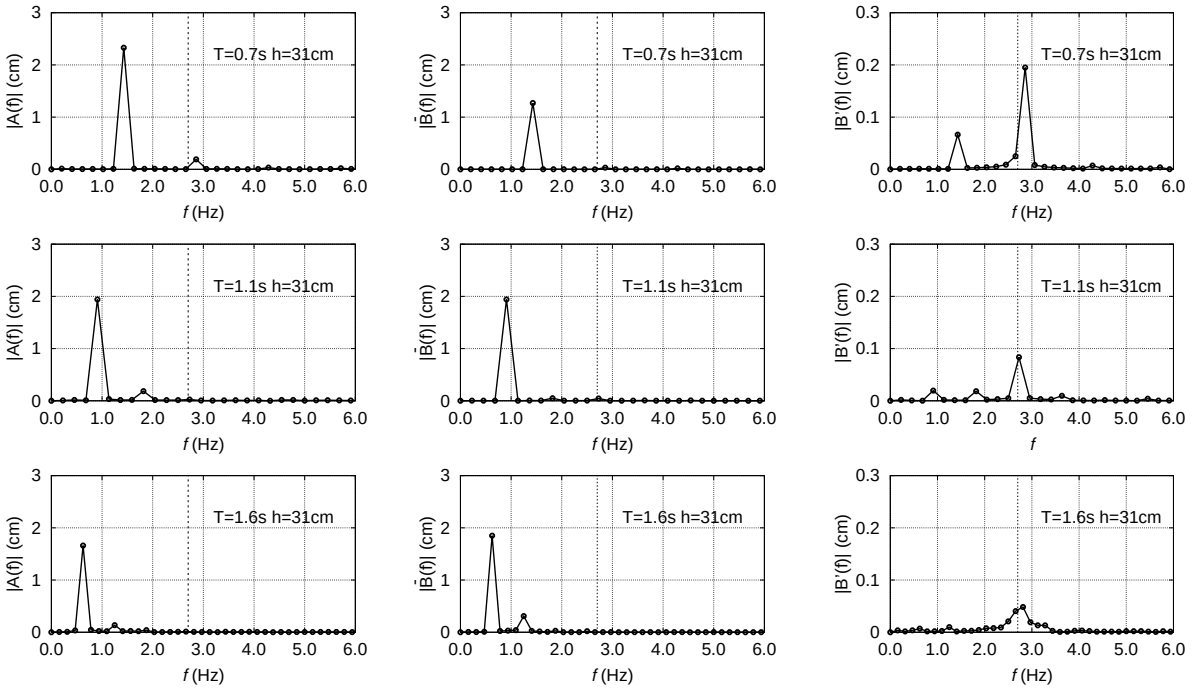

Figure 2.17: The amplitude spectra of $\eta_I(t)$, $\bar{\eta}(t)$ and $\eta'(t)$ for three test cases (T=0.7, 1.1 and 1.6 s) in Experiment B.

in the incident waves for T=1.1 s are too weak to provide enough energy to excite the resonant sloshing; (ii) the resonant sloshing has a wavelength about two times the OWC diameter, which is much shorter than the lengths of the second and third harmonic locked waves, and thus it is not the second or third harmonic locked waves that provide the excitation forcing through wave-wave nonlinear interaction.

Other possible nonlinear mechanisms that may be responsible for exciting the resonant sloshing inside the OWC chamber are: (i) the air flow through the nonlinear PTO and (ii) vortex shedding. Because the PTO in the experiment was an orifice, which has a quadratic relationship with the spatial-average velocity of the water surface inside the OWC chamber, the nonlinear PTO may play a role in exciting the resonant sloshing. Vortex shedding at the lower tip of the OWC front skirt may perturb the flow field inside the OWC chamber and thus may play a role in exciting the resonant sloshing.

Sloshing motion in the OWC chamber without PTO

The nonlinear PTO described by Eq. (2.45) can generate higher harmonic components in the fluctuating air pressure $p(t)$. It is interesting to know whether or not the higher harmonic sloshing in the OWC chamber is related to the nonlinear PTO. For this purpose, another set of CFD simulations are performed with the PTO being removed from the top cover so that the OWC

chamber is fully open to the surrounding air (i.e., the pressure on the water surface is the constant atmospheric pressure). Figures 2.18 and 2.19 show the amplitude spectra of the incident waves, the spatial-average motion and the sloshing motion for Experiment A and Experiment B, respectively. For a fully-opened OWC, the spatial-average motion is dominated by the first harmonic oscillation but the sloshing motion is dominated by higher harmonics.

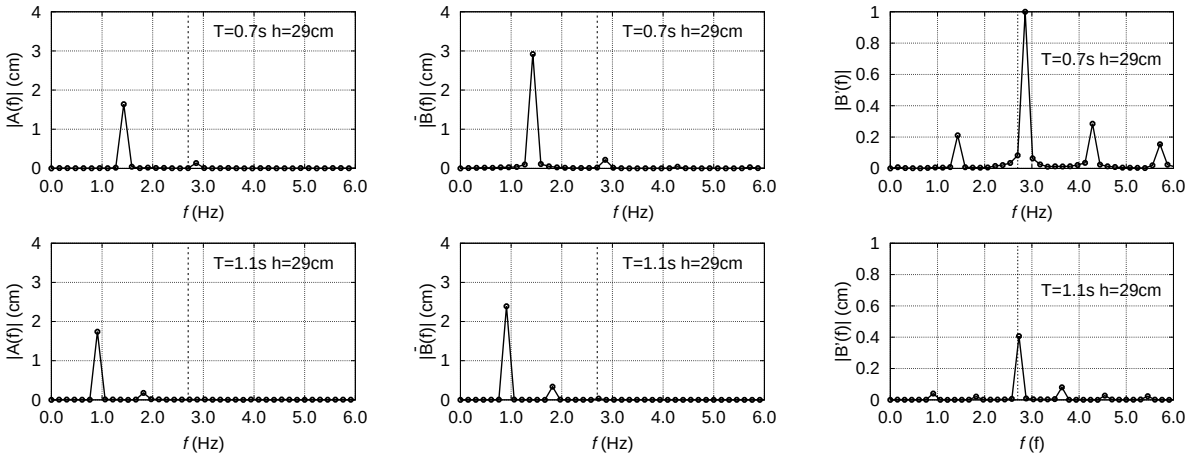

Figure 2.18: Plots of the spectrum analysis results of η_I, $\bar{\eta}(t)$ and $\eta'(t)$ measured at the location G_2 for selected test wave conditions with the OWC chamber fully opened to the air. $h = 0.29$ m.

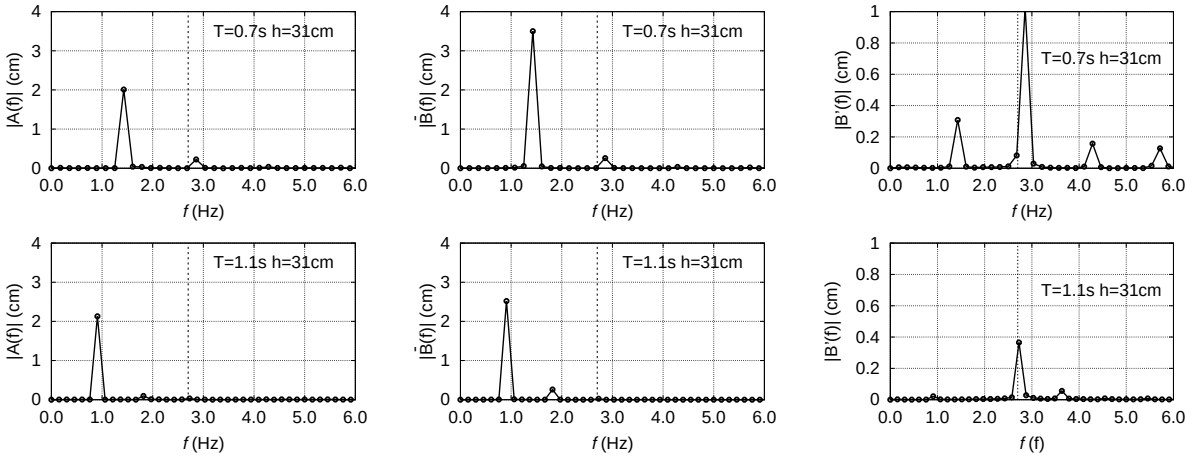

Figure 2.19: Plots of the spectrum analysis results of η_I, $\bar{\eta}(t)$ and $\eta'(t)$ measured at the location G_2 for selected test wave conditions with the OWC chamber fully opened to the air. $h = 0.31$ m.

For T=0.7 s, the amplitude of the first harmonic in the spatial-average motion is almost two times that of the corresponding incident waves, and the sloshing motion is dominated by the second harmonic motion whose amplitude can reach about 60% of the amplitude of the first harmonic in the incident waves. The third and fourth harmonic components can also be identified in the sloshing

motion. In this case, the frequency of the second harmonic is close to that of the resonant sloshing. Note that the third and fourth harmonics are negligibly small in the incident waves. Compared to the case with a PTO, the pressure fluctuation inside the OWC chamber suppresses the amplitudes of both the spatial-average motion and the sloshing motion.

For T=1.1 s, the first harmonic amplitude of the spatial-average motion is almost 1.5 times that of the corresponding incident waves, and the sloshing motion is dominated by the third harmonic motion whose amplitude can reach about 20% of the first harmonic amplitude in the incident waves. The fourth harmonic is also noticeable in the sloshing motion. For this case, the frequency of the third harmonic sloshing motion is close to that of the resonant sloshing. Note also that the third and fourth harmonics are negligibly small in the incident waves. Again, compared to the case with a PTO, the pressure fluctuation inside the pneumatic chamber suppresses the amplitudes of both the spatial-average motion and the sloshing motion.

It can be concluded that the resonant sloshing motion in the OWC chamber is not excited by the nonlinear PTO. Even though the resonant sloshing is not excited by the air-pressure fluctuation introduced by the nonlinear PTO, but the nonlinear PTO can suppress both the spatial-average motion and the sloshing motion through the generation of radiated waves.

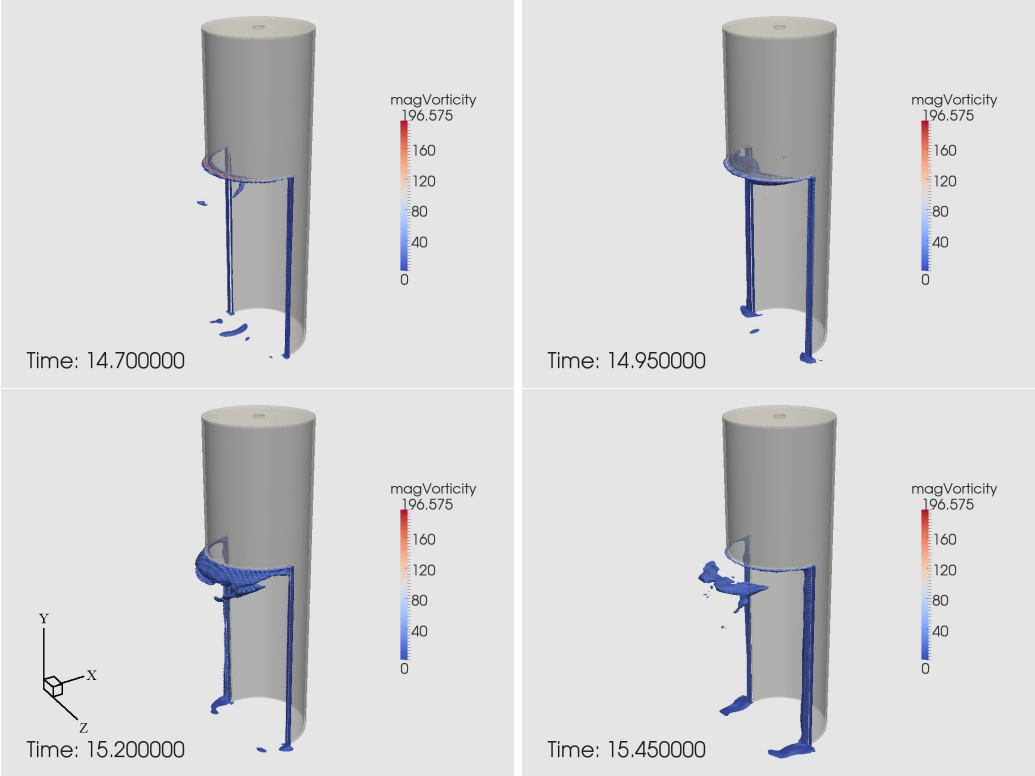

Figure 2.20: Snapshots of the computed magnitudes of the vorticity at four time instants.

Excitation of resonant sloshing by vortex shedding

If the resonant sloshing motion inside the OWC chamber is not excited by the nonlinear PTO or the higher harmonic wave components in the incoming waves, it may be exited by the vortex shedding at the sharp edges of the OWC pile. Wave-induced vortex shedding is a viscous, nonlinear process. To understand the relation between vortex shedding and resonant sloshing, we examine the spectrum of the computed vorticty. Figure 2.20 shows snapshots of the computed magnitudes of the vorticity at four time instants within one wave period for the case of T=1.1 s in Experiment A. The dominant direction of the vorticity should be parallel to the wave crest, which is z direction in the coordinate system used here. The $z-$ component of the vorticity vector at a given location, $\omega_z(t)$ can be written as,

$$\omega_z(t) = \frac{1}{2}\int_{-\infty}^{\infty} \Omega_z(f) e^{-2\pi f t} df \tag{2.52}$$

We denote the amplitude spectrum of the vorticity $\omega_z(t)$ as $\Omega(f) = |\Omega_z(f)|$. Figure 2.21 shows the vorticity spectra at 1 cm below the lower skirt of the OWC chamber along the central axis, for the cases of $T = 0.7$ s and $T = 1.1$ s in Experiment A, but without PTO (i.e., the OWC chamber is fully open to the surrounding air). The vorticity spectrum for $T = 0.7$ s has four harmonics and the vorticity spectrum for T=1.1 s has three harmonics. The vortex shedding can generate fluctuating pressure, which can generate free waves of various frequency components: for $T = 0.7$ s the second harmonic fluctuation of the vorticity is able to excite the resonant sloshing; for T=1.1 s the third harmonic fluctuation of the vorticity is able to excite the resonant sloshing. The nonlinear PTO will modify the amplitude spectrum of the vorticity through the generation of the radiated waves.

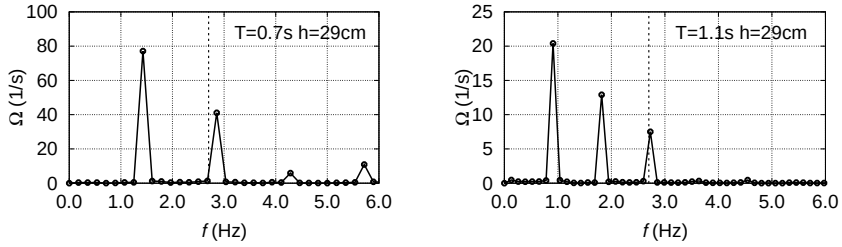

Figure 2.21: Amplitude spectra of the vorticity component ω_y for T= 0.7 s (left) and T=1.1 s (right). The OWC chamber is fully open to the air.

2.3.5 Effects of sloshing motion inside the OWC chamber

Due to the lack of a good method to accurately measure the complex 3D motion of the water surface inside the OWC chamber, wave-flume experiments rely on a very limited number of wave gauges to measure the displacements of the water surface at one (Morris-Thomas et al., 2007; Xu et al., 2016; Ning et al., 2016b) or two locations (He and Huang, 2014; Bingham et al., 2015) inside the OWC chamber. The existence of the surface sloshing inside the OWC chamber causes the

velocity measured at a single point to be larger than the spatial-average velocity, and thus affects the experimentally-determined capture width ratio and measured characteristics of the nonlinear PTO because the calculation of both needs the spatial-average velocity of the water surface inside the OWC chamber.

Effects on parameterization of the nonlinear PTO

Data fitting using Eq. (2.45) to both laboratory data (Xu et al., 2016) and simulation data indicate that for the small-scale model as tested, the effect of inertia in $p(t)$ is very small (less than 3%) and thus negligible. Figure 2.22 shows the values of the quadratic loss coefficient C_f obtained using the velocity measured at one point and the spatial-average velocity. Difference between $\tilde{C}_f$ and C_f can be observed. As expected, this difference is smaller for longer waves and deeper draft. Sloshing will make the velocity measured at a point larger than spatial-average velocity and thus makes $\tilde{C}_f$ smaller than C_f; this is especially true when resonant sloshing occurs. The values of $\tilde{C}_f$ are smaller at L/D=6.0186 and 12.4495 (i.e.,T=0.7 s and 1.1 s), the two periods at which resonant sloshing occurred. The following conclusions can be drawn from Figure 2.22:

1. The quadratic loss coefficient C_f is not sensitive to wave period.
2. The values of C_f and $\tilde{C}_f$ for long waves are almost the same for both Experiment A and Experiment B.

Therefore, it is possible to use the values of $\tilde{C}_f$ obtained for long waves as the average of C_f.

Effects on capture width ratio

Recall that the pneumatic power extraction is calculated by

$$P_{OWC} = \frac{1}{NT}\int_{t_0}^{t_0+NT}\left[\iint_S p(t)v(x,z,t)dxdz\right]dt. \tag{2.53}$$

When using the velocity measured at one point to calculate the pneumatic power extraction, we have instead

$$\tilde{P}_{OWC} = \frac{A_0}{NT}\int_{t_0}^{t_0+NT} p(t)\bar{v}(t)dt + \frac{1}{NT}\int_{t_0}^{t_0+T}\left[\iint_S p(t)v'(x,z,t)dxdz\right]dt, \tag{2.54}$$

where $\bar{v}(t)$ is the spatial average velocity and $v'(x,z,t)$ is the sloshing velocity. Note that the second term on the right hand side of Eq. (2.54) is zero if $v'(x,z,t)$ is known at every point on the water surface. In the experiment, $v'(x,z,t)$ is usually approximated by the value obtained at one location (x_G, z_G), i.e., $v'(x,z,t) \approx v'(x_G, z_G, t)$, which is denoted by $\tilde{v}(t)$ for simplicity hereinafter.

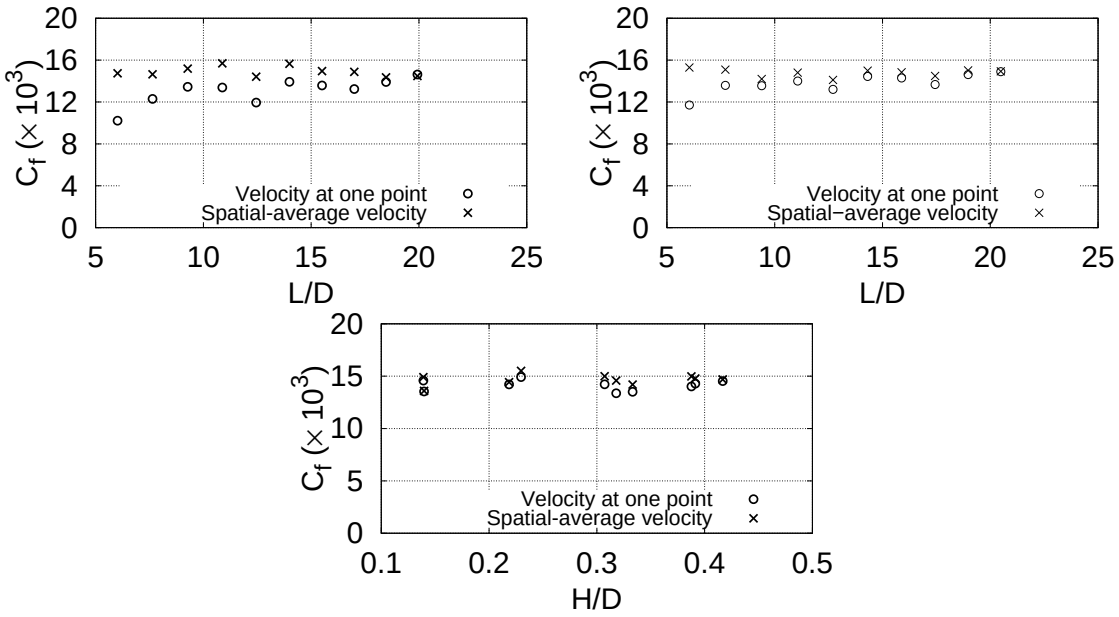

Figure 2.22: Comparisons between the values of C_f from simulation determined using the velocity at location G_1 and the cross-sectional averaged velocity Experiment A (upper left), Experiment B (upper right) and Experiment C (lower panel). The results presented here are based on numerical simulations.

Therefore, the approximate pneumatic power extraction is

$$\tilde{P}_{OWC} = \frac{A_0}{NT}\int_{t_0}^{t_0+NT} p(t)[\bar{v}(t)+\tilde{v}(t)]dt. \tag{2.55}$$

The capture width ratio obtained based on one-point measurement is

$$\tilde{\lambda}/D = \tilde{P}_{OWC}/(E_I C_g D). \tag{2.56}$$

The error introduced by the one-point measurement method to the capture width ratio is

$$\frac{\Delta P_{OWC}}{E_I C_g D} = \frac{A_0}{E_I C_g D N T}\int_{t_0}^{t_0+NT} p(t)\tilde{v}(t)dt, \tag{2.57}$$

which clearly shows that the sloshing motion will affect the capture width ratio calculated using the local velocity measured at one point inside the OWC chamber. Figure 2.23 shows a comparison between $\tilde{\lambda}/D$ and λ/D for Experiments A, B and C. In general the values of the capture width ratios calculated using spatial-average velocity and the local velocity measured at one point agree well except for the two shortest waves in the Experiment A. For L/D=6.0186 (T=0.7 s) in Experiment A, $\tilde{\lambda}/D$ is about 20% larger than λ/D. It is interesting to note that the resonant sloshing at L/D=12.4495 (T=1.1 s) does not have a significant influence on the calculated capture width

ratio. In the next section, a method will be proposed to improve the accuracy of the capture width ratio calculated using one-point measurement results.

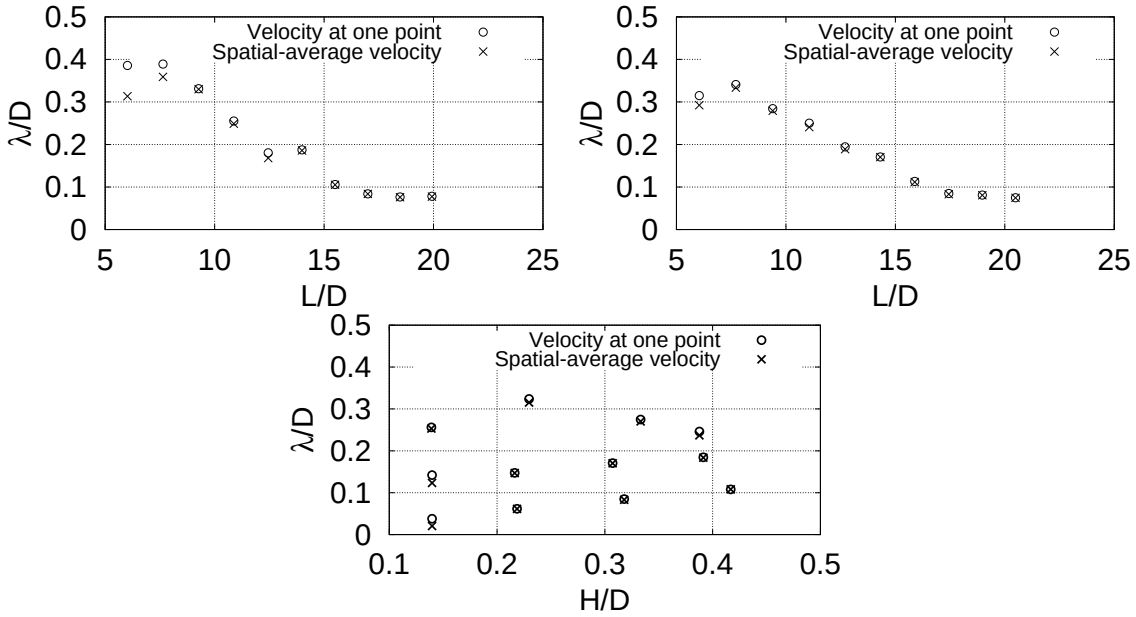

Figure 2.23: Comparisons between the values of capture length determined using the velocity at location G_2 and the cross-sectional averaged velocity for Experiment A (upper left), Experiment B (upper right) and Experiment C (lower panel).

2.3.6 One method to improve the accuracy of the calculated capture width

One method to reduce the measurement error in capture width ratio determined by using the velocity obtained from one wave gauge is to use the PTO model given by Eq. (2.45) and a constant quadratic loss coefficient determined for long waves. Because inertial effect is not important for small OWC models tested in wave-flume tests (Xu et al., 2016), we can set $L_g = 0$, and then the pressure can be written as

$$p(t) = \frac{1}{2} C_f \rho_a \left|\bar{v}(t)\right| \bar{v}(t). \tag{2.58}$$

Using Eq. (2.58) in Eq. (2.40) gives

$$P_{OWC} = \frac{A_0}{NT} \int_{t_0}^{t_0+NT} p(t)\bar{v}(t)dt = \frac{1}{2} C_f \rho_a \frac{A_0}{NT} \int_{t_0}^{t_0+NT} \left|\bar{v}(t)\right|^3 dt. \tag{2.59}$$

From Eq. (2.58), we have

$$|p(t)| = \frac{1}{2} C_f \rho_a |\bar{v}(t)|^2 \rightarrow |\bar{v}(t)|^3 = 2\sqrt{2} \left[\frac{|p(t)|}{C_f \rho_a} \right]^{3/2}. \tag{2.60}$$

Using Eq. (2.60) in Eq. (2.59) gives

$$P_{OWC} = \frac{\sqrt{2} A_0}{NT \sqrt{C_f \rho_a}} \int_{t_0}^{t_0+NT} |p(t)|^{\frac{3}{2}} dt. \tag{2.61}$$

Because the pressure measured in wave-flume experiment is not affected by the sloshing, if we can have a better estimation of C_f, then Eq. (2.61) can be used to calculate the capture width ratio for waves that may cause large errors due to the surface sloshing inside the OWC chamber.

Figure 2.24 show three comparisons based on numerical simulation data to support the use of Eq. (2.61) to calculate the capture width ratio. The left panel of Figure 2.24 shows a comparison between the values of the capture width ratios calculated using Eq. (2.54) with the spatial average velocity and pressure and Eq. (2.61) with individual values of C_f obtained from spatial averaged velocities. This suggests that Eq. (2.61) can provide an accurate determination of the capture width ratio if accurate estimation of C_f is available. The middle panel of Figure 2.24 shows a comparison between the values of the capture width ratios calculated using Eq. (2.61) with individual values of C_f from spatial averaged velocities and a mean value of $\tilde{C}_f$ obtained from the one point measurement for the longest two waves. This suggests that it is possible to use a mean C_f from long waves to determine the capture width ratio with good accuracy. The right panel of Figure 2.24 shows a comparison between the values of the capture width ratio calculated using Eq. (2.61) with a mean $\tilde{C}_f$ from the two longest waves and using Eq. (2.43) with the pressure and velocity measurements from respective numerical probes. This suggests that using the mean $\tilde{C}_f$ from long waves provides more accurate results for the estimation of the capture width ratio, especially for short waves such as $T = 0.7$ and 0.8 s.

Therefore, it is possible to use the measured pressure and a good estimation of C_f to reduce the measurement error introduced to the capture width ratio by the one-point measurement method. Because the sloshing motion for longer waves is negligible, a mean value of C_f can be determined using long waves in wave-flume experiment and this mean value of C_f can be used with the measured pressure for other wave periods to calculate the capture width ratio using Eq. (2.61).

2.4 Performance of a row of loosely spaced OWC-piles as a shore protection wave barrier and wave farm

This section presents an estimation of a scaled-up prototype wave farm with a single layer of loosely-spaced OWC-piles covering a 1000-m long coast. In the present study, although only a standalone

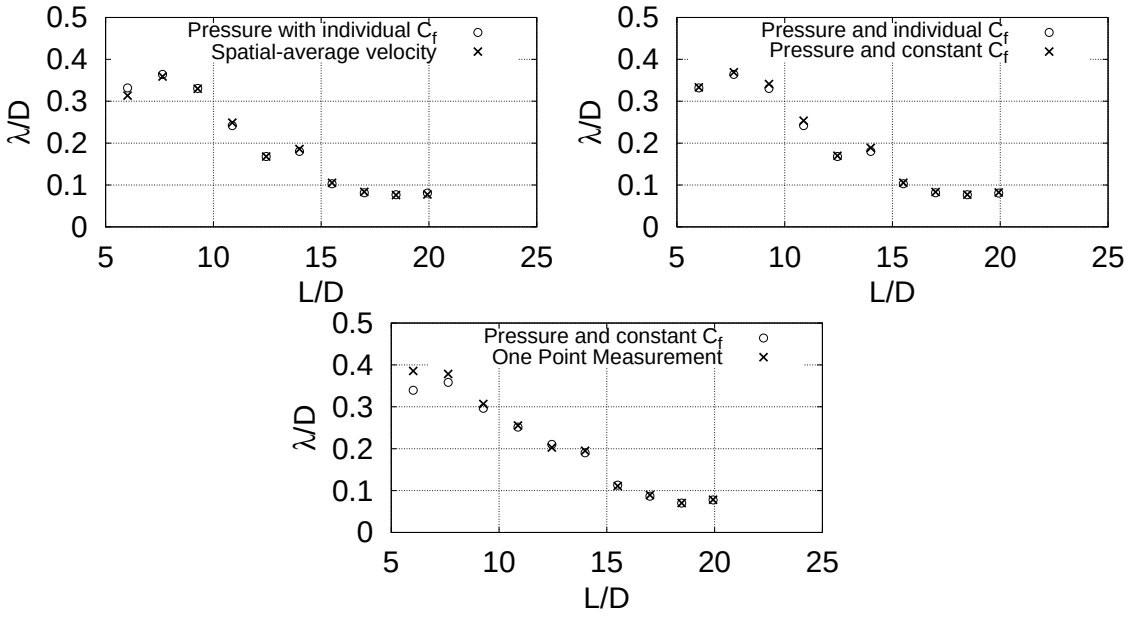

Figure 2.24: Comparisons of the capture-width ratios obtained using various method. Upper left: using pressure and spatial-average velocity and using pressure alone with individual values of C_f. Upper right: using pressure alone with individual values of C_f and using pressure alone with the mean value of C_f determined for longer waves. Lower panel: using pressure alone with the mean value of C_f determined for long waves and using pressure and the local velocity obtained at a single point.

OWC-pile device is tested, the numerical results can still be extended to study a configuration of a single-layered wave farm in the form of loosely spaced OWC-piles. This is achieved by considering the wave flume side walls as symmetrical boundaries, as shown in Figure 2.25. In the present experiment, since the width of the wave flume is 54 cm, the diameter of the OWC-pile is $D = 12.5$ cm, the wave farm thus have a nominal gap-diameter ratio of $G/D = 4.32$, where G is the gap size as shown in Figure 2.25. Note that this gap-diameter ratio indicates that the current configuration represents a looser arrangement as compared to what was tested in Abanade et al. (2014) and Mendoza et al. (2014). It is thus possible to use the computed transmission coefficient C_t in the present study to represent the transmission coefficient C_t of a wave farm of loosely spaced OWC-piles with a gap-diameter ration of 4.32. As will be discussed in Section 3.8, a geometric scale factor of $s_c = 25$ is used in this scale up, representing a diameter of pile $D = 3.125$ m and a water depth of 7.25 m and 7.75 m based on the experimental values. The total electric power output of the wave farm consisting of N OWC-piles can be estimated by

$$P^{(N)} = \eta_{gen}\,\eta_{rtr}\,\eta_{air}\,\eta_{pneu}(ND)P_i, \tag{2.62}$$

where η_{gen} is the efficiency of the generator, η_{rtr} is the efficiency of the turbine, η_{pneu} is the pneumatic efficiency of the OWC-pile, which is equal to λ/D, η_{air} is a correction factor for air compressibility. Here we take $\eta_{gen} = 0.9$, $\eta_{rtr} = 0.7$, $\eta_{air} = 0.88$, η_{pneu} is taken from the respective experimental values of λ/D. In the case of gap-diaemter ratio $n = 4.32$ and a 1000-m coastline, N is 74. A detailed discussion of the scale-up model and the values of efficiencies is presented in Section 3.8.

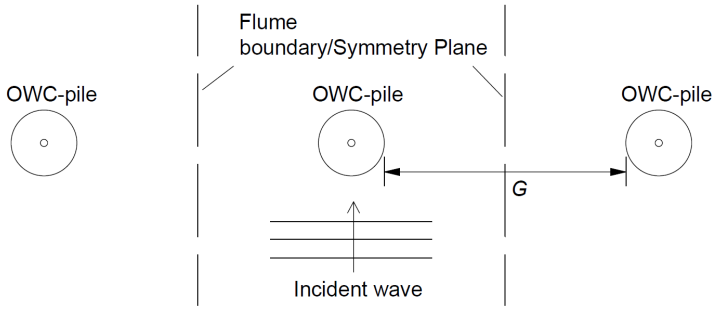

Figure 2.25: A sketch of a wave farm of infinite length in the form of loosely spaced OWC-piles, the flume side walls are treated as symmetrical boundaries.

2.4.1 Estimation of transmission coefficient based on numerical data

The numerical studies conducted in Abanade et al. (2014) and Mendoza et al. (2014) investigated the impact of offshore wave farms consisting of loosely spaced wave energy converters. In these

numerical investigations, the effect of wave damping induced by the wave farms is modeled as transmission coefficients. In both studies, for loosely spaced wave energy converters with gap size between adjacent devices approximately equal to the span-wise dimension of the device, the target transmission coefficients are set at $C_t = 0.7$ to 0.76. It was found in their study that for the tested location of the wave farm, the coastal erosion could be reduced and beach accretion could be observed in better-protected regions. However, the parametrization of the transmission coefficient of these tested wave farms is estimated values, which calls for a more accurate description of the wave transmission through loosely spaced WEC devices.

Utilizing data from the numerical simulation, a two-point wave separation method is utilized with water surface elevation time series extracted at 1.5 m and 1.3 m in front of and in back of the model. The data from the two locations in front of the model are used to provide the incident wave amplitude A_i after wave separation. The data from the two locations in back of the model are used to provide the transmitted wave amplitude A_t, so that the transmission coefficient could be computed by

$$C_t = \frac{A_t}{A_i}. \tag{2.63}$$

The computed transmission coefficient C_t for the test case 1b, 1e and 1j (refer to Table 2.1 for test conditions) are 0.9004, 0.9516, and 0.9890, respectively. They are all smaller than the estimated target transmission coefficient as tested in Abanade et al. (2014) and Mendoza et al. (2014). It is thus safe to conclude that under a loose configuration with a gap-diameter ratio of $G/D = 4.32$, a wave farm of OWC-piles does not attenuate enough wave energy to produce good shore protection under short, intermediate and long wave conditions. To improve the performance of the wave farm for shore protection, a closely spaced configuration must be employed. In the next chapter, a closely spaced wave farm consists of the presently studied OWC-pile is investigated.

2.4.2 Estimation of the electric power output

Table 2.2 shows a summary of the performance of the scaled-up prototype wave farm in terms of electric power output. The six wave conditions selected in this scale-up are test cases 1e, 2e, 1b, 2b, 2c and 2h, respectively (see Table 2.1 for test conditions). These conditions are selected to reflect tidal variation (water depth difference of 0.5m) and seasonal variation (wave height and wave period) of wave conditions. These conditions are also the same as the conditions used in Section 3.8 for the purpose of comparison. The electric power output of the wave farm of loosely spaced OWC-piles at given gap-diameter ratio varies between 0.131MW and 0.271MN, which could potentially power around 100 households.

Because this loosely spaced configuration cannot provide enough shore protection as a breakwater, the structure is purely intended for wave energy utilization. However, the amount of electricity

Table 2.2: Electric power output estimates for the hypothetical power plant

Scenario	T [s]	h [m]	H [m]	P_i [kW]	$T/\sqrt{g/D}$	H/D	η_{pneu}	Power [MW]
1	5.5	7.25	0.94	5.57	9.74	0.300	0.203	0.145
2	5.5	7.75	0.94	5.60	9.74	0.301	0.220	0.158
3	4	7.25	0.92	3.64	7.08	0.294	0.379	0.177
4	4	7.75	0.92	3.58	7.08	0.294	0.345	0.158
5	4.5	7.75	1.17	6.80	7.97	0.374	0.310	0.271
6	7	7.75	1.14	10.02	12.39	0.364	0.102	0.131

generated cannot justify the significant investment. Therefore, it is necessary to consider the performance of the closely spaced configuration.

2.5 Visualization of the vortex structure near the bed

The formation of vortices, including horseshoe vortex and wake vortices, can have significant impact on the pattern of sediment transport around an OWC-pile device. Consequently, these flow features determine the scouring at the foundation of the structure, which is directly related to structural safety. In this section, a visualization of the three-dimensional flow field near the bed obtained from simulation is presented in the form of 2-D streamlines at the slice planes. Three test conditions: test cases 1a, 1e, and 1i (refer to Table 2.1 for detailed conditions), representing short ($T = 0.7$ s), intermediate ($T = 1.1$ s) and long wave ($T = 1.5$ s) conditions, are selected for visualization. A detailed explanation of the flow field visualization technique used here and how to interpret the different flow features found in these limiting streamline-like representations will be discussed in detail in Chapter 4. In this section, we refer to these limiting streamline-like flow visualization elements away from the bottom as "sectional streamlines" following Perry and Steiner (1987).

The time instances selected for the visualization are shown in the time series plot at the top of each of the flow visualization plot. These time instances are selected to cover a complete wave cycle with an in-flow phase, which is defined as the phase of flow oscillation when the water mass is entering the OWC chamber causes the OWC chamber water displacement η to rise, and an out-flow phase, which defined as the phase of flow oscillation when the water mass is leaving the OWC chamber cause η to drop. Between these two phases, a flow reversal is present, but may not necessarily be captured by the selected time instances or geometric region.

It must be noted that since the CFD simulation carried out did not include sediment phase, the turbulence modulation due to the presence of suspended sediment cannot be considered. The existence of turbulence modulation may significantly impact the existence and development of weak or small vortices. The large vortices found in the flow field should not be significantly modified by

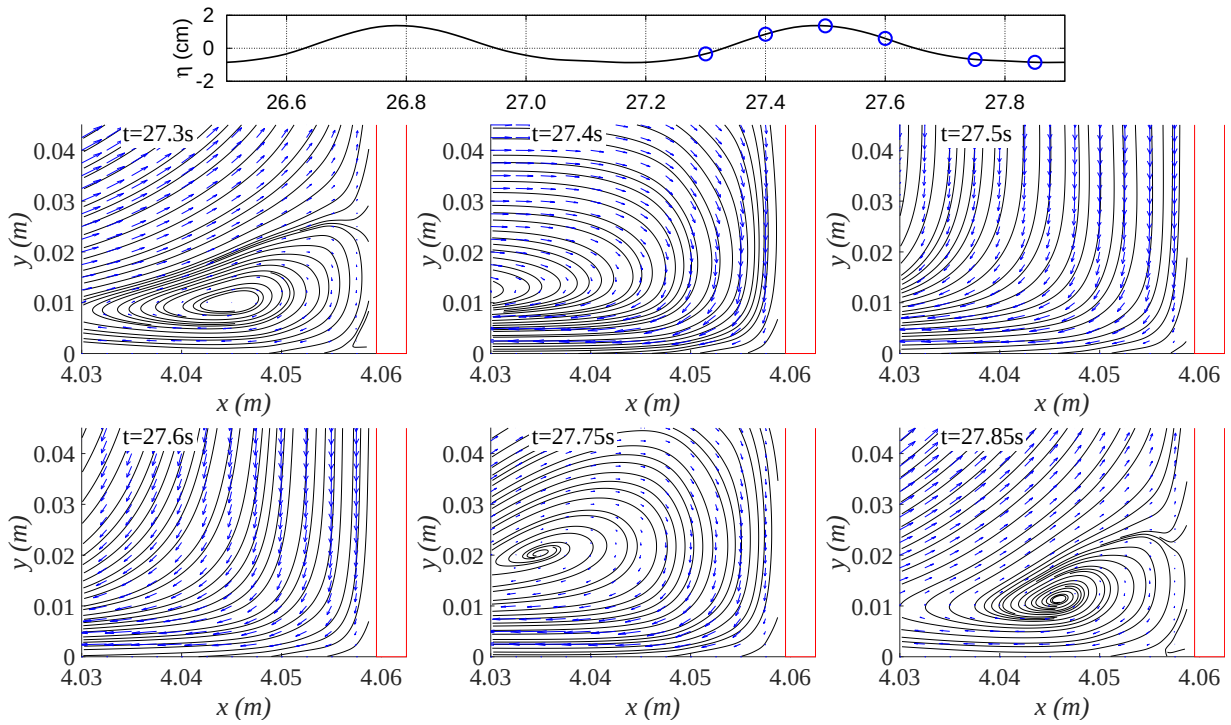

Figure 2.26: The u-v velocity field and sectional streamlines near the back wall of the OWC-pile structure along the slice plane A of a standalone OWC-pile simulation, showing the test condition T=0.7s. The scale at y-axis is compressed by a factor of 2.

turbulence modulation due to suspended sediment.

Figures 2.26 and 2.27 show the flow fields and sectional streamlines around a standalone OWC-pile at the slice planes A and B, respectively, for the test condition T=0.7s. It can be seen from Figure 2.26 that a large horseshoe vortex system is formed during the in-flow phase of the wave cycle. However, the formed horseshoe vortex is periodically shed during the subsequent out-flow phase. The size of the horseshoe vortex changes as the flow oscillates, reaching a maximum vertical size of about 3.0 cm.

From Figure 2.27, the negative open bifurcation line, indicating the horseshoe vortex is evident during the in-flow phase of the wave cycle (i.e., when the water surface inside the chamber is moving up), which is in accordance with the findings from Figure 2.26. The horseshoe vortex does not extend over the full width of the model, indicating that the horseshoe vortex in the case of a standalone OWC-pile is relatively weak. The formation of lee wake vortex is not significant in the case of a standalone OWC-pile for $T = 0.7$ s, and only small vortices can be seen being shed from the side edge of the back wall due to flow separation. The seemingly "stagnant" of flow found inside the concave region up-wave of the back wall in fact indicates a net up-draft or down-draft of flow, with the actual velocity vectors pointing upward or downward normal to the $x - y$ plane

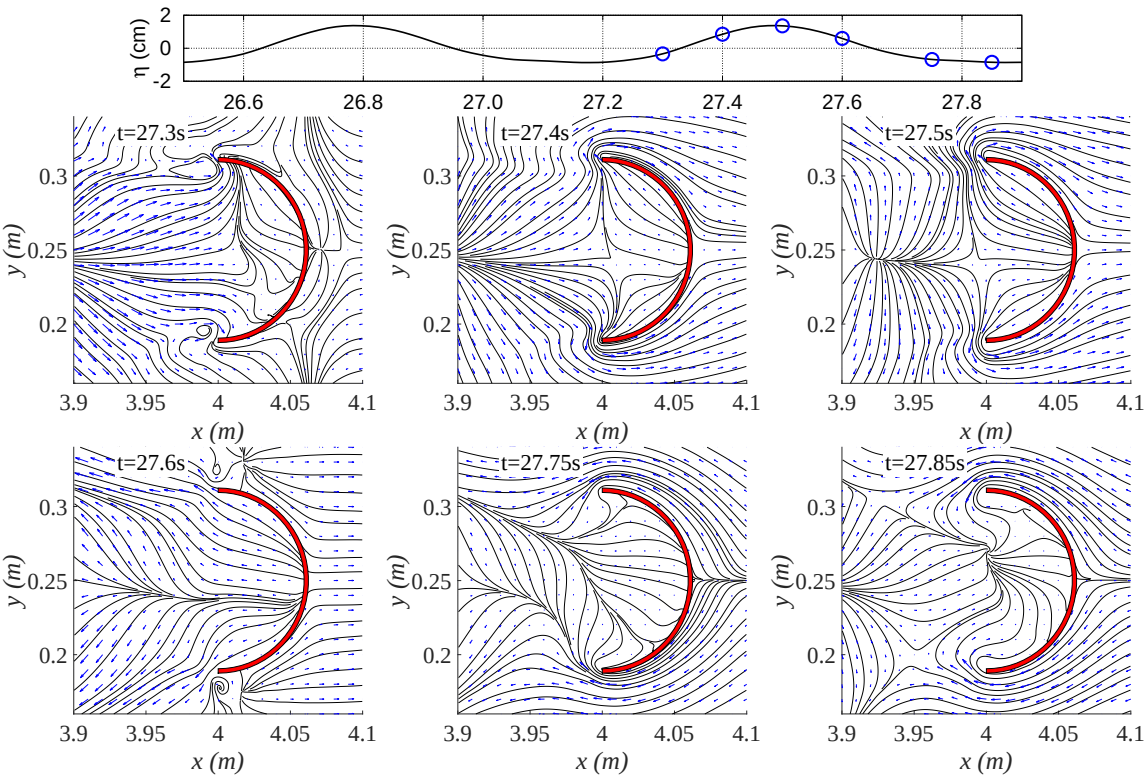

Figure 2.27: The u-w velocity field and sectional streamlines near the back wall of the OWC-pile structure along the slice plane B of a standalone OWC-piles simulation, showing the test condition T=0.7s.

(i.e., with large w component but small $u - v$ components), which is induced by the oscillation of the water surface inside the OWC chamber.

Figures 2.28 and 2.29 show the flow field and limiting streamline at the slice planes A and B , respectively, for $T = 1.1$ s. For this case, the size of the horseshoe vortex is significantly smaller compared to the test case with $T = 0.7$ s; the vertical size of the horseshoe vortex is less than 1 cm. It is interesting to note how the size of the horseshoe vortex system actually decreases with a slight increase of the flow KC number (refer to Table 2.3 for the KC numbers of the visualized test conditions). The horseshoe vortex is persistent throughout the wave cycle but its center becomes unclear during the in-flow phase of the wave cycle, indicating the size of the horseshoe vortex is smaller than what the mesh could resolve clearly. The horseshoe vortex structure is clearly visible during the out-flow phase. It is interesting to note that near the toe of the structure back wall, flow reversal is not evident: the $u - v$ velocity vector is always pointing towards the back wall of the structure, indicating the existence of normal flow component from the central axis of the model towards the two sides. A large vortical structure could be observed at the top of the visualized region during the out-flow phase and the flow reversal could be observed near this large vortical

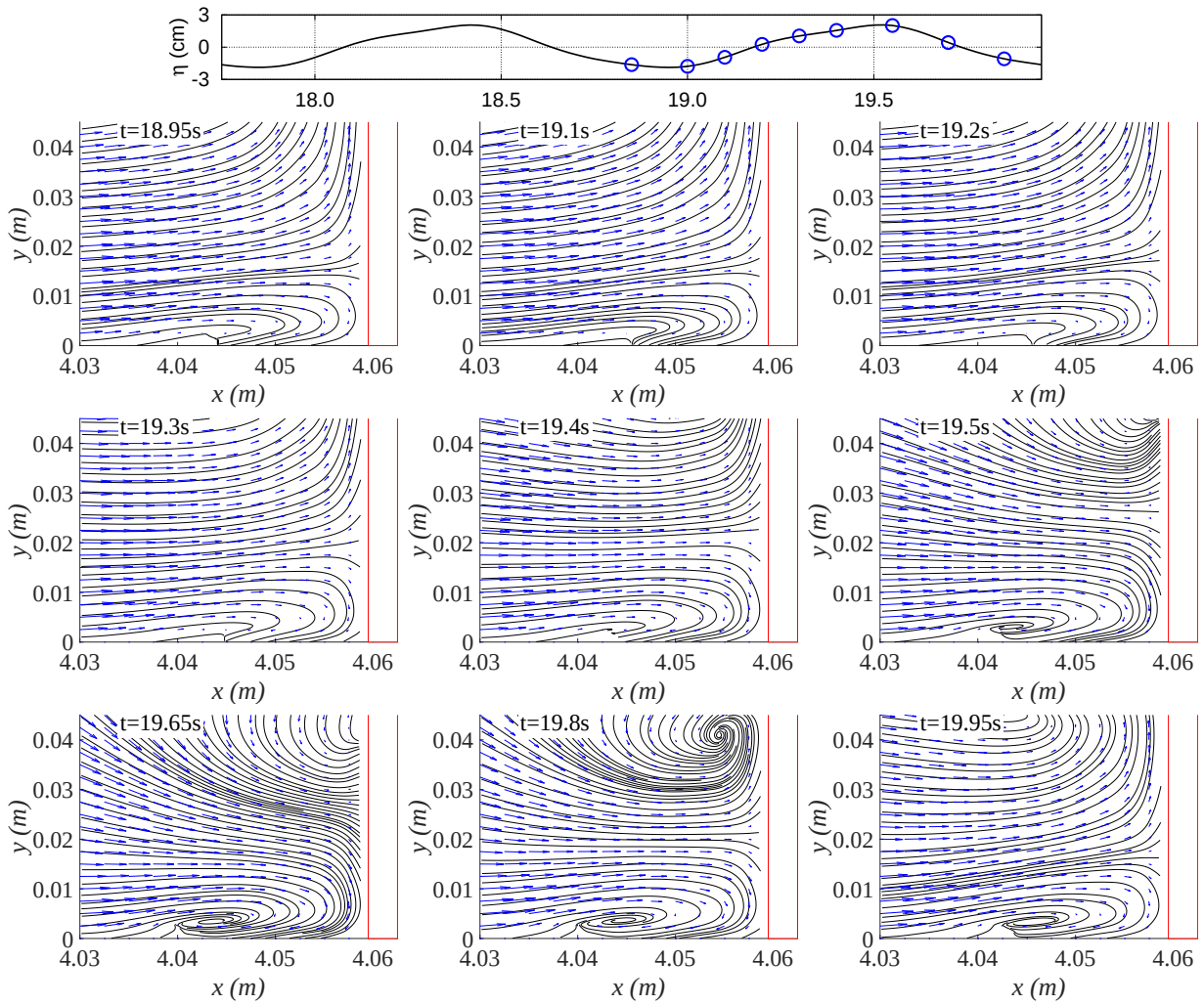

Figure 2.28: The u-v velocity field and sectional streamlines near the back wall of the OWC-pile structure along the slice plane A for a standalone OWC-pile simulation, showing the test condition T=1.1s. The scale at y-axis is compressed by a factor of 2.

structure. This appears to imply that the flow reversal on the $x-y$ plane should be evident above this vortical structure.

From the top view of the slice plane B shown in Figure 2.29, two large vortices are clearly visible on the up-wave side of the back wall. These two vortices are not shed or destroyed by the flow reversal during a wave cycle and their position is relatively stable throughout the wave cycle. A constant inflow towards the concave region formed by the back wall of the OWC-pile can be observed regardless of the phase in the wave cycle, which is in accordance with the findings in Figure 2.28. This inflow reaches the back wall and then separates to flow towards the two sides of the back wall to form an outflow. This outflow is then sheared with the inflow on the outside of the

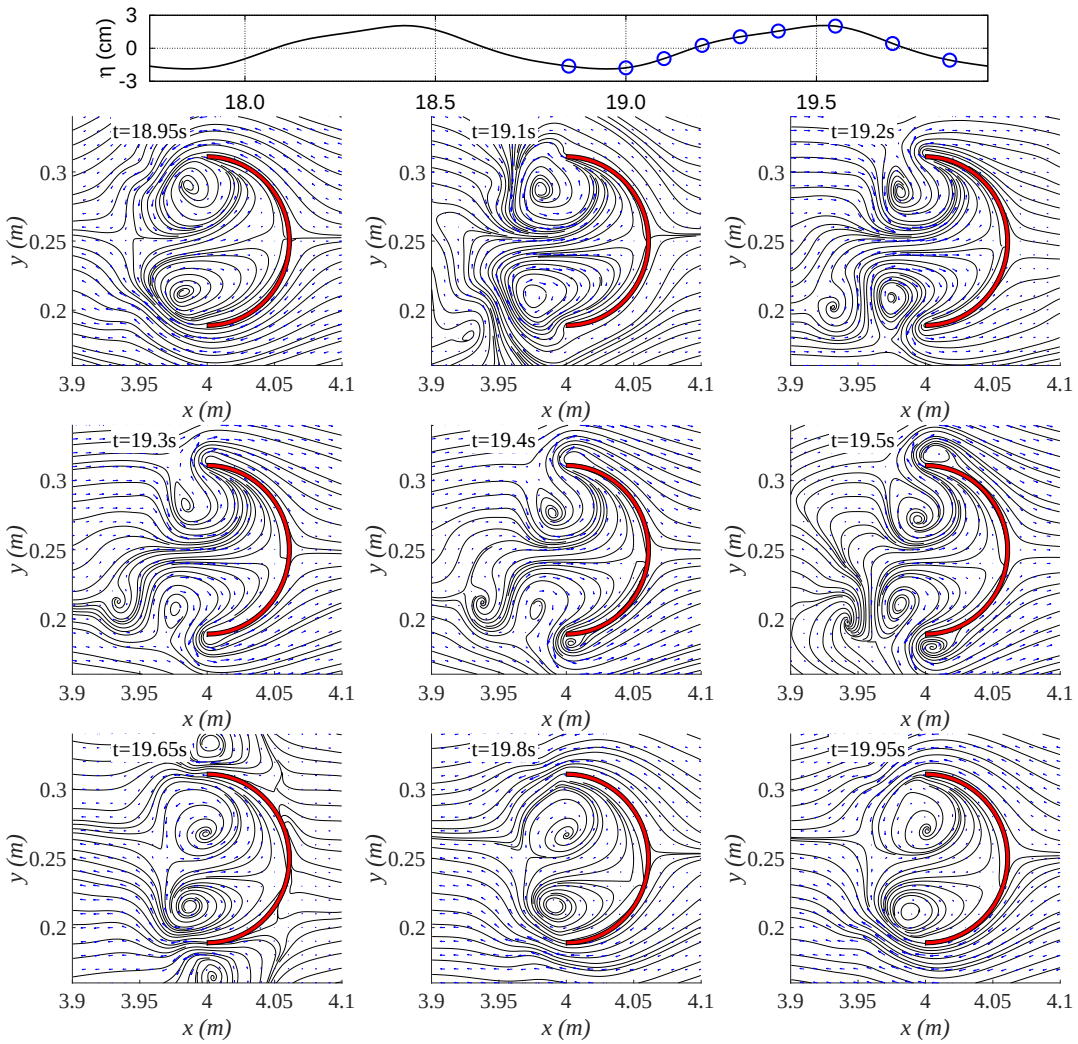

Figure 2.29: The u-w velocity field and sectional streamlines near the back wall of the OWC-pile structure along slice plane B for a standalone OWC-piles simulation, showing the test condition T=1.1s.

concave region at the two sides, which may contribute to the generation and maintaining of the two large vortices on the up-wave side of the back wall. Another two smaller vortices are periodically shed from the two side edges of the back wall due to flow separation. These two vortices, however, appear to be moving out of the region, instead of moving towards the down-wave side of the model.

Figures 2.30 and 2.31 shows the flow field and limiting streamline around a standalone OWC-pile at slice planes A and B , respectively, for the test condition $T = 1.5$ s. From the flow field in the slice plane A shown in Figure 2.30, a clear horseshoe vortex system is not visible. However, a very small vortical pattern can be observed at the time instance $t = 16.05$ s with its center unclear, indicating that the horseshoe vortex system may still be present, but at much smaller temporal

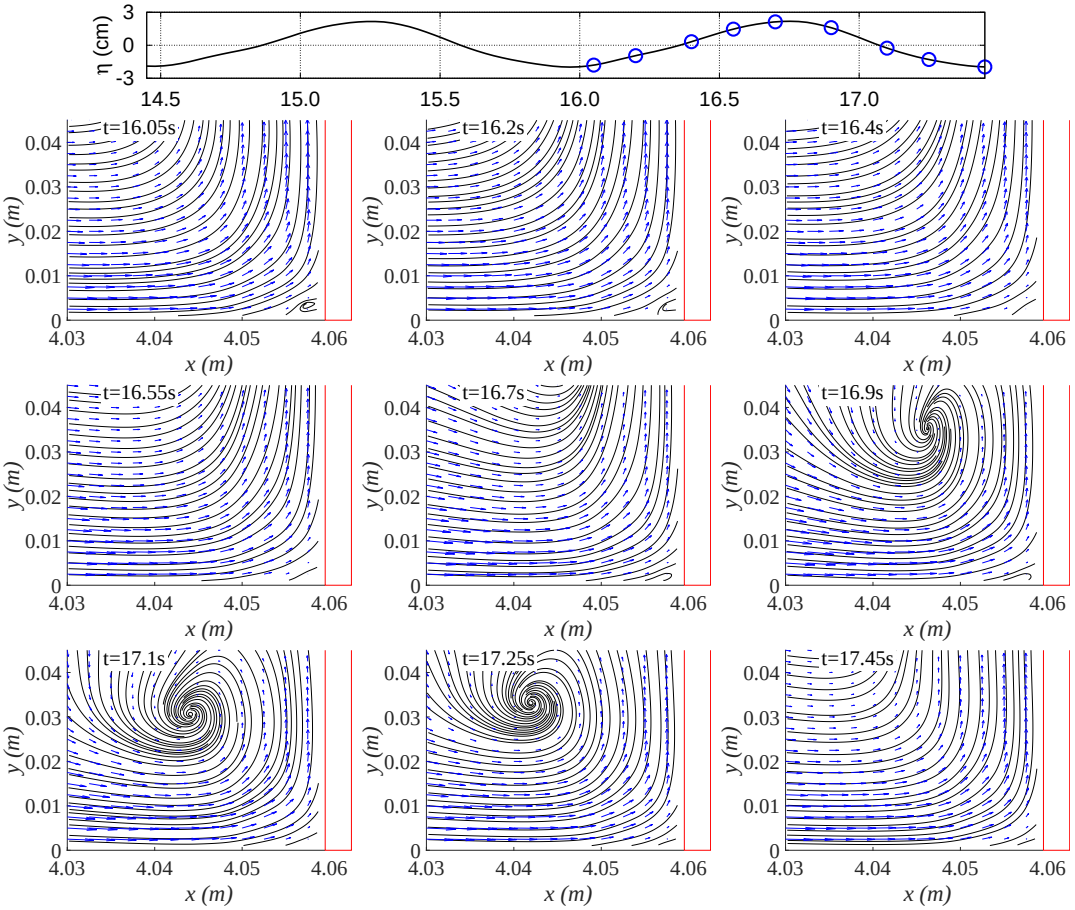

Figure 2.30: The u-v velocity field and sectional streamlines near the back wall of the OWC-pile structure along slice plane A for a standalone OWC-pile simulation, showing the test condition T=1.5s. The scale at y-axis is compressed by a factor of 2.

and spatial scales that cannot be fully resolved using the current mesh.

From Figure 2.31, two large vortices can also be observed in slice plane B, similar to the pattern found for $T = 1.1$ s. Again, the existence and location of these two large vortices are relatively stable, while the vortices on the outside of the side edges are also observed. A constant $u - v$ inflow into the concave region formed by the back wall is also observed, which is similar to the inflow observed in $T = 1.1$ s. This indicates that this constant inflow into the concave region is present near the bed at a 5-mm elevation, for intermediate to long wave conditions.

In order to estimate the strength of the vortices visualized, a measure of vortex strength is defined as (Muzzammil and Gangadhariah, 2003)

$$S_v = \pi U_v D_v \tag{2.64}$$

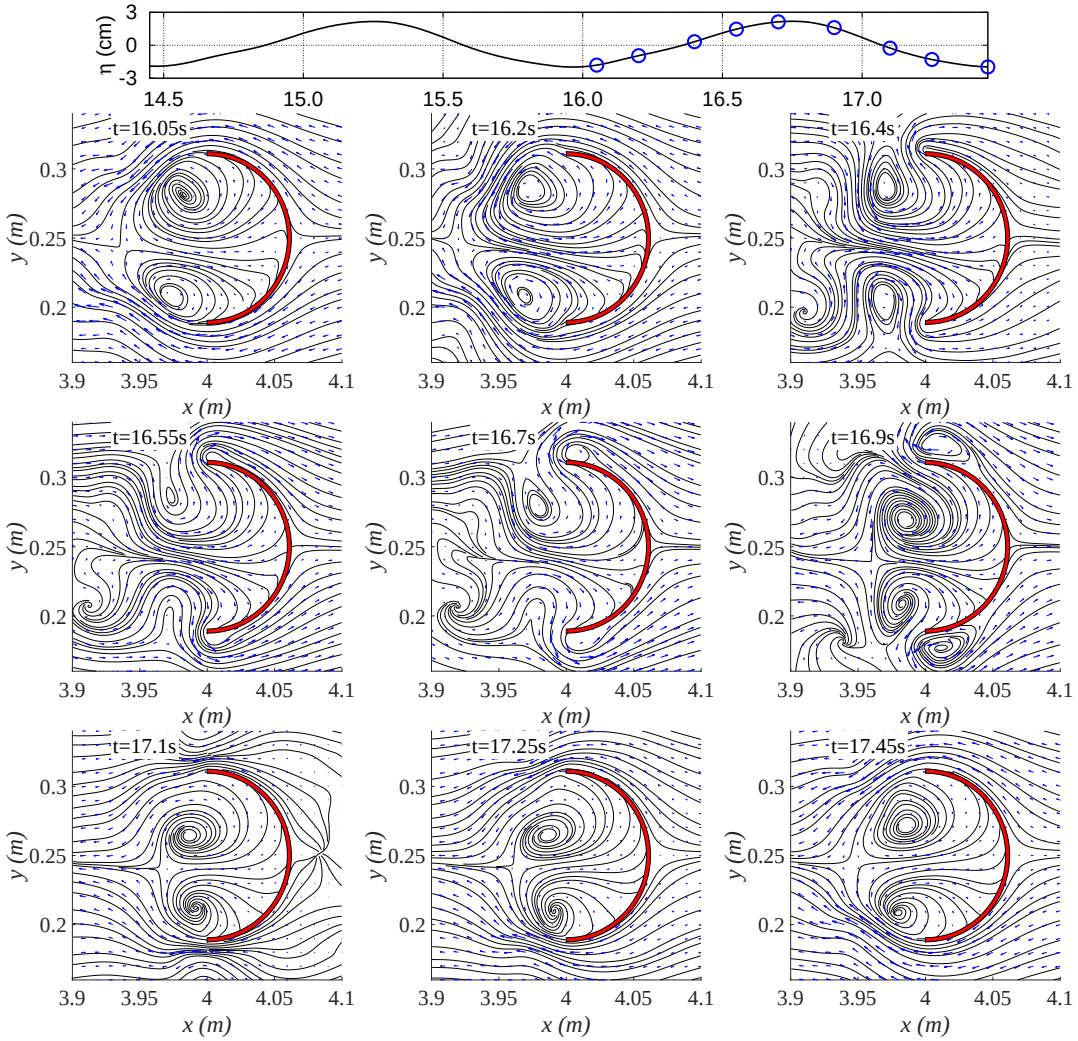

Figure 2.31: The u-w velocity field and sectional streamlines near the back wall of the OWC-pile structure along slice plane B for a standalone OWC-piles simulation, showing the test condition T=1.5s.

where U_v is the representative vortex velocity and D_v is a scale for the vortex size. For the detailed definitions and determination of these two characteristic values, please refer to section 4.4, where the details of vortex visualization and vortex analysis used in this study are described. Table 2.3 shows a summary of the maximum non-dimensional vortex strength $S_v^{hs}/\pi U_m D$ of the vortices found in the current study, for a standalone OWC-pile in a wave field. The KC numbers computed by $KC = U_m T/D$ for each condition is also listed for reference. In Table 2.3, the superscript "hs" means horseshoe vortex, "lw1" means lee wake vortex on the up-wave direction, "lw2" means lee wake vortex on the down-wave direction, "B" means the slice plane B. The strength of the horseshoe vortices found in the present study is very weak compared to the wake vortices. Moreover, the

strength of the horseshoe vortices found in the present study is one order of magnitude lower than the typical horseshoe vortices observed under laboratory condition for circular piles under steady current conditions as summarized by Dargahi (1989). Therefore, these horseshoe vortices are likely not the cause of enhanced sediment scour in this case. The strength of the large vortices in the concave region up-wave of the back wall is high for intermediate to long waves, which may move sand and enhance local scouring. The two small vortices formed on the outside of the concave region of the back wall are also strong despite their small size and relatively short lifespan in the near field. These vortices may also be responsible for sediment scouring around the OWC-pile device in wave condition.

Table 2.3: Computed vortex strengths and normalized vortex strengths for different vortices found in the simulated flow field for different test conditions.

Model	T	KC number	$\frac{S_v^{hs}}{\pi UD}$	$\frac{S_v^{lw1B}}{\pi UD}$	$\frac{S_v^{lw2B}}{\pi UD}$
standalone	0.7	1.02	0.00237	0.0247	0.0007
standalone	1.1	1.22	0.00202	0.364	0.310
standalone	1.5	1.53	0.00012	0.341	0.250

Based on the flow visualization presented above, a number of preliminary conclusions regarding the flow field and consequently the scour around the structure can be drawn.

1. For a large vertical standalone OWC-pile with concave-shaped back wall support exposed to waves with small KC numbers (less than 1.6), a horseshoe vortex system is still present in the flow. This extends the lower bound of the existence of horseshoe vortex found by Sumer et al. (1997) from about 4 for square piles to about 1.0 for concave thin-wall structure as tested here.

2. Despite the existence of this horseshoe vortex system, it is interesting to note how the size and strength of the horseshoe vortex system found in the present test conditions decreases with increasing KC number, suggesting that while the current definition for KC number is suitable for prediction of horseshoe vortex systems near circular and square piles, it may not be very suitable in the case of the concave thin-wall formed by the back wall of the OWC-pile. Considering the difference in the mechanisms of flow separation in the wake vortices found in this study, it is possible that different velocity and time scales should be used.

3. The horseshoe vortices in this case are too weak to cause significant scouring. The effect of turbulence modulation due to presence of sediment suspension may effectively reduce or destroy this vortex, hence it is not responsible for the enhanced scouring around the standalone OWC-pile structure exposed to low KC number regular waves. Instead, the steady streaming effect resulting from phase-averaged velocity could be the cause (Sumer and Fredsöe, 2001a).

4. The two large vortices formed in front of the back wall of the OWC-pile are persistent throughout the wave cycle, indicating that it may create steady streaming effect in a vortical pattern. Thus it may suspend and redistribute sediment particles, resulting in large scour holes at the location of these vortices.

5. The persistent inflow towards the concave region of the back wall found for intermediate to long waves near the bottom may entrain sediment suspended by the two aforementioned large vortices inside the concave region, and transport the sand to near the toe of the back wall near the central slice plane (slice plane A), causing net deposition at the toe of the back wall. This needs to be verified by either laboratory tests or numerical simulations.

These conclusions are interesting qualitative discoveries that help to understand the potential scour pattern and mechanism around the structure under representative experimental conditions.

2.6 Summary

In this chapter, a combined experimental, theoretical and numerical study of an OWC-pile device is discussed. The main conclusions of this study are summarized as follows.

1. The quadratic pressure loss coefficient C_f is only very weakly dependent on wave conditions.

2. The quasi-linear PTO mechanism allowed us to investigate theoretically the effects of wavelength and wave height on capture length of the OWC device accurately.

3. The power loss due to viscous effect induced by the flow separation from the OWC device has a stronger dependence on incident wave period than wave height. The effect of this viscous loss is noticeable in shortwave conditions.

4. The CFD model is able to numerically reproduce, with acceptable accuracy, the key measured quantities, including the free surface displacements inside and outside the OWC chamber, pressure variation inside the OWC chamber, quadratic loss coefficient of the PTO-simulating orifice, and the capture width of the OWC device. This indicates that the CFD model and the numerical setup are capable of simulating the key physical processes involved.

5. The method of using single point measurement inside the OWC chamber introduced error in the measured capture length and quadratic loss coefficient due to spatial non-uniformity inside the chamber. By using the potential theory with quasi-linear PTO to correct for the spatial non-uniformity introduced by the fundamental wave component, this error can be reduced.

6. Further numerical simulation showed that other than the spatial non-uniformity induced by the fundamental wave component, which could be resolved by the potential flow theory, another important source of spatial non-uniformity exists for certain incident wave conditions. The vortex shedding at the lower skirt of the OWC chamber could excite higher harmonic resonant sloshing modes inside the OWC chamber, resulting in significantly enhanced spatial non-uniformity.

7. Two-point wave separation analysis has shown that if the side walls of the wave flume is treated as a symmetrical boundary, the resulting loosely spaced wave farm configuration consists of OWC-pile members does not provide enough wave energy attenuation for effective shore protection. To improve the performance of the wave farm for shore protection, the gap between adjacent OWC-piles must be reduced, calling for the need to investigate the performance of the closely spaced OWC-piles as a wave farm and breakwater for shore protection.

8. Detailed flow visualization analysis has shown that for the tested OWC-pile device, the presence of the concave-shaped back wall induces weak horseshoe vortex systems that have not been observed before at such low KC numbers for other cross-section shapes. However, these horseshoe vortices are too weak to be responsible for enhanced sediment scour. Instead, the large wake vortices and mean flow found in intermediate to long waves may be responsible for enhanced sediment scouring through a steady streaming effect as found by Sumer and Fredsöe (2001a).

CHAPTER 3
ON THE HYDRODYNAMICS AND WAVE ENERGY EXTRACTION EFFICIENCY OF A ROW OF CLOSELY SPACED OWC-PILES FOR WAVE-ENERGY UTILIZATION AND SHORE PROTECTION: A WAVE FLUME STUDY

The material presented in this Chapter is based on "C. H. Xu, Z. H. Huang, A dual-functional wave-power plant for wave-energy extraction and shore protection: A wave flume study. Applied Energy. 229:963-976,2018 "

3.1 Introduction

In Section 2.4, the performance of the OWC-pile in a loosely spaced wave farm for shore protection was examined and it was found that this configuration does not provide enough wave energy attenuation for the purpose of reducing shoreline erosion. This chapter investigates the performance of a wave farm of OWC-piles in a closely spaced configuration in terms of both wave energy extraction and shore protection.

The motivation of the study in this chapter is to experimentally examine how reducing the spacing between OWC-piles in a wave farm could affect the performance and cost-return of such a wave farm design in terms of wave energy extraction and shore protection. A new wave-power plant concept with closely spaced OWC-piles as shown in Figure 1.3 is tested. This explores a new integration of OWC devices with a pile breakwater for wave energy extraction and shore protection for sustainable coastal development. Traditional breakwaters such as caisson or rubble mound breakwaters are expensive to build in deep water(on the order of 10 million Euros if they are built in shallow waters according to Sheehan and Harrington (2012)), which makes them unsuitable in places where water is relatively deep and wave energy resources are rich. Pile breakwaters, however, can be constructed outside the surf zone at relatively low cost. Existing laboratory and numerical studies have mainly focused on investigating the performance of OWC devices in a standalone configuration, without considering the impact of adjacent OWC devices (for example Morris-Thomas et al., 2007; Zhang et al., 2012; Fleming et al., 2012; He et al., 2013; He and Huang, 2014; Bingham et al., 2015; He et al., 2016; Ning et al., 2016b; Vyzikas et al., 2017). In this study, due to the closely spaced nature of the OWC-piles and the three-dimensional OWC chamber geometry (i.e., circular), the impact of neighboring OWC-piles must be considered explicitly in the experimental and numerical investigations. The research described in this chapter is built upon the theoretical and experimental work described in Deng et al. (2014) and Xu et al. (2016) (as discussed in chapter 2), where an OWC chamber is integrated into a single circular pile (a.k.a. OWC-pile). We report here our experimental results from a series of wave-flume tests designed to

understand the performance of a dual-functional wave-power plant in the form of a row of closely spaced OWC-piles. Results include the characteristics of the nonlinear PTO-simulating device, the measured capture width ratio, reflection and transmission coefficients, and estimated viscous dissipation due to vortex shedding from the piles. An evaluation of the performance of a scaled-up wave-power plant is also discussed.

3.2 OWC-pile wave farm model, experimental setup and test conditions

3.2.1 OWC-pile wave farm model

Figure 3.1 shows a small physical model of the proposed dual-functional wave farm. The model is a row of four identical closely spaced OWC-piles. Each OWC-pile is an axisymmetric OWC device supported by a coaxial tube-sector-shaped structure (see Figure2.10), which has been studied theoretically and experimentally by Deng et al. (2013) and Xu et al. (2016).

Figure 3.1: A row of four OWC-piles before deployment in the wave flume.

As seen in Figure 2.10, the model is made of stainless steel plate. The overall height of the OWC-pile is 40 cm, outer diameter D is 12.5 cm, thickness of the plate is 3 mm, distance between the lower skirt of the chamber and the bottom of the wave flume D_s is 24.4 cm, and the opening angle of coaxial tube-sector-shaped structure is 180° . On the top of each OWC-pile, an orifice is used to simulate a power take-off (PTO) mechanism. The diameter of the orifice D_o is 1.4 cm, which results in an opening-to-chamber ratio (the ratio of the opening area of the orifice to the inner cross-sectional area of the OWC chamber) $\alpha = 0.0138$. In the experiment, each OWC-pile is made of stainless steel, and the lower skirt of the OWC chamber is carefully rounded using a rubber band to reduce possible energy loss associated with vortex shedding. Referring to Figure 3.1, four

identical OWC-piles are closely mounted in a row onto a PVC plate of 3 mm in thickness to form a dual-functional OWC-pile wave-power plant model. The gap size between two adjacent OWC-piles G is 0.6 cm. The PVC top plate shown in Figure 3.1 ensures that all OWC-piles are upright and evenly spaced. After the model is placed in the wave flume, the bottom and top plates are firmly fixed with metal fixers on a structure attached to the wave flume, and the row of four OWC-piles is aligned to be perpendicular to the direction of wave incidence. To calculate the pneumatic power extraction, the air pressure and surface displacement in one of the OWC chambers (the second from the right in Figure 3.1) are measured using a pressure sensor and a wave gauge, respectively. See also Figure 2.10 for the locations of the pressure sensor and wave gauge.

To determine gap size, one should consider the following key factors: wave transmission; water exchange across the structure; and wave power-extraction efficiency. Based on previous theoretical studies of slotted/pile barrier breakwaters (e.g., Isaacson et al., 1998; Huang, 2007), a porosity of about 0.05 is shown to provide an acceptable transmission coefficient for shore protection. For the OWC-pile diameter, a gap size of 0.6cm corresponds to a porosity of $n = 0.048$. The effects of the gap size on water exchange across the structure and wave power extraction efficiency are worth further investigation.

3.2.2 Experimental setup

A wave flume in the Hydraulic Modeling Laboratory at Nanyang Technological University was used for the experiment. The dimension of the wave flume is 32.5-m long, 0.54-m wide and 0.6-m deep. At one end of the wave flume, a piston type wave maker is installed; at the other end of the wave flume, an 1:15 wave-absorbing beach covered by porous material is installed to minimize wave reflection. The reflection coefficient of the wave-absorbing beach is less than 0.05 for wave periods ranging from 0.7 s to 1.6 s (He et al., 2013).

In Figure 3.2, the model is placed at 18.5 m from the wave maker. Two UltraLab ultrasonic sensors, S1 and S2, are installed at 7.5 m and 12.5 m from the wave maker, respectively. These two sensors are used to monitor the incident waves. In order to obtain the wave reflection coefficient using a two-point wave separation method (Goda and Suzuki, 1976), two resistance-type wave gauges, G4 and G5, are placed 15.7 cm apart in tandem, with gauge G5 installed at 5 m from the model (i.e., 13.5 m from the wave maker). To determine the wave transmission through the dual-functional wave-power plant model and the beach reflection, two resistance-type wave gauges, G6 and G7, are placed 15.7 cm apart in tandem, with G6 being installed at 23.5 m from the wave maker. Wave gauge G2 is used to measure the surface displacement inside the OWC chamber, and wave gauges G1 and G3 are placed 30.5 cm in front of and behind the model to provide additional information for later numerical model validation. A piezo-electric type pressure sensor (P1) is mounted onto the top cover of the OWC chamber to measure the air pressure inside the OWC chamber. A camera (C1) is also installed on the front side of the flume to provide a side view of the

waves interacting with the wave-power plant model. All sensors and camera are synchronized using a digital data acquisition device (DEWESoft DEWE-43), and the sampling rates of all devices are set to 50Hz.

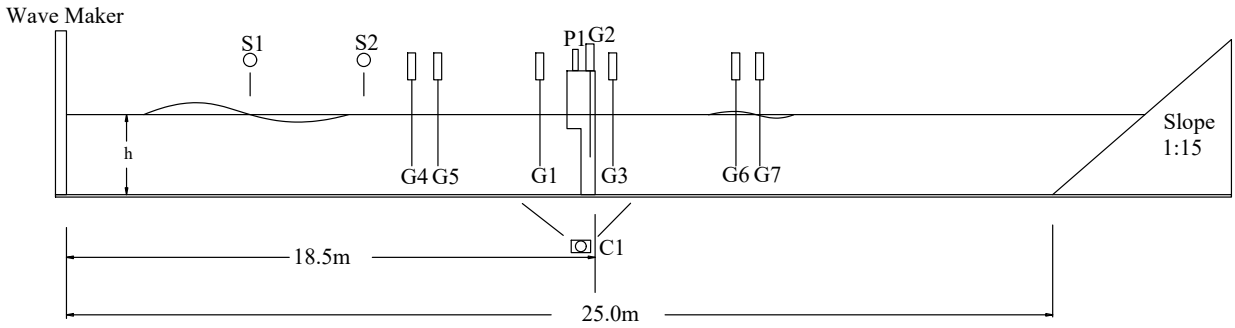

Figure 3.2: Sketch of experimental setup. Not drawn to scale.

3.2.3 Test conditions

The test conditions are summarized in Table 3.1. To test the effects of wave period and water depth on wave scattering and wave energy extraction, nine wave periods with a fixed wave height are tested at two water depths: $h = 0.29$ m (case 1) and 0.31 m (case 2). To test the effects of wave height on wave scattering and wave energy extraction, four wave heights, in combination with three wave periods are tested for a fixed water depth $h = 0.31$ m (case 3). To evaluate the effects of the OWC chambers on wave reflection and transmission, which are important parameters for shore protection, the results from cases 1-3 are compared with a set of existing tests for a row of circular piles (without OWC chambers) of the same diameter and spacing in water depth of $h = 0.15$-0.3 m reported in Su (2013) (cases 4-6). Specifically, water depth is fixed at $h = 0.25$ m in cases 4 and 5, and varied from $h = 0.15$ to 0.3 m in case 6. For all test conditions listed in Table 3.1, each test condition is repeated at least three times to minimize possible random error and ensure the repeatability of the test. The wave heights listed in the table are averaged values over three test runs; the relative error in the measured wave heights for each test condition is less than 4%.

Typical piston-type wave generators for large wave flumes have a limitation on the shortest waves that can be generated, which is typically in the range of 0.7-1.0s. The test conditions are chosen in consideration of the waves that the wave maker can generate and the resonant period of the OWC-pile model. For a single OWC-pile device identical to the individual OWC pile in the present dual-functional wave farm model, the resonant period T_r is 0.617 s for $h/D = 2.32$ (0.694 s for $h/D = 2.48$) according to the quasi-linear theory of Xu et al. (2016). Viscous effects may slightly increase the value of the resonant period obtained by potential flow theory, therefore, the period of the shortest waves tested in the present experiment (T=0.7 s) should be very close to the actual resonant period of the standalone OWC-pile. Because the resonant period is mainly a

Table 3.1: Summary of test conditions, unit for period T is seconds, unit for water depth h and wave height H is cm.

With OWCs						Without OWCs						
Case 1		Case 2		Case 3		Case 4		Case 5		Case 6		
T	H	T	H	T	H	T	H	T	H	T	h	H
0.7	3.63	0.7	3.73	0.9	1.95	0.8	2.40	1.1	1.43	1.1	15	0.0292
0.8	3.69	0.8	3.69	0.9	2.68	0.9	2.62	1.1	2.15	1.1	20	0.0293
0.9	3.69	0.9	3.78	0.9	3.78	1.0	2.72	1.1	2.82	1.1	25	0.0286
1.0	3.68	1.0	3.77	0.9	4.67	1.1	2.70	1.1	3.59	1.1	30	0.0269
1.1	3.75	1.1	3.77	1.2	1.79	1.2	2.80	1.1	4.19	-	-	-
1.2	3.64	1.2	3.65	1.2	2.76	1.3	2.88	1.1	4.64	-	-	-
1.3	3.67	1.3	3.58	1.2	3.65	1.4	2.94	-	-	-	-	-
1.4	3.71	1.4	3.63	1.2	4.75	1.5	2.92	-	-	-	-	-
1.5	3.68	1.5	3.61	1.4	1.94	1.6	3.00	-	-	-	-	-
1.6	3.64	1.6	3.72	1.4	2.76	-	-	-	-	-	-	-
-	-	-	-	1.4	3.63	-	-	-	-	-	-	-
-	-	-	-	1.4	4.54	-	-	-	-	-	-	-

property of the geometric configuration of an individual OWC pile, it is not expected to be affected by the presence of neighboring OWC piles.

3.3 Experimental data analysis

3.3.1 Determination of the characteristic coefficient of the quadratic PTO

Existing experimental studies of small-scale OWC devices usually use orifices to simulate power take-off devices. Orifices in small-scale tests can simulate the velocity-pressure relationship, which is a key characteristic of PTO devices.

For small-scale OWC models tested in wave flumes, the air can be treated as being incompressible (He and Huang, 2017). The relative pressure between the two sides of the orifice, $p(t)$, can be computed by Eq. (2.2), which is re-written here

$$p(t) = \frac{1}{2} C_f \rho_a |v(t)| v(t) + \rho_a L_g \frac{dv(t)}{dt}, \tag{3.1}$$

where $v(t)$ is the cross-sectional average velocity of the air in the OWC chamber, ρ_a the density of air, C_f the quadratic loss coefficient, and L_g a length scale related to the inertia effect (Xu et al., 2016). The pressure-velocity model given in Eq.(3.1) is formally the same as the pressure-velocity relationship for waves through a slotted barrier (Mei, 1989). For incompressible air, $v(t)$ is simply the cross-sectional average velocity of the water surface inside the OWC chamber.

A previous experimental study of a single OWC-pile of identical dimensions showed that the

inertia effect in Eq. (3.1) is not important (Xu et al., 2016). Therefore, the pressure-velocity relationship can be approximated by

$$p(t) = \frac{1}{2} C_f \rho_a |v(t)| v(t), \tag{3.2}$$

In the present experiment, the water surface inside the chamber is measured by a wave gauge at a single point from which the vertical velocity at this point $v(t)$ can be calculated. This wave gauge is located 3.7 cm behind the center point of the orifice (see Figure2.10).

3.3.2 Capture width ratio and pneumatic power extraction

The average pneumatic power extracted by one of the four OWC-piles within one wave period can be calculated by using the measured pressure $p(t)$ and the velocity $\tilde{v}(t)$

$$P_{OWC}^{(1)} = \frac{A_0}{NT} \int_{t_0}^{t_0+NT} p(t)\tilde{v}(t)dt, \tag{3.3}$$

where A_0 is the cross-sectional area of the pneumatic chamber, T is the wave period, N is the number of waves considered, and t_0 is a reference instant of time. In view of Eq.(3.2), the average power extracted by one OWC-pile in the wave-power plant model can be calculated by the measured pressure alone if the quadratic loss coefficient C_f is known,

$$P_{OWC}^{(1)} = \frac{A_0}{NT} \int_{t_0}^{t_0+NT} \sqrt{\frac{2|p(t)|^3}{C_f \rho_a}} dt, \tag{3.4}$$

The air pressure in the pneumatic chamber is approximately uniform except in a small region close to the orifice. One advantage of using Eq.(3.4) is that the calculated pneumatic power is not affected by (i) the location of the pressure sensor as long as the sensor is installed in a location away from the orifice, and (ii) the non-uniformity of the water surface inside the OWC chamber.

Again, in this study the wave energy extraction efficiency is measured by capture width λ computed by

$$\lambda = \frac{P_{OWC}^{(1)}}{P_i}, \tag{3.5}$$

where P_i is the mean incident wave power per unit crest width. Physically the average power extracted by an OWC device is equal to λP_i. According to linear wave theory, P_i is calculated by

$$P_i = \frac{1}{8} \rho_w g H^2 C_g, \tag{3.6}$$

where ρ_w is the density of water, g the gravitational acceleration, H the measured height of incident

waves, and C_g the group velocity. The group velocity is calculated by linear wave theory as

$$C_g = \frac{1}{2}\left(1 + \frac{2kh}{\sinh(2kh)}\right)\frac{\omega}{k}, \tag{3.7}$$

where $\omega = 2\pi/T$ and $k = 2\pi/L$ with L being the wave length.

The capture width ratio is calculated by

$$\eta_{pneu} = \frac{\lambda}{D} = \frac{P_{OWC}^{(1)}}{P_i D}. \tag{3.8}$$

With the capture width ratio known, the power extracted by one of the OWC-piles in the wave-power plant model is

$$P_{OWC}^{(1)} = \eta_{pneu} D P_i. \tag{3.9}$$

Therefore, the total pneumatic power that can be extracted by an OWC-pile wave-power plant consisting of N OWC-piles is

$$P_{OWC}^{(N)} = \eta_{pneu}(ND)P_i. \tag{3.10}$$

The air compressibility is not important for small-scale models, but can be important for prototypes. If the model is scaled up by the Froude's law of similarity law, the power-extraction efficiency for the prototype is smaller than that for the model. The estimation of the power-extraction efficiency will be discussed later in Section 3.8.

3.3.3 Reflection and transmission coefficients

The sediment transport between the dual-functional wave-power plant and the shoreline is related to the waves transmitted through the power plant, while the waves reflected from the wave-power plant is related to the dynamic loading on the wave-power plant. To determine the wave reflection and transmission coefficients, four wave gauges (G4-G7) are installed at the locations shown in Figure3.2. From the surface displacements measured by the wave gauges G4 and G5, the amplitudes of the incident (A_i) and reflected (A_r) waves can be obtained through a two-point wave separation analysis. From the surface displacements measured by the wave gauges G6 and G7, the amplitudes of the transmitted waves (A_t) and the waves reflected from the wave-absorbing beach can be obtained through a two-point wave separation analysis. The reflection (C_r) and transmission (C_t)

coefficients are defined by

$$C_r = \frac{A_r}{A_i}, \quad C_t = \frac{A_t}{A_i}. \tag{3.11}$$

These two coefficients are defined for the fundamental frequency. Higher harmonic waves may exist in the vicinity of the OWC-pile breakwater due to the following three reasons: (1) weakly nonlinear wave-wave interaction, (2) pressure oscillation due to vortex shedding and (3) the radiated waves generated by the weakly nonlinear fluctuation of the air pressure inside the OWC chamber (see section 3.3.1 for the quadratic nature of the air pressure). In general, the strength of higher harmonic components needs to be investigated in subsequent numerical simulation, which will be covered in chapter 4.

3.3.4 Dimensional analysis

For the model examined in this study, the capture width ratio λ/D (defined by Eq.(3.8)), the reflection coefficient C_r and the transmission coefficient C_t of the OWC-pile breakwater can be expressed in functional forms as

$$(\lambda/D, C_r, C_t) = f(h, H, T, D, D_t, G, D_r, D_o, \rho_w, \rho_a, g, \nu_w, \nu_a), \tag{3.12}$$

where h is the water depth, H the incident wave height, T the wave period, D the outer diameter of the OWC-pile, G the gap between two adjacent OWC-piles, D_r is the draft of the OWC chamber, D_o is the opening diameter of the orifice, and D_t is the thickness of the skirt of the OWC chamber. The distance between the tip of the OWC skirt and the bottom is $D_s = h - D_r$. The physical constants g, ρ_w, ρ_a, ν_w, and ν_a are the gravitational acceleration, density of the water, density of the air, kinematic viscosity of the water, and kinematic viscosity of the air, respectively.

Using the Buckingham Π -theorem, Eq. (3.12) can be reduced to the following dimensionless form

$$\left(\frac{\lambda}{D}, C_r, C_t\right) = f\left(\frac{gT^2}{D}, \frac{h}{D}, \frac{H}{D}, \frac{\rho_w}{\rho_a}, \frac{\nu_a T}{D^2}, \frac{\nu_w T}{D^2}, \frac{D_t}{D}, \frac{G}{D}, \frac{D_s}{D}, \frac{D_o}{D}\right). \tag{3.13}$$

Combining H/D with $\nu_w T/D^2$ (or $\nu_a T/D^2$) gives $\nu_w T/(DH)$ (or $\nu_a T/(DH)$), which can be written as ν_w/DU (or ν_a/DU), respectively, with $U = H/T$ being a velocity scale. Combining D_o/D with ν_a/DU gives ν_a/D_oU. Therefore, Eq. (3.13) can be further written as

$$\left(\frac{\lambda}{D}, C_r, C_t\right) = f\left(T\sqrt{\frac{g}{D}}, \frac{h}{D}, \frac{H}{D}, \frac{D_t U}{\nu_w}, \frac{D_o U}{\nu_a}, \frac{DU}{\nu_w}, \frac{D_t}{D}, \frac{D_s}{D}, \frac{G}{D}, \frac{D_o}{D}\right). \tag{3.14}$$

In this experiment,the last four parameters are constant. In this study, both ν_w and ν_a are fixed: if

$T\sqrt{g/D}$ and h/D are fixed, then $D_tU/\nu_w, DU/\nu_w$ and D_oU/ν_a will be functions of H/D; if H/D and h/D are fixed, then $D_tU/\nu_w, DU/\nu_w$ and D_oU/ν_a will be functions of $T\sqrt{g/D}$. Therefore, all the results related to λ/D, C_r and C_t can be presented and discussed in terms of $T\sqrt{g/D}, H/D$ and h/D in this study.

3.4 Results

In this study, the following parameters are fixed: diameter of the OWC-piles (D); distance between the lower tip of the skirt of the OWC chamber and the bottom (D_s); the diameter of the orifice (D_o); and the gap size between two adjacent OWC-piles (G). As shown in the dimensional analysis presented in Section 3.3.4, all the results related to λ/D, C_r and C_t can be presented and discussed in terms of the following three dimensionless parameters: $T\sqrt{g/D}, H/D$ and h/D.

3.4.1 Characteristic coefficient of the quadratic PTO model

In this study, the characteristic coefficient used to describe the behavior of the quadratic PTO model is the quadratic loss coefficient, C_f, defined by Eq.(3.2). It was been concluded in chapter 2 that for an OWC-pile in standalone or loosely spaced configuration, C_f is not sensitive to incident wave conditions. It is shown here that the parameter C_f is not sensitive to both H/D and $T\sqrt{g/D}$ for OWC-piles in a row and thus can be treated as a constant in the calculation of the capture width ratio in this study.

Figure 3.3 shows the fitted values of quadratic loss coefficient C_f for cases 1 and 2, which are calculated using the velocity measured at one point inside the OWC chamber. Cases 1 and 2 are designed to show how C_f changes with $T\sqrt{g/D}$. All values of C_f vary around a mean value $\bar{C}_f$ of 14,619 with a relative error less than $\pm 9\%$ (note that $\bar{C}_f$ is computed with results from both Figure 3.3 and Figure 3.4), except for $T\sqrt{g/D} = 6.20$ and 9.74 where the values of C_f are about 24% smaller than the mean. The values of C_f at these two wave periods are not included in the computation of the mean value of C_f due to large deviation. We attribute the deviation of C_f from the mean at $T\sqrt{g/D} = 6.20$ and 9.74 to the sloshing modes excited by higher harmonic waves and the one-point measurement method as explained in section 2.3.4.

To show the change of C_f with the dimensionless wave height H/D, three wave periods ($T\sqrt{g/D} = 7.97, 10.63$ and 12.40) are selected and the dimensionless wave height H/D varies from about 0.144 to about 0.40. The change in C_f with H/D is shown in Figure 3.4, from which it can be concluded that C_f is not sensitive to the variation of wave height in our experiment. Note that higher harmonic waves of these three periods cannot excite sloshing mode according to the analysis given in Section 2.3.4.

In the following, an explanation of the behaviors of C_f shown in Figures 3.3 and 3.4 is provided. In this study the PTO is modeled by an orifice. The key parameter to describe the flow through an

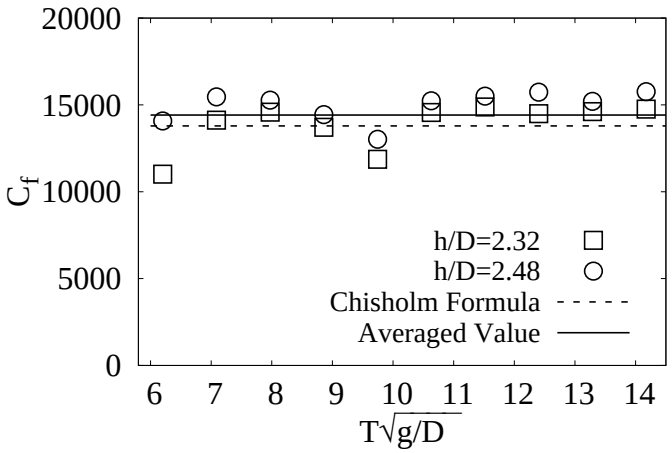

Figure 3.3: Quadratic loss coefficient obtained using the one-point measured water surface elevation, results from cases 1 (squares) and 2 (circles) shown.

orifice is the contraction coefficient C_c, which characterizes the ratio between the orifice area and the area at *vena contracta*. The quadratic loss coefficient of the orifice, C_f, can be determined by the following expression for oscillatory flow through an orifice,

$$C_f = (\frac{1}{\alpha C_c} - 1)^2, \tag{3.15}$$

where $\alpha = [D_o/D]^2$ is the opening ratio of the orifice (the reader is referred to Mei (1989) for a derivation of Eq.(3.15)). According to Eq. (3.15), the contraction coefficient corresponding to $\bar{C}_f$=14,619 in Figures 3.3 and 3.4 is $C_c = 0.5945$. Previous experimental studies (Chisholm, 1983; Fossa and Guglielmini, 2002) suggest the value of contraction coefficient can be determined by

$$C_c = \frac{1}{[0.639(1-\alpha)^{0.5} + 1]}. \tag{3.16}$$

For the present study, the opening ratio $\alpha = 1.38\%$, and Eq.(3.16) gives $C_c = 0.6118$, which corresponds to $C_f = 13,793$ according to Eq. (3.15).

For the results shown in Figures3.3 and 3.4, the difference between the measured mean and the predicted values of C_f is 5.7%, which suggests that even though Eq.(3.16) is originally proposed for uni-directional flows, it nevertheless can provide a satisfactory prediction of the contraction coefficient C_c for oscillatory flow as well. This is consistent with the conclusions in our previous studies. As mentioned in chapter 2, Xu et al. (2016) tested a standalone OWC-pile of identical opening ratio in the same flume with identical wave conditions, and found that the fitted values of C_f fell within the range of 14,000 to 16,000 and are not sensitive to H/D and $T\sqrt{g/D}$. He and Huang (2017) performed a series of tests for circular orifices with opening ratio ranging from 0.625% to 1.875%, and the contraction coefficient obtained using Eq. (3.15) fell within the range

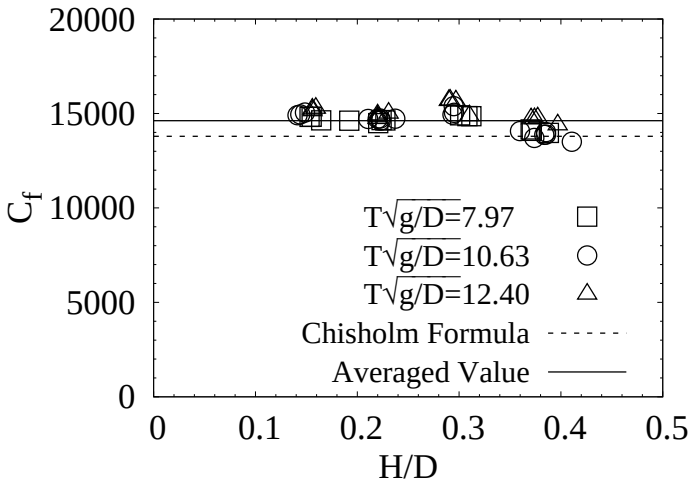

Figure 3.4: Quadratic loss coefficient obtained using the one-point measured water surface elevation (case 3).

of 0.6109 to 0.6124, which is very close to the values predicted by Eq. (3.16), with relative error less than 1%.

The following conclusions can be drawn about the contraction coefficient C_c and the quadratic loss coefficient C_f. (1) For an OWC chamber with a thin-wall circular orifice, the values of C_f and C_c are influenced mainly by the opening ratio and are not sensitive to both H/D and $T\sqrt{g/D}$ for small opening ratios under normal wave conditions. (2) The value of C_f is also not affected by the presence of other structures in the vicinity of the OWC chamber. (3) If the turbulent flows remain in the same regime, it is expected that Eq. (3.16) and Eq. (3.15) can be used to estimate the contraction coefficient C_c and quadratic loss coefficient C_f for thin-walled circular orifices with a relative error less than 6%. In the following section, the OWC pneumatic power is calculated using C_f=14,619.

3.4.2 Measured capture width ratio

The capture width ratio is an important parameter describing the wave energy extraction function of an OWC-pile dual-functional wave farm. The variations of capture width ratio λ/D with $T\sqrt{g/D}$ for two values of h/D are shown in Figure3.5, where the capture width ratio for a standalone OWC-pile tested in Xu et al. (2016) is also included for comparison. In general, the capture width ratio of an individual OWC-pile in the dual-functional wave farm model is about 1.5-2.0 times larger than the capture width ratio of the corresponding standalone OWC-pile within the tested range of $T\sqrt{g/D}$. This illustrates the significant influence of adjacent closely spaced OWC-piles on the performance of individual OWC-piles in the dual-functional wave farm model. The capture width ratio is not sensitive to small changes in water depth, except for the shorter waves tested in the

experiment. Larger values of capture width ratio occurred at smaller values of $T\sqrt{g/D}$ for all the cases shown in Figure 3.5.

It is remarked that the maximum power output of a WEC device does not necessarily coincide with the maximum capture width ratio because the incident wave power changes with $T\sqrt{g/D}$. For real sea states, there is a joint distribution of wave height and period (Longuet-Higgins, 1983; Goda, 1999); therefore, the maximum capture width ratio of a wave energy converter in a real sea state cannot be directly obtained from the CWR-frequency curve for a fixed height.

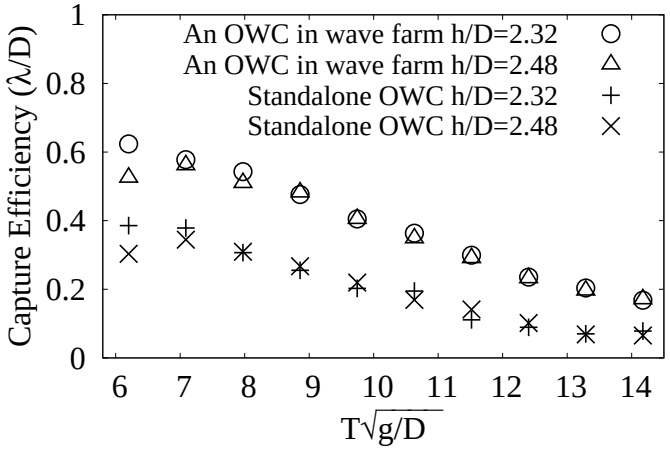

Figure 3.5: Variations of capture width ratio with dimensionless wave period $T\sqrt{g/D}$ ($H/D = 0.296$).

The variations of capture width ratio λ/D with dimensionless wave height H/D are shown in Figure3.6 for all the cases listed in Table 3.1. The capture width ratio λ/D slightly increased with increasing H/D for $T\sqrt{g/D} = 10.63$ and 12.40, but the capture width ratio slightly decreased with H/D for $T\sqrt{g/D} = 7.97$. For practical purposes, the variation of capture width ratio with H/D is insignificant for $H/D > 0.2$.

The quasi-linear theory of Xu et al. (2016) shows that the capture width ratio of a standalone OWC-pile device increases with increasing wave non-linearity (i.e., the wave height for a fixed wave period) until a threshold value, then begins to decrease with increasing wave non-linearity, which is in agreement with the numerical and experimental findings of López et al. (2015b) and Wang et al. (2018). The same effect of wave non-linearity is expected for a row of OWC-piles; however, due to the limitation of the highest waves that can be tested in the experiment, the peak capture width ratios are outside the tested range of H/D in Figure3.6.

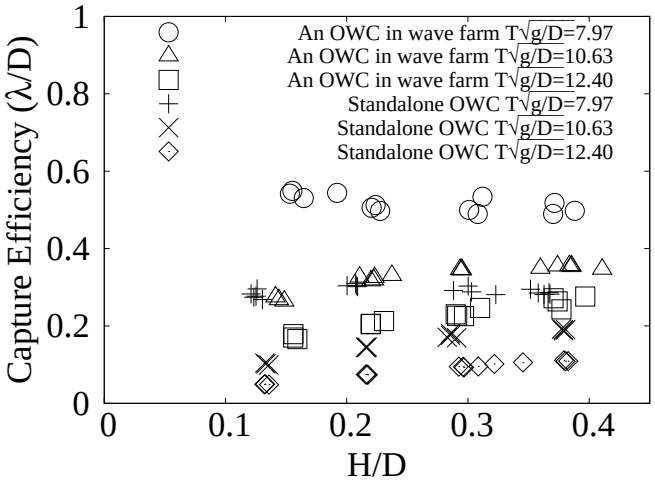

Figure 3.6: Variations of capture width ratio with dimensionless wave height H/D ($h/D = 2.48$).

3.5 Wave reflection and transmission

In places where cross-shore sediment transport is responsible for beach erosion, it is desirable to reduce the wave energy reaching the shore. Wave transmission and reflection coefficients are two important hydrodynamic parameters describing the shore protection function of an OWC-pile dual-functional wave farm. To understand the possible effects of the power extraction by OWC chambers on the reflection coefficient (C_r) and the transmission coefficient (C_t), these two coefficients are compared for the OWC-pile dual-functional wave-power plant model and a row of closely spaced piles of the same dimensions (i.e., the same pile diameter and the same gap size) under the same wave conditions.

3.5.1 Wave reflection and transmission of a row of closely spaced piles without OWC

Su (2013) measured the reflection and transmission coefficients of a row of closely spaced piles, which had a pile diameter and gap size identical to those used in the present study. The effects of $T\sqrt{g/D}$ on C_r and C_t for one water depth ($h/D = 2.0$) and the effects of water depth h/D on C_r and C_t under a fixed wave height and wave period were studied in the experiment of Su (2013).

Figure3.7 shows the effects of dimensionless water depth h/D on C_r and C_t at $T\sqrt{g/D} = 9.74$. Within the range of $h/D = 1.2$ to 2.4, the measured reflection coefficient C_r is not sensitive to changes in water depth, with a variation being less than 2%; the transmission coefficient C_t increases slightly with the dimensionless water depth h/D. However, within the range of $h/D = 2.0$ to 2.4, the variation of C_t with h/D is less than 4.8%. For the two water depths examined in the present study of the dual-functional wave farm ($h/D = 2.32$ and $h/D = 2.48$), it has been shown in section

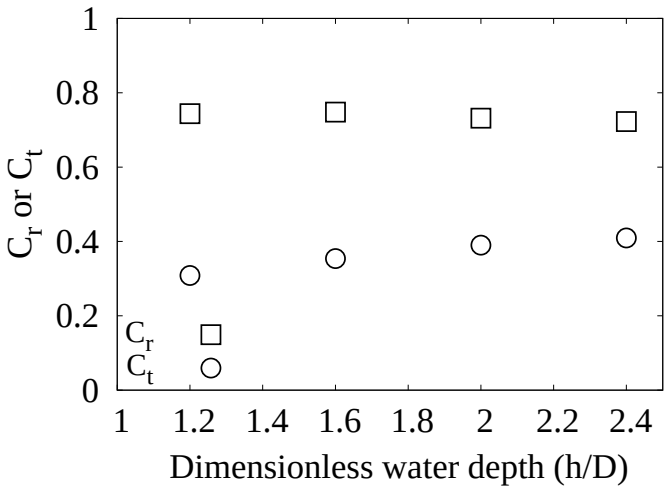

Figure 3.7: Variation of reflection coefficient and transmission coefficient with dimensionless water depth h/D for a pile breakwater with $T\sqrt{g/D} = 9.74$ and $H/D = 0.228$.

3.4.2 that the capture width ratio is not sensitive to h/D in the tested range. It will be shown later in section 3.5.2 that both the reflection and transmission coefficients obtained for these two water depths are almost the same for the dual-functional wave farm model.

The variation of C_r and C_t with incident wave height of the pile breakwater at a fixed water depth of $h/D = 2.0$ and a fixed wave period of $T = 1.1$ s (case 5 in Table 3.1) is shown in Figure3.8. It is observed that both C_r and C_t decrease with increasing wave height, but the correlation is only weakly sensitive to the tested variations of H/D, for a small variation of incident wave height. For example, $H/D = 0.22$ to 0.32 with the former value corresponding to the wave heights tested in Su (2013) and the latter value corresponding to the wave heights tested in the current experiment, the change in C_r is less than 4% and the change in C_t is less than 4.8%.

Based on the information presented above, it can be concluded that by accepting a small amount of error within the range of $h/D = 2.0$ to $h/D = 2.48$ for water depth and $H/D = 0.22$ to $H/D = 0.32$ for wave height, the effects of h/D and H/D on wave scattering can be ignored for a row of closely spaced piles under tested conditions, and thus the effects of wave power extraction on C_r and C_t can be evaluated by comparing the reflection and transmission coefficients obtained from the following two experiments: (1) an OWC-pile wave-power plant model with $h/D = 2.32$ and $h/D = 2.48$ and representative wave height $H/D = 0.32$, and (2) a row of closely spaced piles of the same dimensions with $h/D = 2.0$ and representative wave height $H/D = 0.22$. The error introduced from this assumption should be less than 10%.

3.5.2 Effects of power extraction on wave reflection and transmission

Variations of the measured reflection and transmission coefficients with dimensionless wave height H/D are shown in Figure 3.8 for h/D=2.48 and three values of $T\sqrt{g/D}$. The results of Su (2013) for a row-of closely spaced piles of the same dimensions are also included in Figure 3.8 for comparison. For a row of closely spaced piles, because both C_r and C_t are not sensitive to h/D within the range of 2.0 to 2.4 (see Figure 3.7), the values obtained for $h/D = 2.0$ are expected to be close to those for $h/D = 2.48$. For the three values of $T\sqrt{g/D}$, the reflection coefficients for the OWC-pile wave farm are generally significantly smaller than those for a row of closely spaced piles of the same dimensions. While the reflection coefficient for a row of closely spaced piles slightly decreases with H/D, the reflection coefficient of the OWC-pile wave farm model is not sensitive to H/D. The transmission coefficients for a row of closely spaced piles are slightly larger than those for the OWC-pile wave farm model; however, the transmission coefficients decrease slightly with H/D, regardless of the presence of the OWCs.

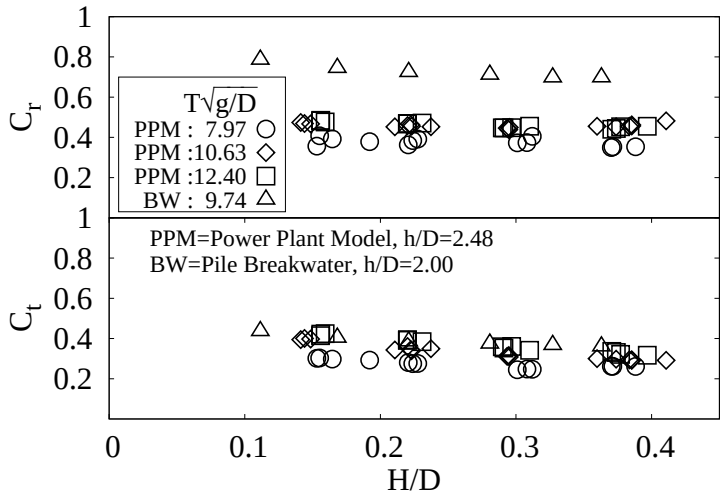

Figure 3.8: Variations of C_r (top panel) and C_t (bottom panel) with dimensionless wave height H/D for various dimensionless wave period $T\sqrt{g/D}$.

Variations of the measured reflection and transmission coefficients with $T\sqrt{g/D}$ are shown in Figure 3.9 for two values of h/D. The results for a row of closely spaced piles of the same dimensions, studied by Su (2013), are also included in Figure 3.9 for comparison. Within the tested range of h/D, the transmission coefficient increased with $T\sqrt{g/D}$ for a fixed wave height, regardless of the presence of the OWCs. It is interesting to note that the power extraction by the nonlinear PTO only slightly reduced the transmission coefficient. The reflection coefficient for a row of closely spaced piles decreased noticeably with $T\sqrt{g/D}$, but the reflection coefficient for the OWC-pile wave farm model is not very sensitive to $T\sqrt{g/D}$. As far as shore protection is concerned, integrating OWCs into a pile breakwater can not only achieve a better degree of shore

protection than a pile breakwater does, but it also effectively reduces the reflected waves (i.e., the wave loading on the structure), which can improve the structural reliability.

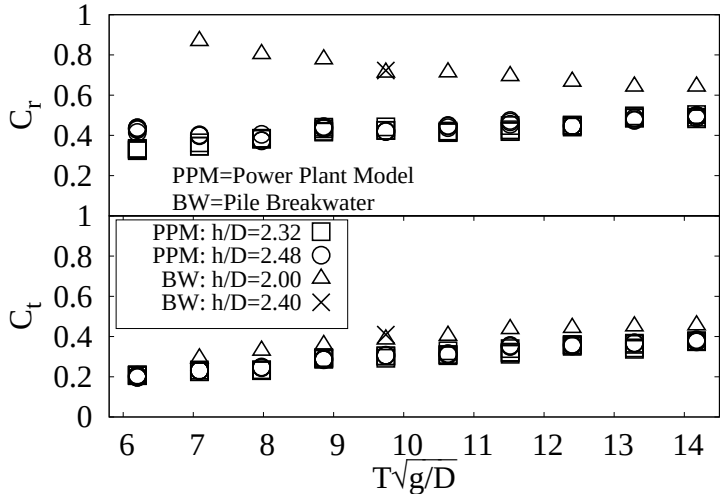

Figure 3.9: Variations of C_r (top panel) and C_t (bottom panel) with dimensionless wave period $T\sqrt{g/D}$ for different dimensionless water depth h/D.

An intuitive explanation is provided here to help understand the results presented in Figures3.5 and 3.9. Wave energy extraction is directly related to the up-and-down motion of the water surface inside the OWC chamber. For a given wave period and chamber-PTO design, a larger up-and-down motion always results in a larger fluctuation of the air pressure inside the OWC pneumatic chamber, and thus more energy is extracted by the PTO [see Eq. (3.4)].

In the absence of OWC chambers, wave reflection is caused by the outer surface of the piles, resulting in a partial standing wave and thus an enhanced up-and-down motion of the water surface in front of the breakwater. Experimental and theoretical results (e.g., Kakuno and Liu, 1993) have shown that shorter waves tend to have stronger reflection (i.e., a larger up-and-down motion in front of the breakwater). When OWC chambers are integrated into the pile breakwater, wave reflection is caused by the outer surface of the OWC chamber, back wall of the OWC chamber, and the support structure underneath the OWC chamber. In addition to wave reflection, the fluctuation of the air pressure inside the OWC chamber also generates radiated waves, which can affect the wave field in front of the OWC-piles. The wave reflection caused by the back wall of the OWC chamber and the support structure enhances the up-and-down motion inside the OWC chamber, which is stronger for shorter waves. The up-and-down motion inside the OWC chamber is responsible for the energy extraction by the PTO and the generation of the radiated waves. Because only a fraction of the energy associated with the radiated waves and the waves reflected by the back wall of the OWC chamber and the support structure can propagate out of the OWC chamber, the reflected wave is not as strong as that by a pile of the same dimensions. The support structure and the small gap make it difficult for the radiated waves to propagate to the lee side of the OWC-piles, and it is

the gap-diameter ratio that largely controls the transmitted waves. This explains (1) why larger capture width ratio occurred towards the end of shorter waves (see Figure 3.5), (2) why integrating OWCs into a pile breakwater can reduce both the reflection and transmission coefficients, and (3) why the power extraction has a more significant effect on the reflection coefficients of shorter waves but less on the transmission coefficients.

3.6 Wave power removal from wave field and viscous dissipation

For the OWC-pile dual-functional wave power plants, in addition to the wave energy removed from the wave field by the PTO to generate electricity, another portion of energy is dissipated into the unusable energy of turbulence (and eventually internal energy) through vortex shedding. Therefore, it is important to know how much wave energy is unusable for the OWC-pile dual-functional wave power plants to generate electricity due to viscous dissipation.

It is remarked that both the energy dissipated into turbulence and the energy extracted by the PTO are removed from the wave field. For a row of closely spaced piles, wave energy is removed from the wave field only through viscous dissipation associated with the vortex shedding from the piles. A dissipation coefficient is often used in the literature to quantify the wave power dissipated into turbulence energy and eventually internal energy. Next, the conservation of wave power is examined to quantify the energy dissipated by vortex shedding and the energy extracted by the PTO.

Assuming that a row of N OWC-piles fits the width of the wave flume B, the conservation of wave power requires that

$$P_i B = \underbrace{C_r^2 P_i B + C_t^2 P_i B}_{(i)} + \underbrace{N \eta_{pneu} D P_i}_{(ii)} + \underbrace{C_d^{(vis)} P_i B}_{(iii)} \tag{3.17}$$

where the left-hand side is the incident wave power, the term (i) is the wave power in the reflected and transmitted waves, term (ii) is the wave power extracted by the PTO, and term (iii) is the wave power dissipated into turbulence. The coefficient $C_d^{(vis)}$ is the so-called viscous dissipation coefficient. It is remarked here that in steady state (e.g., in regular waves after the ramping-up process), the amount of the energy associated with the heave motion of the water column inside an OWC chamber does not change with time, therefore, it should not be included in the conservation of wave power as a sink or source term.

Eq. (3.17) can be rewritten as

$$1 = C_t^2 + C_r^2 + C_d^{(OWC)} + C_d^{(vis)} \tag{3.18}$$

where $C_d^{(OWC)}$ is the power extraction coefficient of the dual-functional wave-power plant and

defined by $C_d^{(OWC)} = (1-\epsilon)\eta_{pneu}$ with $\epsilon = (B-ND)/B \ll 1$ being the porosity of the row of OWC-piles. Because $\epsilon \ll 1$ in the dual-functional wave farm, $C_d^{(OWC)} \approx \eta_{pneu}$, which is independent of the number of OWC-piles used in the power plant. Therefore, it is possible to use Eq. (3.18) to provide an estimate of the viscous dissipation coefficient $C_d^{(vis)}$ from the measured values of C_t, C_r and η_{pneu}. For later discussion, a wave-power removal coefficient C_d is introduced, which is defined by

$$C_d = C_d^{(OWC)} + C_d^{(vis)} \tag{3.19}$$

Note that for a row of closely spaced piles without OWCs, $C_d = C_d^{(vis)}$.

The top panel in Figure 3.10 shows the variation of the wave-power removal coefficient C_d with dimensionless wave height H/D, and the bottom panel in Figure 3.10 shows the variation of the wave-power removal coefficient C_d with dimensionless wave period $T\sqrt{g/D}$. The wave-power removal coefficients C_d for a row of piles without OWCs are also included in Figure 3.10 for comparison.

For the pile breakwater studied by Su (2013), the wave-power removal coefficient $C_d = C_d^{(vis)}$, which is simply the traditional dissipation coefficient. It can be seen from Figure 3.10 that C_d increases with increasing either H/D or $T\sqrt{g/D}$ when other parameters are fixed. The wave-power removal coefficient through the vortex shedding from the piles (i.e., the viscous dissipation coefficient $C_d^{(vis)}$) increases from about 20% of the incident wave power for $T\sqrt{g/D}$=7.08 to about 40% for $T\sqrt{g/D}$=14.17. For the OWC-pile dual-functional wave-power plant model, the wave-power removal coefficient C_d, which includes both viscous dissipation and wave energy extraction by the PTO, is significantly larger than that for the pile breakwater, reaching 80% for short waves. The value of C_d is only weakly sensitive to the variation in wave height, but decreases with increasing wave period.

The wave-power removal coefficient $C_d = C_d^{(OWC)} + C_d^{(vis)}$ can be calculated from the measured wave reflection and transmission coefficients using Eq. (3.18). The wave power extraction coefficient, $C_d^{(OWC)}$, can be calculated from the measured air pressure and the surface displacement in the OWC chamber using Eqs. (3.4) and (3.8). As a result, the viscous dissipation coefficient $C_d^{(vis)}$ for the dual-functional wave farm can be calculated and compared with that for the pile breakwater.

In the following, a semi-theoretical model is presented to understand the behaviors of $C_d^{(vis)}$ for an OWC-pile dual-functional wave farm model and a pile breakwater of the same dimensions. In particular, the semi-theoretical model will show that $C_d^{(vis)}$ increases with wave steepness kH (k is the wave number and H is the wave height) and the third power of transmission coefficient C_t^3, which causes C_d for the pile breakwater to increase with $T\sqrt{g/D}$.

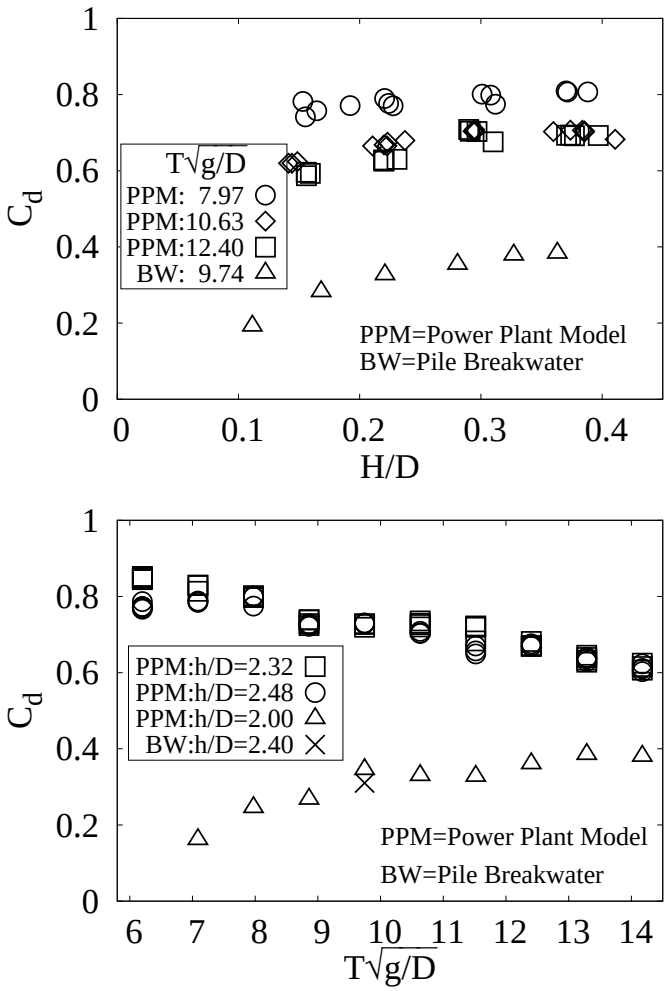

Figure 3.10: Variations of wave-power removal coefficient C_d with dimensionless wave height H/D (top panel) and dimensionless wave period $T\sqrt{g/D}$ (bottom panel).

3.7 A semi-theoretical model for viscous dissipation

Because the work done by the wave force acting on the piles is directly related to the wave power dissipation into turbulence, a semi-theoretical model can be devised to help understand the change of $C_d^{(vis)}$ with H/D, D/h and $T\sqrt{g/D}$.

The semi-theoretical model is based on the work done by the wave force acting on a single pile is denoted by $W^{(1)}$. The wave force acting on a segment of a pile /OWC-pile of length dy can be estimated by the following Morrison equation (Mei, 1989)

$$dF = \frac{1}{2}\rho_w C_D D|u|udy + \rho_w C_M \frac{\pi D^2}{4}\frac{du}{dt}dy, \tag{3.20}$$

where u is the horizontal orbital velocity immediately downstream of the pile/OWC-pile, and C_D

and C_M are empirical drag and inertia coefficients, respectively. It is remarked that the values of C_D and C_M for piles may be different than those for OWC-piles. For one pile/OWC-pile, the net work done by the inertia force over one wave period is zero; therefore, the net work done by the wave force dF over one wave period is

$$dW^{(1)} = T\left(\overline{dF\,u}\right) \equiv \frac{C_D T}{2}\rho_w D\overline{|u|^3}dz, \tag{3.21}$$

where the over-bar means taking a time average over one wave period. It then follows that the net work done by the drag force acting on a pile/OWC-pile over one wave period is

$$W^{(1)} = T\int_{-h}^{0}\frac{C_D}{2}\rho_w D\overline{|u|^3}dz. \tag{3.22}$$

As a first estimate, the empirical drag coefficient C_D is assumed to be a constant for the values of Reynolds number (Re) and Keulegan-Carpenter number (KC) used in the model tests. The drag coefficient C_D is treated as a fitting parameter in this semi-theoretical model.

The total wave power dissipated by a row of closely spaced piles/OWC-piles over one wave period is

$$W^{(N)} = NW^{(1)}, \tag{3.23}$$

where N is the total number of the piles/OWC-piles. According to conservation of wave power, $W^{(N)}$ should be equal to $TC_d^{(vis)}P_iB$ with B being the width of the row. It then follows that

$$C_d^{(vis)} = \rho_w\frac{C_D}{2P_i}\frac{ND}{B}\int_{-h}^{0}\overline{|u|^3}dz \sim \rho_w\frac{C_D}{2P_i}\int_{-h}^{0}\overline{|u|^3}dz, \tag{3.24}$$

where $B \sim (ND)$ has been used in the last equation for closely spaced piles/OWC-piles. For linear waves, the downstream velocity u can be expressed in terms of the transmission coefficient C_t as

$$u = \frac{\omega H C_t}{2}\frac{\cosh(k(h+z)}{\sinh(kh)}\sin(\omega t), \tag{3.25}$$

and the wave power P_i is

$$P_i = \frac{1}{8}\rho_w g H^2 C_g, C_g = \frac{1}{2}\left(1+\frac{2kh}{\sinh(2kh)}\right)\frac{\omega}{k}. \tag{3.26}$$

It then follows that

$$C_d^{(vis)} \sim \frac{4C_D C_t^3 kH}{3}N(kh), \tag{3.27}$$

where the function $N(kh)$ is given by

$$N(kh) = \frac{[\sinh(3kh) + 9\sinh(kh)]\tanh(kh)}{12\sinh^2(kh)[\sinh(kh) + 2kh]}. \tag{3.28}$$

Note that kH can be written in terms of kh, H/D and D/h as

$$kH = (kh)\left(\frac{H}{D}\right)\left(\frac{D}{h}\right). \tag{3.29}$$

The linear wave dispersion

$$\frac{\omega^2 h}{g} = kh\tanh kh, \tag{3.30}$$

can be rewritten as

$$\left(T\sqrt{g/D}\right)\left(\sqrt{D/h}\right) = \frac{2\pi}{\sqrt{kh\tanh(kh)}}. \tag{3.31}$$

From Eq. (3.31) the dimensionless parameter kh is an implicit function of D/h and $T\sqrt{g/D}$. From Eqs. (3.29) and (3.31) the dimensionless parameter kH is an implicit function of D/h, H/D and $T\sqrt{g/D}$. Therefore, the viscous dissipation coefficient $C_d^{(vis)}$ given in Eq. (3.27) is a function of H/D, D/h, $T\sqrt{g/D}$, C_D and C_t.

For a circular cylinder in waves, the drag coefficient C_D is a function of the Keulegan-Carpenter number (in this case, $KC = \pi H/D$) and Reynolds number (Re). For a pile/OWC-pile, the Reynolds number can be defined by

$$Re = \frac{C_t\omega(H/2)D}{\nu}. \tag{3.32}$$

According to the DNV guideline (DNV-GL, 2007), C_D can be written as

$$C_D = C_D^0\psi(KC) \tag{3.33}$$

where C_D^0 is the drag coefficient for steady flow and $\psi(KC)$ is a wave amplification factor. For the tested range of Reynolds Number (1604.7 to 2213.8) and KC number (0.15 to 0.360), the value of C_D^0 can be treated as a constant and the value of $\psi(KC)$ has a variation of less than 25% (refer to Item 6.7 of DNV-GL (2007) for details). Therefore, it is reasonable to assume a constant C_D in all tested conditions for the purpose of providing a rough estimation of the variation of the viscous dissipation coefficient $C_d^{(vis)}$.

Using the measured transmission coefficients C_t corresponding to given values of H/D, D/h and $T\sqrt{g/D}$, a non-linear least square data fitting of Eq. (3.27) to the measured $C_d^{(vis)}$ can be performed

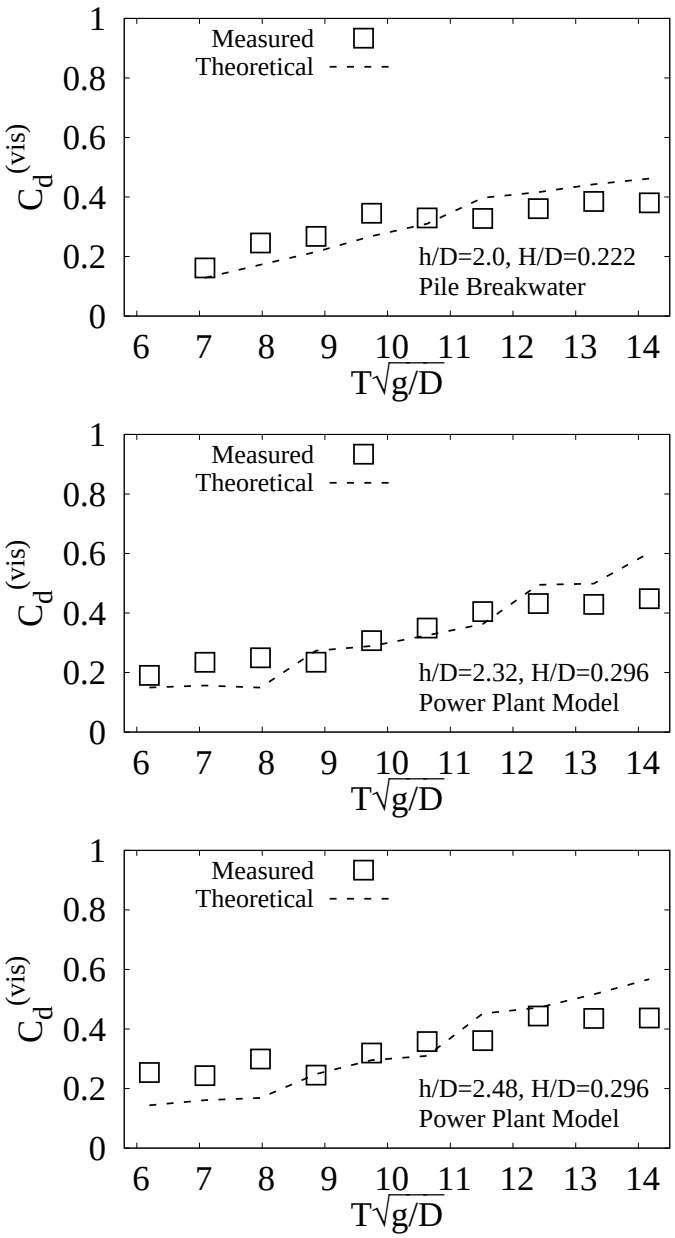

Figure 3.11: Changes of predicted and measured viscous dissipation coefficients with dimensionless period for the pile breakwater model (top panel) and the dual-functional wave farm model (middle and bottom panels).

to determine a constant value of C_D. The predicted and measured viscous dissipation coefficients for the pile breakwater model and the dual-functional wave-power plant model are shown in Figure 3.11 for cases 1, 2 and 4, and in Figure 3.12 for cases 3 and 5. For the pile breakwater model, the fitted value of C_D is 107.2. For the OWC-pile dual-functional wave farm model, the fitted value of C_D is 216.6. As expected, the drag coefficient for the OWC-pile is larger than that for a circular

pile, which has a more streamlined shape.

It can be seen from Figures 3.11 and 3.12 that the semi-theoretical model can capture the variation of $C_d^{(vis)}$ with $T\sqrt{g/D}$ and D/h reasonably well. Because the transmission coefficient C_t used in producing Figures 3.11 and 3.12 are measured, which contains random error, the predicted curves for $C_d^{(vis)}$ are not smooth. The values of viscous dissipation coefficients $C_d^{(vis)}$ are similar for both structures (an OWC-pile dual functional wave farm model and a pile breakwater model of the same dimensions). For both structures, $C_d^{(vis)}$ increases with increasing $T\sqrt{g/D}$ for given values of D/h and H/D. For the pile breakwater model $C_d^{(vis)}$ increases with increasing H/D for given values of D/h and $T\sqrt{g/D}$. For the dual-functional wave-power plant model, $C_d^{(vis)}$ appears to be less sensitive to H/D.

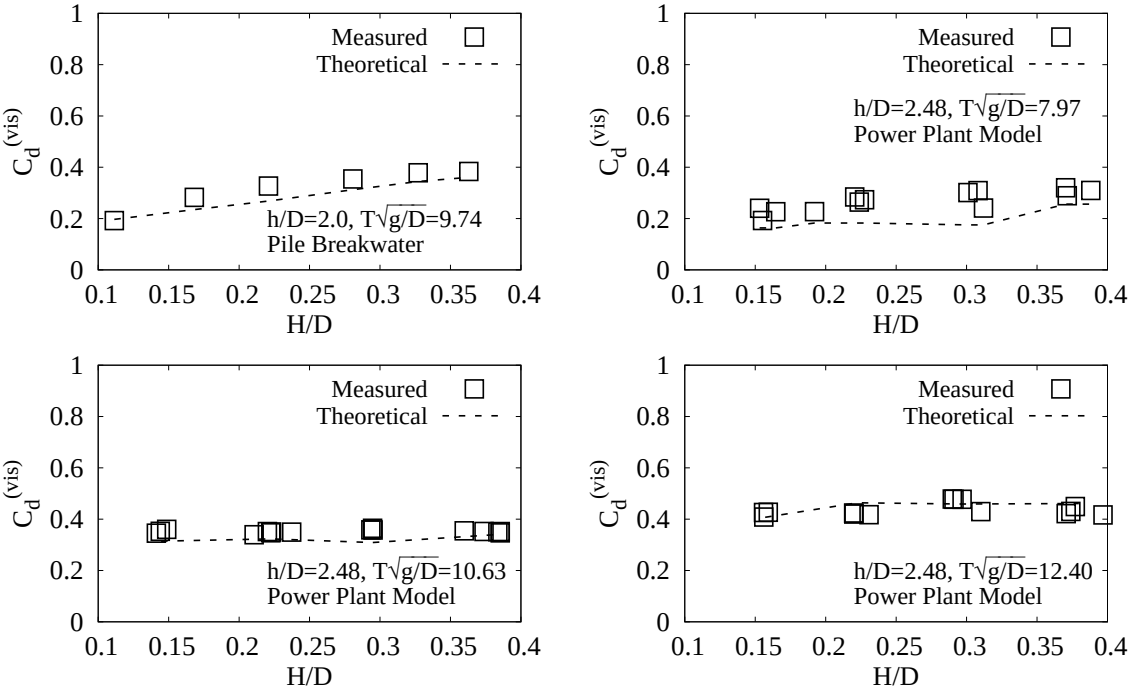

Figure 3.12: Changes of predicted and measured viscous dissipation coefficients with dimensionless wave height for the pile breakwater model (top left panel) and the dual-functional power plant model.

It is remarked that the dual-functional wave-power plant model and the pile breakwater model of the same dimensions have similar values of viscous dissipation coefficients. This also implies a larger drag coefficient for the dual-functional wave farm model because the transmission coefficient of the dual-functional wave farm model is about 20% smaller than that of the pile breakwater model of the same dimensions. Numerical simulations are needed to further understand the increase of drag coefficient C_D caused by integrating OWC chambers into a pile breakwater. Three-dimensional numerical simulations of the OWC-pile dual functional wave-power plants are computationally

challenging if the PTO is explicitly modeled. This is mainly due to the challenge posed by modeling the thin walls and high velocity in the PTO, which requires very fine grid size and very small time steps in order to satisfy the CFL stability condition. The small time step and a large number of cells created by three-dimensional mesh require the simulation being run on a high-performance computing facility.

3.8 A full-scale dual-functional wave-power plant

For a full-scale dual-functional wave-power plant designed according to Froude's law of similarity, the Keulegan-Carpenter number is invariant and the Reynolds number is scaled by $s_c^{3/2}$ where s_c is the geometric scale factor. If the diameter of the full-scale OWC-pile is 3.13 m, the geometric scale factor is $s_c = 25$ based on the model tested in this study. From the range of Re in the model test, one can obtain $Re = 1.9 \times 10^5 - 2.6 \times 10^5$ at the full scale. It is expected that the drag coefficient C_D used in Eq. (3.27) for estimating the viscous dissipation coefficient is not very sensitive to Reynolds numbers because C_D^0 is not sensitive to Reynolds number in the range of $O(10^3)$ to $O(10^5)$. Therefore, it is reasonable to assume that the viscous dissipation coefficient $C_d^{(vis)}$ presented in Figure 3.11 is approximately valid at the full scale, which would allow us to evaluate the performance of a dual-functional wave-power plant at full scale.

The electric power output of a single OWC device is affected by its pneumatic efficiency, η_{pneu}, the rotor efficiency η_{rtr}, and the efficiency of electric generator η_{gen}. For typical impulse turbines, η_{rtr} can be as large as 0.5 (Setoguchi et al., 2001). A recent study (ao et al., 2013) showed that η_{rtr} for self-rectifying radial-flow air turbines can be as large as 0.7. Modern electric generators are very efficient, and can achieve $\eta_{gen} \sim 1$.

For any OWC-pile in a dual-functional wave-power plant consisting of N OWC-piles, the electric power output of the OWC-pile is related to the pneumatic power $P_{OWC}^{(1)}$ by

$$P^{(1)} = \eta_{gen} \underbrace{\left[\eta_{rtr}\, \eta_{air}\, P_{OWC}^{(1)}\right]}_{\text{shaft power output}}, \tag{3.34}$$

where η_{air} is a compressibility-effect coefficient representing the effects of air compressibility on the pneumatic power efficiency. According to Elhanafi et al. (2016b), $\eta_{air} \sim 1$ for small scale models and $\eta_{air} \sim 0.88$ for prototype models. After using the expression for $P_{OWC}^{(1)}$ given in Eq. (3.9), the following expression is obtained

$$P^{(1)} = \eta_{gen}\, \eta_{rtr}\, \eta_{air}\, \eta_{pneu} D P_i. \tag{3.35}$$

Therefore, the total electric power output of a dual-functional wave-power plant consisting of N

OWC-piles can be estimated by

$$P^{(N)} = \eta_{gen}\,\eta_{rtr}\,\eta_{air}\,\eta_{pneu}(ND)P_i. \tag{3.36}$$

Eq.(3.36) is to be used to estimate the electric power output of a dual-functional wave-power plant at full scale. The following values are used in the calculation: the OWC pneumatic efficiency η_{pneu} from respective scaled-down wave periods in Figure3.5 and Figure 3.6, the rotor efficiency $\eta_{rtr} = 0.7$ for the turbine (ao et al., 2013), the generator efficiency of $\eta_{gen} = 0.9$. The dual-functional wave farm is to be designed according to $D = 3.13$ m and $h/D = 2.40$, which corresponds to a geometric scale of about 25 and a water depth of 7.25 m to 7.75 m. The air compressibility effect coefficient $\eta_{air} = 0.88$ is used to reflect the effects of air compressibility on the pneumatic power efficiency at full scale.

The dual-functional wave-power plant is deployed along a 1000-m straight coastline, making the total number of OWC-piles $N = 305$ for the tested gap-diameter ratio. The electric power outputs for six wave conditions are listed in Table 3.2. These six wave conditions reflect the tidal and seasonal change of wave climate at the site. Mean wave period T and root-mean-square wave height H are used to estimate the wave power P_i. scenario 1 and 2 correspond to T=1.1 s for case 1 and 2 in Table 3.1, scenario 3 and 4 correspond to T=0.8 s for case 1 and 2 in Table 3.1, scenario 5 corresponds to T=0.9 s and H=0.0467 m for case 3 in Table 3.1, and scenario 6 corresponds to T=1.4 s and H=0.0454 m for case 3 in Table 3.1. The wave heights used in this scale-up is the corresponding wave heights listed in Table 3.1. It is remarked that these six wave conditions given in Table 3.2 are representative of mild wave conditions. It can be seen from Table 3.2 that the power output of about 1.1-1.8 MW is achieved under seasonal changes of wave conditions, which could potentially provide power for around 700 to 1000 households. The electric power output of this dual-functional wave-power plant is roughly equivalent to three wind turbines with a rotor diameter of 40 m under typical wind speeds suitable for wind turbines. However, the main advantages of the dual-functional wave-power plant include: (i) low construction costs by sharing the construction cost with breakwaters and (ii) shore-protection functionality.

Based on the experimental results for pile breakwaters without OWC and the assumption discussed in Section 3.5.1, the reflection and transmission coefficients for the six scenarios listed in Table 3.2 can be estimated to evaluate the shore-protection performance of the dual-functional wave-power plant. The estimated reflection coefficients for the corresponding pile breakwater are $C_r = 0.72$ for scenarios 1 and 2, $C_r = 0.87$ for scenario 3 and 4, $C_r = 0.80$ for scenario 5, and $C_r = 0.67$ for scenario 6, which are 67-71%, 118-148%, 129% and 48% larger than those listed in Table 3.2 for scenarios 1 and 2, scenarios 3 and 4, scenario 5, and scenario 6, respectively. The transmission coefficients for the corresponding pile breakwater are $C_t = 0.41$ for scenarios 1 and 2, $C_t = 0.29$ for scenarios 3 and 4, $C_t = 0.33$ for scenario 5, and $C_t = 0.44$ for scenario 6, which

Table 3.2: Electric power output estimates for the hypothetical power plant

Scenario	T [s]	h [m]	H [m]	C_r	C_t	P_i [kW]	$T/\sqrt{g/D}$	H/D	η_{pneu}	Power [MW]
1	5.5	7.25	0.94	0.43	0.30	5.57	9.74	0.300	0.41	1.21
2	5.5	7.75	0.94	0.42	0.31	5.60	9.74	0.301	0.41	1.22
3	4	7.25	0.92	0.35	0.23	3.64	7.08	0.294	0.58	1.12
4	4	7.75	0.92	0.40	0.23	3.58	7.08	0.294	0.56	1.07
5	4.5	7.75	1.17	0.35	0.26	6.80	7.97	0.374	0.50	1.81
6	7	7.75	1.14	0.45	0.36	10.02	12.39	0.364	0.27	1.44

are about $32-37\%$, $26-27\%$, 27% and 22% larger than those in Table 3.2 for scenarios 1 and 2, scenarios 3 and 4, scenario 5, and scenario 6, respectively. Therefore, integrating the OWC into the pile breakwater can significantly improve the breakwater's performance in reducing wave transmission and cross-shore sediment movement between the wave-power plant and the shoreline.

3.9 A comparison between the loosely spaced configuration and closely spaced configuration

Compared to the electric power output results of a wave farm of loosely spaced OWC-piles as presented in Section 2.4.2, the dual functional wave farm and breakwater of closely spaced OWC-piles can achieve 6.7 to 11 times better electric power output with three times more OWC-piles covering the same length of coastline, indicating that the closely spaced configuration is economically more viable than the loosely spaced configuration in terms of wave energy utilization.

Compared to the transmission coefficients of the wave farm in the form of a row of loosely spaced OWC-piles as tested in Section 2.4.2, the transmission coefficient of the present wave farm of closely spaced OWC-piles configuration is significantly reduced by at least two-thirds, significantly increasing the structure's performance in terms of shore protection. The transmission coefficient of the wave farm of closely spaced OWC-pile design is also significantly smaller than the estimated transmission coefficients of the wave farms studied previously(Millar et al., 2007; Abanade et al., 2014; Mendoza et al., 2014).

Because the costs of wave-power plant increase sharply with increased requirements for structural strength, it is desirable, from an economical point of view, to have wave farms designed for mild wave conditions but that can still survive extreme wave conditions, which is exactly the design principle behind pile breakwaters. The significant reduction of the reflection coefficient by integrating the OWCs into the pile breakwater can also increase the survivability of the dual-functional wave farm. The OWC-pile type of dual-functional wave farm is recommended for places where pile breakwaters are to be built for shore protection. The additional costs (other than the necessary

equipment related to PTO and Power Grid connection) to integrate the OWC chambers into the pile breakwater may not be a concern due to the simplicity of the OWC-pile structure. Integrating OWC chambers into the pile breakwater may improve the survivability of structure through reduction of the reflection coefficient (see Figure 3.9). However, the structural strength aspect of the OWC-pile wave farm still needs to be evaluated separately. The findings of the present research promote close collaboration between the wave-energy utilization community and shore-protection community for commercial-scale deployment of WECs and contribute to making wave energy economically competitive.

3.10 Summary

In this study, the performance of a dual-functional wave-power plant based on the concept of integrating oscillating water column (OWC) chambers into a pile breakwater is evaluated through a series of wave flume tests. The OWC-pile wave-power plant can serve as a breakwater for shore protection for sustainable coastal development, which provides a viable way to achieve cost sharing between two functions of the structure and to improve the structure's survivability. The main conclusions drawn in this study are briefly summarized as follows.

1. Our results showed that integrating OWC chambers into a pile breakwater can significantly increase the capture width ratio of the OWC chambers as compared with standalone OWC-piles. This would make it possible to design the OWC-pile type of dual-functional wave-power plants to operate under mild wave conditions.

2. Integrating OWC chamber into the pile breakwater can also reduce both the reflection coefficient and transmission coefficients. This additional reduction in wave reflection and transmission can improve shore-protection performance, reduce the wave loading on the structure, and improve the survivability of the structure.

3. A semi-theoretical model for the estimation of energy dissipation due to viscous effect and vortex shedding is developed, model results indicate that compared to a row of closely spaced piles without an OWC device, the addition of the OWC structure increased the drag coefficient. The total amount of energy lost due to viscous effect remained similar due to the reduced availability of energy in the wave field. This suggests that the additional reduction of transmission coefficient observed in the experiment is introduced mainly by the wave-power extraction of the power take-off device.

4. A dual-functional full-scale wave-power plant proposed for a 1000 m-long coastline with typical mild coastal wave conditions can provide an electric power output of about 1.1 to 1.8 MW, which is significantly higher than the wave farm of loosely spaced piles discussed in Section 2.4.

Compared to the wave farm of loosely spaced piles, the present wave farm and breakwater in the form of a row of closely spaced piles achieves 6.7 to 11 times higher electric power output with only three times more OWC devices along a same length of coastline. Moreover, the present wave farm and breakwater of closely spaced piles can achieve significantly better shore protection functions compared to the loosely spaced configuration studied in section 2.4.

In this study, we found that compared to a row of closely spaced piles without OWC devices, the viscous dissipation due to vortex shedding is stronger with the addition of the sharp edges of the OWC chambers and their support structureThe total amount of energy dissipated by vortex shedding, however, remains less influenced. This is mainly due to the decreased availability of wave energy due to wave-power extraction of the power take-off device. To understand further the detailed mechanics in vortex shedding induced viscous loss, a detailed investigation of the vortex dynamics and the associated energy dissipation are presented in chapter 4, where a numerical simulation of a row of closely spaced OWC-pile devices in waves is conducted.

CHAPTER 4
ON THE HYDRODYNAMICS AND WAVE ENERGY EXTRACTION EFFICIENCY OF A ROW OF CLOSELY SPACED OWC-PILES FOR WAVE-ENERGY UTILIZATION AND SHORE PROTECTION: A NUMERICAL STUDY

4.1 Introduction

The vortex dynamics around a standalone OWC-pile device or a row of closely spaced OWC-pile device under wave condition can influence the hydrodynamics and wave energy extraction efficiency of the structure in two ways. First, the lee wake vortex and the vortex shed from the lower skirt of the OWC chamber are the main sources of dissipation of wave energy into unusable turbulent kinetic energy and, eventually, internal energy. Second, the lee wake vortices and horseshoe vortex are found to be responsible for enhanced sediment scouring around pile structures exposed to steady currents and waves (Sumer et al., 1997; Sumer and Fredsøe, 1998; Muzzammil and Gangadhariah, 2003, etc). For a standalone circular pile structure in waves, it has been found that the existence and life span of the vortices strongly depends on the KC number. In the laboratory experimental study of Sumer et al. (1997), it was found that no horseshoe vortex exists when $KC < 6$ for a standalone circular pile exposed to regular waves. However, as the KC number increases, the horseshoe vortex come into existence and increases in terms of size and lifespan. Changing the cross-sectional shape of the pile can have significant impact on the formation and development of horseshoe vortex. For a square pile in a wave field, a horseshoe vortex can form at a KC number as low as 4. The near-bed lee wake vortex flow also strongly depends on the KC number. The lee wake flow pattern can be categorized into different regimes under different KC numbers (Williamson, 1985). For standalone circular pile under oscillatory flow with $KC < 7$, no lee wake vortex is shed from the structure, but a pair of small vortices are formed when the flow reverses. When $KC > 7$, lee wake vortex shedding occurs, however, no lee wake vortex street is observed in the existing literature for KC number smaller than 20.1 (Sumer et al., 1997).

A row of closely spaced OWC-piles as tested experimentally in chapter 3 is very different from the circular piles and square piles tested in existing literature in that: (1) The cross-sectional shape of the structure at the bed is a concave "ring", which has never been studied before; (2) The existence of neighboring piles creates contraction jet flows, which can create a significantly higher flow speed at the sides of the OWC-pile structure compared to a standalone circular pile tested in previous studies. These differences may lead to significant differences in terms of how the KC number should be defined, the lower bound of KC number for the existence of horseshoe vortex, and the patterns of horseshoe vortex and lee wake vortices. It is thus interesting to investigate the flow field of the proposed structure exposed to waves in detail, so that the patterns of vortex

dynamics and its potential influence to scour and wave energy extraction can be discussed. In this chapter, based on the CFD model described in Chapter 2, a numerical investigation of the hydrodynamics and wave energy extraction of a row of closely spaced OWC-piles is reported with a focus on vortex dynamics. Numerical reproduction of several test conditions tested experimentally in chapter 3 is performed. The numerical model setup is articulated in section 4.2. The numerical results are first validated using experimental measurements in section 4.3, then the detailed flow fields are inspected in section 4.5.

4.2 Numerical wave flume setup

The mathematical formulation used in this numerical study is identical to the one used in chapter 2. As illustrated in Figure 4.1, the dimensions of the computational domain are 17 m long, 0.6 m high and 0.54 m wide. The numerical wave flume used here is 3 m longer than the one used in chapter 2, mainly due to the need to accommodate four additional wave gauges for the two-point wave separation, which will help improve wave separation accuracy. Similar to the numerical wave flume used in chapter 2,the first 4 m and last 4m of the flume are the wave making relaxation zone and wave absorption relaxation zone, respectively. The test section has a length of 9m. The model of a row of closely spaced OWC-piles, identical to the one tested in chapter 3, is placed at the middle of the test section. Two numerical wave gauges, G1 and G3, are placed 30.5 cm from the model on the up-wave and down-wave directions. Another numerical wave gauge, G2, is placed inside the corresponding OWC chamber at 3.7-cm down-wave from the geometric axis of the chamber which is consistent with the setup in the laboratory experiment. Two pairs of wave gauges, G4-G5 and G6-G7, are placed on the up-wave and down-wave side of the model with the wave gauge near the model being 2-m away from the model. These wave gauges are used to perform wave separation analysis.

Similar to the computational domain used in chapter 2, the computational domain used here is covered by an unstructured mesh. For the most part, the mesh setup of the present numerical simulation is identical to the one used in chapter 2, with the exception of the region near the row of closely spaced OWC-piles. The mesh size in the test section is refined to at least 0.82 cm $\times$ 1.00 cm $\times$ 2.50 cm ($\Delta x \times \Delta y \times \Delta z$), and the mesh within 10cm around the still water line is further refined to 0.82 cm $\times$ 0.25 cm $\times$ 1.25 cm ($\Delta x \times \Delta y \times \Delta z$). Near the row of closely spaced OWC-piles model, the mesh is further refined to at least 0.205cm $\times$ 0.25 cm $\times$ 0.15 cm. The mesh is further refined to 0.1cm $\times$ 0.125 cm $\times$ 0.075 cm inside the narrow gap formed by adjacent OWC-piles. This more refined mesh is to ensure that there are at least eight cells to cover the narrowest gap location between adjacent piles so that an accurate representation of the contraction jet flow can be obtained. Close to the surface of the OWC-piles, an additional layer of mesh with even finer resolution is used: the mesh in this layer is of irregular shape and the characteristic mesh resolution of this layer of mesh is around 0.1 cm $\times$ 0.1 cm $\times$ 0.075 cm. The details of the mesh near the

OWC-piles model and in between the narrowest location of the gap are shown in Figure 4.2. The resulting total mesh count is about 5.8 million.

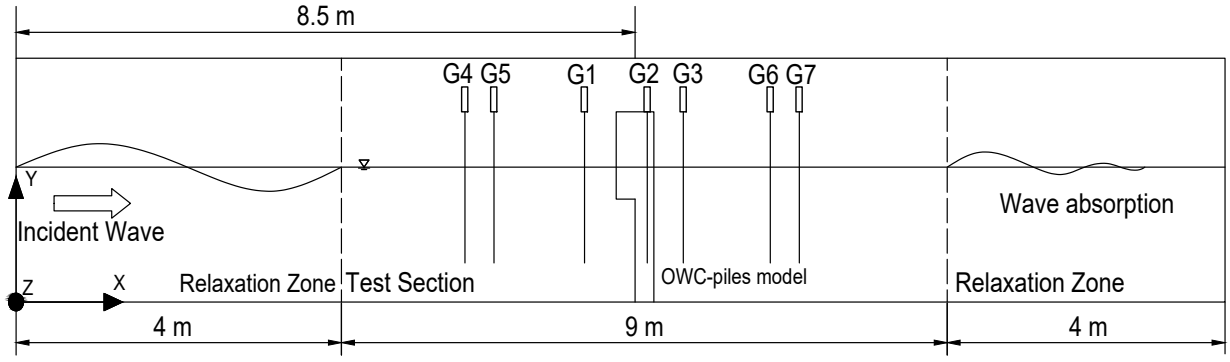

Figure 4.1: Sketch of the computational domain.

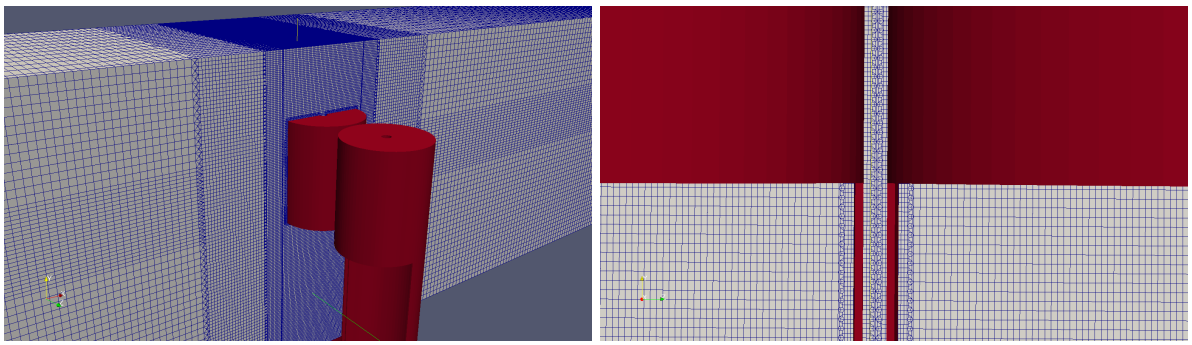

Figure 4.2: Details of the computational mesh, showing the mesh detail near the model (left) and the mesh near the narrowest location of the gap formed by adjacent OWC-piles (right).

4.3 Model verification and validation

In this section, the numerical simulations are validated using the experimental measurements reported in chapter 3. Due to the limitation of available computational resources, three test conditions are selected from case 1 in Table 3.1 for a fixed water depth of $h = 0.29$ m: T=0.7 s and H=3.63 cm; T=1.1 s and H=3.75 cm; and T=1.5 s and H=3.68 cm. These wave conditions represent typical short waves, intermediate waves and long waves. A typical simulation of 20 wave periods takes five to eight wall-clock days when running on five computational nodes on the TACC supercomputing facility Stampede2, with each node equipped with two 24-core Intel Xeon Skylake-X processors and 192GB of DDR4 memory.

4.3.1 Surface displacement and air pressure inside the OWC chamber

A comparison between the experimental measurement and numerical simulation of the water surface displacement sampled 30.5-cm on the up-wave and down-wave side of the model(wave gauges G1 and G3) is shown in Figure 4.3. The comparisons between simulations and experimental measurements of the water surface elevation sampled inside the OWC chamber, as well as the measured pressure inside the OWC chamber, are shown in Figure 4.4. The agreement between the numerical simulations and the experimental measurements is very good. The higher harmonic components in the measured water surface displacement are captured reasonably well. The variation of pneumatic pressure inside the OWC chamber is also captured reasonably well, with only slight underestimation for $T = 1.5$ s.

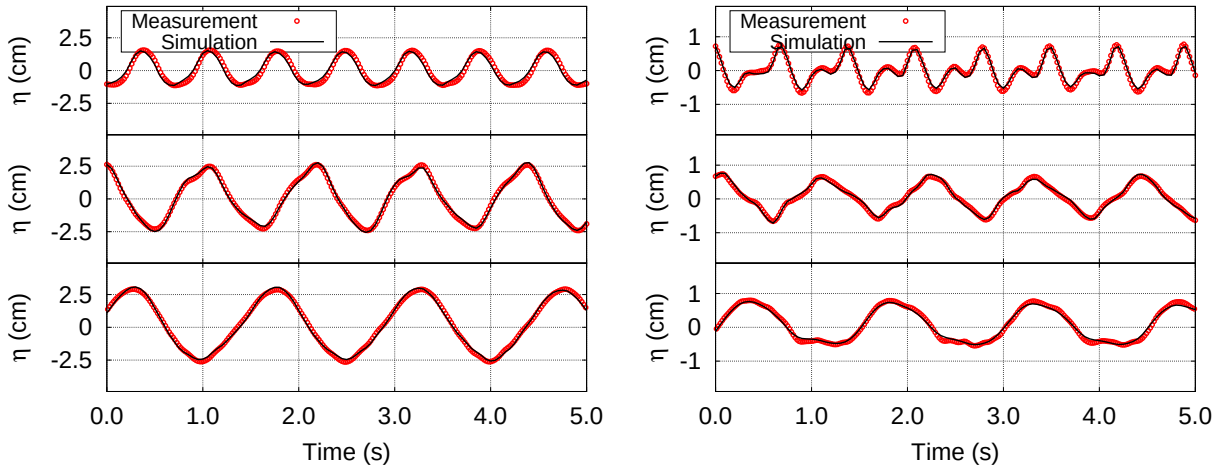

Figure 4.3: Comparison between the experimental measurement and numerical simulation of the water surface displacement measured at G1 (left panel) and G3 (right panel). For each panel from top down: $T = 0.7$ s, $T = 1.1$ s, $T = 1.5$ s.

4.3.2 Wave energy extraction efficiency, wave transmission, and wave reflection

Table 4.1 shows a summary of the comparison between the numerical simulations and the experimental measurements on wave energy extraction efficiency (measured by capture width ratio λ/D) and the wave transmission and reflection coefficients C_t and C_r. The KC number is also included in this table as a reference for further discussion on the flow field and vortex dynamics. The numerical simulation predicted these parameters reasonably well, with a maximum difference of 16 % for λ/D and 8.9 % for C_r and C_t.

The good agreement between the numerical simulation and laboratory measurements indicates that the numerical model, which was validated for the case of a standalone OWC-pile device in regular waves, can also simulate a row of closely spaced OWC-piles in regular waves with necessary changes to the mesh to accommodate the narrow gap formed by adjacent piles. Previous studies

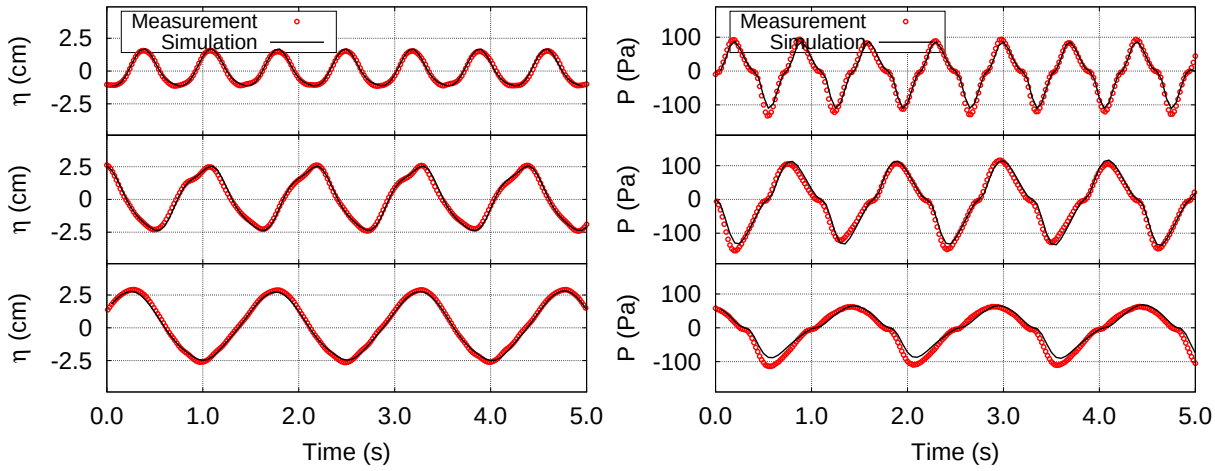

Figure 4.4: Comparison between the experimental measurements and numerical simulations of the water surface displacement measured by wave gauge G2 (left panel) and the OWC pneumatic chamber pressure (right panel). For each panel from top down: $T = 0.7$ s, $T = 1.1$ s, $T = 1.5$ s.

Table 4.1: Comparison of λ/D, C_r and C_t between the numerical simulation result and laboratory measuremnets.

Wave period (s)	KC number	Measurement			Simulation		
		λ/D	C_r	C_t	λ/D	C_r	C_t
0.7	1.02	0.624	0.330	0.207	0.581	0.335	0.204
1.1	1.22	0.405	0.425	0.304	0.421	0.408	0.319
1.5	1.53	0.204	0.497	0.337	0.171	0.474	0.370

involving comparison between numerical simulation results and PIV wave field measurements have shown that variants of $k - \omega$ turbulence models can be applied to study the detailed flow fields around small scale OWC models with sufficient accuracy to resolve the formation, development and motion of large-scale vortices (Elhanafi et al., 2016a). In the following sections, based on the validated numerical results presented in this section, a discussion of the detailed flow field near the row of closely spaced OWC-piles, with a focus on vortex dynamics, is carried out to visualize and quantify various vortical features. The numerical results of a standalone OWC-pile as reported in chapter 2 are also included in this discussion to highlight the difference between the two configurations.

4.4 Three-dimensional flow field visualization and vortex characteristics calculation

The visualization of a complex 3-D flow field is a challenging task in hydrodynamic and aerodynamic research in that it involves very large data sets consisting of multiple variables and components

at dense grid points and multiple time instances. In order to provide a clear presentation of the characteristic flow features discussed in this chapter, such as horseshoe vortex and lee wake vortices, a flow visualization method must be carefully chosen.

Existing flow visualization techniques can be generally categorized into five types (Post et al., 2003; Laramee et al., 2004):

1. Direct flow visualization: The flow field is visualized directly as color maps or vector fields shown as array of arrows. This method is suitable for 2-D flow fields.

2. Geometric flow visualization: The flow field is first processed to obtain certain geometric objects, such as streamlines, streaklines or pathlines. Then the geometric objects are visualized. This method applies to both 2-D and 3-D flow fields, regardless of whether the flow is steady or not. For complex 3-D flow, direct application of this technique to visualize the flow field in a 2-D format may result in an overlap of features and make the presentation difficult to interpret.

3. Texture-based flow visualization: The flow field is first processed to show the directional structure, and then visualized in the form of streamlines or random textures. Examples of this type of flow visualization include skin-friction lines or limiting streamlines, usually used to visualize flow field patterns in 2-D slices or surfaces of a 3-D flow field. This method does not resolve the global flow field. However, when carefully done, this visualization can provide a very clear presentation of many important flow features related to vortical flows, boundary layer flows, and wake flows.

4. Feature-based flow visualization: This approach abstracts the detailed flow field by processing the flow field into discrete features, such as singularities (critical points) on a 2-D slice. Only these singularities are visualized in 2-D format since they are of interest to the researchers. This technique is closely related to the texture-based visualization technique.

5. Partition-based flow visualization (Salzbrunn et al., 2008): The flow field is visualized as a cluster of partitions where the flow field vectors show similar direction, or have other similar properties such as vorticity or singularity. This visualization method can be concise and clear, but leaves out details of the flow pattern.

In this study, the flow field around the standalone or a row of closely spaced OWC-piles is essentially 3-D, and has relatively complex geometry (as compared to circular cylinders or air foils, which are commonly visualized in many existing CFD studies). It is thus preferable to partially visualize the 3-D flow field in a 2-D format. Maskell (1955) proposed a concept of "limiting streamlines" to visualize and study 3-D turbulent flow separation near a surface. On an impermeable surface, the velocity vector normal to the surface is always zero, allowing the visualization of the 3-D flow field

on the surface in a 2-D format. This type of visualization can be correlated with experimental flow visualization technique such as oil flow surface visualization in wind tunnels. The associated mathematical problem arises from the study of limiting streamlines, i.e., singularities (critical points) of limiting streamlines, are later further investigated by a number of researchers. Perry and Fairlie (1975) expanded the application of this technique to regions away from boundaries or surfaces, highlighting its significance in visualizing turbulent wakes. In order to differentiate from the conventional streamlines in 2-D flows and the limiting streamlines on surfaces and boundaries, the limiting streamline-like flow visualization away from boundaries is referred to as "sectional streamlines" by Perry and Steiner (1987). Using this method, horseshoe vortices and lee wake vortices are visualized in detail successfully by many studies (e.g., Perry and Steiner, 1987; Steiner and Perry, 1987; Dargahi, 1989; Yen et al., 2008; Yen and Yang, 2011; Liu et al., 2015). In this chapter, the detailed flow field will also be visualized using this technique (e.g., by visualizing sectional streamlines on selected two-dimensional slices with the velocity normal to the slice ignored), accompanied with a loose velocity vector glyph to show the direction of the flow.

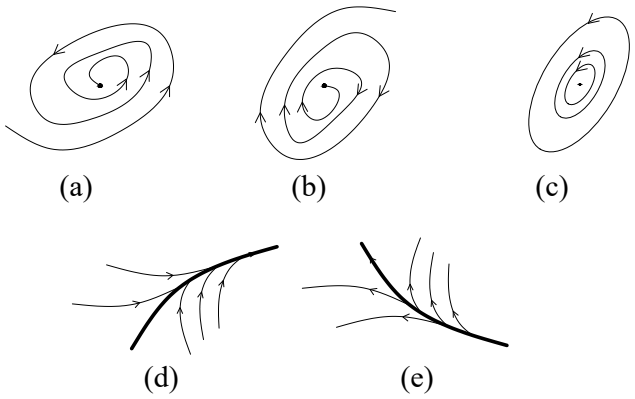

Figure 4.5: A sketch of several critical points and flow features that are of interest in the present study: (a) stable focus, (b) unstable focus, (c) center, (d) negative open bifurcation line, (e) positive open bifurcation line.

In order to facilitate further discussion of the flow field, a sketch showing the sectional streamline representation of several flow features is shown in Figure 4.5. Particularly, the flow features (a) to (c) shown in Figure 4.5 indicate the existence of a vortex with its vorticity vector pointing normal to the paper. Flow features represented by (a) and (b) indicate a normal component that cannot be visualized in this 2-D visualization format, while the flow feature represented by (c) indicates a vortex with zero normal component at the slice plane of visualization, i.e., on the plane of symmetry. The flow features represented by (d) and (e) indicate a vortex with its vorticity vector pointing towards the thick streamline to which all other streamlines merge. The flow feature represented by (d) corresponds to the "top-view" of horseshoe vortices (Perry and Steiner, 1987).

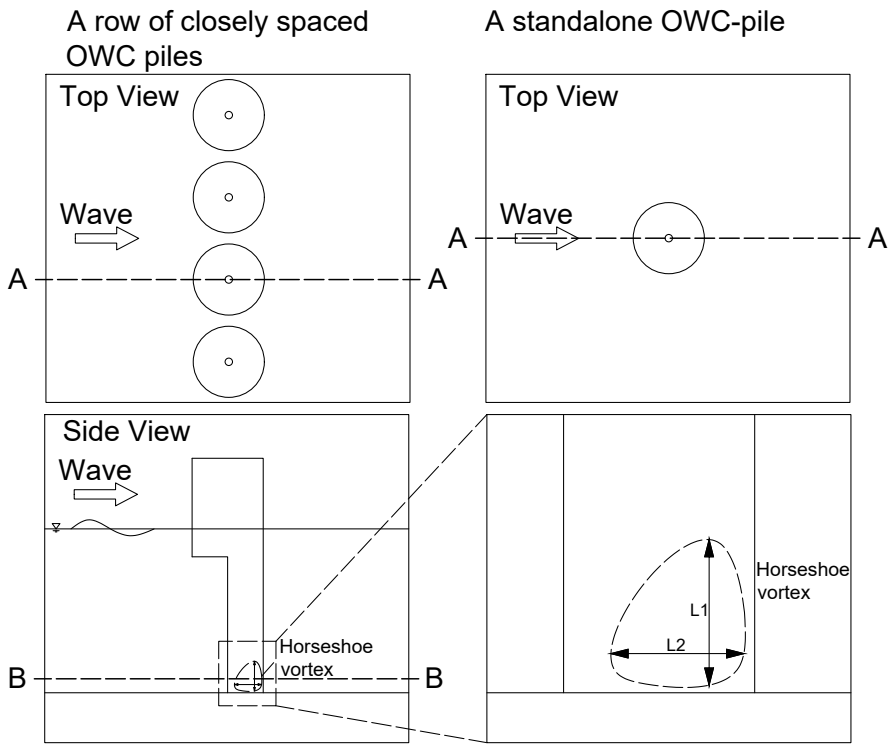

Figure 4.6: A sketch of the slice planes and points at which data is extracted and visualized, for both the row of closely spaced OWC-piles (left) and a standalone OWC-pile (top-right). The bottom-right panel shows an example of computation for the mean vortex size of the horseshoe vortex using two vortex lengths L_1 and L_2.

Figure 4.6 shows the slice planes at which data are visualized. The slice plane A is vertical and cuts through the middle of an OWC-pile; visualization of different local details on this slice plane can show the possible existance of horseshoe vortex and the vortex shed from the lower skirt of the OWC chamber. The slice plane B is horizontal and cuts through the horizontal plane 5 mm above the actual bottom; visualization of this plane can show the span-wise shape of the horseshoe vortex as well as the lee wake vortex shed from the structure.

Following Muzzammil and Gangadhariah (2003), a vortex strength S_v is defined by

$$S_v = \pi U_v D_v \tag{4.1}$$

where U_v is a characteristic vortex flow velocity and D_v is the mean vortex size defined as the mean of the size of the vortex along its long axis and short axis (as illustrated in Figure 4.6). For steady current, Muzzammil and Gangadhariah (2003) used $U_v = \pi\Omega D_v$, Qadar (1981) computed U_v based on an empirical formula with the assumption that U_v is related to the mean velocity of the

approaching flow. For oscillatory flow conditions, there is no well-tested method for the calculation of U_v. In this study, U_v is extracted directly from the numerical flow field at the boundary of the horseshoe vortex. For the horseshoe vortex, the flow velocity (with the normal component ignored) at the highest location of the vortex is used as the characteristic vortex velocity U_v.

4.5 Horseshoe vortex and lee wake vortices

In order to show the temporal variation of the flow field within one wave cycle, flow visualizations are performed at six selected time instances for $T = 0.7$ s, and nine time instances $T = 1.1$ s and $T = 1.5$ s, for a row of closely spaced OWC-piles. The time instances used in the visualization are marked out with blue 'o' symbols in the time series figure at the top of each visualization figure. Similar to the analysis presented in section 2.5, the time instances cover the in-flow phase, in which water mass flows into the OWC chamber and cause the water surface in the chamber to rise, and the out-flow phase, where the water mass flows out of the OWC chamber and the water surface in the chamber drops.

4.5.1 A row of closely spaced OWC-piles

Figures 4.7 and 4.8 show the flow fields and sectional streamlines at the slice planes A and B, respectively, for the test condition T=0.7s. It is evident that for waves interacting with a row of closely spaced OWC-piles, the incoming flow builds up in front of the back wall of the OWC chamber where the flow rolls down to form a large horseshoe vortex system at the toe. Throughout a wave cycle, the horseshoe vortex maintains its existence and the vertical size of the horseshoe vortex, characterized by the highest point of the horseshoe vortex-induced circulation zone, fluctuates between 1.5 cm to 4 cm. The horizontal location of the center of the horseshoe vortex, characterized by the stable focus or center patterns in the sectional streamlines, varies between 1 cm to 2.7 cm from the toe. It is interesting to note that for the small region depicted here, flow reversal during a wave cycle does not have a significant impact on the $u-v$ velocity directions in the case of a row of closely spaced OWC-piles. In fact, in the region visualized in the plots, the $u-v$ velocity directions shows a constant inflow towards the back wall throughout the wave cycle. This phenomenon is also observed in the intermediate to long waves in a standalone OWC-pile case discussed in section 2.5.

Because the slice plane B as shown in Figure 4.8 is only 5 mm above the actual bottom, the horseshoe vortex structure is also visible in the plots, characterized by the negative open bifurcation line pattern within the concave region formed by the back wall of the OWC-piles (refer to Figure 4.5 for sketches of flow patterns). A long horseshoe vortex occupies the entire width of the OWC-pile structure and has a concave shape. This horseshoe vortex wraps around the edges of the back wall at the narrow gap and is destroyed in the contraction jet flow. From the sectional streamlines on the down-wave side of the row of OWC-piles, the existence of horseshoe vortex at the back side

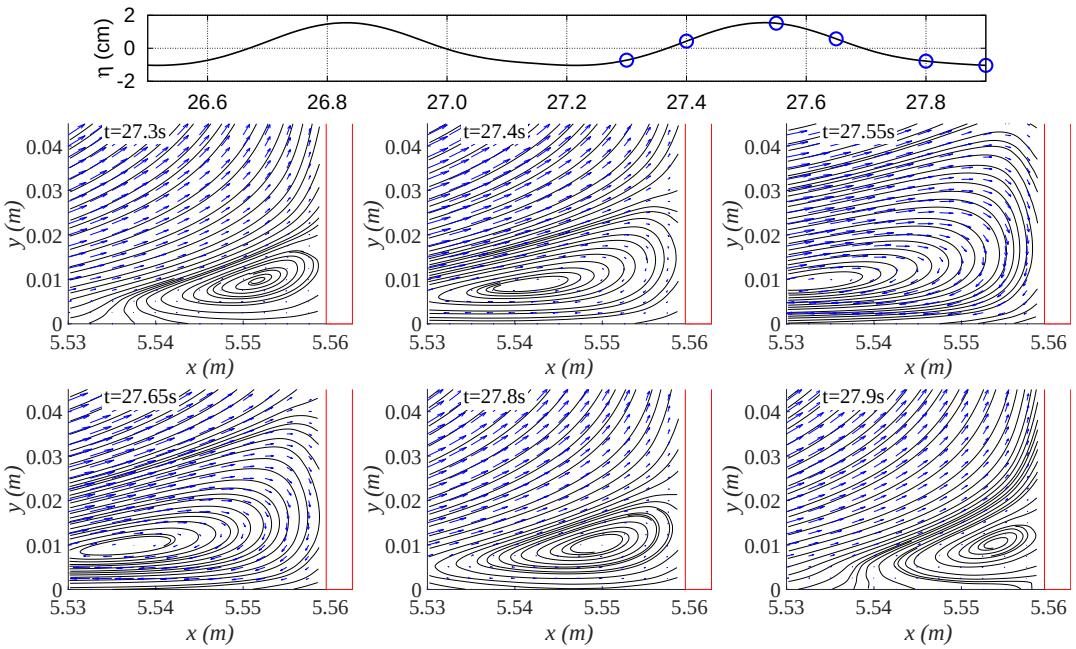

Figure 4.7: The u-v velocity field and sectional streamlines near the back wall of the OWC-pile structure along the slice plane A of a row of closely spaced OWC-piles simulation, showing the test condition T=0.7s.

of the OWC-piles is not evident. The wake vortices are characterized by the stable nodes and center patterns directly up-wave and down-wave of the narrow gap, these wake vortices are nearly symmetric and are relatively small compared to the dimensions of the OWC-piles. The lee wake vortices on both sides of the model are formed by the separation of the contraction jet flow when it hits opposite flow during flow reversal, which persists without being shed until it is destroyed by the subsequent flow reversal.

Figures 4.9 and 4.10 show the flow field and sectional streamlines at the slice planes A and B, respectively, for $T = 1.1$ s. Again a horseshoe vortex system exists at the toe of the structure, however, compared to the case of $T = 0.7$ s, the size of the horseshoe vortex is smaller. The vertical size of the horseshoe vortex varies between about 0.8 cm and 2.0 cm throughout the wave cycle. The horizontal location of the center of the horseshoe vortex varies between 0.5 cm and 0.8 cm from the toe.

From Figure 4.10, the contraction jet flow can be clearly observed during the in-flow and out-flow phases, characterized by the dense parallel sectional streamlines through the narrow gap. During the in-flow phase of the wave cycle, two large wake vortices can be clearly observed on the up-wave side the model. These two vortices are formed by the flow separation of the contraction jet flow due to the out-flow phase hitting the reversal flow. As the contraction jet flow forms towards the down-wave direction, two small vortices are formed on the down-wave side of the model due to

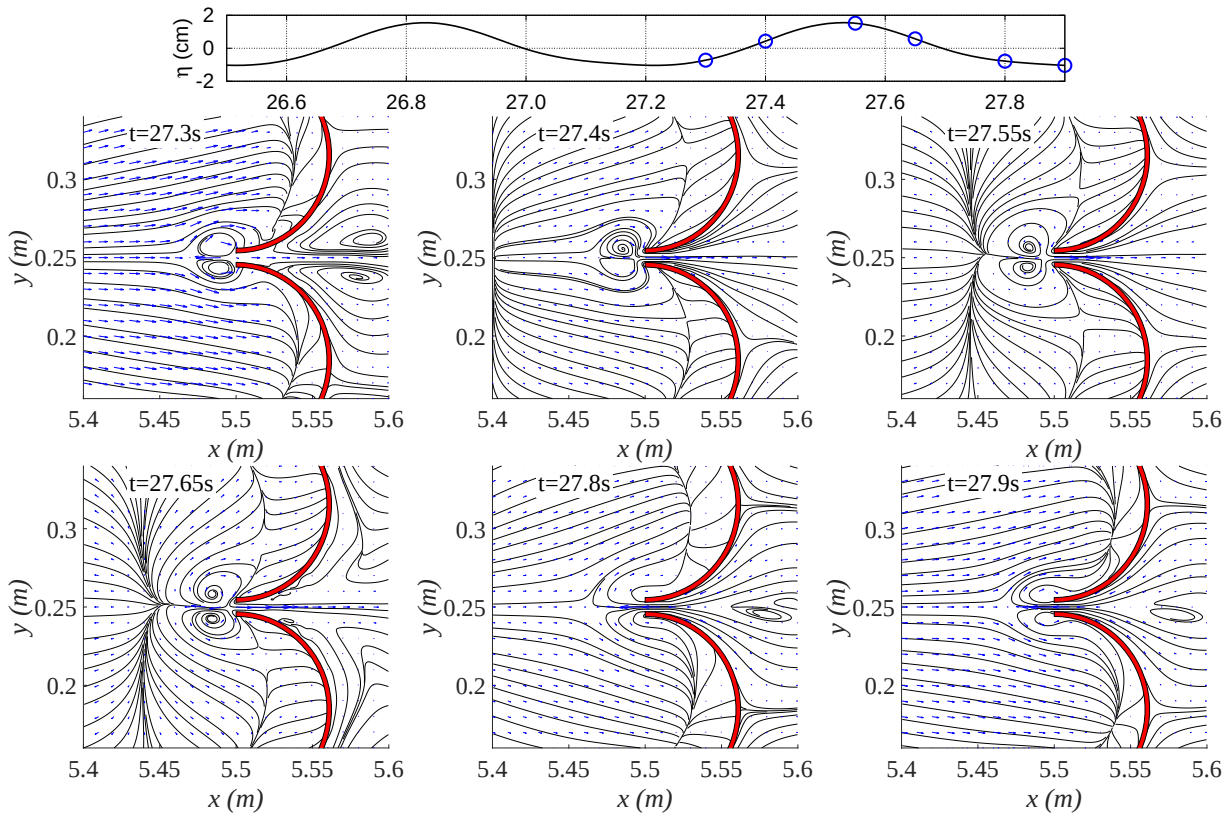

Figure 4.8: The u-w velocity field and sectional streamlines near the back wall of the OWC-pile structure along the slice plane B of a row of closely spaced OWC-piles simulation, showing the test condition T=0.7s.

boundary flow separation and flow reversal. The size of the vortices formed on the up-wave side is much larger than that of the vortices on the down-wave side mainly because the vortices on the up-wave side are formed by the flow separation caused by a sharp discontinuity of the boundary layer, with no lateral confinement to limit its development. However, the vortices formed on the down wave side are controlled by the boundary flow separation from a continuous surface, which also becomes a confining boundary that limits the development of these vortices on the down-wave side. Compared to the wake vortices found in $T = 0.7$ s, the wake vortices for $T = 1.1$ s are larger and have a longer lifespan. For $T = 1.1$ s the wake vortical structure on the up-wave side of the model remains in existence throughout the wave cycle. Similar to the findings in the case of a standalone OWC-pile case, a persistent in-flow towards the concave region formed by the back walls of OWC-piles is evident, and the "stagnation" flow field in the concave region actually indicates a normal flow in the upward or downward directions. Inside the concave region formed by the back wall of the model, negative open bifurcation lines are evident, showing the presence of horseshoe vortices. These negative open bifurcation lines are much closer to the back wall compared to that

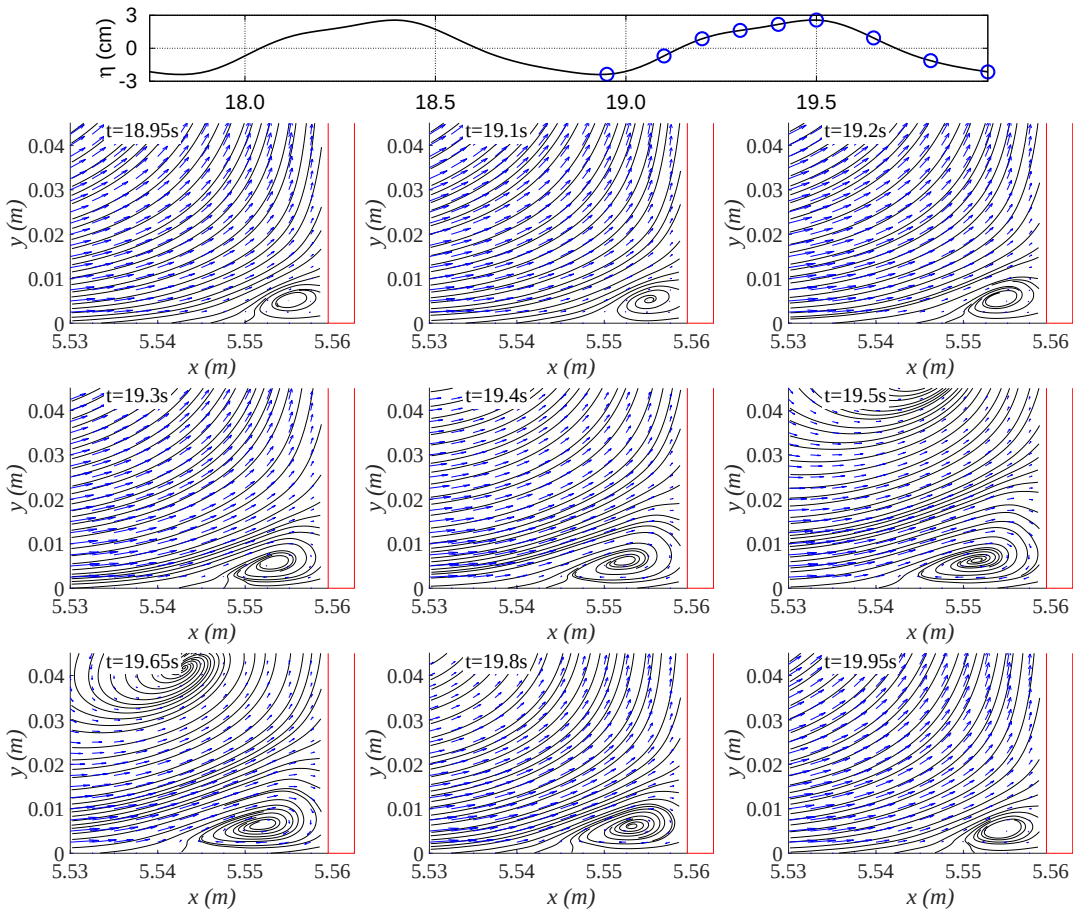

Figure 4.9: The u-v velocity field and sectional streamlines near the back wall of the OWC-pile structure along the slice plane A of a row of closely spaced OWC-piles simulation, showing the test condition T=1.1s.

for $T = 0.7$ s, indicating that the size of the horseshoe vortices are smaller than that for $T = 0.7$ s.

Figures 4.11 and 4.12 show the flow field and sectional streamlines at the slice planes A and B, respectively, for $T = 1.5$ s. A horseshoe vortex system is still visible throughout the wave cycle. However, its size is smaller than $T = 0.7$ s and $T = 1.1$ s, with vertical size ranging from 0.5 cm to 1.5 cm throughout the wave cycle. Generally speaking, the flow pattern in the slice plane B under the test condition $T = 1.5$ s is very similar to that in the test condition $T = 1.1$ s.

From Figure 4.12, flow patterns similar to the test condition $T = 1.1$ s can be observed. Compared to the flow field for the test condition $T = 1.1$ s, the sizes of the wake vortices are similar, and the lifespans of them are longer than that for the test condition $T = 1.1$ s. The negative open bifurcation lines in the concave region of the back wall is clearly observed, with its location being even closer to the back wall, indicating a smaller size horseshoe vortex compared to the test conditions of $T = 0.7$ s and $T = 1.1$ s, which is in accordance to the size of the horseshoe

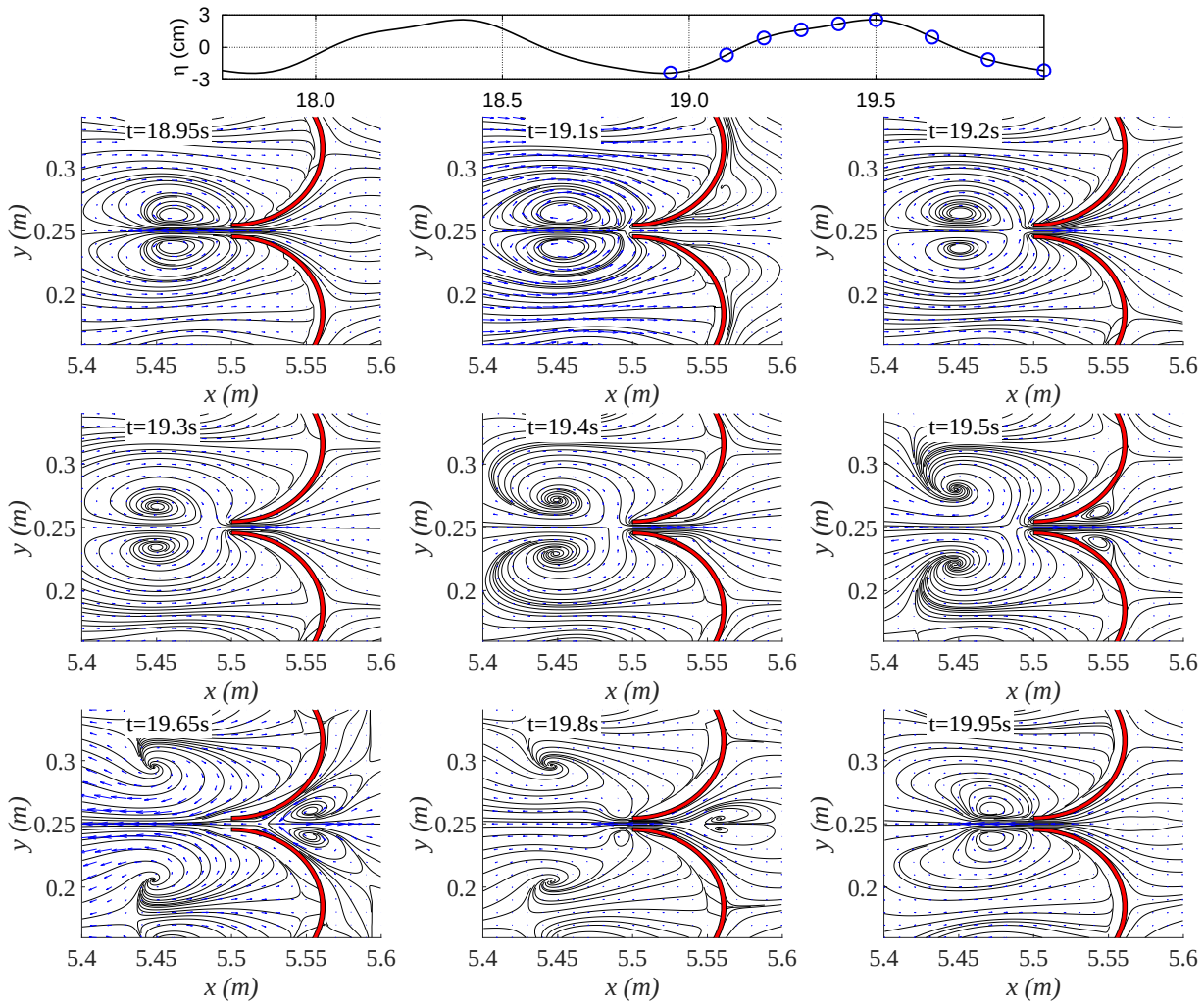

Figure 4.10: The u-w velocity field and sectional streamlines near the back wall of the OWC-pile structure along the slice plane B of a row of closely spaced OWC-piles simulation, showing the test condition T=1.1s.

vortex shown in Figure 4.11.

4.5.2 Vortex strengths and implications to scouring

Table 4.2 shows a summary of the normalized vortex strengths for the vortices found in the simulated flow fields under the test conditions discussed above. In the table, the superscript "hs" means horseshoe vortex, "lw1" means lee wake vortex on the up-wave direction, "lw2" means lee wake vortex on the down-wave direction, "B" means the slice plane B. It can be seen that the vortex strengths of the horseshoe vortex systems found in the present tests are only slightly larger than the strength of the horseshoe vortex system found in the case of a standalone OWC-pile (please refer to

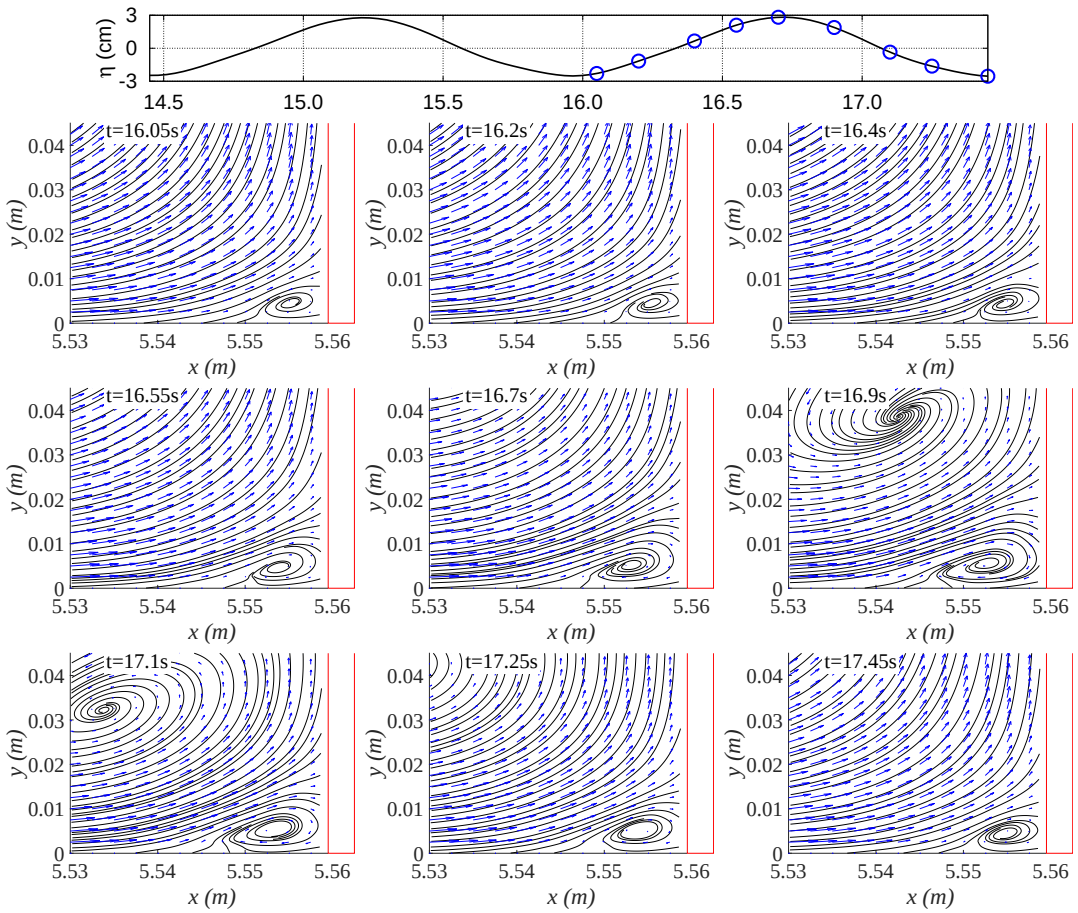

Figure 4.11: The u-v velocity field and sectional streamlines near the back wall of the OWC-pile structure along the slice plane A of a row of closely spaced OWC-piles simulation, showing the test condition T=1.5s.

Table 2.3 for vortex strengths of the standalone OWC-pile), which is an order of magnitude weaker than the typical horseshoe vortices observed in steady currents in laboratory conditions. The wake vortices on the up-wave side of the model generally have a higher vortex strength compared to those on the down-wave side. The strength of the wake vortices for the row of closely spaced OWC-piles is significantly higher than that of the standalone configuration, particularly for the wake vortices on the up-wave side, reaching a maximum value of 1.3 at slice plane B close to the bottom. Generally speaking, the wake vortices have a much higher vortex strength than the horseshoe vortices, and the vortex strengths of the row of closely spaced OWC-piles are higher than that for the standalone configuration.

In terms of sediment transport and scouring, similar to the conclusion drawn for the case of standalone OWC-pile configuration, the strength of the horseshoe vortex is too small. Because of this, it is likely that for the tested KC numbers (less than 1.6, refer to Table 4.1) and the model

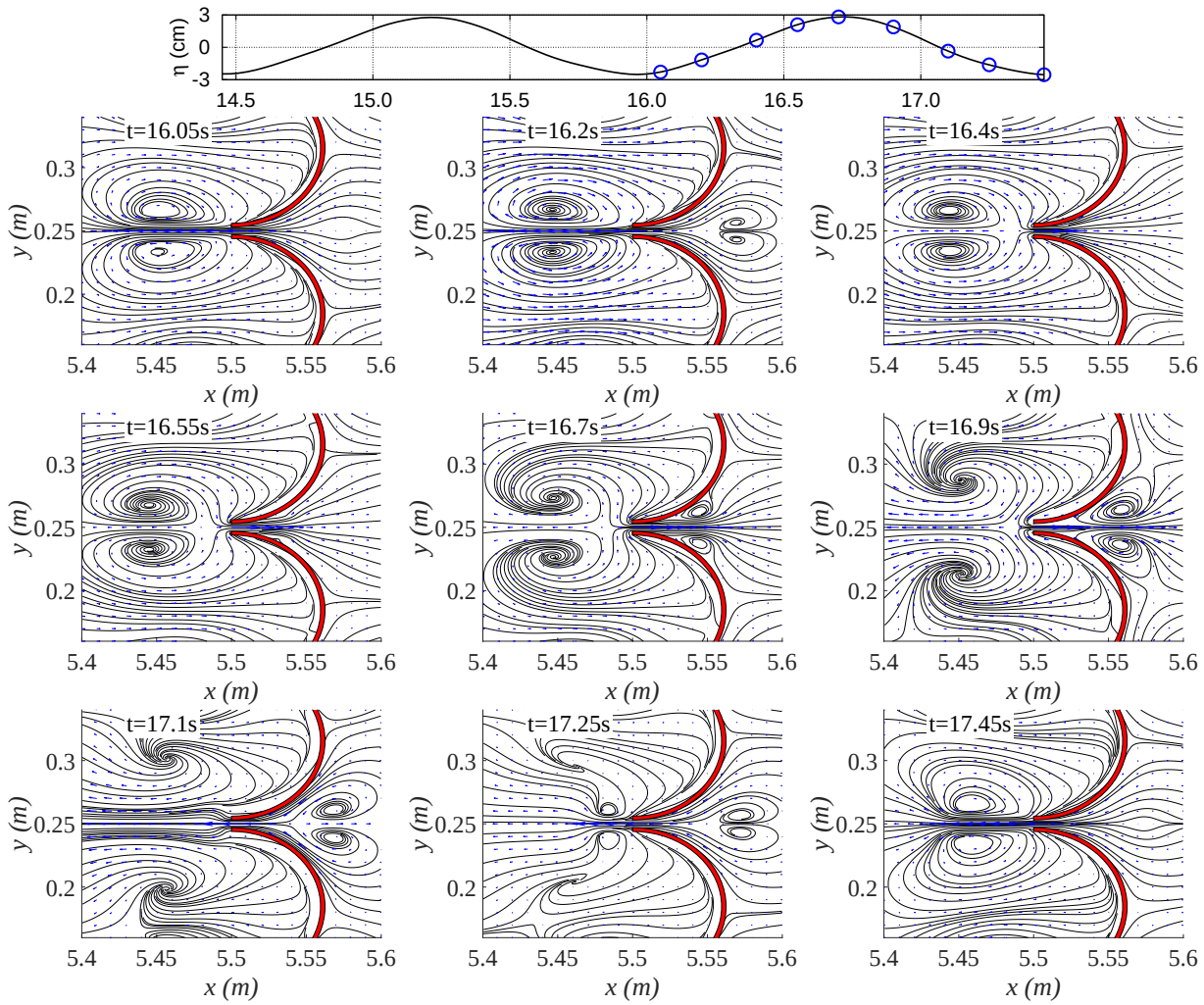

Figure 4.12: The u-w velocity field and sectional streamlines near the back wall of the OWC-pile structure along the slice plane B of a row of closely spaced OWC-piles simulation, showing the test condition T=1.5s.

configuration, despite the existence of weak horseshoe vortex structures, the horseshoe vortex is not the governing factor in sediment scouring around the structure. However, the wake vortices are strong, and for some cases, very persistent. For example, the two large vortices found for $T = 1.1$ s and $T = 1.5$ s are persistent near the bed. It is thus very likely that the wake vortices on the up-wave side of the model can mobilize and redistribute sand, thus influencing sediment transport and scouring. The effect of these wake vortices, combined with the oscillating contraction jet flow in the narrow gap, and the persistent in-flow near the bottom observed in the concave region of the back walls, could lead to significant scouring at the up-wave and down-wave directions of the narrow gaps as well as inside the narrow gaps. Deposition is possible in the concave region formed by the back walls due to the steady streaming effect induced by the persistent in-flow near the bed.

Table 4.2: Computed vortex strengths and normalized vortex strengths for different vortices found in the simulated flow field for different test conditions.

Model	T	KC number	$\frac{S_v^{hs}}{\pi UD}$	$\frac{S_v^{lw1B}}{\pi UD}$	$\frac{S_v^{lw2B}}{\pi UD}$
standalone	0.7	1.02	0.00378	0.0614	0.0130
row	0.7	1.02	0.00378	0.0614	0.0130
row	1.1	1.22	0.00347	1.300	0.195
row	1.5	1.53	0.00321	1.286	0.483

4.6 Summary

Based on the flow visualization for a row of closely spaced OWC-piles presented above, the following conclusions regarding the flow field and scour around the structure can be drawn:

1. Compared to a vertical standalone OWC-pile, a row of closely spaced OWC-piles has a larger and stronger horseshoe vortex at the toe. This is likely due to the enhanced wave motion and blockage effect due to adjacent OWC-piles.

2. Similar to the observation for the case of standalone OWC-pile configuration, the size and strength of the horseshoe vortex system decreases with increasing KC number.

3. The strength of the wake vortices formed near a row of closely spaced OWC-piles is much higher than that found in the case of a standalone OWC-pile. This is mainly due to a difference in the mechanism of how these wake vortices are formed. For a row of closely spaced OWC-piles, the vortices are formed by the flow separation of the oscillating contraction jet flow in the narrow gaps, which has a significantly larger flow velocity than the flow responsible for the generation of wake vortices in the case of a standalone OWC-pile.

4. Similar to the conclusions drawn for a standalone OWC-pile, the horseshoe vortex systems are too weak to be the main driving force for local sediment scour. Instead, the very strong wake vortices formed by the contraction jets can effectively suspend and transport sediment particles, causing significant scour both up-wave and down-wave of the structure. This indicates that apart from the expected strong scouring within the narrow gaps, scour depth on the up-wave and down-wave of the narrow gaps could be also very significant, and the size of scour may be dependent on the size of the wake vortices.

5. A persistent inflow towards the concave region of the back wall is found for all examined wave conditions. This inflow may contribute to possible sediment deposition in this concave region. However, unlike the standalone OWC-pile case, where steady streaming formed by these persistent flow patterns could be the controlling factor in the local scour, in the case of a row of closely spaced piles, the effect of persistent flow is obvious, but it cannot be the

controlling factor. This is mainly due to the very strong effect of the contraction jet flow and the consequential wake vortices.

The results presented in this chapter can be used to facilitate the design of subsequent laboratory experiments studying the local scour around a row of closely spaced OWC-piles and numerical simulations of the same topic using a three-phase rheology based model. The current understanding about the flow structure and its influence on sediment transport can also help optimize mesh and identify points of interest in these subsequent sediment scour investigations. Moreover, further investigations are needed on the energy balance for a row of closely spaced OWC-piles in waves, which involves quantification of the wave energy lost due to vortex dynamics and turbulent kinetic energy.

CHAPTER 5
AN EXPERIMENTAL STUDY OF SCOUR AROUND A ROW OF CLOSELY SPACED PILES: SOLITARY WAVES

This chapter is based on the author's manuscript submitted to Applied Ocean Research: "C. H. Xu, Z. H. Huang, and Y. Yao. A wave-flume study of scour at a pile breakwater: solitary waves. Applied Ocean Research, 82:89-108, 2019."

The aim of the work presented in this chapter is to study the scour process around a pile breakwater in the form of a row of closely spaced piles without OWC devices in a tsunami event. The purposes of this study are to: (1) provide understanding on scouring around a row of closely spaced piles when OWC devices are not present; and (2) serve as a first step towards the numerical simulation of the scour around a row of closely spaced OWC-piles as proposed and tested in chapter 3. This work will provide experimental data for the purpose of validating a three-phase numerical model for sediment transport and wave energy extraction. Solitary waves are used in this study as a proxy for tsunami waves due mainly to the good repeatability of solitary waves generated in laboratory conditions, as well as the relatively fast development of scouring, which is beneficial in a numerical simulation as it saves computational time.

5.1 Introduction

Scour around structures built in a coastal erodible bed is an important phenomenon that influences the foundation stability of various coastal structures. Vertical-pile or pile-group structures are commonly seen marine structures in engineering practice, such as offshore wind turbine monopiles, pile breakwaters, and slotted wave screens. The presence of such structures in a wave field changes the local flow pattern, creates high flow velocity locally and enhances turbulence intensity, which in turn amplifies the bed shear stress and enhances the local scour around the vertical piles. Survivability of the structure during extreme events such as tsunamis and storm surges is an important factor to consider when designing coastal structures. Field surveys and laboratory experiments have shown that the combined effect of enhanced local scours and heavy hydrodynamic loading may have been responsible for the failures of some coastal structures (Tonkin et al., 2003; Nakamura et al., 2008; Chen et al., 2013). Modeling these extreme events in wave flume tests is a challenge because of the long spatial and temporal scales associated with these events. Historically, solitary waves have been used to mimic tsunami waves in wave flume tests.

There is a rich literature in local scour around vertical-pile structures in steady current or regular waves (Zhao et al., 2010; Roulund et al., 2005; Sheppard et al., 2004; Amini et al., 2012; Sumer and Fredsöe, 2001a; Baykal et al., 2017), there are also studies on the tide-induced scour around vertical

pile structures (McGovern et al., 2014; Sumer et al., 1992b; Escarameia and May, 1999). The complex interaction between near-field turbulence structures and particles that effectively enhances bed shear stress is studied experimentally and theoretically by Mattioli et al. (2012) and Manes and Brocchini (2015) for single vertical or horizontal piles among other studies. Scour develops when the bed shear stress, which is affected by the thickness of the bottom boundary layer (Sumer et al., 1992a), exceeds critical bed shear stress at the bed. Both the near-bed turbulent flow condition and bed roughness which is related to the particle size distribution (Raudkivi and Ettema, 1983) can affect the thickness of the bottom (wave or current) boundary layer (see Part III of CEM, 2002). For the scour around a single vertical pile in steady or oscillatory flow conditions, the main nearfield turbulent flow feature that controls the sediment scour around a vertical pile has been identified as the horseshoe vortex (Melville and Raudkivi, 1977; Ahmed and Rajaratnam, 1998; Qadar, 1981): horseshoe vortex significantly enhances the bed shear stress around the structure(Sumer et al., 2002). Experimental observations of steady current scour around a single vertical pile and the flow around it have highlighted the geometric or dynamic relationships between the horseshoe vortex at equilibrium and the equilibrium scour hole: Muzzammil and Gangadhariah (2003) reported that the horseshoe vortex is about 20% the size of the vertical pile at initial formation. After the scour hole is deeper than 20% of the size of the pile, the primary horseshoe vortex grows linearly in size along with the increase of the scour depth and remains fully buried within the scour hole (Unger and Hager, 2007; Kirkil et al., 2008). For a typical sand particle size distribution, the equilibrium scour depth around a single vertical pile can be predicted based on the assumption that at equilibrium, the maximum scour depth is similar to the size of the horseshoe vortex at the toe (Qadar, 1981; Manes and Brocchini, 2015). Manes and Brocchini (2015) proposed a theory, that utilizes the method of phenomenology of turbulence and a canonical assumption that the characteristic length scale of the horseshoe vortex approximates the depth of the scour hole. They are able to predict equilibrium scour depth under steady current condition well in comparison with experiment findings, highlighting the close relationship between scour profile and horseshoe vortices. At equilibrium, the horseshoe vortex size is similar to the size of the vertical pile, therefore the equilibrium scour depth in steady flow over a sand bed of typical particle size was found to be in the range of 1.0 to $1.5D$ by numerous experimental studies (Breusers et al., 1977; Sumer et al., 1992a,b), where D is the diameter of the cylinder. For a single pile in pure waves or waves on a current, the equilibrium scour depth is known to be limited by the Keulegan-Carpenter number (KC number), which describes the relative importance of the drag force over the inertia force acting on a body in an oscillatory fluid flow, and is smaller than that under steady current conditions (Sumer et al., 1992a; Sumer and Fredsöe, 2001a; Sumer et al., 2002; Ong et al., 2013).

Major relevant experimental studies found in the literature are listed in Table 5.1. In particular, Sumer et al. (1992b); Sumer and Fredsöe (2001a) reported a laboratory experiment investigating the scour around a standalone vertical circular cylinder in currents and regular waves with moderate

to large KC numbers. For larger KC numbers, the horseshoe vortex induced by the local down streaming and lee wake vortex was responsible for local sediment suspension and the sediment removal from around the vertical pile. The equilibrium scour depth obtained under oscillatory flow conditions approach those obtained under unidirectional current conditions (Sumer et al., 1992b). For smaller KC numbers (for example, $KC < 1.0$), the scour is mainly attributed to the steady streaming effect (Sumer and Fredsöe, 2001a). Sumer et al. (1992b) also proposed an empirical formula for predicting the evolution of the scour depth.

For a given layout of a group of piles, the influence of neighboring piles disappears and all the knowledge obtained for a single pile can be applied to the local scour at a pile in a group when the distance between pile is larger than a certain distance, usually when $n = G/D > 2 - 4$ (Sumer and Fredsöe, 1999; Ataie-Ashtiani and Beheshti, 2006; Amini and Solaimani, 2017) where G is the gap size and n is the gap-diameter ratio; however, the local flow near a pile can be affected by the presence of neighboring piles when the distance between piles is smaller than a critical distance (Sumer and Fredsöe, 1999; Ataie-Ashtiani and Beheshti, 2006; Amini et al., 2012; Lanca et al., 2013). The value of this critical distance is known to be affected by the incoming flow condition and layout of the piles (Zdravkovich, 1987). For example, for side-by-side arrangements, the scour depth first increases with reducing the gap size between adjacent piles, then decreases after reaching a maximum at $n \approx 0.3$ as the gap size continues to reduce, and eventually the scour depth approaches that for a single pile with an equivalent diameter when the gap size is very small (Sumer and Fredsøe, 1998). For a pile breakwater consisting of a row of closely spaced slender piles in regular waves, Hayashi et al. (1969) found that the scour depth is strongly related to the ratio of the jet flow velocity in the gap and the fall velocity of the sediment particles, they found the scour depth around the closely spaced piles in regular waves reached 1.5 to 2 times the diameter of piles, exceeding the maximum values observed in case of a single pile even in steady currents. It is worth noticing that in the experiment of Hayashi et al. (1969), artificial particles instead of natural quartz sand was used as sediment particles, and only equilibrium scour depth was provided.

The pile layouts of major existing laboratory tests on the scour at a group of piles are summarized in Table 5.2, from which it can be seen that the pile-group layouts in all but one existing studies are three dimensional (i.e., the pile groups are not long enough so that the influence of the two ends of the group is negligible to the center ones). In particular, Sumer and Fredsøe (1998) conducted laboratory tests investigating the scour around 3-D circular pile groups in regular waves. Several 3-D group layouts, including side-by-side, tandem and staggered pile groups were tested (while only the side-by-side case is shown in Table 5.2). A range of gap-diameter ratio of n=0.01 to 3.0 was tested and it was found that for smaller gap-diameter ratios (for example, for a gap-diameter ratio $n < 0.1$), the pile group behaved like a single pile with an increased diameter. For larger gap-diameter ratios (e.g., $n > 2$), the influence of neighboring piles diminishes and the piles in the pile group behave like standalone piles. As the sole study that has investigated closely

spaced piles, Sumer and Fredsøe (1998) found that for similar gap-diameter ratio ($n < 0.5$), a row of two piles in side-by-side arrangement had shallower equilibrium scour depth compared to a row of three piles in side-by-side arrangement, which may be due to the influence of the enlarged area of bed exposure to the pile group in the latter case. Sumer and Fredsøe (1998) reported that for a short row of closely spaced side-by-side piles in a normal wave condition, the maximum equilibrium scour depth reaches about $0.83D$, which is significantly smaller than that in a steady current. It is expected that under local extreme conditions such as tsunami waves, the scour depth should be deeper than that in a normal wave condition. Although Sumer and Fredsøe (1998) highlighted the difference between a standalone pile and pile group in wave conditions, no information was provided for: (i) highly nonlinear waves such as solitary waves; and (ii) possible end effects of the piles at both ends on the middle piles in a pile group of finite width.

Compared to the rich literature in the local scour around vertical piles under steady current and regular waves, research on local scour at pile structures due to highly nonlinear waves such as solitary waves is scarce (Madsen et al., 2008; Sumer et al., 2011). Tonkin et al. (2003) conducted laboratory tests investigating the local scour at a standalone vertical circular pile under the action of solitary waves. The pile was placed on a 1:20 slope sandy beach model, near the still-water shoreline. Nakamura et al. (2008) reported an experimental study of the solitary-wave induced local scour at a square pile sitting on a dry sandy beach close to still water shoreline. The results showed that the scour depth around the structure was related to the incident solitary wave height and the depth of the pile foundation. Some of the key scour patterns observed in post-tsunami field survey in Kalapakkon (India) and Banda Aceh (Indonesia) after the 2004 Sumatra-Andaman earthquake tsunami were reproduced in the experiment. Experimental investigations found that pore pressure may induce a reduction of the effective stress, which may enhance scouring during the back-wash process (Tonkin et al., 2003; Sumer et al., 2011).

Local scour around vertical structures due to solitary wave is different from that due to steady or tidal current because the flow associated with solitary waves is not steady. There are significant changes in flow speed and depth in a relatively short period of time during the passage of a solitary wave. It is also different from that due to regular waves or oscillatory flow in that solitary waves are unsteady but not periodic. Because the unsteady velocity of a solitary wave is unidirectional, there is no periodic two-way formation and destruction of wake vortex and horseshoe vortices. It is not clear whether or not a parameter similar to the KC number can be defined for solitary waves. A major difference between a 3-D pile group (or a single pile) and a pile breakwater (a 2-D pile group) is the blockage effect of the pile breakwater and the resulting strong flow in the gaps of a pile breakwater, which is expected to enhance the scour depth and shorten the time required to reach the equilibrium. Compared to the abundant literature on the hydrodynamics of pile breakwaters (e.g., Kakuno and Liu, 1993; Suh et al., 2011; Huang et al., 2011), less work has been done on the scour at pile breakwaters, which is important for the survivability of such coastal structures during

extreme wave events such as tsunamis and storm surges.

In the following, a description of the pile breakwater, experimental setup and test conditions is given in section 5.2. Effects of wave height and water depth on the evolution of scour-hole pattern and scour-hole characteristics are discussed in section 5.3. An analysis of the equilibrium scour depth is presented in section 5.4. Major scour profile characteristics are summarized in section 5.5. Main conclusions are listed in section 5.6.

Table 5.1: A summary of existing experimental studies related to scour around vertical piles.

Authors	Structure type	Flow type	Key parameters
Hayashi et al. (1969)	Pile groups	RW	$T = 1.7$ s $h = 29.1$ cm $H = 2.68 - 9.37$ cm $D = 0.065$m; $d_{50} = 0.34 - 0.75$mm
Zhao et al. (2010)	Submerged piles	SC	$h = 0.5$m; $D = 0.1$m; $d_{50} = 0.4mm$; $U = 0.362 - 0.441$m/s
Sumer and Fredsøe (1998)	Pile groups	RW	$h = 0.4$m; $D = 0.032 - 0.09$m; $d_{50} = 0.2$mm; $T = 1.8 - 4.5$s; $KC = 3.0 - 37$
Sumer and Fredsöe (2001b)	Large standalone pile	RW	$h = 0.4$m; $D = 0.54 - 1.53$m; $d_{50} = 0.2$mm; $T = 2.0 - 3.5$s; $H = 2.5 - 12.0$cm; KC<1.4
Roulund et al. (2005)	Standalone pile	SC	$h = 0.4$m; $D = 0.1$m; $d_{50} = 0.26$mm; $U = 0.46$m/s
McGovern et al. (2014)	Standalone pile	SC/TC	$h = 0.1 - 0.4$m; $D = 0.2$m; $d_{50} = 0.135$mm; $U = 0.15 - 0.31$m/s; $T_{tide} = 54$min
Baykal et al. (2017)	Standalone pile	SC/RW	$D = 0.04$m; $d_{50} = 0.17$mm; $h = 0.4$m; $U = 0.413$(Current); $T = 1.79 - 4.0$s
Amini et al. (2012)	Pile group	SC	$h = 0.24$m; $D = 0.06$m; $d_{50} = 0.8$mm; $U = 0.3534 - 0.3645$
Sumer et al. (1992b)	Standalone circular pile	RW SC/TC	h=0.4m; D=0.01-0.2m; $d_{50} = 0.18 - 0.38$ mm; $T = 1.19 - 3.57$s; $KC = 4.9 -$ inf

Table 5.1: A summary of existing experimental studies related to scour around vertical piles.

Authors	Structure type	Flow type	Key parameters
Escarameia and May (1999)	Standalone pile	TC	$h = 0.0375 - 0.075$m; $d_{50} = 0.75$mm; $U = 0.239 - 0.430$m/s; D =various
Sheppard et al. (2004)	Standalone large pile	SC	$h = 0.18 - 1.19$m; $D = 0.114 - 0.914$m; $d_{50} = 0.22 - 2.90$mm; $U = 0.29 - 0.76$m/s
Nakamura et al. (2008)	Standalone large pile	SW	$h = 0.265 - 0.315$m; $D = 0.14$m; $H = 0.2 - 0.7$m; $d_{50} = 0.2 - 0.45$mm
Tonkin et al. (2003)	Standalone pile	SW	$h = 2.45$m; $d_{50} = 0.35$mm; $D = 0.5$m; $H = 0.1 - 0.3$m
Chiew and Melville (1987)	Standalone pile	SC	$h = 0.17$m; $D = 0.0318 - 0.045$m; $d_{50} = 0.24 - 3.2$mm
Lanca et al. (2013)	Pile groups	SC	$U = 0.31$ m/s $h = 0.20$m; $D = 0.05$m; $d_{50} = 0.86$mm
Ataie-Ashtiani and Beheshti (2006)	Pile groups	SC	$U = 0.21$ m/s $D = 0.016 - 0.028$m; $d_{50} = 0.25 - 0.98$mm
Amini and Solaimani (2017)	Pile groups	SC	$U = 0.31$ m/s $D = 0.04$m; $d_{50} = 0.9$mm
Melville and Chiew (1999)	Standalone pile	SC	$h = 0.02 - 0.2$m; $D = 0.016 - 0.2$m; $d_{50} = 0.90 - 5.35$mm; $U = 0.171 - 1.00$m/s

Table 5.2: A summary of the pile layouts in the existing studies involving more than two piles.

No.	Authors	Model layout	Gap-diameter ratio	Comments

1	Zhao et al. (2010)	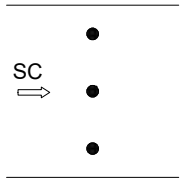	$n = 12.5$	Submerged
2	Sumer and Fredsøe (1998)		$n = 0.0 - 3.0$	Emergent
3	Amini et al. (2012)	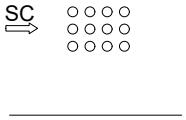	$n = 2.0 - 4.5$	Emergent
4	Ataie-Ashtiani and Beheshti (2006)		$n = 0.0 - 6.0$	Emergent
5	Lanca et al. (2013)	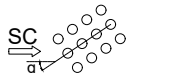	$n = 0.0 - 5.0$	Emergent
6	Amini and Solaimani (2017)	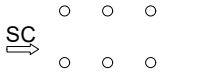	$n = 0.0 - 5.0$	Emergent
7	Hayashi et al. (1969)	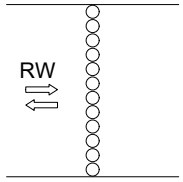	$n = 0.041 - 0.20$	Emergent
8	Present Study	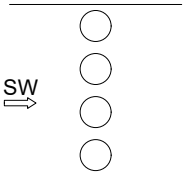	$n = 0.389$	Emergent

5.2 The pile breakwater model, experimental set up and test conditions

5.2.1 Experimental set up

Referring to Fig 5.1, the circular pile breakwater model is made of perspex. The model consists of a base plate, a top plate, and four circular tubes. The width of the model is 0.495 m, slightly smaller than that of the wave flume. The diameter of each tube D is 0.09 m. The width of the wave flume is 0.5 m and the width of gaps between two adjacent piles is 3.5 cm, resulting in a gap-to-diameter ratio of 0.39. Each vertical circular pile has two sections: a lower section and an upper section. The lower section has a height of 25 cm, and is firmly glued to the base plate; the upper section is connected to the lower section via a specially designed "cross-connector", and the top plate is mounted to the top of circular piles via similar cross-connectors. The overall height of the model is the same as the flume depth so that the top plate can be firmly fixed onto the side rails of the wave flume using clamps. The use of clamps and cross-connectors is to ensure that: (i) the model is stiff enough to withstand wave loading, and (ii) the upper section can be easily disassembled without causing disturbance to the sand bed for bed profile measurement using a laser scanner.

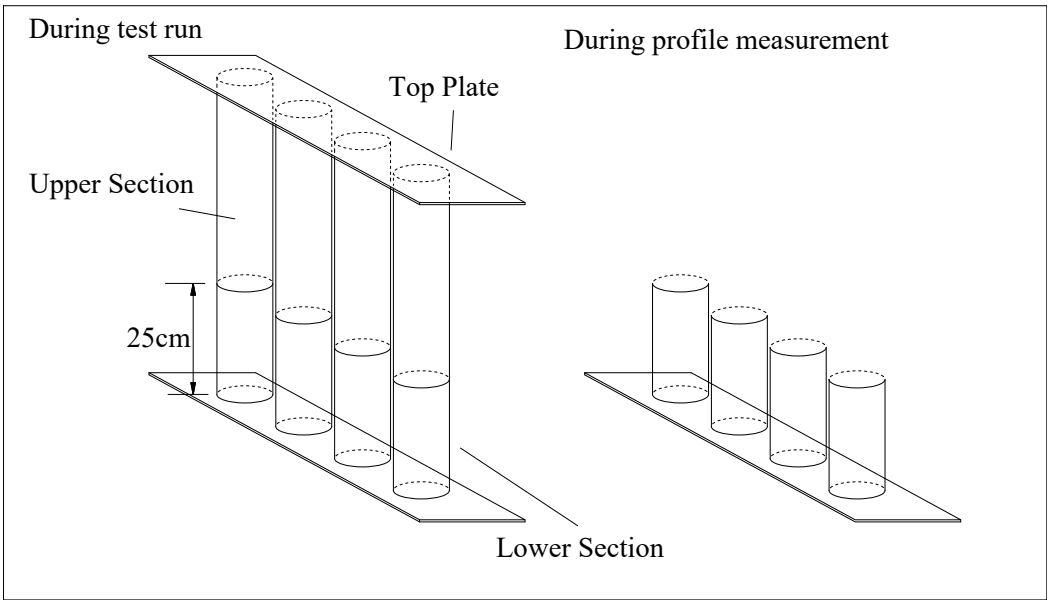

Figure 5.1: Sketch of the pile breakwater model. Left panel shows the model with the top section when running solitary waves, and the right panel shows the model without the top section when measuring the bed profile using the underwater laser scanner.

The model shown in Figure 5.1 was tested in a wave flume in the Hydraulic Laboratory at the Changsha University of Science and Technology, China. A sketch of the experimental set up is shown in Fig 5.2. The dimensions of the wave flume are 40-m long, 0.5-m wide and 0.8-m deep.

At one end of the wave flume, a piston type wave maker is installed; at the other end of the wave flume, a 1 : 10 wave absorbing beach is installed to reduce wave reflection. The wave absorbing beach is covered by a layer of porous material to further reduce wave reflection from the beach. The weak reflected wave coming from the absorbing beach is not able to cause any change in the bed profile in this study. In order to eliminate multiple reflections of the generated solitary wave between the paddle of the wave maker and the breakwater model, a special wave-blocking plate is designed and installed at 8 m from the paddle. The operation and effect of the wave-blocking plate will be further explained in section 5.2.2.

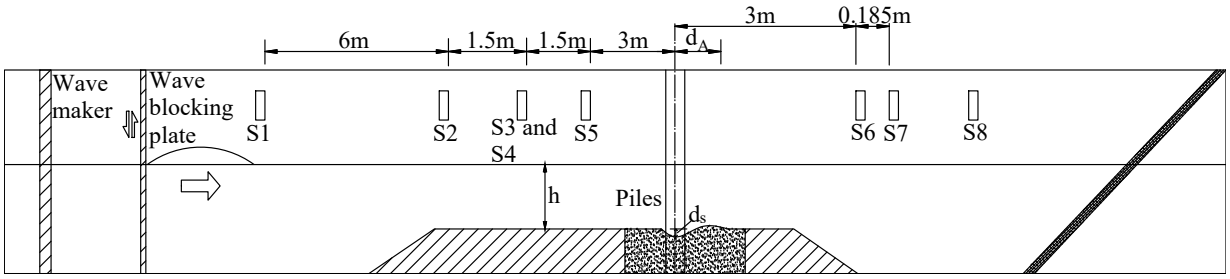

Figure 5.2: Sketch of Experimental setup

Because the wave making paddle itself is almost perfectly reflective, multiple reflections will exist between the model and the paddle if no special measures are implemented to remove the wave reflection from the paddle. To eliminate the reflected wave coming from the wave paddle, a special wave blocking system is designed (refer to Figure 5.2) and installed, which prevented the re-reflection of the wave coming from the model. This wave blocking system is operated as follows:

1. The wave blocking plate is first lifted from water to a height that allows the passage of the generated solitary wave.

2. After the water surface inside the wave flume is free from any sensible residual waves (this usually means allowing a waiting time of at least 4 minutes), a solitary wave is generated. This is to ensure the quality and repeatability of the solitary waves generated for the same test condition.

3. When the reflected wave coming from the model has just passed the wave blocking plate, the wave blocking plate is lowered down immediately so the that the reflected solitary wave coming from the model is trapped between the wave paddle and wave blocking gate. This can prevent the multiple reflections between the model and the wave paddle.

4. Only after the solitary wave trapped between the wave paddle and the wave blocking plate diminishes can the wave blocking plate be lifted again for generating the next solitary wave.

The circular pile breakwater model is placed 22.6 m from the wave generator. To create a 1.9 m long and 0.2 m deep sand bed (or sand pit) for installation of the breakwater model, two false bottoms are used. The false bottom on the up-wave side of the sand pit is 20 cm high, with a $1:5$ slope and a flat section. The total length of the false bottom on the up-wave side of the pile breakwater is 5.8 m. The length of the sand bed on the up-wave side of the model is 0.8 m. The length of the sand bed on the down-wave side of the model is 1.2 m, which is long enough for the scour hole to develop without being interfered with by the end on the down-wave side. The total length of the elevated sand bed and the false bottom on the up-wave side of the model is 6.6 m, which helps the incident wave to deform and stabilize before reaching the model. The sand pit is filled with natural beach sand of diameter $d_{50} = 0.25$ mm and a specific weight of $\gamma = 2.6$. Note that in this experiment the water depth h is specified as the one measured from the false bottom, therefore the actual water depth at the wave maker is the water depth h plus the height of the false bottom (20 cm), as shown in Fig 5.2.

After finishing each test run, the sand bed is returned to a flat bed condition using a perspex sheet board. Eight Ultralab ultrasound sensors (S1 to S8) are used to monitor the water surface. Referring to Figure 5.2, S1 is placed 12 m on the up-wave side of the breakwater model to measure the incident wave; S2, S3 and S4 are placed 6 m, 4.5 m and 3 m, respectively, on the up-wave side of the breakwater model to monitor the wave deformation and reflection by the false bottom and the model; S5 is placed 4.5 m on the up-wave side of the breakwater model, parallel to S3 with a distance of 0.15 m in between to monitor the lateral variation of the waves inside the flume; S6 and S7 are placed 3 m and 3.185 m, respectively, on the down-wave side of the breakwater model, respectively, to monitor the wave reflected from the wave absorbing beach, and S8 is a redundant gauge.

In order to measure the 3-D sand bed profile near the pile model, an underwater laser scanner (2GRobotics ULS-100®) is used to scan the sand bed profile. Prior to actual measurement, the upper section of the model is removed so that only the lower section of the model is left in the sand bed (see the right panel of Figure 5.1). Due to the limitation in the size of the area that the scanner can cover, the entire bed profile is a combination of $12 - 18$ scanned patches. In order to ensure the accuracy of the final profile after combining measurement patches, the lateral scanner positions are precisely determined using a high-precision measurement bridge and the longitudinal positions of the bridge are determined on a ruler with a spatial accuracy of less than 1 mm. Figure 5.3 shows a photo of the underwater laser scanner during one test run.

The accuracy of the underwater laser scanner deteriorates when measuring regions very close to the narrow gaps formed by the piles because of the inevitable "laser footprint error", which is due to the unwanted reflection of laser beam from the model. The laser footprint error or "edge effect" may be induced when scanning sharp edges, this may lead to erroneous measurements near sharp edges, such as the edge of the lower portion of the pile model. In the present experiment,

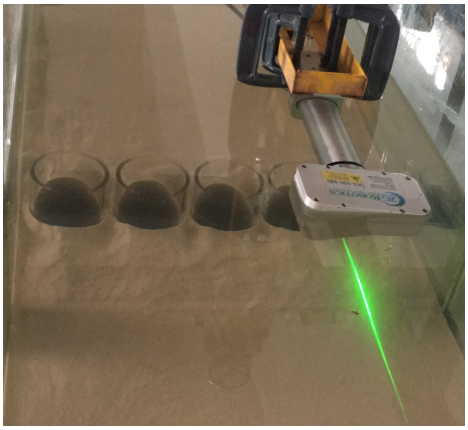

Figure 5.3: A photo of the laser scanner measuring bed profile near the disassembled row of piles.

another source of error may also be present, which is the refraction of laser beams through the perspex layer of the pile model. To provide data in the regions affected by the laser footprint error, a point probe was used in the experiment to supplement data inside the narrow gaps by measuring the scour depth at fixed locations inside the gap.

In the following we describe how these two sources of error occur when measuring bed profile near the edge of the lower portion of a pile and in region between two piles. As shown in Figure 5.4, the laser scanner has two optical parts: the laser emitter shown in the figure as the right arm of the laser scanner, and the receiver lens, which is the left arm of the laser scanner. The laser beam emitted from the scanner is labeled as beam A. We illustrate here the two sources of error based on two scenarios shown in Figure 5.4.

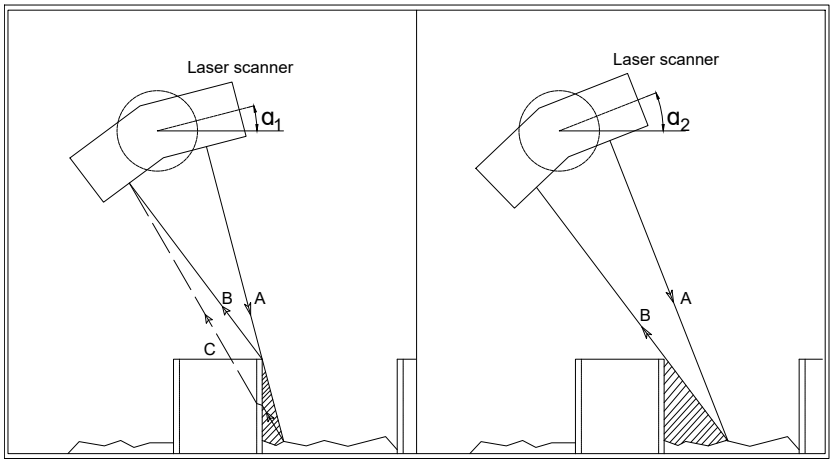

Figure 5.4: An illustration of the optical path of the laser scanner near the lower portion of the piles.

The first scenario is shown in the left panel of Figure 5.4. When the laser beam A reaches the bed profile, the reflected light as seen by the receiver window is a combination of the refracted beam C and the reflected beam B coming from the top edge of the lower portion of the pile. Therefore, the scanned profile in the small shadowed region is erroneous with inaccurate points from beam C and wrong points from beam B. The other scenario is shown in the right panel of Figure 5.4. When beam A from the laser emitter reaches the bed profile, and the reflected beam B reaches the receiver lens without being blocked, refracted or reflected by the pile, in this scenario it can provide reliable measurements. It is clear that the region in the shadow is erroneous. As the scour hole gets deeper, the size of the shadowed region increases.

5.2.2 Test conditions and procedure

Solitary waves are used in this study as a proxy for tsunami waves due mainly to the good repeatability of solitary waves generated in the laboratory condition. As pointed out by Madsen et al. (2008), solitary waves as a proxy for tsunami waves are able to capture some of the physical phenomenon found in a typical tsunami event (Yeh et al., 1994; Briggs et al., 1995; Liu et al., 1995) but it also suffers from scale issues. Compared to real tsunami waves, solitary waves tend to have too high non-linearity and are much shorter in both temporal and spatial scales. Because it is not possible to generate a wave in a wave flume that satisfies all similarity requirements, scale distortion has to be accepted in experimental studies of tsunami-related problems, which is especially true when studying tsunami-induced sediment transport because it is impossible to scale tsunamis properly in the laboratory such that sensible sediment transport can be generated (Yeh et al., 1994; Chen et al., 2012). To partially solve this issue, some recent studies of tsunami-induced local scours have used multiple solitary waves to compensate for the short duration due to the use of solitary waves (Young et al., 2010; Chen et al., 2012). Even though dam-break waves or moving bores have also been used in the past as a proxy for tsunami waves to study tsunami-induced runup (Rossetto et al., 2011; Shafiei et al., 2016), this approach may pose a serious problem in the repeatability of the results since they are much less controllable than solitary waves. Nakamura et al. (2008) reported that solitary waves were able to capture tsunami-wave induced sediment scour patterns, indicating that application of solitary wave to study tsunami-induced scour is still at least plausible.

A summary of the test conditions is given in Table 5.3, where u_* is the shear velocity, θ is the Shields parameter calculated using u_* and the equivalent period T_s for a solitary wave (Goring and Raichlen, 1980; Huang and Yuan, 2010) is calculated by

$$T_s = 4\pi\sqrt{\frac{h^3}{3gH(h+H)}} \tag{5.1}$$

where h is the local water depth at the model, H the incident wave height, and g the gravitational

acceleration. The calculation of the shear velocity u_* will be given in Section 5.4.

Table 5.3: Test Conditions

Case	h(m)	H(m)	h/D	H/D	T_s (s)	u_* (m/s)	R_e	θ
1	0.25	0.06	2.778	0.667	2.12	0.030	3.08×10^4	0.227
2	0.25	0.04	2.778	0.444	2.69	0.024	2.16×10^4	0.142
3	0.25	0.08	2.778	0.889	1.78	0.034	3.85×10^4	0.277
4	0.23	0.06	2.556	0.667	1.94	0.031	3.18×10^4	0.231
5	0.20	0.06	2.222	0.667	1.66	0.031	3.51×10^4	0.241

In Table 5.3 the Reynolds number Re is defined as

$$Re = \frac{U_m D}{\nu} \tag{5.2}$$

where D is the diameter of the pile and U_m is the maximum velocity in a solitary wave, calculated using the solitary wave theory of Grimshaw (1971). The wave heights listed in Table 5.3 are target wave heights used to prepare input files for wave maker. The actual measured incident wave height may slightly differ from the target value, within a maximum difference of 5%.

The typical water depth for prototype pile breakwaters is slightly less than 10 m. Take h=10 m for prototypes and h=0.25 m for the model as an example, the geometrical scale is about 40. The maximum height of tsunami targeted in this study is about 3.2 m at a water depth of 10 m.

5.3 Results and discussion

In this section, the experimental results will be presented in dimensionless forms: all lengths are non-dimensionalized using pile diameter D; and all time dimensions are non-dimensionalized using the following time scale T_0 (Sumer et al., 1992b):

$$T_0 = \frac{D^2}{[g(\gamma - 1)d^3]^{1/2}} \tag{5.3}$$

where γ is the specific weight of the sand, and all volumes are non-dimensionalized using $\pi D^3/4$.

5.3.1 Measured surface elevations

An example of the temporal variation of the water surface measured by the Ultralab sensor S1 for a target wave height of $H/D = 0.667$ is shown in Figure 5.5, where the theoretical profile using the solitary wave theory of Grimshaw (1971) is also included for comparison. The measured wave front agrees well with the theoretical solitary wave profile; however, the tail of the measured wave is slightly steeper than the theoretical one, and a slight set-down in the surface elevation can be observed. This minor difference between the actual measured wave and theoretical solitary wave

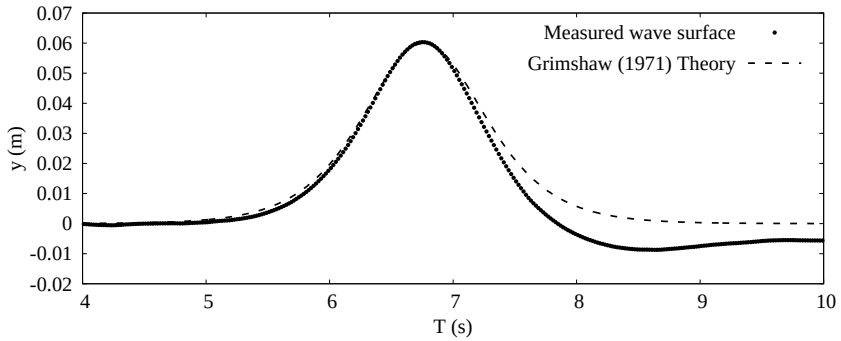

Figure 5.5: A comparison of the measured surface displacement and the theoretical surface displacement of Grimshaw (1971).

has also been observed in other experimental studies involving solitary waves (Chen et al., 2013; Li et al., 2011; Huang and Yuan, 2010).

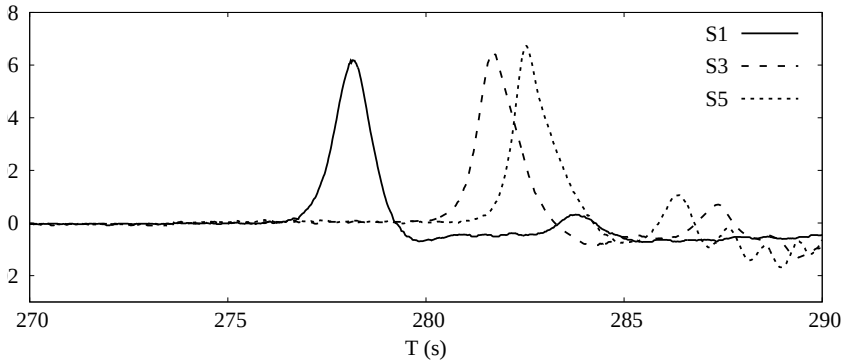

Figure 5.6: Sample time series of a solitary wave signal measured at S1, S3 and S5 in front of the model.

Figure 5.6 shows one example of the surface displacements measured by wave gauges S1, S3 and S5 for h/D=2.556 and H/D=0.667. The shoaling of the incident solitary wave on the false bottom makes the wave front slightly steeper and the back of the wave slightly gentler. An increase of 6.1% in wave height can also be observed from S1 to S5.

Figure 5.7 shows one example of the time series of the surface displacement measured at wave gauge S7 for h/D=2.778 and H/D=0.667. The weak reflected wave is significantly elongated compared to the incident solitary wave. If we define the height of the reflected wave as the difference between the lowest elevation and the highest elevation immediately after the main solitary wave passed the wave gauge S7, the heights of the reflected solitary waves are in the range of 0.2 and 0.3 for all tested waves. If we use the long wave theory to estimate the peak velocity and the wave friction factor (Soulsby, 1997) to estimate the friction velocity, the Shields parameter associated with the reflected wave is too small to cause any sensible scour according to the experimental results

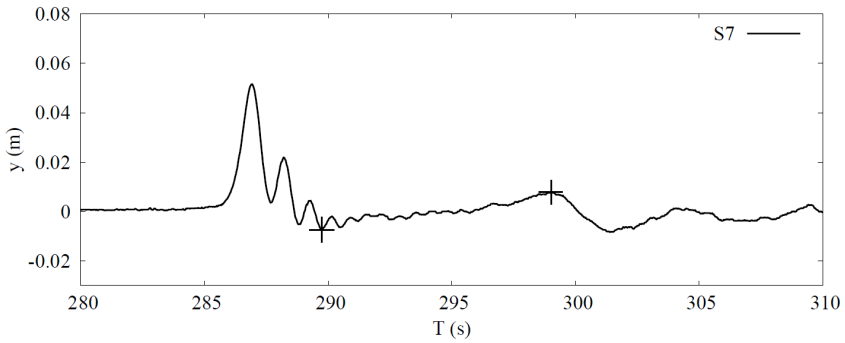

Figure 5.7: An example of water surface elevation behind the model measured by S7. The two + signs indicate the locations used to determine the height of the reflected wave.

of Sumer and Fredsøe (1998) for two/three side-by-side piles with a similar gap-diameter ratio in regular waves.

5.3.2 Change of the bed profile measured by laser scanner

Figure 5.8 shows an example of the scanned 3-D bed profile on the down-wave side of the pile breakwater model for case 2 listed in Table 5.3. The scanned region can only reveal scour patterns at the three gaps away from the two side walls. The scanned bed profile in the regions between the two ends of the pile breakwater model and the two side walls may be affected by the interference between the side walls and the laser beam, and thus are not included in Fig 5.8. During the early stage of the scour process (e.g., after running 7, 13, and 24 waves for the case shown in Figure 5.8), the scour at the central gap is different from that at the adjacent gap on each side due to the sidewall effect. The difference in the scour patterns at the three gaps significantly reduces in the later stage of the scour process. We remark that the difference in the scour patterns at the three gaps due to sidewall effect is not significant in all other test conditions with larger incident wave heights.

Because the bed profile in the gap between two piles may not be accurately measured using the laser scanner, a point gauge is also used to measure the scour depths at nine selected locations between the two piles: three locations are on the A-A transect shown in Figure 5.8; another six on the two sides of the transect A-A with three on each side. Technically, the A-A transect should coincide with the center line of the wave flume. The scour profiles along the A-A transect corresponding to the four results shown in Figure 5.8, which are obtained by combining the data from the laser scanner and the point gauge, are shown in Figure 5.9. It can be seen that the point-gauge data can merge well with the scanned profiles. After running 99 waves, the bed profile along the A-A transect is characterized by a scour hole at the gap and a sandbar on the down-wave side of the pile breakwater. The scour hole deepened with increasing number of solitary waves. Even though solitary wave has a unidirectional velocity, the sand can be removed on both the up-wave

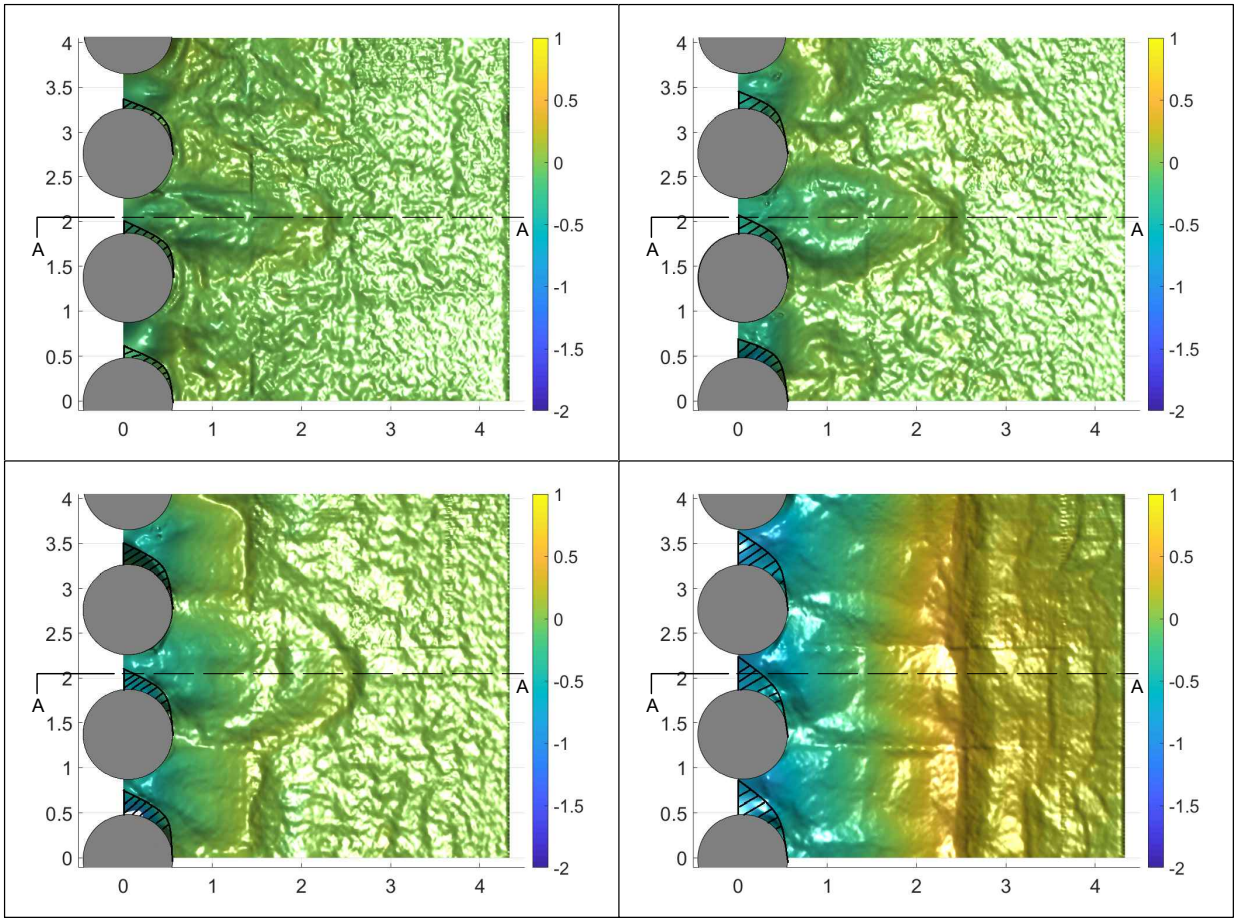

Figure 5.8: Samples of scanned bed profiles taken for Case 2, measured after 7 (top left), 13 (top right), 24 (bottom left) and 99 (bottom right) waves. The shaded regions are affected by the "laser footprint error". All lengths are normalized by D.

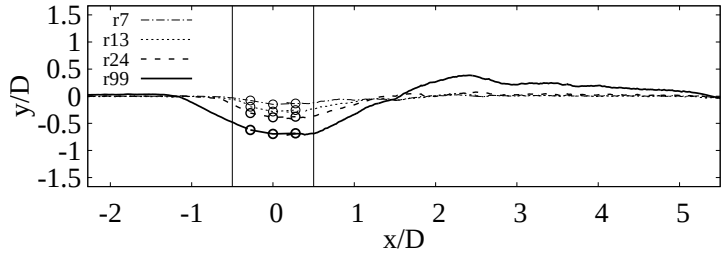

Figure 5.9: 2D bed profiles for Case 2, taken at the transect A-A shown in Fig 5.8. Note that the symbols "o" in the plot represent point gauge measurements.

and down-wave sides of the pile breakwater. However, the sand deposits mainly on the down-wave side of the breakwater, eventually forming a sandbar on the down-wave side of the pile breakwater. Because of the 3D features of scour holes at the pile breakwater, we stress two points here:

1. conservation of mass cannot be evaluated based on the 2-D bed profile along the A-A transect, and

2. maximum scour depth in a scour hole between two piles may or may not occur along the A-A transect.

For later discussion of our experimental results, Figure 5.10 shows a definition sketch of the important dimensions that characterize the scour at a pile breakwater.

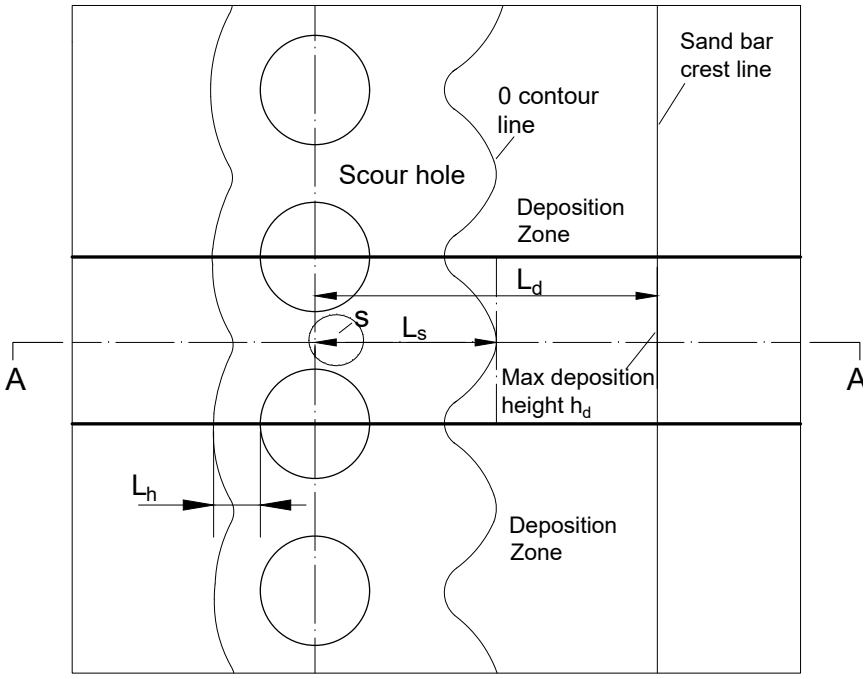

Figure 5.10: A sketch showing definitions of four key characteristic dimensions. The maximum scour hole depth is determined in a small region between two piles, as shown by the dashed oval circle. Not drawn to scale.

For discussing effects of wave height and water depth on bed-profile characteristic dimensions, the following four key characteristic dimensions of scoured bed profile are defined in Figure 5.10:

1. The maximum scour depth s is defined as the deepest location in the scour hole.

2. The length of the scour hole on the down-wave side of the pile breakwater L_s is defined as the distance between the center axis of the pile breakwater to the first zero-contour line on the down-wave side of the pile breakwater.

3. The maximum deposition height h_d is defined as the highest point of the deposition region on the down-wave side of the scour hole. When a sand bar can be clearly identified at the later stage of the scour process, the maximum deposition height is the sand-bar height.

4. The length of the scour hole on the up-wave side of the pile breakwater L_h is defined as the distance between the up-wave edge of the pile breakwater to the first zero-contour line on the up-wave side of the pile breakwater.

When discussing these characteristic dimensions in this section and the scour and deposition volumes in the next section, we only focus on the scour profile within the two bold lines (between the central axis of the second pile and the central axis of the third pile), as shown in Figure 5.10.

The repeatability of the experiment is verified by carrying out repeating tests for the case of $h/D = 2.778$ and $H/D = 0.889$, as reported in section 5.3.6 , where an uncertainty analysis is performed on the measured characteristic dimensions using this set of repeating tests. Only the results with low uncertainty are presented and discussed in the rest of this section.

5.3.3 Effect of water depth and wave height on the 3D scour profile

The development of the 3-D scour profile at the central gap (the region between two thick horizontal lines in Figure 5.10) with the number of solitary waves passing is shown in Figure 5.11 for H/D=0.444 and h/D= 2.778. The scour profiles shown in the Figure 5.11 are the change in the bed elevation obtained by subtracting the initial bed profile from the scoured bed profiles caused by solitary waves passed the pile breakwater. The scour at the pile breakwater shown in the Figure 5.11 is induced by the jet flow through the gap between two adjacent piles. The evolution of the scour profile is characterized by two stages: at the early stage, the scour-hole depth contours are characterized by 3-D U-shaped contour lines. At this stage, the scour hole deepens with an increasing number of solitary waves passing the pile breakwater, and the scour hole formed near a gap has not connected with neighboring scour holes on the two sides. At the later stage of the scour process, the scour hole gradually merges with neighboring scour holes, and the depth contour lines gradually straighten, and eventually, a sandbar forms some distance on the down-wave side of the scour hole. The zero contour line in the scour profile separates the scour hole and the sandbar. When the scour hole approaches its maximum depth, the slope between the scour hole and the sandbar approaches the angle of repose.

Figure 5.12 shows the development of the 3-D scour profile at the central gap for H/D= 0.667 and h/D= 2.778. From this figure, conclusions similar to Figure 5.11 can be drawn, except that the time required for the scour holes to connect with neighboring scour holes reduces with increasing wave height.

The time required for a scour hole to reach its equilibrium state will be discussed later in Section 5.4, where it will be shown that after running 99 waves, the scour hole has almost reached its equilibrium state. Near the equilibrium state, the slope at the edge of the scour hole approaches the angle of repose, and the location of the zero-contour line representing the edge of the scour hole has less measurement error as compared to that at the initial stage of the scour process (refer to section 5.3.6 for details).

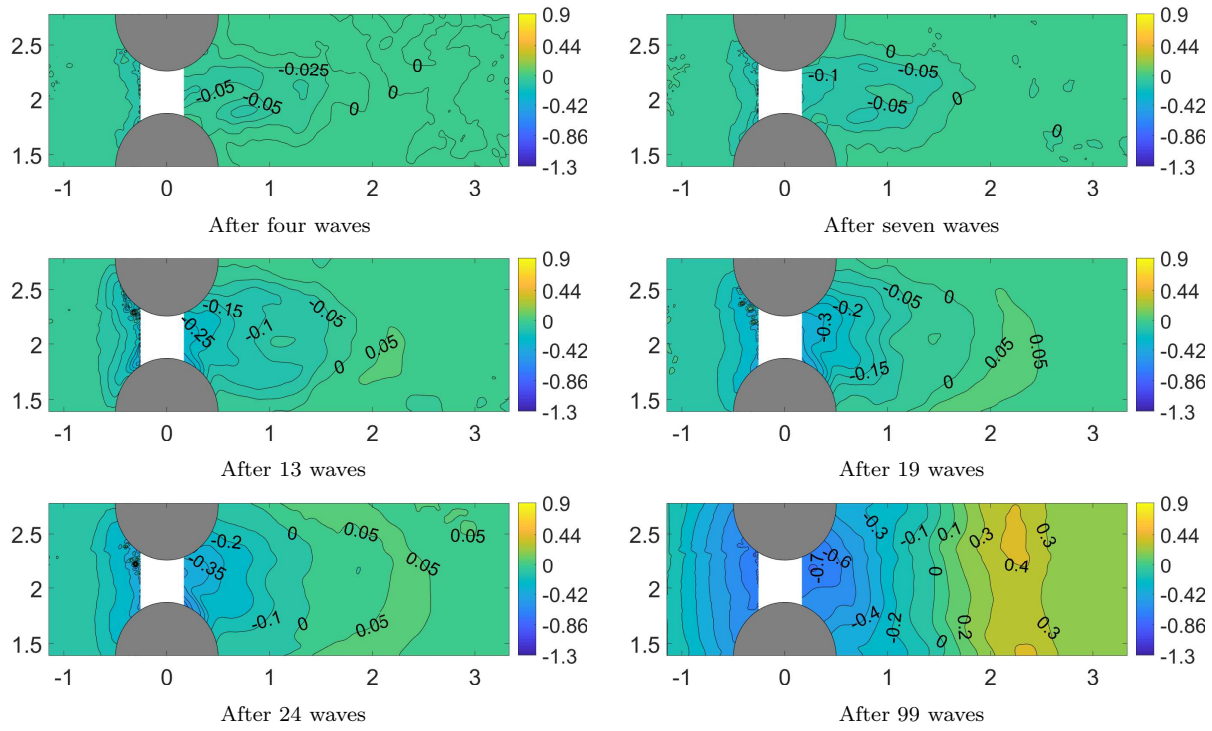

Figure 5.11: Change of the 3-D scour profile for H/D= 0.444 and h/D = 2.778. The regions that are affected by the "laser footprint error" are not marked out as in Figure 5.8. All lengths have been normalized by D.

Experimental results showed that for the three tested water depths the scour hole patterns are generally similar. Only a minor difference in the scour depth could be observed in the measured scour hole data.

5.3.4 Effects of wave height and water depth on the characteristics of the scoured bed profile

To address the uncertainty in these four characteristic dimensions, repeating tests are conducted under one test condition: H/D=0.889 and h/D=0.278. Analysis of the source of uncertainty and results with error bars for this set of repeating tests are given in section 5.3.6. The main sources of uncertainty come from the preparation of the initial bed profile, which affects the determination of L_s and L_h in the early stage of the scour process. This is because these two quantities need to be determined by the zero-contour lines, which can be strongly affected by fine turbulent flow structures associated with the initial bed profile in the early stage of the scour process. The uncertainties in the scour and deposition sand volumes, maximum scour depth s, and maximum deposition height h_d are very small after running two waves. The uncertainties in the measured L_s and L_h are small after running 19 waves and 99 waves. Therefore, the results of L_s before 19

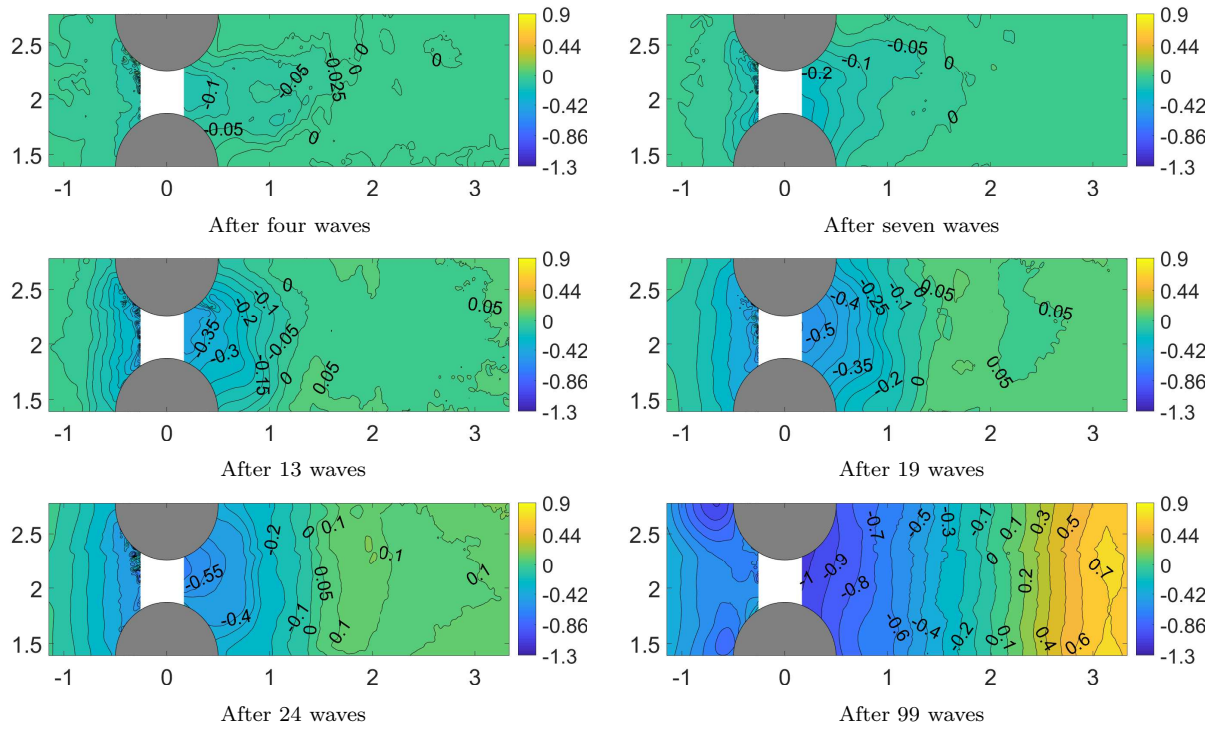

Figure 5.12: Change of the 3-D scour profile for H/D=0.667 and h/D = 2.778. The regions that are affected by the "laser footprint error" are not marked out as in Figure 5.8. All lengths have been normalized by D.

waves are not included in the following discussion. Likewise, for L_h, only the results obtained after running 99 waves are given in Table 5.6 where the measured key characteristics of the final bed profile are summarized.

Figure 5.13 shows the temporal evolutions of sand deposition height, maximum scour-hole depth, and the length of the scour hole on the down-wave side of the pile breakwater for three different wave heights (H/D = 0.444, 0.667 and 0.889) and a fixed water depth h/D =2.778.

As expected, the scour hole depth, s/D, increased with the number of solitary waves that passed the pile breakwater and a larger wave height generally resulted in a deeper scour hole. Because the dimensionless scour hole depth s/D is still less than 0.22 in the initial stage of the scour process (say, after running seven waves), the slight difference in the initial bed profiles for different test runs might have contributed to minor measurement errors observed in the initial stage of the scour process. The influence of the slight difference in the initial bed profiles for different test runs gradually diminishes with the development of the scour hole.

Sand deposition height h_d/D increased with the number of solitary waves that passed the pile breakwater. In general, the sand deposition height increased with increasing solitary wave height. The measured sand deposition heights for H/D=0.667 are slightly higher than those for

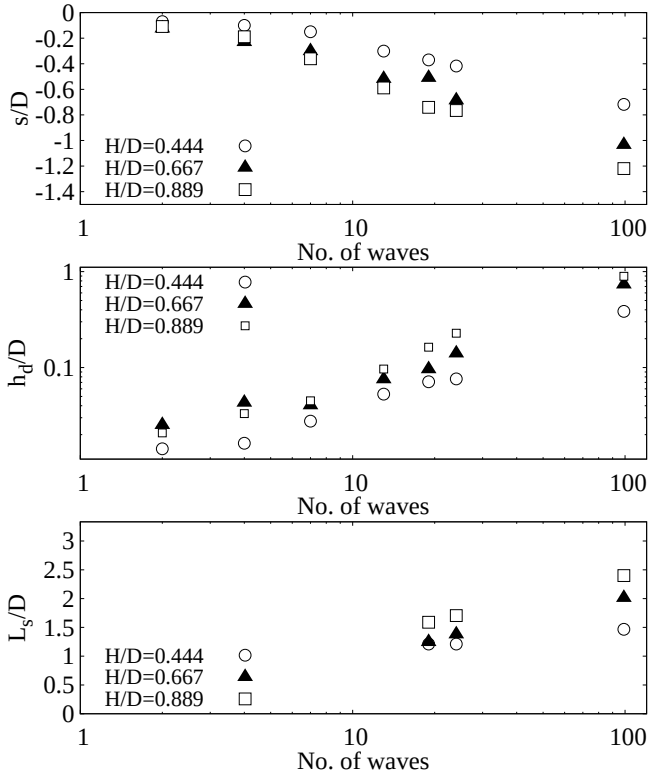

Figure 5.13: The measured maximum scour depth (top panel), maximum deposition height (middle panel), and length of the scour hole (bottom panel) for three wave heights and a fixed water depth of h/D=2.778. The values of L_s/D for the first 13 waves are not included due to the high uncertainty associated with the preparation of the initial bed profile.

H/D=0.889, possibly due to the slight difference in the initial bed profiles for different test runs.

For the length of the scour hole L_s/D, the uncertainty in L_s/D is small enough after running 19 solitary waves so that a correlation between the wave height and the scour-hole length can be observed: a higher wave height resulted in a longer scour-hole length.

Figure 5.14 shows the measured maximum scour depth, maximum sand deposition height, and the length of the scour hole for three different water depths (h/D = 2.222, 2.556, and 2.778) and a fixed wave height of H/D=0.667. As expected, both the maximum scour hole depth s/D and the maximum deposition height h_d/D increased with increasing number of solitary waves passed the pile breakwater. It is observed that both the maximum scour hole depth and the maximum deposition height are not significantly affected by the three water depths examined in this study.

On the up-wave side of the pile breakwater, L_h indicates the horizontal size of the horseshoe vortex on the up-wave side of a pile (Roulund et al., 2005). The distance for the case shown in Figure 5.12 is L_h/D = 1.000 after running 99 waves. The values of L_h/D after running 99 waves for all test conditions are summarized in Table 5.6.

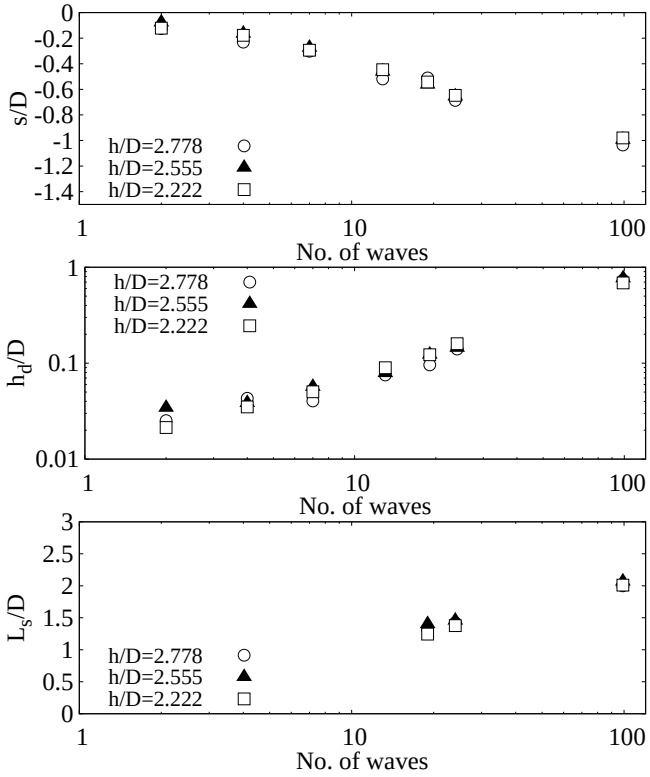

Figure 5.14: The measured maximum scour depth (top panel), maximum deposition height (middle panel), and length of the scour hole (bottom panel) for three water depths and a fixed wave height of H/D=0.667. The values of L_s/D for the first 13 waves are not included due to the high uncertainty associated with the preparation of the initial bed profile.

It may be concluded from the results in this section that: (i) sand deposition height and maximum scour depth are good characteristic dimensions for comparison with numerical simulations; and (ii) there may be large relative uncertainty in the measured scour-hole lengths L_s/D and L_h/D during the initial stage of the scour development, which means they are not good characteristic dimensions for comparison with numerical simulations.

5.3.5 Total scour and deposition volumes

The total scour and deposition volumes are two good candidates for comparison with numerical simulations. In consideration of the symmetry about the center line of the flume and possible effects of side walls, only the region within the two bold horizontal lines as shown in Figure 5.10 is used to calculate the volume of scoured sand (V_s) or the volume of deposition (V_d). Mathematically, V_s and V_d are calculated by

$$V_s = \int_\Omega s(x,y)dxdy, \quad V_d = \int_\Omega d(x,y)dxdy \tag{5.4}$$

where Ω is in the area between the two bold horizontal lines as shown in Figure 5.10, and $s(x, y)$ and $d(x, y)$ are the scour depth and deposition height at a given location (x, y), respectively. To calculate the scour and deposition volumes using Eq. (5.4), the integration is carried out numerically on a mesh of size 1 mm in both directions.

Because of possible measurement error due to the blockage of the laser beams by the lower section of the piles, the region between two adjacent piles needs special treatment using symmetric data mapping and point gauge data mapping. Referring to Figure 5.8, the data in the shaded region may have a large error and thus should be discarded. The data in the shaded region can be filled in, through one of the following two methods, to compute the total scour volume:

1. Symmetric data mapping: If the data on the symmetrical side with respect to the central axis of the gap is available (e.g., the scenarios shown in the panels (a) and (b) of Figure 5.8), they can be used to replace the discarded data.

2. Point gauge data mapping: If the data on the symmetrical side with respect to the central axis of the gap is not available (e.g. the scenarios shown in the panels (c) and (d) of Figure 5.8), the data obtained using a point gauge can be used to provide low-resolution data to replace the discarded data.

The error induced by the data mapping described above is less than 5% of the overall scour or deposition volume.

Figure 5.15 shows the calculated total scour volume for three different incident wave heights ($H/D = 0.444$, 0.667 and 0.889) and a fixed water depth of $h/D = 2.778$. The total scour volume increases with increases in the number of solitary waves that passed the pile breakwater. The incident wave height has a very significant effect on the calculated scour volume. For the smallest wave height ($H/D = 0.444$), the total scour volume reached only $V_s = 0.144 \times [(1/4)\pi D^3]$ after 24 waves, while for the largest wave height ($H/D = 0.889$) the total scour volume reached $V_s = 0.908 \times [(1/4)\pi D^3]$ after 24 waves, which is more than six times larger than that for the smallest wave height. For the case of $H/D = 0.667$, the total scour volume reached $V_s = 0.551 \times [(1/4)\pi D^3]$ after 24 waves.The values of the scour volume after 99 waves for all three wave heights are summarized in Table 5.6.

Figure 5.16 shows the calculated scour volumes for three water depths tested ($h/D = 2.222$, 2.556 and 2.778) and a fixed incident wave height of $H/D = 0.667$. It can be seen that the water depth variation tested does not have a significant influence on the scour volume, which increased almost linearly with the number of solitary waves that passed the pile breakwater. The scour volume decreased only slightly with decreasing water depth after running 13 solitary waves. For all three water depths, the scour volume reached about $V_s = 0.524 \times [(1/4)\pi D^3]$ after running 24 waves. The total scour volumes for all three water depths after 99 waves are summarized in Table 5.6.

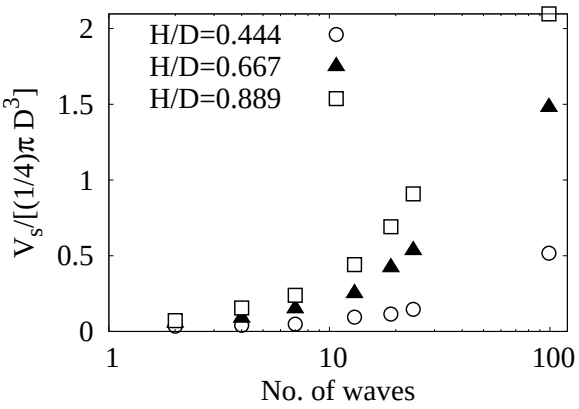

Figure 5.15: The calculated total scour volumes for three different incident wave heights and a fixed water depth $h/D = 2.778$.

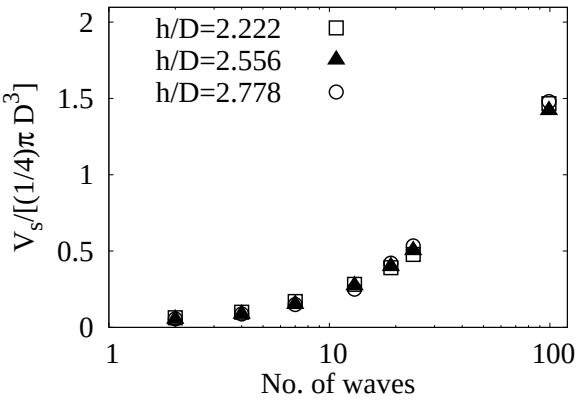

Figure 5.16: The calculated total scour volumes for three water depths and a fixed wave height $H/D = 0.667$.

Figure 5.17 shows the calculated deposition volumes for three different incident wave heights and a fixed water depth of h/D=2.778. Similar to the calculated scour volume, the total deposition volume increased with both wave height and the number of solitary waves that passed the pile breakwater. Figure 5.18 shows the calculated deposition volumes for three water depths and a fixed wave height of H/D=0.667. Again, water depth had no significant influence on the calculated deposition volume, which increased with the number of solitary waves that passed the pile breakwater. The values of the total deposition volumes after 99 waves are summarized in Table 5.6.

It can be found by comparing the total scour volumes and the corresponding total deposition volumes that the total deposition volume is slightly smaller than the scour volume. This is mainly because a certain amount of sand has been transported outside the scanned area during the scour

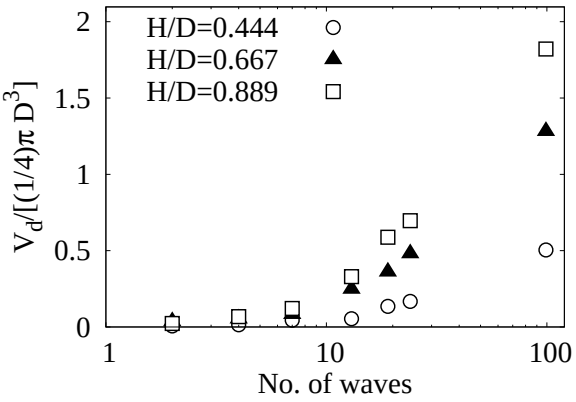

Figure 5.17: The calculated deposition volumes for three incident wave heights and a fixed water depth of $h/D = 2.778$.

process.

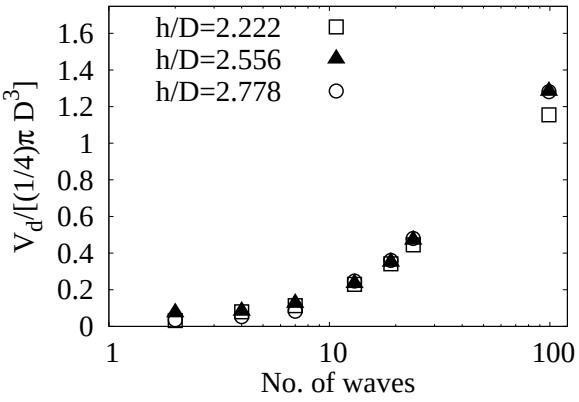

Figure 5.18: The calculated total deposition volumes for three different water depth and a fixed wave height $H/D = 0.667$.

5.3.6 Repeatability and uncertainty

In order to evaluate the repeatability and uncertainty of the experimental results, repeating tests are conducted under the same test condition (H/D=0.889, h/D=0.278). An uncertainty analysis is conducted using the data collected for this set of repeating tests. The major source of uncertainty comes from the small difference in the initial bed profiles prepared for the repeating tests. When preparing the initial bed profiles for the repeating tests, a small difference in initial bed profile is inevitably introduced, which might alter small-scale turbulence features and thus induce a difference in the scour patterns in the early stage of the scour process.

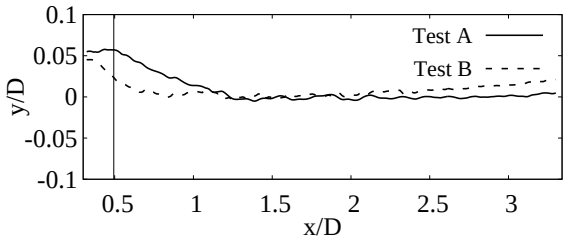

Figure 5.19: A comparison of the initial bed profiles along the transect A-A for the two repeating tests. The vertical line indicates the down-wave edge of the piles.

Figure 5.19 shows a comparison of the initial bed profiles along the transect A-A prepared for the two repeating tests (refer to Figure 5.8 for the definition of the transect A-A). For later discussion, we refer to these two repeating tests as Test A and Test B. Away from the model the initial profiles are relatively flat and agree reasonably well with each other. However, close to the model, especially inside the gap, the difference in the bed profiles prepared for Tests A and B is as large as 4.26 mm.

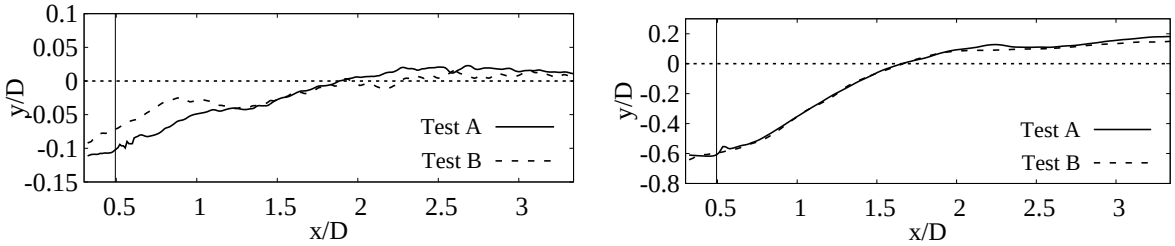

Figure 5.20: A comparison of the scour profiles along the transect A-A for the two repeating tests after four waves (left panel) and 19 waves (right panel). The vertical line indicates the edge of the piles.

Figure 5.20 shows a comparison of the scour profile along the transect A-A for the two repeating tests after four waves (left panel) and 19 waves (right panel). After four waves, the difference between the two scour profiles is significant near the model, reaching as large as 3.74 mm in depth. The scour profile shown in left panel of Figure 5.20 is a good example of how a very minor change in local scour depth could significantly alter the measurement of the length of the scour hole L_s in the early stage of the scour process; therefore, the scour hole length is not a good quantity for numerical model validation in the early stage of the scour process. After 19 waves, the difference in scour profile is small. A comparison of scour profiles after 24 waves (not shown here) has shown similar agreement. It can be concluded that uncertainty in the initial bed profile does not introduce noticeable uncertainty in the scour profile in the later stage of the scour process (i.e., after 19 waves for the present experiment).

Main results with error bars for the repeating tests ($h/D = 2.778$ and $H/D = 0.889$) are given in Figure 5.21.

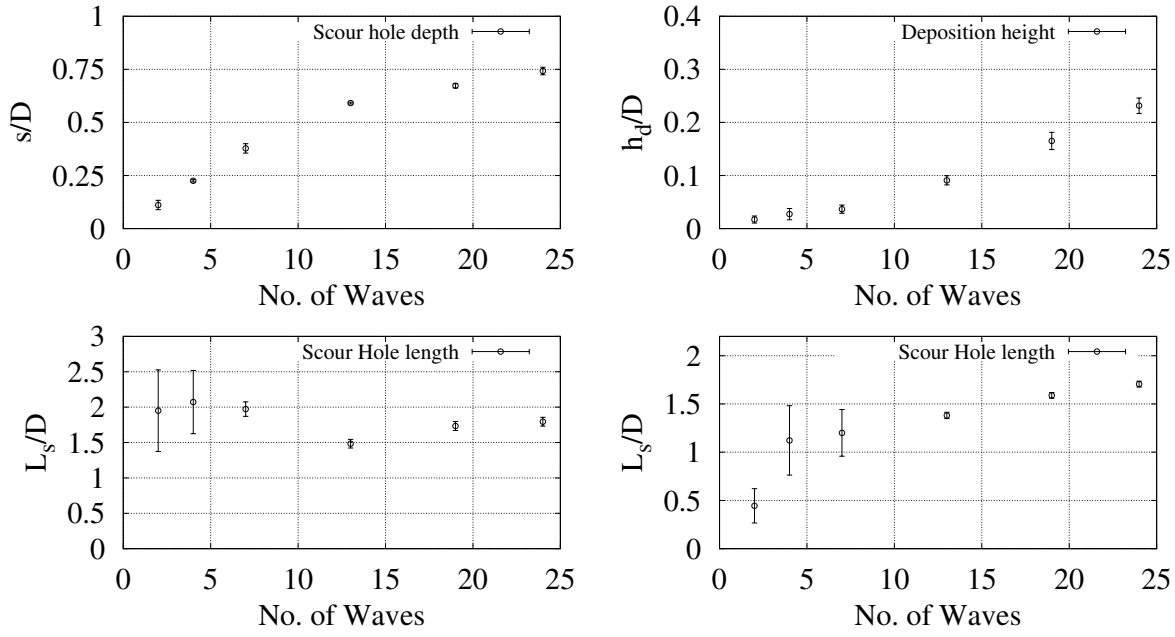

Figure 5.21: Error-bar plots of the scour hole depth s/D, deposition height h_d/D and scour hole length L_s/D of the repeatability tests. The bottom left panel is for the L_s/D determined based on zero-contour lines and the bottom right panel is for the L_s/D determined using -4 mm contour lines.

As seen in Figure 5.21, the uncertainty in the maximum scour depth s/D and the maximum deposition height h_d/D is relatively small, in both the early stage and the later stage of the scour process. However, in early stage, the measurement of scour hole length L_s has a very large uncertainty when the zero-contour line is used (the same is true for L_h). We also attempted to use -4 mm contour line to determine the scour hole length L_s/D, included in the results in right panel of Figure 5.21. For both methods used to determine L_s, the error bars of L_s/D before 13 waves are large but small after 19 waves, this indicates the overall uncertainty of L_s/D is very small in the later stage of the scour process. Therefore, for model validation purposes, only the results of L_s/D after 19 waves are included in this study.

Compared to the key scouring characteristic dimensions such as L_s and L_h, the uncertainties of the measured scour and deposition volumes are much smaller. A comparison of the measured scour and deposition volumes between Test A and Test B showed that the maximum difference in these two repeating tests is less than 3% for the total scour volume and 5% for the total deposition volume.

Based on the analysis given above, we conclude that the main difficulty in reducing the uncertainty in the measured L_s/D for the early stage of the scour process is because of the following reasons:

1. it is impossible to have the exact same initial bed profile;

2. small differences in the initial bed profile will affect the fine turbulence features which may affect sediment transport; and

3. L_s is defined by the zero-contour line, which has a very small slope in the early stage of scour process. Therefore, in the early stage of scour process, L_s can be greatly affected by a small difference in the initial bed profile.

Therefore, it is impossible to have an acceptable estimation of the error bar for L_s/D by repeating the test once or twice for each test condition.

Because Tests A and B showed good repeatability and small measurement error and uncertainty in the scour-profile characteristics except for L_s/D and because repeating the test once or twice for each test condition cannot produce an acceptable estimation of the error bar for L_s/D, the experiment is designed to run each test condition once.

In view of the results presented above, we consider that the results of s/D, h_d/D, the total scour volume, and the total deposition volume have good repeatability and low uncertainty even in the early stage, and the result of L_s/D has good repeatability and low uncertainty after 13 waves. The results of L_s/D for the early stage of the scour process (before 19 waves) should be excluded.

5.4 A discussion of equilibrium scour depth

5.4.1 Equilibrium scour depths and time scale of the present experiment

A number of empirical formulas exist for predicting the time development of the scour depth for a single circular pile in steady currents for clear-water scour conditions (Melville and Chiew, 1999) and live-bed scour (Sumer et al., 1992a). The present test cases are for live-bed scour. This is because the values of the Shields parameter for all the test cases (see Table 5.3) are larger than the critical Shields parameter of about 0.06 according to Madsen and Grant (1976).

For live-bed scour, the following empirical formula has been proposed by Sumer et al. (1992a) to estimate the dimensionless instantaneous scour depth $s(t_n)/D$,

$$\frac{s(t_n)}{D} = \left[1 - \exp\frac{-t_n}{t_*}\right]\frac{s_e}{D}, \tag{5.5}$$

where s_e is the equilibrium scour depth, t_* is a dimensionless characteristic time scale for the scour process, and t_n is a dimensionless scour time. Both t_* and t_n must use the same time scale to make them dimensionless. This formula has been applied to both steady currents and tidal currents (McGovern et al., 2014) and oscillatory flows such as regular and irregular waves (Baykal et al., 2017).

To use Eq. (5.5) to analyze the measured scour-hole depth, we can relate the number of waves that passed the pile breakwater to a dimensionless equivalent scour time t_n by using the equivalent

period T_s for a solitary wave defined in Eq. (5.1). The dimensionless equivalent scour time t_n after running n waves can be calculated by

$$t_n = nT_s/T_0 \tag{5.6}$$

where the time scale T_0 has been defined in Eq. (5.3). Both the dimensionless times t_* and t_n are normalized by T_0 given by Eq. (5.3) in this section. Using Eq. (5.6) in Eq. (5.5), it is possible to fit Eq. (5.5) to the measured scour depths to obtain the values of s_e/D and t_*. The fitting results are shown in Figure 5.22 for all test cases. The fitted values of s_e/D and t_* for all test cases are listed in Table 5.4. Note that all test cases have almost reached their equilibrium states after running 99 waves.

Table 5.4: Data fitting results for s_e/D and t_*.

Effects of Wave Height			Effects of Water Depth		
H/D	s_e/D	t_*	h/D	s_e/D	t_*
0.444	0.736	0.1438	2.222	0.984	0.0712
0.667	1.032	0.0905	2.556	1.004	0.0849
0.889	1.222	0.0750	2.778	1.032	0.0905

The good agreement between the measured and predicted evolutions of the scour hole depth, as shown in Figure 5.22, suggests the following two points:

1. Using Eq. (5.6) to convert the number of solitary waves into an equivalent time is appropriate.
2. Eq. (5.5), which was originally proposed for a single cylinder under steady currents or oscillatory flows, can be used to predict the evolution of the maximum depth of the scour at a row of closely spaced cylinders under various solitary-wave conditions.

5.4.2 A discussion of the empirical formula of Sumer and Fredsöe (2001a) for equilibrium scour depth at a single vertical pile

The following formula of Sumer et al. (1992b) was proposed for the prediction of equilibrium scour depth s_e around a single vertical circular pile in waves:

$$\frac{s_e}{D} = 1.3\left[1 - e^{-0.03(KC-6)}\right], KC \geq 6.0 \tag{5.7}$$

where D is the diameter of the circular pile and KC is the Keulegan-Carpenter number expressed by

$$KC = \frac{U_m T}{D} \tag{5.8}$$

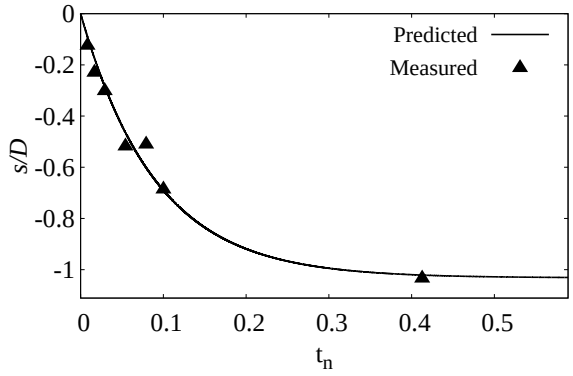

Case 1: $h/D = 2.778$ and $H/D = 0.667$

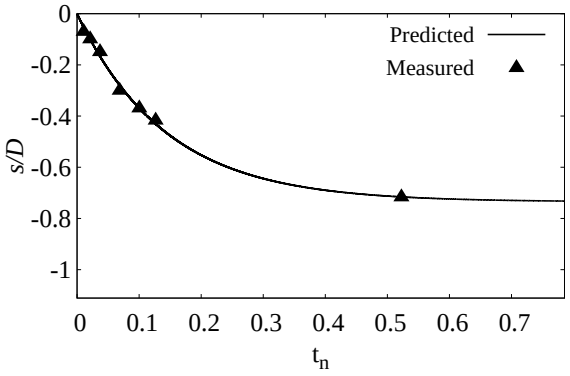

Case 2: $h/D = 2.778$ and $H/D = 0.444$

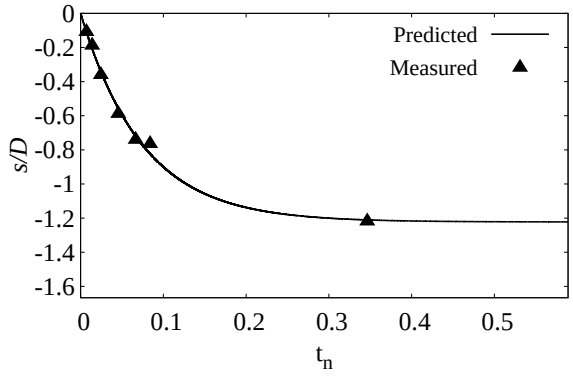

Case 3: $h/D = 2.778$ and $H/D = 0.889$

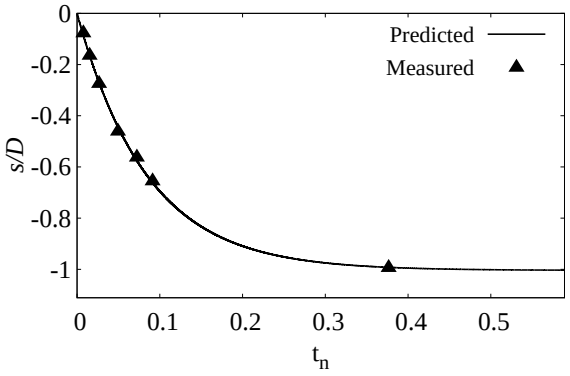

Case 4: $h/D = 2.556$ and $H/D = 0.667$

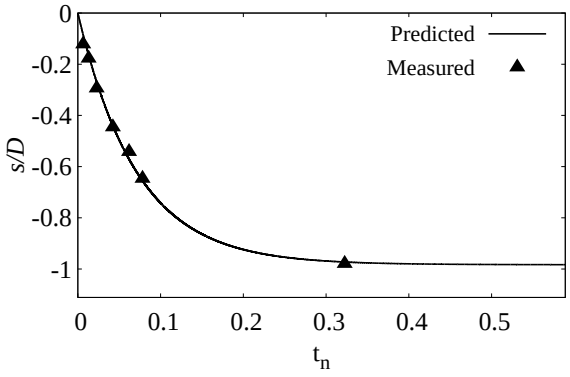

Case 5: $h/D = 2.222$ and $H/D = 0.667$

Figure 5.22: Results obtained from fitting Eq. (5.5) to the measured scour-hole depth for the five tested cases.

with U_m being the maximum orbital flow velocity outside the wave bottom boundary layer and T the wave period. Later, Sumer and Fredsöe (2001a) extended the use of this formula to irregular waves and random waves plus a current. By inspecting the results using a number of combinations of statistical parameters, they found if the root mean square velocity U_{rms} and peak period T_p are

used to compute KC number, Eq. (5.7) could be applied to irregular waves as well. Sumer and Fredsøe remarked that in the case of random wave plus current, Eq. (5.7) could be adapted to the following formal expression

$$\frac{s_e}{D} = c\left[1 - e^{a(KC-b)}\right], KC \geq b \tag{5.9}$$

where the coefficients a and b are calculated by:

$$a = -0.03 + 0.75U^{2.6} \tag{5.10}$$

$$b = 6e^{-4.7U} \tag{5.11}$$

In the expressions for a and b, the representative velocity $U = U_c/(U_c + U_{rms})$, where U_c is the current velocity outside the bottom boundary layer, and the coefficient c in Eq. (5.9) represents the maximum possible dimensionless scour depth, and Sumer et al. (1992b) suggested $c = 1.3$, corresponding to the scenario of a steady current. Sumer et al. (2002) also suggested the use of slightly larger values for c as a design safety measure. More recently, Ong et al. (2013) proposed a stochastic method to predict the maximum equilibrium scour depth around a vertical pile under the influence of long-crested or short-crested random waves combined with currents. Based on Eq. (5.9), Ong et al. (2013) developed a sophisticated stochastic method to determine the expected value of s_e/D by considering the probability distribution of the incident wave and the effects of the largest $1/n$ waves.

Two major differences between regular/irregular waves and solitary waves are: (i) the lack of flow reversal in solitary wave conditions; and (ii) the lack of periodicity in a solitary wave. These differences require a new definition for the KC number for solitary waves in order to use Eq. (5.9) to estimate the equilibrium scour depth for the present experimental study. The reversal flow in regular/irregular waves can limit the maximum distance a water particle can travel in one direction. A solitary wave has a limited duration, which can also limit the maximum distance a water particle can travel in one direction. Therefore, if an equivalent period can be defined such that there are flow acceleration and deceleration within this equivalent period, it is possible to define a new KC number for solitary waves. Here we use the following equivalent wave period of a solitary wave for the wave period in Eq. (5.8).

$$T_s = 4\pi\sqrt{\frac{h^3}{3gH(h+H)}} \tag{5.12}$$

For the characteristic velocity U_m in Eq. (5.8), we use the maximum wave orbital velocity computed by using Grimshaw (1971)'s solitary wave theory.

Table 5.5 shows the relevant parameters and the equilibrium scour depth predicted by using Eq. (5.7). The s_e/D results as predicted by Eq. (5.7) agree poorly with our experimental data: equilibrium scour depth is significantly under-predicted. This is partly because Eq. (5.7) was calibrated against a single vertical pile in a wave field. For an array of piles, the amplification

Table 5.5: A summary of the calculation of equilibrium scour depth s_e/D using Eq. C1.

Case No.	$U_m[m/s]$	$T_s[s]$	KC	Measured s_e/D	s_e/D
1	0.343	2.12	8.084	1.032	0.079
2	0.240	2.69	7.170	0.736	0.045
3	0.428	1.78	8.461	1.222	0.093
4	0.354	1.94	7.624	1.004	0.062
5	0.383	1.66	7.064	0.984	0.041

of bed shear stress due to the jet flow formed in between the piles is much stronger than the amplification of bed shear stress due to flow around a single vertical pile as tested by Sumer et al. (1992b).

Therefore, we attempt to use Eq. (5.9) by obtaining a different set of coefficients using our present experimental data. We treated the value of coefficient c in Eq. (5.9) as a constant of 1.3. This is because $s_e/D = 1.3$ is the steady current equilibrium scour depth limit as KC goes to infinity and we believe the scours induced by solitary waves are not likely to exceed this limit. A nonlinear-least-square data fitting gave $a = -0.7383$ and $b = 5.6253$. Therefore, the following empirical formula for our data is obtained:

$$\frac{s_e}{D} = 1.3\left[1 - e^{-0.7383(KC-5.6253)}\right], KC = \frac{U_m T_s}{D} \tag{5.13}$$

Figure 5.23 shows a comparison between the prediction using Eq. (5.13) and the measured equilibrium depth. The agreement between the predicted and measured equilibrium scour depths is only moderately acceptable, with a maximum difference of about 21.9%.

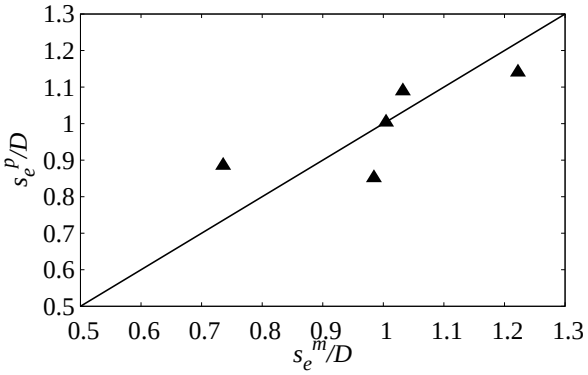

Figure 5.23: Comparison of the predicted equilibrium scour depth s_e^p and the measured equilibrium scour depth s_e^m.

5.4.3 A discussion of time scale of the scour in the present experiment

For dimensionless time scale t_*, Sumer et al. (1992a) proposed Eq. (5.14) to calculate the t_* for given sediment characteristics, the dimensions of the cylinder and the steady current flow condition.

$$t_* = \beta_1 \frac{h}{D} \left[\frac{u_*^2}{g(\gamma - 1)d} \right]^{\beta_2} \tag{5.14}$$

where γ is the specific gravity of sediment, $u_* = \sqrt{\tau_b / \rho_w}$ is the shear velocity and τ_b is the bed shear stress, d is the mean sediment particle diameter, and β_1 and β_2 are two fitting parameters. For steady current, Sumer et al. (1992a) proposed $\beta_1 = 1/2000$ and $\beta_2 = -2.2$. Sumer et al. (1992a) also proposed a formula for computing t_* for regular waves, which involves Keulegan-Carpenter number. In our case the solitary wave is supposedly unidirectional, hence starting from the formula for steady current is reasonable (see 5.4.2 for a discussion of using KC number in equilibrium scour depth prediction of solitary waves). However, the parameters β_1 and β_2 obtained for steady currents may not be directly applicable to scour induced by solitary waves. The parameters β_1 and β_2 for the current test conditions are obtained by fitting Eq. (5.14) to the data for t_* given in Table 5.4.

To use Eq. (5.14) for solitary waves, we need to calculate the shear velocity u_* for a given solitary wave. Unlike steady current, shear velocity for a solitary wave varies with time. In anticipation that the sediment transport caused by solitary waves is controlled mainly by the maximum bottom shear stress, the theoretical solution of Liu et al. (2007) for the bottom shear stress associated with a passing solitary wave (Figure 2 in Liu et al. (2007)) is used to calculate the maximum bed shear velocity u_* during a solitary wave. With u_* known, we can fit Eq. (5.14) to the data of t^* given in Table 5.4 to obtain an estimation of β_1 and β_2 in Eq. (5.14). The fitted values of β_1 and β_2 for the scour at a pile breakwater caused by solitary waves are found to be $\beta_1 = 0.0078$ and $\beta_2 = -0.9691$, i.e., the time scale t_* for the present tests is

$$t^* = \frac{0.0078h}{D} \left[\frac{u_*^2}{g(\gamma - 1)d} \right]^{-0.9691} \tag{5.15}$$

The left panel of Figure 5.24 shows a comparison between the measured and predicted t_* values using Eq. (5.15), and the agreement between the measured and predicted values of t_* is very good.

For solitary waves, $\beta_1 = 0.0078$ is significantly larger than the value of $\beta_1 = 1/2000$ for steady currents. This can be attributed to the use of the maximum bed shear velocity as u_* in this analysis. This may overestimate the bed shear stress and hence requires a larger value of β_1 to compensate the effect.

Using the KC number defined in Eq. (5.13), we can also use the following formula given in Eq. (5.16) for t_* proposed by Sumer et al. (1992a) for regular waves. Sumer et al. (1992a) proposed $\beta_3 = 10^{-6}$ and $\beta_4 = 3$ for regular wave condition and a single vertical pile. Fitting Eq. (5.16) to

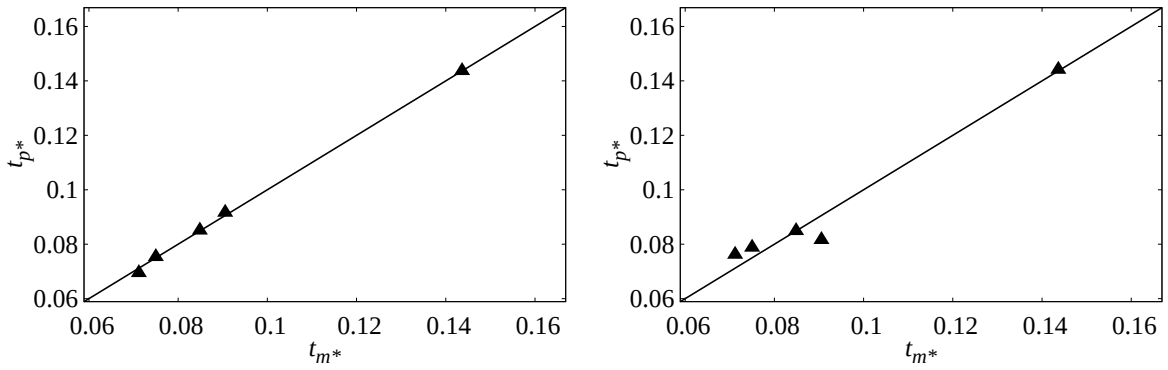

Figure 5.24: A comparison of the measured and predicted values of the time scale t_*. The horizontal axis t_{m*} is the fitted value of t_* obtained from the measurement and the vertical axis t_{p*} is the predicted t_*using Eq. (5.15) or Eq. (5.16). Left panel is for from Eq. (5.15) and right panel is for Eq. (5.16) .

the values of t_* given in Table 5.4 gives $\beta_3 = 0.0028$ and $\beta_4 = 0.9738$ for the pile breakwater model in tested solitary wave conditions.

$$t_* = \beta_3 \left(\frac{KC(\gamma - 1)gd}{u_*^2} \right)^{\beta_4} \tag{5.16}$$

The right panel of Figure 5.24 shows a comparison between the measured and predicted t_* values using Eq. (5.16). The values of t_* predicted by Eq. (5.16) agree reasonably well with the measured. Comparing the two plots in Figure 5.24, Eq. (5.15) performs better than Eq. (5.16).

The good agreement between t_{p*} and t_{m*} as shown in Figure 5.24 suggests that Eq. (5.14), which was originally proposed for a single cylinder under steady currents and oscillatory flows, can also be applied to a row of closely spaced cylinders under various solitary-wave conditions. However, it must be noted that the fitted values of β_1 and β_2 given in Eq. (5.15) are only valid for the tested pile breakwater configuration. It is expected that the values of these two fitting parameters depend on other factors such as the diameter of the piles and gap size, which is worth further investigation.

Table 5.6: A summary of the characteristics of the final bed profile

Case	s/D	L_s/D	h_d/D	L_h/D	s_e/D	$V_s/[(1/4)\pi D^3]$	$V_d/[(1/4)\pi D^3]$
1	1.033	2.156	0.733	1.000	1.032	1.479	1.281
2	0.722	1.567	0.389	0.644	0.736	0.517	0.504
3	1.222	2.533	0.889	1.222	1.222	2.097	1.821
4	1.000	2.200	0.767	1.044	1.004	1.421	1.284
5	0.978	2.122	0.689	1.011	0.984	1.466	1.155

5.5 The characteristics of the final bed profile

Table 5.6 summarizes the key characteristics of the final bed profiles for the five test cases. The values of these characteristics are obtained after running 99 solitary waves. The equilibrium scour hole depth s_e/D, which is calculated using Eq. (5.5) through a data fitting, is also included. These characteristics can be used for comparison with numerical simulations. One advantage of using solitary waves to verify and validate numerical models developed for studying scour at pile breakwaters is that it can avoid the computing time spent on establishing a steady state of the multiple reflections of nonlinear periodic waves between the model and wave generator.

5.6 Summary

In this study, the sediment scour around a pile breakwater (a row of closely spaced piles) under the action of multiple solitary waves is investigated experimentally. Using a high resolution underwater laser scanner, in combination with a point probe, the temporal evolutions of detailed 3-D bed profiles near the pile breakwater are measured for three water depths and three wave heights. The following conclusions can be drawn from the experimental results reported in this study.

1. Scour occurs on both sides of the pile breakwater, and the maximum scour depth occurs in the gap between two piles. The maximum scour depth at the pile breakwater increases with increasing wave height under the same other test conditions. The maximum depth of the scour at the equilibrium state is found to be in the range of 0.73 D and 1.22 D .

2. At the early stage of the scour process, the scour hole at the gap between two piles is shallow and not connected with the neighboring scour holes. The scour-depth contours have a U-shaped pattern and no sandbar on the down-wave side is observed. At a later stage of the scour process, scour holes gradually joins with neighboring scour holes. When the scour profile approaches its equilibrium state, a sandbar forms on the down-wave side of the scour hole. The sand bar height at the equilibrium state is found to be in the range of 0.35 D and 0.80 D.

3. For a fixed water depth, both the total scour volume and deposition volume increase with increasing wave height. The total scour volume at the equilibrium is found to be in the range of 0.52 $\times[(1/4)\pi D^3]$ and 2.10 $\times[(1/4)\pi D^3]$.

4. Existing formulas, which were originally proposed for the evolution of the maximum depth of the scour at a single vertical cylinder under steady current or oscillatory flow conditions, are extended to a row of closely spaced piles under solitary wave conditions. New empirical coefficients are obtained by fitting the formulas to the new experimental data.

5. Comparisons between the data fittings using existing formulas for temporal development and equilibrium of scour depth for steady current and regular waves have shown that for solitary wave conditions, the empirical formula for steady currents generally performs better than the formula for regular waves.

6. The maximum scour depth and total scour volume are two reliable quantities that can be used for comparison with numerical simulations.

The experimental results provide a data set for the validation of numerical models developed for scour around pile breakwaters under highly nonlinear wave conditions. The coefficients for the empirical formula describing the development of the scour hole depth are valid only for the test conditions examined in this study. The jet flow between two adjacent piles, which is affected by the gap size, caused the local scour at the breakwater. Effects of gap size on the local scour at the pile breakwater is worth further investigation.

CHAPTER 6
CONCLUSIONS AND FUTURE WORK

This research work is concerned with understanding an innovative Oscillating Water Column (OWC) device integrated with piles for the purposes of wave energy extraction and shore protection. A theoretical model for the consideration of the nonlinear power take-off mechanism was proposed and validated with the experiment. The nonlinear power take-off mechanism, wave power extraction efficiency, spatial non-uniformity inside the OWC chamber, and the effect of row arrangements of OWC-pile devices on the performance of the structure as a wave farm and shore protection breakwater are investigated experimentally and numerically. The detailed flow fields for the standalone OWC-pile device and a row of closely spaced OWC-piles exposed to regular waves were investigated using a validated numerical model and the implications to sediment transport and the resulting scour around the structures were discussed. The scour around a row of closely spaced piles without OWC devices under highly nonlinear solitary waves was investigated experimentally. Contributions were made to improve the understanding of integrating OWC devices with pile structures and key physical processes involved.

As a closure to all the research work reported in the previous chapters and a summary of the answers to some of the questions raised in section 1.2 at the beginning of this dissertation, major conclusions acquired from this work are summarized in the first section, and suggestions and plans for future work are presented in the second section.

6.1 Main conclusions

Detailed conclusions of the respective parts of the present research work were articulated in the previous chapters. In this section, the most important conclusions that help to provide answers to the questions raised in Section 1.2 are summarized.

1. A new dual function wave farm and shore protection breakwater consisting of multiple piles integrated with OWC devices is proposed in this study. Under laboratory conditions, the proposed OWC-pile in a standalone configuration (or loosely spaced configuration) provides a pneumatic capture width ratio between 0.08 to 0.37, and a transmission coefficient between 0.90 to 0.99. A 1000-m scale-up calculation shows that a standalone OWC-pile or a loosely spaced OWC-piles configuration as a wave farm is economically infeasible for both wave energy extraction and shore protection purposes, implying the need for a closely spaced configuration.

2. A theoretical treatment of the nonlinear power take-off mechanism based on the Lorentz principle of equivalent work is proposed and its incorporation with the theoretical solution of linear wave diffraction and radiation for the standalone OWC-pile device shows very good agreement with experimental results, particularly for long waves.

3. It is found in this study that when resonant sloshing modes are not excited in the OWC-chambers, the spatial non-uniformity inside the OWC chamber may introduce relative error as large as 8% if only one wave gauge is placed inside the OWC chamber to measure the water surface oscillation (Xu et al., 2016). Sloshing modes inside OWC chambers may reduce energy extraction efficiency and cause water spray over-topping at the PTO device and should ideally be avoided. For some wave conditions, a resonant sloshing mode can be triggered by free harmonic waves inside the OWC chamber. These free harmonic waves are generated by pressure oscillations due to vortex shedding at the sharp edges of the OWC device. In laboratory conditions, these resonant sloshing modes can significantly increase the error induced by one-point measurement method. One method to reduce the error induced by one-point measurement method is to identify and discard test conditions with resonant sloshing using a spectral analysis, and use an averaged quadratic loss coefficient obtained from long waves to compute capture width ratio. It is thus concluded from this study that when designing OWC devices, not only the sloshing from fundamental components should be avoided, the sloshing modes from higher harmonic frequency also need to be avoided where possible.

4. The performance of the OWC-pile in a closely spaced configuration performs significantly better when compared to the performance of the OWC-pile in a standalone, or loosely spaced configuration. The measured capture width ratio is about 1.5 to 2 times larger than the capture width ratio obtained for the standalone or loosely spaced configurations under the same wave condition. This finding signifies the economic and engineering value of the dual functional structure proposed in this study as a wave conversion structure.

5. In a closely spaced configuration, a comparison between OWC-piles and ordinary vertical piles with identical geometry and dimensions shows that the addition of wave power extraction due to the OWC devices can significantly reduce the wave reflection coefficient and wave transmission coefficient. Experimental results show that with the addition of OWC device induced wave energy extraction, 2-3 times more energy can be removed from the wave field for short wave conditions, and 70% to 105% more energy can be removed from the wave field for long wave conditions. This finding shows the value of the proposed structure in terms of shore protection and integrated coastal management.

6. For a row of OWC-piles in a closely spaced configuration, the wave power removed due to viscous dissipation is not significantly affected by the presence of additional OWC device. This is mainly due to the decreased availability of wave energy due to wave power extraction by the OWC device. A semi-theoretical model with empirical coefficient indicates that the drag coefficient of the pile device increases with the addition of OWC structures to the piles, and the semi-theoretical model shows the potential in explaining the viscous loss due to vortex shedding for both pile structures and OWC-pile structures in closely spaced configuration.

7. It is found in this study that despite a KC number of less than 1.6, weak horseshoe vortices are still observed at the toe of the OWC-pile in different configurations. The strength of the horseshoe vortex in a closely spaced OWC-pile configuration is slightly higher than that in a standalone configuration however, all horseshoe vortices observed in the current study are too weak to be responsible for enhanced sediment scouring. It is found that for both the standalone and closely spaced configurations, the wake vortices on the up-wave side of the OWC-piles are larger and stronger, particularly for the closely spaced OWC-piles configuration in which a strong contraction jet flow is present. The addition of the OWC devices to the otherwise smooth circular pile can enhance the flow separation on the up-wave side of the structure, which can lead to enhanced energy dissipation and enhanced sediment scouring at the foundation of the piles.

8. Present experimental investigations show that in highly nonlinear solitary waves, a row of closely spaced piles without OWC devices sitting in a sand bed have significant scouring on the up-wave side, in the narrow gaps between adjacent piles, and on the down-wave side of the structure. Adaptation of existing scour depth formulas for regular waves can extend the application of these formulas to highly nonlinear solitary waves. The results from existing formulas show that the equilibrium scour depth of a row of closely spaced piles in solitary wave under the tested conditions is scaled by the diameter of the pile, reaching as large as 1.22 times the diameter of the pile, which is very close to the steady current scour depth limit. These experimental results can be used to validate the subsequent rheology based three-phase flow model development for sediment transport and hydrodynamics.

6.2 Future work

As mentioned in chapter 1, the present study should be regarded as an important starting step towards a more complete understanding of the hydrodynamics, energy balance and sediment transport around a row of closely spaced OWC-piles. In order to fully answer the questions raised in chapter 1 and beyond, the following research topics are suggested and some of them are planned for the near future.

1. With detailed flow fields available from the numerical methods, it is necessary to perform a more quantitative investigation on the vortex dynamics and its implication to sediment transport and energy dissipation. Moreover, with the validation of the rheology based three-phase model for sediment transport, the effect of turbulence modulation on small and weak vortices, such as the horseshoe vortex, can be investigated in a systematic way. This work should also be accompanied by a validation of a detailed flow field with PIV data in a 2-D configuration.

2. To provide a comprehensive evaluation of the foundation erosion pattern of the proposed structure, it is important to investigate experimentally and numerically how the closely spaced OWC-piles perform in regular waves on a sandy bottom. This involves two interesting research problems. (1) How would the sediment transport pattern and scour pattern be? (2) How would the equilibrium scour profile inside the OWC chamber affect the wave power extraction performance of the device?

3. With the validated numerical model for hydrodynamics and wave energy, it is necessary to perform numerical investigations to study further the influence of OWC-pile spacing, different layers of OWC-piles, and PTO damping on the performance of the wave farm and breakwater structure.

APPENDIX A
PART OF OPENFOAM CODES FOR TURBULENCE MODELING, WAVE GENERATION AND SOLVER

Attached here is a part of the OpenFOAM code and the solver code used in the present study, note that only the part that are different from the stock OpenFOAM code and relevant to the numerical study presented in this report is included for simplicity. The full version of the solver, which is a complete three-phase flow model for sediment transport and hydrodynamics, is under further validation and optimization. The full version of the code is open-source and will be made available online once the validation and optimization work is complete.

turbulenceModel.H

```
...
class turbulenceModel
{

protected:

    // Protected data

        const Time& runTime_;
        const fvMesh& mesh_;

        const volVectorField& U_;
    const volScalarField& rho_;
        const surfaceScalarField& phi_;

        transportModel& transportModel_;


private:

    // Private Member Functions

        //- Disallow default bitwise copy construct
        turbulenceModel(const turbulenceModel&);
```

```
        //- Disallow default bitwise assignment
        void operator=(const turbulenceModel&);


public:

    //- Runtime type information
    TypeName("turbulenceModel");


    // Declare run-time New selection table

#ifndef SWIG
        declareRunTimeNewSelectionTable
        (
            autoPtr,
            turbulenceModel,
            turbulenceModel,
            (
                const volVectorField& U,
            const volScalarField& rho,
                const surfaceScalarField& phi,
                transportModel& lamTransportModel
            ),
            (U, rho, phi, lamTransportModel)
        );
#endif


    // Constructors

        //- Construct from components
        turbulenceModel
        (
            const volVectorField& U,
        const volScalarField& rho,
```

```
        const surfaceScalarField& phi,
        transportModel& lamTransportModel
    );


// Selectors

    //- Return a reference to the selected turbulence model
    static autoPtr<incompressible::turbulenceModel> New
    (
        const volVectorField& U,
    const volScalarField& rho,
        const surfaceScalarField& phi,
        transportModel& lamTransportModel
    );


// Destructor

    virtual ~turbulenceModel()
    {}


// Member Functions

    //- Access function to velocity field
    inline const volVectorField& U() const
    {
        return U_;
    }

    //- Access function to density field
    inline const volScalarField& rho() const
    {
        return rho_;
    }
```

```
//- Access function to flux field
inline const surfaceScalarField& phi() const
{
    return phi_;
}

//- Access function to incompressible transport model
inline transportModel& transport() const
{
    return transportModel_;
}

//- Return the laminar viscosity
const volScalarField& nu() const
{
    return transportModel_.nu();
}

//- Return the turbulence viscosity
virtual tmp<volScalarField> nut() const = 0;

//- Return the effective viscosity
virtual tmp<volScalarField> nuEff() const = 0;

//- Return the turbulence kinetic energy
virtual tmp<volScalarField> k() const = 0;

//- Return the turbulence kinetic energy dissipation rate
virtual tmp<volScalarField> epsilon() const = 0;

//- Return the Reynolds stress tensor
virtual tmp<volSymmTensorField> R() const = 0;

//- Return the effective stress tensor including the laminar stress
virtual tmp<volSymmTensorField> devReff() const = 0;

//- Return the source term for the momentum equation
```

```
        virtual tmp<fvVectorMatrix> divDevReff(volVectorField& U) const = 0;

        //- Solve the turbulence equations and correct the turbulence viscosity
        virtual void correct() = 0;

        //- Read turbulenceProperties dictionary
        virtual bool read() = 0;
};
...
```

turbulenceModel.C

```
...
turbulenceModel::turbulenceModel
(
    const volVectorField& U,
    const volScalarField& rho,
    const surfaceScalarField& phi,
    transportModel& lamTransportModel
)
:
    runTime_(U.time()),
    mesh_(U.mesh()),

    U_(U),
    rho_(rho),
    phi_(phi),
    transportModel_(lamTransportModel)
{
}
...
autoPtr<turbulenceModel> turbulenceModel::New
(
    const volVectorField& U,
    const volScalarField& rho,
    const surfaceScalarField& phi,
    transportModel& transport
```

```
)
{
    word modelName;

    // Enclose the creation of the dictionary to ensure it is deleted
    // before the turbulenceModel is created otherwise the dictionary is
    // entered in the database twice
    {
        IOdictionary dict
        (
            IOobject
            (
                "turbulenceProperties",
                U.time().constant(),
                U.db(),
                IOobject::MUST_READ,
                IOobject::NO_WRITE
            )
        );

        dict.lookup("simulationType") >> modelName;
    }

...
return autoPtr<turbulenceModel>(cstrIter()(U, rho, phi, transport));
}
...
```

kOmega.C

```
kOmega::kOmega
(
    const volVectorField& U,
    const volScalarField& rho,
    const surfaceScalarField& phi,
    transportModel& lamTransportModel
)
```

```
:
    RASModel(typeName, U, rho, phi, lamTransportModel),

...

    )
{
    nut_ = k_/(omega_ + omegaSmall_);
    nut_ = min(nut_, nuRatio()*nu());
    nut_.correctBoundaryConditions();

    printCoeffs();
}

...
...
tmp<volSymmTensorField> kOmega::R() const
{
    return tmp<volSymmTensorField>
    (
        new volSymmTensorField
        (
            IOobject
            (
                "R",
                runTime_.timeName(),
                U_.db(),
                IOobject::NO_READ,
                IOobject::NO_WRITE
            ),
            rho_*((2.0/3.0)*I)*k_ - rho_*nut_*twoSymm(fvc::grad(U_)),
            k_.boundaryField().types()
        )
    );
}
...
...
```

```
tmp<volSymmTensorField> kOmega::devReff() const
{
    return tmp<volSymmTensorField>
    (
        new volSymmTensorField
        (
            IOobject
            (
                "devRhoReff",
                runTime_.timeName(),
                U_.db(),
                IOobject::NO_READ,
                IOobject::NO_WRITE
            ),
           -rho_*nuEff()*dev(twoSymm(fvc::grad(U_)))
        )
    );
}

tmp<fvVectorMatrix> kOmega::divDevReff(volVectorField& U) const
{
    volScalarField muEff=rho_*nuEff();
    return
    (
      - fvm::laplacian(muEff, U)
      - fvc::div(muEff*dev(fvc::grad(U)().T()))
    );
}

...

void kOmega::correct()
{
    // Bound in case of topological change
    // HJ, 22/Aug/2007
    Info << "Modified kOmega Model..Conghao Xu..." << endl;
    if (mesh_.changing())
```

```
{
    bound(k_, k0_);
    bound(omega_, omega0_);
}

RASModel::correct();

if (!turbulence_)
{
    return;
}

//volScalarField G("RASModel::G", nut_*2*magSqr(symm(fvc::grad(U_))));
//volScalarField G("RASModel::G", rho_*nut_*magSqr(2*skew(fvc::grad(U_))));
//modified according to mayer and madsen (2000) for suppression of
//excessive k generation
volScalarField G("RASModel::G", rho_*nut_*magSqr(fvc::curl(U_)));
surfaceScalarField rhoPhi_=fvc::interpolate(rho_)*phi_;
// Update omega and G at the wall
omega_.boundaryField().updateCoeffs();

// Turbulence specific dissipation rate equation
tmp<fvScalarMatrix> omegaEqn
(
    fvm::ddt(rho_,omega_)
  + fvm::div(rhoPhi_, omega_)
  + fvm::SuSp(-fvc::div(rhoPhi_), omega_)
  - fvm::laplacian(DomegaEff(), omega_)
 ==
    alpha_*G*omega_/k_
  - fvm::Sp(beta_*omega_*rho_, omega_)
);

omegaEqn().relax();

// No longer needed: matrix completes at the point of solution
// HJ, 17/Apr/2012
```

```
//      omegaEqn().completeAssembly();

    solve(omegaEqn);
    bound(omega_, omega0_);


    // Turbulent kinetic energy equation
    tmp<fvScalarMatrix> kEqn
    (
        fvm::ddt(rho_,k_)
      + fvm::div(rhoPhi_, k_)
      + fvm::SuSp(-fvc::div(rhoPhi_), k_)
      - fvm::laplacian(DkEff(), k_)
     ==
        G
      - fvm::Sp(Cmu_*omega_*rho_, k_)
    );

    kEqn().relax();
    solve(kEqn);
    bound(k_, k0_);
    //volScalarField nutMax=sqrt(2.0/3.0)*k_/(mag(G)+1.0*max(G));

    // Re-calculate viscosity
    nut_ = k_/(omega_ + omegaSmall_);
    nut_ = min(nut_, nuRatio()*nu());
    //nut_ = min(nut_, nutMax);
    nut_.correctBoundaryConditions();
}

...
```

waves2Foam: waveTheory.C

```
...

    wind_( lookupOrDefault<vector>( "wind", vector::zero ) )
```

```
{
    {
        IOdictionary transProp
        (
            IOobject
            (
                "transportProperties",
                "constant",
                mesh_,
                IOobject::MUST_READ,
                IOobject::NO_WRITE
            )
        );
        dictionary sD(transProp.subDict(Foam::waves2Foam::waterPhase()));
        Info << "\nSearch rhoWater_" << endl;
        rhoWater_ = 1010; //XCH: assuming water
        //--this is to be compatible with transportProperties
        //of the new threePhaseSedFoam

    }
}

...
```

newSolver: createFields.H

```
...

    volScalarField curlU1
    (
        IOobject
        (
            "curlU1",
            runTime.timeName(),
            mesh,
            IOobject::NO_READ,
            IOobject::AUTO_WRITE
```

```
        ),
        magSqr(2*(skew(fvc::grad(U))))
    );

    volVectorField curlU2
    (
        IOobject
        (
            "curlU2",
            runTime.timeName(),
            mesh,
            IOobject::NO_READ,
            IOobject::AUTO_WRITE
        ),
        fvc::curl(U)
    );

...

 // Construct incompressible turbulence model
    autoPtr<incompressible::turbulenceModel> turbulence
    (
        incompressible::turbulenceModel::New(U, rho, phi, twoPhaseProperties)
    //incompressible::turbulenceModel::New(U, phi, twoPhaseProperties)
    );

    relaxationZone relaxing(mesh, U, alpha1);
```

newSolver: newSolver.C

```
...

        curlU1=magSqr(2*(skew(fvc::grad(U))));
        curlU2=fvc::curl(U);
        turbulence->correct();
...
```

BIBLIOGRAPHY

J. Abanade, D. Greaves, and G. Iglesias. Wave farm impact on the beach profile: A case study. *Coastal Engineering*, 86:36–44, 2014.

F. Ahmed and N. Rajaratnam. Flow around bridge piers. *Journal of Hydraulic Engineering*, 124 (3):288–300, 1998.

A. Amini and N. Solaimani. The effects of uniform and nonuniform pile spacing variations on local scour at pile groups. *Marine Georesources & Geotechnology*, 0618(November):1–6, 2017.

A. Amini, B. W. Melville, T. M. Ali, and A. H. Ghazali. Clear-water local scour around pile groups in shallow-water flow. *Journal of Hydraulic Engineering*, 138(2):177–185, 2012.

A. F. O. Falcão. The shoreline owc wave power plant at the azores. In *Proceedings of 4th European Wave Energy Conference*, pages 42–47, 2000.

A. F. O. Falcão, L.M.C. Gato, and E.P.A.S. Nunes. A novel radial self-rectifying air turbine for use in wave energy converters. Part 2. results from model testing. *Renewable Energy*, 53:159–164, 2013.

F. Arena, A. Romolo, G. Malara, and A. Ascanelli. On design and building of a U-OWC wave energy converter in the mediterranean sea: a case study. In *ASME 2013 32nd International Conference on Ocean, Offshore and Arctic Engineering*, pages 1–8. American Society of Mechanical Engineers, 2013.

B. Ataie-Ashtiani and A. A. Beheshti. Experimental investigation of clear-water local scour at pile groups. *Journal of Hydraulic Engineering*, 132(10):1100–1104, 2006.

C. J. Baker. The laminar horseshoe vortex. *Journal of Fluid Mechanics*, 95(2):347–367, 1979.

C. Barbi, D. P. Favier, C. A. Maresca, and D. P. Telionis. Vortex shedding and lock-on of a circular cylinder in oscillatory flow. *Journal of Fluid Mechanics*, 170:527–544, 1986.

C. Baykal, B. M. Sumer, D. R. Fuhrman, N. G. Jacobsen, and J. Fredsøe. Numerical simulation of scour and backfilling processes around a circular pile in waves. *Coastal Engineering*, 122 (February):87–107, 2017.

A. Bayram and M. Larson. Analysis of scour around a group of vertical piles in the field. *Journal of Waterway, Port, Coastal, and Ocean Engineering*, 126(4):215–220, 2000.

H. B. Bingham, D. Ducasse, K. Nielsen, and R. Read. Hydrodynamic analysis of oscillating water column wave energy devices. *Journal of Ocean Engineering and Marine Energy*, 1(4):405–419, 2015. ISSN 21986452.

P. Boccotti. Caisson breakwaters embodying an owc with a small opening. Part i: Theory. *Ocean Engineering*, 34(5-6):806–819, 2007a.

P. Boccotti. Comparison between a U-OWC and a conventional owc. *Ocean Engineering*, 34(5-6): 799–805, 2007b.

P. Boccotti, P. Filianoti, V. Fiamma, and F. Arena. Caisson breakwaters embodying an owc with a small opening. Part ii: A small-scale field experiment. *Ocean Engineering*, 34(5-6):820–841, 2007.

A. Brendmo, J. Falnes, and P. M. Lillebekken. Lineår modelling of oscillating water columns including viscous loss. *Applied Ocean Research*, 18(2-3):65–75, 1996.

H. N. C. Breusers, G. Nicollet, and H. W. Shen. Local scour around cylindrical piers. *Journal of Hydraulic Research*, 15(3):211–252, 1977.

M. J. Briggs, C. E. Synolakis, G. S. Harkins, and D. R. Green. Laboratory experiments of tsunami runup on a circular island. *Pure and Applied Geophysics*, 144(3-4):569–593, 1995.

A. Brito-Melo, L. M. C. Gato, and A. J. N. A. Sarmento. Analysis of wells turbine design parameters by numerical simulation of the owc performance. *Ocean Engineering*, 29(12):1463–1477, 2002.

C. Brun, D. Tenchine, and E. J. Hopfinger. Role of the shear layer instability in the near wake behavior of two side-by-side circular cylinders. *Experiments in Fluids*, 36(2):334–343, 2004.

Bureau of Ocean Energy Management. Ocean Wave Energy. `http://www.boem.gov/Renewable-Energy-Program/Renewable-Energy-Guide/Ocean-Wave-Energy.aspx`, 2017. Accessed: 2017-07-07.

J. Cederberg, R. H. Sasso, and B. Flynn. Morphological Changes at the 32nd Street Breakwater. `http://www.coastalsystemsint.com/media/pop_morphological_changes.htm`, 2018. Accessed July 20, 2018.

CEM. *Coastal Engineering Manual*. US Army Corps of Engineers, 2002.

J. Chen, Z. Huang, C. Jiang, B. Deng, and Y. Long. An experimental study of changes of beach profile and mean grain size caused by tsunami-like waves. *Journal of Coastal Research*, 28(5): 1303–1312, 2012.

J. Chen, Z. H. Huang, C. B. Jiang, B. Deng, and Y. N. Long. Tsunami-induced scour at coastal roadways: a laboratory study. *Natural Hazards*, 69:655–674, 2013.

Y. M. Chiew and B. W. Melville. Local scour around bridge piers. *Journal of Hydraulic Research*, 25(1):15–26, 1987.

D. Chisholm. *Two-Phase Flow in Pipelines and Heat Exchangers*. G. Godwin in association with Institution of Chemical Engineers, London, UK, 1983.

W. R. Dally and J. Pope. Detached breakwaters for shore protection. Technical report, Coastal Engineering Research Center Vicksburg MS, 1986.

B. Dargahi. The turbulent flow field around a circular cylinder. *Experiments in Fluids*, 8(1-2):1–12, 1989.

Z. Z. Deng, Z. H. Huang, and A. W. K. Law. Wave power extraction by an axisymmetric oscillating-water-column converter supported by a coaxial tube-sector-shaped structure. *Applied Ocean Research*, 42:114–123, 2013.

Z. Z. Deng, Z. H. Huang, and A. W. K. Law. Wave power extraction from a bottom-mounted oscillating water column converter with a v-shaped channel. *Proceedings of the Royal Society A: Mathematical, Physical and Engineering Sciences*, 470:20140074, 2014.

DNV-GL. *DNV-RP-C205: Environmental conditions and environmental loads*. Det Norske Veritas, 2007.

A. Elhanafi, A. Fleming, G. Macfarlane, and Z. Leong. Numerical energy balance analysis for an onshore oscillating water columnwave energy converter. *Energy*, 116:539–557, 2016a. ISSN 03605442.

A. Elhanafi, G. Macfarlane, A. Fleming, and Z. Leong. Scaling and air compressibility effects on a three-dimensional offshore stationary owc wave energy converter. *Applied Energy*, 189:1–20, 2016b.

A. Elhanafi, A. Fleming, G. Macfarlane, and Z. Leong. Underwater geometrical impact on the hydrodynamic performance of an offshore oscillating water columnwave energy converter. *Renewable Energy*, 105:209–231, 2017a. ISSN 18790682.

A. Elhanafi, G. Macfarlane, A. Fleming, and Z. Leong. Scaling and air compressibility effects on a three-dimensional offshore stationary OWC wave energy converter. *Applied Energy*, 189:1–20, 2017b.

M. Escarameia and R. W. P. May. Scour around structures in tidal flows. Technical Report SR-522, HR Wallingford, Wallingford, 1999.

D. Evans. The oscillating water column wave-energy device. *IMA Journal of Applied Mathematics*, 22:423–433, 1978.

D. Evans. Wave-power absorption by systems of oscillating surface pressure distributions. *Journal of Fluid Mechanics*, 114:481–499, 1982.

D. V. Evans and R. Porter. Hydrodynamic characteristics of an oscillating water column device. *Applied Ocean Research*, 17(3):155–164, 1995.

A. F. O. Falcão. Wave energy utilization: A review of the technologies. *Renewable and sustainable energy reviews*, 14(3):899–918, 2010.

A. F. O. Falcão and J. C. C. Henriques. Model-prototype similarity of oscillating-water-column wave energy converters. *International Journal of Marine Energy*, 6:18–34, 2014.

A. F. O. Falcão, J. C. C. Henriques, and J. J. Cândido. Dynamics and optimization of the owc spar buoy wave energy converter. *Renewable energy*, 48:369–381, 2012.

J. Falnes. A review of wave-energy extraction. *Marine Structures*, 4:185–201, 2007.

A. Fleming and G. Macfarlane. Experimental flow field comparison for a series of scale model oscillating water column wave energy converters. *Marine Structures*, 52:108–125, 2017.

A. Fleming, I. Penesis, G. Macfarlane, N. Bose, and T. Denniss. Energy balance analysis for an oscillating water column wave energy converter. *Ocean Engineering*, 54:26–33, 2012.

M. Fossa and G. Guglielmini. Pressure drop and void fraction profiles during horizontal flow through thin and thick orifices. *Experimental Thermal and Fluid Science*, 26:513–523, 2002.

L. M. C. Gato, V. Warfield, and A. Thakker. Performance of a high-solidity wells turbine for an owc wave power plant. *Journal of energy resources technology*, 118(4):263–268, 1996.

Y. Goda. A comparative review on the functional forms of directional wave spectrum. *Coastal Engineering Journal*, 41(1):1–20, 1999.

Y. Goda and T. Suzuki. Estimation of incident and reflected waves in random wave experiments. In *Proceedings of the 15th Conference of Coastal Engineering*, pages 828–845, Reston, VA, USA, 1976. ASCE.

Y. Goda, H. Nakada, H. Ohneda, M. Suzuki, S. Takahashi, and M. Shikamori. Results of field experiment of a wave power extracting caisson breakwater. In *PROCEEDINGS OF CIVIL ENGINEERING IN THE OCEAN*, volume 7, pages 143–148. Japan Society of Civil Engineers, 1991.

D. Goring and F. Raichlen. The generation of long waves in the laboratory. In *Seventeenth International Conference on Coastal Engineering Conference*, volume 1, pages 763–783. American Society of Civil Engineers, 1980.

K. U. Graw, S. Schimmels, and J. Lengricht. Quantifying losses around the lip of an owc by use of particle image velocimetry (piv). *LACER-Leipzig Annual Civil Engineering Report, Aalborg, Denmark*, 2000.

R. Grimshaw. The solitary wave in water of variable depth. Part 2. *Journal of Fluid Mechanics*, 42(03):639–656, 1971.

Hawaii State Energy Office. State of Hawaii Energy Policy Directives. `http://energy.hawaii.gov/energypolicy`, 2007. Accessed: 2017-07-07.

T. Hayashi, M. Hattori, and M. Shirai. Closely spaced pile breakwater as a protection structure against beach erosion. In *Coastal Engineering 1968*, pages 606–621. 1969.

F. He and Z. Huang. Characteristics of orifices for modeling nonlinear power take-off in wave-flume tests of oscillating water column devices. *Journal of Zhejiang University-Science A*, 18(5): 329–345, 2017.

F. He and Z. H. Huang. Hydrodynamic performance of pile-supported owc-type structures as breakwaters: An experimental study. *Ocean Engineering*, 88:618–626, 2014.

F. He, Z. H. Huang, and A. W. K. Law. Hydrodynamic performance of a rectangular floating breakwater with and without pneumatic chambers: An experimental study. *Ocean Engineering*, 51:16–27, 2012.

F. He, Z. H. Huang, and A. W. K. Law. An experimental study of a floating breakwater with asymmetric pneumatic chambers for wave energy extraction. *Applied Energy*, 106:222–231, 2013.

F. He, M. Li, and Z. Huang. An experimental study of pile-supported owc-type breakwaters: energy extraction and vortex-induced energy loss. *Energies*, 9(7):540, 2016.

J. C. C. Henriques, J. J. Cândido, M. T. Pontes, and A. F. O. Falcão. Wave energy resource assessment for a breakwater-integrated oscillating water column plant at porto, portugal. *Energy*, 63:52–60, 2013.

J. C. Hu and Y. Zhou. Flow structure behind two staggered circular cylinders. Part 2. Heat and momentum transport. *Journal of Fluid Mechanics*, 607:81–107, 2008a.

J. C. Hu and Y. Zhou. Flow structure behind two staggered circular cylinders. Part 1. Downstream evolution and classification. *Journal of Fluid Mechanics*, 607:51–80, 2008b.

X. Hu and C. T. Chan. Refraction of water waves by periodic cylinder arrays. *Physical Review Letters*, 95(15):154501, 2005.

Z. H. Huang. An experimental study of wave scattering by a vertical slotted barrier in the presence of a current. *Ocean Engineering*, 34(5-6):717–723, 2007.

Z. H. Huang and Z. D. Yuan. Transmission of solitary waves through slotted barriers: A laboratory study with analysis by a long wave approximation. *Journal of Hydro-Environment Research*, 3 (4):179–185, 2010.

Z. H. Huang, Y. C. Li, and Y. Liu. Hydraulic performance and wave loadings of perforated/slotted coastal structures: A review. *Ocean Engineering*, 38(10):1031–1053, 2011.

M. Isaacson, S. Premasiri, and G. Yang. Wave interactions with vertical slotted barrier. *Journal of Waterway, Port, Coastal, and Ocean Engineering*, 124(3):118–126, 1998.

A. Iturrioz, R. Guanche, J. L. Lara, C. Vidal, and I. J. Losada. Validation of OpenFOAM® for oscillating water column three-dimensional modeling. *Ocean Engineering*, 107:222–236, 2015.

N. G. Jacobsen, D. R. Fuhrman, and J. Fredsöe. A wave generation toolbox for the open-source CFD library: OpenFoam®. *International Journal for Numerical Methods in Fluids*, 70(9):1073–1088, 2012.

J. A. Jendrzejczyk and S. S. Chen. Fluid forces on two circular cylinders in crossflow. Technical report, Argonne National Lab., 1985.

C. Jiang, Y. Yao, Y. Deng, and B. Deng. Numerical investigation of solitary wave interaction with a row of vertical slotted piles. *Journal of Coastal Research*, 31(6):1502–1511, 2015.

P. A Johnson. Comparison of pier-scour equations using field data. *Journal of Hydraulic Engineering*, 121(8):626–629, 1995.

S. Kakuno and P.L.F. Liu. Scattering of water waves by vertical cylinders. *Journal of Waterway Port Coastal and Ocean Engineering*, 119:302–322, 1993.

G. Kirkil, S. G. Constantinescu, and R. Ettema. Coherent structures in the flow field around a circular cylinder with scour hole. *Journal of Hydraulic Engineering*, 134(5):572–587, 2008.

D. L. Kriebel. Vertical wave barriers: wave transmission and wave forces. In *Coastal Engineering 1992*, pages 1313–1326. 1993.

R. Lanca, C. Fael, R. Maia, J. P. Pego, and A. H. Cardoso. Clear-water scour at pile groups. *Journal of Hydraulic Engineering*, 139(10):1089–1098, 2013.

R. S. Laramee, H. Hauser, H. Doleisch, B. Vrolijk, F. H. Post, and D. Weiskopf. The state of the art in flow visualization: Dense and texture-based techniques. In *Computer Graphics Forum*, volume 23, pages 203–221. Wiley Online Library, 2004.

W. Li, H. Yeh, and Y. Kodama. On the Mach reflection of a solitary wave: revisited. *Journal of Fluid Mechanics*, 672:1–32, 2011.

Y. Li and C. C. Mei. Multiple resonant scattering of water waves by a two-dimensional array of vertical cylinders: Linear aspects. *Physical Review E*, 76(1):016302, 2007.

D. Liang, H. Gotoh, N. Scott, and H. Tang. Experimental study of local scour around twin piles in oscillatory flows. *Journal of Waterway, Port, Coastal, and Ocean Engineering*, 139(5):404–412, 2012.

C. M. Linton and D. V. Evans. The interaction of waves with arrays of vertical circular cylinders. *Journal of Fluid Mechanics*, 215:549–569, 1990.

J. Liu, G. Xie, and T. W. Simon. Turbulent flow and heat transfer enhancement in rectangular channels with novel cylindrical grooves. *International Journal of Heat and Mass Transfer*, 81: 563–577, 2015.

P. L. F. Liu, Y. S. Cho, M. J. Briggs, U. Kanoglu, and C. E. Synolakis. Runup of solitary waves on a circular island. *Journal of Fluid Mechanics*, 302:259–285, 1995.

P. L. F. Liu, Y. S. Park, and E. A. Cowen. Boundary layer flow and bed shear stress under a solitary wave. *Journal of Fluid Mechanics*, 574:449–463, 2007.

Z. Liu, B. S. Hyun, and K. Y. Hong. Application of numerical wave tank to owc air chamber for wave energy conversion. In *The Eighteenth International Offshore and Polar Engineering Conference*, pages 350–356. International Society of Offshore and Polar Engineers, 2008.

M. S. Longuet-Higgins. On the joint distribution of wave periods and amplitudes in a random wave field. *Proceedings of the Royal Society of London*, 389:241–258, 1983.

I. López, J. Andreu, S. Ceballos, I. Martnez de Alegra, and I. Iigo Kortabarria. Review of wave energy technologies and the necessary power-equipment. *Renewable and Sustainable Energy Reviews*, 27:413–434, 2013.

I. López, A. Castro, and G. Iglesias. Hydrodynamic performance of an oscillating water column wave energy converter by means of particle imaging velocimetry. *Energy*, 83:89–103, 2015a.

I. López, B. Pereiras, F. Castro, and G. Iglesias. Performance of owc wave energy converters: influence of turbine damping and tidal variability. *International Journal of Energy Research*, 39 (4):472–483, 2015b.

I. López, B. Pereiras, F. Castro, and G. Iglesias. Holistic performance analysis and turbine-induced damping for an owc wave energy converter. *Renewable Energy*, 85:1155–1163, 2016.

S. Lovas, C. C. Mei, and Y. Liu. Oscillating water column at a coastal corner for wave power extraction. *Applied Ocean Research*, 32(3):267–283, 2010.

O. S. Madsen and W. D. Grant. Quantitative description of sediment transport by waves. In *Fifteenth International Conference on Coastal Engineering*, volume 2, pages 1093–1112. American Society of Civil Engineers, 1976.

P. A. Madsen, D. R. Fuhrman, and H. A. Schäffer. On the solitary wave paradigm for tsunamis. *Journal of Geophysical Research: Oceans*, 113(C12012):1–22, 2008.

C. Manes and M. Brocchini. Local scour around structures and the phenomenology of turbulence. *Journal of Fluid Mechanics*, 779:309–324, 2015.

H. Martins-Rivas and C. C. Mei. Wave power extraction from an oscillating water column at the tip of a breakwater. *Journal of Fluid Mechanics*, 626:395–414, 2009.

E. C. Maskell. Flow separation in three dimensions. Technical report, Ministry of Supply, Royal Aircraft Establishment, RAE Farnborough, 1955.

M. Mattioli, J. M. Alsina, A. Mancinelli, M. Miozzi, and M. Brocchini. Experimental investigation of the nearbed dynamics around a submarine pipeline laying on different types of seabed: the interaction between turbulent structures and particles. *Advances in Water Resources*, 48:31–46, 2012.

S. Mayer and P. A. Madsen. Simulation of breaking waves in the surf zone using a Navier-Stokes solver. *27th International Conference on Coastal Engineering*, I:928–941, 2000.

D. J. McGovern, S. Ilic, A. M. Folkard, S. J. McLelland, and B. J. Murphy. Time development of scour around a cylinder in simulated tidal currents. *Journal of Hydraulic Engineering*, 140(6): 04014014, 2014.

P. McIver and D. V. Evans. Approximation of wave forces on cylinder arrays. *Applied Ocean Research*, 6(2):101–107, 1984.

C. C. Mei. *The Applied Dynamics of Ocean Surface Waves*. World Scientific Publishing, Singapore, 1989.

B. W. Melville and Y. M. Chiew. Time scale for local scour at bridge piers. *Journal of Hydraulic Engineering*, 125(1):59–65, 1999.

B. W. Melville and A. J. Raudkivi. Flow characteristics in local scour at bridge piers. *Journal of Hydraulic Research*, 15(4):373–380, 1977.

B. W. Melville and A. J. Sutherland. Design method for local scour at bridge piers. *Journal of Hydraulic Engineering*, 114(10):1210–1226, 1988.

E. Mendoza, R. Silva, B. Zanuttigh, E. Angelelli, T. L. Andersen, L. Martinelli, J. Q. H. Nrgaard, and P. Ruolc. Beach response to wave energy converter farms acting as coastal defence. *Coastal Engineering*, 87:97–111, 2014.

D. L. Millar, H. C. M. Smith, and D. E. Reeve. Modelling analysis of the sensitivity of shoreline change to a wave farm. *Ocean Engineering*, 34(5-6):884–901, 2007.

M. T. Morris-Thomas, T. Michael, R. J. Irvin, and K. P. Thiagarajan. An investigation into the hydrodynamic effciency of an oscillating water column. *Journal of Offshore Mechanics and Arctic Engineering*, 129:273–279, 2007.

M. A. Mustapa, O. B. Yaakob, Y. M. Ahmed, C. Rheem, and K. K. Koh. Wave energy device and breakwater integration : A review. *Renewable and Sustainable Energy Reviews*, 77(April):43–58, 2017. ISSN 1364-0321.

M. Muzzammil and T. Gangadhariah. The mean characteristics of horseshoe vortex at a cylindrical pier. *Journal of Hydraulic Research*, 41(3):285–297, 2003.

D. Myrhaug and H. Rue. Scour around group of slender vertical piles in random waves. *Applied Ocean Research*, 27(1):56–63, 2005.

T. Nakamura, Y. Kuramitsu, and N. Mizutani. Tsunami scour around a square structure. *Coastal Engineering Journal*, 23101(2):209–246, 2008.

D. Ning, R. Wang, Y. Gou, M. Zhao, and B. Teng. Numerical and experimental investigation of wave dynamics on a land-fixed owc device. *Energy*, 115:326–337, 2016a.

D. Ning, R. Wang, Q. Zou, and B. Teng. An experimental investigation of hydrodynamics of a fixed owc wave energy converter. *Applied Energy*, 168:636 – 648, 2016b. ISSN 0306-2619.

M. Ohkusu. Wave action on groups of vertical circular cylinders. *Journal of the Society of Naval Architects of Japan*, 1972(131):53–64, 1972.

M. C. Ong, D. Myrhaug, and P. Hesten. Scour around vertical piles due to long-crested and short-crested nonlinear random waves plus a current. *Coastal Engineering*, 73:106–114, 2013.

A. E. Perry and B. D. Fairlie. Critical points in flow patterns. In *Advances in Geophysics*, volume 18, pages 299–315. Elsevier, 1975.

A. E. Perry and T. R. Steiner. Large-scale vortex structures in turbulent wakes behind bluff bodies. Part 1. Vortex formation processes. *Journal of Fluid Mechanics*, 174:233–270, 1987.

F. H. Post, B. Vrolijk, H. Hauser, R. S. Laramee, and H. Doleisch. The state of the art in flow visualisation: Feature extraction and tracking. In *Computer Graphics Forum*, volume 22, pages 775–792. Wiley Online Library, 2003.

A. Qadar. The vortex scour mechanism at bridge piers. In *Institution of Civil Engineers, Proceedings, Pt2*, volume 71, 1981.

E. V. Rapaka, R. Natarajan, and S. Neelamani. Experimental investigation on the dynamic response of a moored wave energy device under regular sea waves. *Ocean Engineering*, 31(5-6):725–743, 2004.

A. J. Raudkivi and R. Ettema. Clear-water scour at cylindrical piers. *Journal of Hydraulic Engineering*, 109(3):338–350, 1983.

E. V. Richardson, L. J. Harrison, J. R. Richardson, and S. R. Davis. Evaluating scour at bridges. Technical report, 1993.

J. E. Richardson and V. G. Panchang. Three-dimensional simulation of scour-inducing flow at bridge piers. *Journal of Hydraulic Engineering*, 124(5):530–540, 1998.

T. Rossetto, W. Allsop, I. Charvet, and D. I. Robinson. Physical modelling of tsunami using a new pneumatic wave generator. *Coastal Engineering*, 58(6):517–527, 2011.

A. Roulund, B. M. Sumer, J. Fredsøe, and J. Michelsen. Numerical and experimental investigation of flow and scour around a circular pile. *Journal of Fluid Mechanics*, 534:351–401, 2005.

H. Rusche. *Computational fluid dynamics of dispersed two-phase flows at high phase fractions*. PhD thesis, Imperial College London (University of London), 2003.

B. Sahin, N. A. Ozturk, and H. Akilli. Horseshoe vortex system in the vicinity of the vertical cylinder mounted on a flat plate. *Flow Measurement and Instrumentation*, 18(2):57–68, 2007.

T. M. Salaheldin, J. Imran, and M. H. Chaudhry. Numerical modeling of three-dimensional flow field around circular piers. *Journal of Hydraulic Engineering*, 130(2):91–100, 2004.

T. Salzbrunn, H. Janicke, T. Wischgoll, and G. Scheuermann. The state of the art in flow visualization: Partition-based techniques. In *Proceedings of the 2008 Simulation and Visualization Conference*, pages 75–92, 2008.

A. J. N. A. Sarmento and A. F. O. Falcão. Wave generation by an oscillating surface-pressure and its application in wave-energy extraction. *Journal of Fluid Mechanics*, 150:467–485, 1985.

T. Setoguchi and M. Takao. Current status of self rectifying air turbines for wave energy conversion. *Energy Conversion and Management*, 47(15-16):2382–2396, 2006.

T. Setoguchi, S. Santhakumar, H. Maeda, M. Takao, and K. Kaneko. A review of impulse turbines for wave energy conversion. *Renewable Energy*, 23:261–292, 2001.

S. Shafiei, B. W. Melville, and A. Y. Shamseldin. Experimental investigation of tsunami bore impact force and pressure on a square prism. *Coastal Engineering*, 110:1–16, 2016.

C. Sheehan and J. Harrington. An environmental and economic analysis for geotube coastal structures retaining dredge material. *Resources, Conservation and Recycling*, 61:91–102, 2012.

D. M. Sheppard, M. Odeh, and T. Glasser. Large scale clear-water local pier scour experiments. *Journal of Hydraulic Engineering*, 130(10):957–963, 2004.

M. J. Simon. Multiple scattering in arrays of axisymmetric wave-energy devices. Part 1. A matrix method using a plane-wave approximation. *Journal of Fluid Mechanics*, 120:1–25, 1982.

I. Simonetti, L. Cappietti, H. El Safti, and H. Oumeraci. Numerical modelling of fixed oscillating water column wave energy conversion devices: Toward geometry hydraulic optimization. In *Proceedings of the ASME 2015 34th International Conference on Ocean, Offshore and Arctic Engineering*, volume 9, pages 1–10, 2015.

R. Soulsby. *Dynamics of Marine Sands: A Manual for Practical Applications*. Thomas Telford, 1997.

B. H. Spring and P. L. Monkmeyer. Interaction of plane waves with vertical cylinders. In *Coastal Engineering 1974*, pages 1828–1847. 1975.

T. R. Steiner and A. E. Perry. Large-scale vortex structures in turbulent wakes behind bluff bodies. Part 2. Far-wake structures. *Journal of Fluid Mechanics*, 174:271–298, 1987.

Z. H. Su. Experimental study of the breakwater efficiency of a cylindrical pile model. Technical report, Final Year Project Report, Department of Civil and Environment Engineering, Nanyang Technological University, Singapore, 2013.

K. D. Suh, H. Y. Jung, and C. K. Pyun. Wave reflection and transmission by curtainwall–pile breakwaters using circular piles. *Ocean Engineering*, 34(14-15):2100–2106, 2007.

K. D. Suh, C. H. Ji, and B. H. Kim. Closed-form solutions for wave reflection and transmission by vertical slotted barrier. *Coastal Engineering*, 58(12):1089–1096, 2011.

B. M. Sumer and J. Fredsøe. Wave scour around group of vertical piles. *Journal of Waterway, Port, Coastal, and Ocean Engineering*, 124(5):248–256, 1998.

B. M. Sumer and J. Fredsöe. Wave scour around structures. In *Advances in Coastal and Ocean Engineering*, pages 191–249. World Scientific, 1999.

B. M. Sumer and J. Fredsöe. Wave scour around a large vertical circular cylinder. *Journal of Waterway, Port, Coastal, and Ocean Engineering*, 127(3):125–134, 2001a.

B. M. Sumer and J. Fredsöe. Scour around pile in combined waves and current. *Journal of Hydraulic Engineering*, 127(5):403–411, 2001b.

B. M. Sumer, N. Christiansen, J. Fredsöe, et al. Time scale of scour around a vertical pile. In *The Second International Offshore and Polar Engineering Conference*, number 3, pages 308–315. International Society of Offshore and Polar Engineers, 1992a.

B. M. Sumer, J. Fredsöe, and N. Christiansen. Scour around vertical pile in waves. *Journal of Waterway, Port, Coastal, and Ocean Engineering*, 118(1):15–31, 1992b.

B. M. Sumer, N. Christiansen, and J. Fredsöe. Influence of cross section on wave scour around piles. *Journal of Waterway, Port, Coastal, and Ocean Engineering*, 119(5):477–495, 1993.

B. M. Sumer, N. Christiansen, and J. Fredsöe. The horseshoe vortex and vortex shedding around a vertical wall-mounted cylinder exposed to waves. *Journal of Fluid Mechanics*, 332:41–70, 1997.

B. M. Sumer, J. Fredsöe, K. Bundgaard, et al. Global and local scour at pile groups. In *The Fifteenth International Offshore and Polar Engineering Conference*. International Society of Offshore and Polar Engineers, 2005.

B. M. Sumer, M. B. Sen, I. Karagali, B. Ceren, J. Fredsöe, M. Sottile, L. Zilioli, and D. R. Fuhrman. Flow and sediment transport induced by a plunging solitary wave. *Journal of Geophysical Research: Oceans*, 116(1):1–15, 2011.

B. M. Sumer et al. *The Mechanics of Scour in the Marine Environment*, volume 17. World Scientific Publishing Company, 2002.

V. Sundar. Hydrodynamic pressures and forces on quadrant front face pile supported breakwater. *Ocean Engineering*, 29(2):193–214, 2002.

W. K. Tease, J. Lees, and A. Hall. Advances in Oscillating Water Column Air Turbine Development. *7th European Wave Energy Conference*, (September), 2007.

P. R. F. Teixeira, D. P. Davyt, E. Didier, and R. Ramalhais. Numerical simulation of an oscillating water column device using a code based on Navier-Stokes equations. *Energy*, 61:513–530, 2013. ISSN 03605442.

F. Thomalla and C. E. Vincent. Beach response to shore-parallel breakwaters at Sea Palling, Norfolk, UK. *Estuarine, coastal and shelf science*, 56(2):203–212, 2003.

S. Tonkin, H. Yeh, F. Kato, and S. Sato. Tsunami scour around a cylinder. *Journal of Fluid Mechanics*, 496:165–192, 2003.

Y. Torre-Enciso, I. Ortubia, L. I. L. de Aguileta, and J. Marqués. Mutriku wave power plant: from the thinking out to the reality. In *Proceedings of the 8th European Wave and Tidal Energy Conference, Uppsala, Sweden*, volume 710, pages 319–329, 2009.

R. S. Tseng, R.H. Wu, and C. C. Huang. Model study of a shoreline wave-power system. *Ocean Engineering*, 27(8):801–821, 2000.

J. Unger and W. H. Hager. Down-flow and horseshoe vortex characteristics of sediment embedded bridge piers. *Experiments in Fluids*, 42(1):1–19, 2007.

H. K. Versteeg and W. Malalasekera. *An Introduction to Computational Fluid Dynamics: The Finite Volume Method*. Pearson Education, 2007.

T. Vyzikas, S. Deshoulières, M. Barton, O. Giroux, D. Greaves, and D. Simmonds. Experimental investigation of different geometries of fixed oscillating water column devices. *Renewable Energy*, 104:248–258, 2017.

C. Z. Wang and G. X. Wu. Interactions between fully nonlinear water waves and cylinder arrays in a wave tank. *Ocean Engineering*, 37(4):400–417, 2010.

D. J. Wang, M. Katory, and Y. S. Li. Analytical and experimental investigation on the hydrodynamic performance of onshore wave-power devices. *Ocean Engineering*, 29(8):871–885, 2002.

R. Wang, D. Ning, C. Zhang, Q. Zou, and Z. Liu. Nonlinear and viscous effects on the hydrodynamic performance of a fixed OWC wave energy converter. *Coastal Engineering*, 131:42–50, 2018.

D. C Wilcox. *Turbulence Modeling for CFD*, volume 2. DCW industries La Canada, CA, 1993.

D. C Wilcox. Formulation of the $k-\omega$ turbulence model revisited. *AIAA Journal*, 46(11):2823–2838, 2008.

C. H. K. Williamson. Sinusoidal flow relative to circular cylinders. *Journal of Fluid Mechanics*, 155:141–174, 1985.

J. Wu, L. W. Welch, M. C. Welsh, J. Sheridan, and G. J. Walker. Spanwise wake structures of a circular cylinder and two circular cylinders in tandem. *Experimental Thermal and Fluid Science*, 9(3):299–308, 1994.

C. H. Xu, Z. H. Huang, and Z. Z. Deng. Experimental and theoretical study of a cylindrical oscillating water column device with a quadratic power take-off model. *Applied Ocean Research*, 57:19–29, 2016.

C. H. Xu and Z. H. Huang. A dual-functional wave-power plant for wave-energy extraction and shore protection: A wave-flume study. *Applied Energy*, 229:963–976, 2018.

H. Yeh, P. Liu, M. Briggs, and C. Synolakis. Propagation and amplification of tsunamis at coastal boundaries. *Nature*, 372(6504):353, 1994.

S. C. Yen and C. W. Yang. Flow patterns and vortex shedding behavior behind a square cylinder. *Journal of Wind Engineering and Industrial Aerodynamics*, 99(8):868–878, 2011.

S. C. Yen, K. C. San, and T. H. Chuang. Interactions of tandem square cylinders at low Reynolds numbers. *Experimental Thermal and Fluid Science*, 32(4):927–938, 2008.

Y. L. Young, H. Xiao, and T. Maddux. Hydro- and morpho-dynamic modeling of breaking solitary waves over a fine sand beach. Part I: Experimental study. *Marine Geology*, 269(3-4):107–118, 2010.

M. M. Zdravkovich. The effects of interference between circular cylinders in cross flow. *Journal of Fluids and Structures*, 1(2):239–261, 1987.

Y. Zhang, Q. Zou, and D. Greaves. Air-water two-phase flow modelling of hydrodynamic performance of an oscillating water column device. *Renewable Energy*, 41:159–170, 2012. ISSN 09601481.

G. Zhao and D. M. Sheppard. The effect of flow skew angle on sediment scour near pile groups. In *Stream Stability and Scour at Highway Bridges: Compendium of Stream Stability and Scour Papers Presented at Conferences Sponsored by the Water Resources Engineering (Hydraulics) Division of the American Society of Civil Engineers*, pages 377–391. ASCE, 1999.

M. Zhao, L. Cheng, and Z. Zang. Experimental and numerical investigation of local scour around a submerged vertical circular cylinder in steady currents. *Coastal Engineering*, 57(8):709–721, 2010.